

AD-A013 922

TRANSIENT RADIATION EFFECTS IN OPTICAL MATERIALS

Michael J. Treadaway, et al

Intelcom Rad Tech

Prepared for:

Space and Missile Systems Organization

29 April 1975

DISTRIBUTED BY:

NTIS

National Technical Information Service
U. S. DEPARTMENT OF COMMERCE

245094

SAMSO-TR-75-174

ADA013922

TRANSIENT RADIATION EFFECTS IN OPTICAL MATERIALS

M. J. Treadaway
B. C. Passenheim
B. D. Kitterer

IRT Corporation
P.O. Box 80817
San Diego, Calif. 92138

April 29, 1975

Final Report for Period February 1974 through April 1975

Contract No.
F04701-74-C-0237

Approved for public release; distribution unlimited

This work sponsored by
Defense Nuclear Agency
under Subtask Z99QAXTA026

Prepared for

Hq Space & Missile Systems Organization/DYR
P.O. Box 92960, Worldway Postal Center
Los Angeles, Calif. 90009

Reproduced by
NATIONAL TECHNICAL
INFORMATION SERVICE
U.S. Department of Commerce
Springfield, VA. 22151



UNCLASSIFIED

SECURITY CLASSIFICATION OF THIS PAGE (When Data Entered)

REPORT DOCUMENTATION PAGE		READ INSTRUCTIONS BEFORE COMPLETING FORM												
1. REPORT NUMBER SAMSO TR-75-174	2. GOVT ACCESSION NO.	3. RECIPIENT'S CATALOG NUMBER												
4. TITLE (and Subtitle) Transient Radiation Effects in Optical Materials		5. TYPE OF REPORT & PERIOD COVERED FINAL: February 1974 through April 1975												
		6. PERFORMING ORG. REPORT NUMBER INTEL-RT 6068-044												
7. AUTHOR(s) Michael J. Treadaway, Burr C. Passenheim, Bob D. Kitterer		8. CONTRACT OR GRANT NUMBER(s) F04701-74-C-0237												
9. PERFORMING ORGANIZATION NAME AND ADDRESS Intelcom Rad Tech (IRT) P.O. Box 80817 San Diego, California 92138		10. PROGRAM ELEMENT, PROJECT, TASK AREA & WORK UNIT NUMBERS												
11. CONTROLLING OFFICE NAME AND ADDRESS Hq Space & Missile Systems Organization/DYR P.O. Box 92960, Worldway Postal Center Los Angeles, California 90009		12. REPORT DATE April 29, 1975												
14. MONITORING AGENCY NAME & ADDRESS (if different from Controlling Office) SAME		13. NUMBER OF PAGES												
		15. SECURITY CLASS. (of this report) UNCLASSIFIED												
		15a. DECLASSIFICATION DOWNGRADING SCHEDULE												
16. DISTRIBUTION STATEMENT (of this Report) Approved for public release; distribution unlimited														
17. DISTRIBUTION STATEMENT (of the abstract entered in Block 20, if different from Report) SAME														
18. SUPPLEMENTARY NOTES This project was sponsored by Hq DNA under Subtask Z99QAXTA026														
19. KEY WORDS (Continue on reverse side if necessary and identify by block number) <table border="0"> <tr> <td>Radioluminescence</td> <td>Color centers</td> <td>Glass</td> </tr> <tr> <td>Luminescence</td> <td>Quartz</td> <td>Ultraviolet spectra</td> </tr> <tr> <td>Absorption</td> <td>Sapphire</td> <td>Visible spectra</td> </tr> <tr> <td>Transient radiation effects</td> <td></td> <td>Annealing</td> </tr> </table>			Radioluminescence	Color centers	Glass	Luminescence	Quartz	Ultraviolet spectra	Absorption	Sapphire	Visible spectra	Transient radiation effects		Annealing
Radioluminescence	Color centers	Glass												
Luminescence	Quartz	Ultraviolet spectra												
Absorption	Sapphire	Visible spectra												
Transient radiation effects		Annealing												
20. ABSTRACT (Continue on reverse side if necessary and identify by block number) The results of an extensive investigation of the optical response of thirteen common optical materials to 2.5-MeV electron irradiation is reported. Radiation-induced absorption and absolute radioluminescence yields were measured in the wavelength range 0.14 to 0.9 μm for dose rates between 5×10^2 to 5×10^5 rad/sec at doses from 2.3×10^3 to 4.5×10^8 rads.														

D D C

AUG 15 1975

B

UNCLASSIFIED

SECURITY CLASSIFICATION OF THIS PAGE(When Data Entered)

20 cont.

Sapphire, fused and crystalline quartz and ten Schott optical glasses were investigated. Determinations were made of (a) the absolute radioluminescence yield, (b) the dose rate dependence yield, (c) the spectral and temporal distribution of the radioluminescence and induced absorption, (d) the growth curve of the induced absorption versus total dose, (e) the dose-rate dependence of the absorption, and (f) the bleaching of the absorption after irradiation. In addition, where available, samples from different melts were investigated to determine the variation in the above effects with manufacturing variation.

UNCLASSIFIED

SECURITY CLASSIFICATION OF THIS PAGE(When Data Entered)

CONTENTS

1. INTRODUCTION	1
1.1 Background	1
1.2 Summary of Results	2
2. EXPERIMENTAL	5
2.1 Samples	5
2.2 Optical System	7
2.2.1 Sample Chamber	9
2.2.2 Vacuum Ultraviolet Monochromator	10
2.2.3 Detector Assembly	11
2.2.4 Calibration	11
2.2.5 Wavelength Calibration	14
2.3 Special Electronics for <u>In Situ</u> Measurements	17
2.3.1 Sample Positioning	18
2.3.2 Ratioing Electronics	18
2.3.3 Beam Steering System	23
2.4 DK-1A	23
2.5 Dosimetry	23
2.5.1 Faraday Cup	27
2.5.2 Cobalt-Glass Dosimetry	27
2.5.3 Stopping Block	27
3. ABSORPTION MEASUREMENTS	30
3.1 Permanent Absorption Measurements	32
3.1.1 Melt-to-Melt Variation of the Induced Absorption	36
3.1.2 Temporal Bleaching	36
3.1.3 Absorption as a Function of Fluence	48
3.1.4 Flux Dependence of the Induced Absorption	69
3.2 Intermediate Absorption Measurements	70
3.3 Transient Absorption Measurements	75
4. RADIOLUMINESCENCE MEASUREMENTS	82
4.1 Spectral Distribution	82
4.2 Temporal Distribution	88
4.3 Flux Dependence of the Radioluminescence Yield	90
4.4 Conversion Efficiency	96
REFERENCES	104
APPENDIX A - ⁶⁰ Co GAMMA IRRADIATION AND OPTICAL BLEACHING MEASUREMENTS	105
APPENDIX B - TRANSMISSION LOSSES AND RECOVERY OF OTHER SCHOTT GLASSES EXPOSED TO 10-MeV ELECTRONS	120
APPENDIX C - ABSOLUTE INTENSITY CALIBRATION OF THE <u>IN-SITU</u> OPTICAL SYSTEM	132
APPENDIX D - TEMPORAL BLEACHING CORRECTION TO DARKENING CURVES	136
APPENDIX E - LITERATURE SURVEY	145

FIGURES

1. Schematic of <u>in situ</u> optical system	7
2. Cutaway drawing of sample chamber.	8
3. Sample wheel and sample holders.	10
4. Typical photomultiplier response characteristics	12
5. Transmission spectra for quartz, glass, and KRS-5 filters	13
6. Tungsten spectral radiant emittance at several temperatures	15
7. Absolute intensity calibration of <u>in situ</u> optical system	16
8. Block diagram of ratioing electronics	19
9. Schematic diagram of log amplifier designed for 10 mA to 10 μ A signals	20
10. Schematic diagram of sample-and-hold, ratioing, and antilog circuitry	21
11. Transmission spectra of Schott SK-7 glass taken with two different instruments. Differences were traced to 50 Å difference in wavelength calibration of two systems	24
12. Pulsing electronics for steering magnet	25
13. Optical diagram of DK-1A spectrophotometer	26
14. Schematic of Faraday cup	28
15. Absorption spectra of irradiated sapphire	33
16. Absorption spectra of irradiated crystalline quartz	34
17. Absorption spectra of irradiated Suprasil 2	35
18. Bleaching of SK-14 absorption spectra	39
19. Bleaching of SK-7 absorption spectra	40
20. Bleaching of LaK-10 absorption spectra	41
21. Bleaching of SF-10 absorption spectra	42
22. Bleaching of SF-11 absorption spectra	43
23. Bleaching of BK-7 absorption spectra	44
24. Bleaching of UBK-7 absorption spectra	45
25. Bleaching of BaK-7 absorption spectra	46
26. Bleaching of KzFS-N4 absorption spectra	47
27. SK-14 absorption spectra at several fluences	49
28. SK-7 absorption spectra at several fluences	50
29. LaK-10 absorption spectra at several fluences.	51
30. SF-10 absorption spectra at several fluences	52

31.	SF-11 absorption spectra at several fluences	53
32.	BK-7 absorption spectra at several fluences	54
33.	UBK-7 absorption spectra at several fluences	55
34.	BaK-4 absorption spectra at several fluences	56
35.	KzFS-N4 absorption spectra at several fluences	57
36.	SK-14 absorption growth curves	59
37.	SK-7 absorption growth curves	60
38.	LaK-10 absorption growth curves	61
39.	SF-10 absorption growth curves	62
40.	SF-11 absorption growth curves	63
41.	BK-7 absorption growth curves	64
42.	UBK-7 absorption growth curves	65
43.	BaK-4 absorption growth curves	66
44.	KzFS-N4 absorption growth curves	67
45.	SF-10 absorption spectra at two fluxes	71
46.	SF-11 absorption spectra at two fluxes	72
47.	Apparatus for making transient absorption measurements	77
48.	Transient absorption spectrum of sapphire	78
49.	Transient absorption spectrum of BaK-4	79
50.	Sapphire radioluminescence spectrum at 10^{11} e/cm ² -sec	83
51.	Sapphire radioluminescence spectrum at 10^{12} e/cm ² -sec	84
52.	Crystalline quartz radioluminescence spectra	85
53.	Suprasil 2 radioluminescence spectrum	86
54.	BK7-G14 radioluminescence spectrum	87
55.	Sapphire radioluminescence intensity versus dose rate at 6928 and 3005 Å	92
56.	Crystalline quartz radioluminescence intensity versus dose rate at 3200 and 1950 Å	93
57.	BK7-G14 radioluminescence intensity versus dose rate at 4200 Å	94
58.	Spectrally integrated radioluminescence intensity versus dose rate: crystalline quartz, sapphire, Suprasil 2, BK7-G14.	95
59.	Spectrally integrated radioluminescence intensity versus dose rate: Schott BK-7, BaK-4, SF-10.	97
60.	Spectrally integrated radioluminescence intensity versus dose rate: Schott SK-7, SK-14, SF-11	98
61.	Spectrally integrated radioluminescence intensity versus dose rate: Schott KzFS-N4, LaK-10, UBK-7	99

ACKNOWLEDGMENTS

We wish to acknowledge the assistance of Captain Wayne Schober of SAMSO, who has acted as contract monitor, and Dr. Paul Schall of Aerospace Corporation, who has acted as technical advisor during this investigation. Their assistance in the initial planning and suggestions throughout the course of the investigation have been of great assistance.

In addition, we gratefully acknowledge the assistance of Dr. Bruce Anspaugh of Jet Propulsion Laboratory, who gave freely of his expertise and personal time during our irradiations at the JPL Dynamitron facility. We further appreciate technical communications from Dr. Leonard Larks of Jet Propulsion Laboratory.

1. INTRODUCTION

1.1 BACKGROUND

Refractive optical components aboard earth-orbiting satellites and exploratory spacecraft are subject to bombardment by high-energy ionizing radiation which can severely impact the optical properties of these components (Refs. 1-3). Many space-borne optical systems operate in the ultraviolet, visible, and near-infrared range.

Transmission losses due to the formation of color centers in refractive components degrade the system's performance by reducing signal strengths. In addition, exposure to ionizing radiation may cause refractive components to luminesce with sufficient intensity to cause an increase in optical noise, flash blindness of photo detectors, or, in extreme cases, detector failure. Information on the magnitude of these effects in typical optical materials is required to provide the basis for selection of appropriate materials and assess system performance capabilities in radiation environments.

The nature and intensity of the radiation environment encountered depend upon the mission of each spacecraft and can vary greatly. The earth's natural charged-particle radiation is trapped in a magnetic bottle formed by the earth's magnetosphere, and electron fluxes can be as high as 10^8 e/cm²-sec, with 99% of the particles having energy less than 1.6 MeV (Ref. 4). In addition, trapped artificial radiation resulting from high-altitude nuclear explosions can alter the intensity and energy spectrum of the earth's radiation environment. For example, after the high-altitude explosion of July 9, 1962, flux levels of 10^9 e/cm²-sec were observed, with only 55% of the particles having energies less than 1 MeV. Exploratory spacecraft may also encounter intense radiation levels such as those discovered in the Jovian magnetosphere (Ref. 5).

This report describes a room-temperature investigation of the radio-luminescence and radiation-induced absorption of thirteen common optical

materials: ten common Schott optical glasses, crystalline quartz, Suprasil, and sapphire in the spectral range 1400 to 9000 Å. The samples were exposed to 2.5-MeV electrons at flux levels from 10^{10} to 10^{13} e/cm²-sec to total fluences from 5×10^{10} to 10^{16} e/cm².

Determinations were made of (a) the absolute radioluminescent yield, (b) the flux dependence of the radioluminescent yield, (c) the spectral and temporal distribution of the radioluminescence, (d) the growth of the induced absorption as a function of total dose, (e) the dose-rate dependence of the absorption, and (f) the bleaching of the absorption after irradiation. In addition, to determine the variation in the above effects with manufacturing variations, duplicate glass samples from different melts were tested.

Prior to making the above measurements, a preliminary investigation, designed to give an indication of the magnitude and spectral distribution of the darkening in the Schott glasses, was carried out before launching the full-scale investigation. These samples were subsequently used to study the optical bleaching of the induced absorption, and the results of these measurements are included in Appendix A.

In addition, radiation darkening measurements of five additional Schott glass types are presented in Appendix B. These measurements were made before and after irradiation with 10-MeV electrons for Dr. Leonard Larks of Jet Propulsion Laboratory by IRT.

1.2 SUMMARY OF RESULTS

During the course of this investigation, a mountain of data was accumulated, and the authors feel that it would be highly instructive to summarize the results at this point.

After exposure to a fluence of 1×10^{16} e/cm², Schott BK7-G14 displayed no radiation-induced absorption, while sapphire, crystalline quartz, and Suprasil displayed a small amount of absorption near 2000 to 2200 Å. The remaining Schott glasses proved to be very "soft"; all of them displayed noticeable darkening after exposure to 5×10^{12} e/cm², with some glasses darkening noticeably after exposure to 5×10^{11} e/cm². Of these glasses, SF-10 and SF-11 appeared to be the most resistant to

radiation darkening, based on the results of measurements made 90 sec after irradiation. Subsequent measurements showed that the SF-10 and SF-11 samples were as susceptible as the other glass samples, but that the darkening bleached significantly within the first 90 sec after irradiation.

A dose-rate dependence of the radiation darkening (measured 90 sec after irradiation) was observed in Schott SF-10 and SF-11. This dependence was not observed for exposure at 4.5×10^4 rad/sec (1×10^{12} e/cm²-sec) but was dramatic at 2.5×10^5 rad/sec (5.5×10^{12} e/cm²-sec). The measured darkening was less when the samples were exposed at the higher rate. This should be kept in mind when planning future accelerated tests.

Transient absorption measurements in the 1-msec to 1-sec time regime showed that only sapphire and Schott BaK4 displayed transient absorption. The transient absorption appeared in the 3000 to 3500 Å region and had lifetimes on the order of 50 msec.

Luminescence measurements showed that the spectrally integrated radioluminescence intensity of sapphire was an order of magnitude greater than quartz and BK7-G14 glass, which was an order of magnitude greater than Suprasil and the rest of the Schott glasses.

The radioluminescence from crystalline quartz and Suprasil was limited to the near UV. Sapphire samples also displayed broad-band UV luminescence in addition to a sharp red line which is undoubtedly attributable to chromium impurity. Schott BK7-G14 displayed a broad luminescence band which peaked near 4200 Å. The radioluminescence intensity of the remaining Schott glasses was too weak to be observed spectrally, but must be in the visible and near IR due to self-absorption of luminescence produced at wavelengths shorter than the "band edge." (The band edge of most of these samples is between 3000 and 3900 Å).

In view of these results, the samples can be divided into four categories:

1. Crystalline quartz and sapphire
 - a. Darken only slightly in the UV
 - b. Luminesces with high efficiency mainly in UV (sapphire has red chromium luminescence)

2. BK7-G14
 - a. Does not darken
 - b. Luminesces with high efficiency (broad-band centered at 4200 Å).
3. Suprasil 2
 - a. Darkens only slightly in UV
 - b. Luminesces with low efficiency in UV
4. Remaining Schott glasses
 - a. Darken readily
 - b. Luminesces at wavelengths greater than 4000 Å, with very low efficiency.

Since these components are being considered for use in a spaceborne optical system which will employ active optical components (detectors) and will be subject to a radiation environment, the optimum material should (1) be radiation-hard, (2) have a low radioluminescence efficiency, and (3) have optical properties amenable to the function of the specific system. Of the materials used in this investigation, Suprasil 2 appears to fit these parameters best. In cases where indices of refraction and Abbe numbers such as those possessed by the Schott glasses are desired, a two-element system could be used, with the first element being a Suprasil 2 flat. The Suprasil 2 flat would (1) attenuate the radiation, (2) not darken in the wavelength region where the Schott glasses transmit, and (3) have its luminescence absorbed in the Schott glasses, thereby eliminating optical noise received by the detector.

2. EXPERIMENTAL

2.1 SAMPLES

The samples were procured from various vendors:

Sapphire (UV grade) - Union Carbide, Linde Division

Suprasil 2 - Amersil

Crystalline quartz (Z cut) - Sawyer Research Products, Inc.

10 glasses - Schott Optical Glass

Table 1 summarizes the physical and optical properties of the samples. Column 1 is the material name; for the glasses, Schott's nomenclature is used. Column 2 indicates the "index of refraction - Abbe number" coordinates of each glass. The first three digits are $(n_d - 1)$, where n_d is the index of refraction of the helium yellow line (5867 Å); so if $n_d = 1.540$, then $(n_d - 1) = 0.540$. The second three digits represent ten times the Abbe number, v , where $v = (n_e - 1)/(n_F - n_C)$, in which n_F is the index of refraction of the blue cadmium line (4861 Å), n_C is the index of refraction at the red cadmium line (6563 Å), and n_e is at the mercury green line (5416 Å). Each material (type and melt) was assigned a code number, shown in column 3. Column 4 gives the Schott melt identification. Column 5 gives the sample thickness which, for the Schott glasses, was chosen such that exposure to equivalent fluences resulted in equivalent energy deposition. The density is given in column 6, and the number of samples procured is given in column 7.

The Schott glass samples were polished by Optico Glass Fabrication, San Dimas, California. The remaining samples were polished by the respective manufacturers. All samples were scribed with the appropriate code which identified the sample type, melt, and individual sample. In addition, the code was used as a reference to ensure consistent sample orientation during repetitive measurements to minimize those effects which may result from slight non-parallelism of the sample surfaces. Typically, the samples were parallel to within 12 sec of arc.

Table 1
SAMPLES

Sample Type	$\frac{(n_d-1)}{10v}$	Code ^a	Melt No.	Thickness ^b (cm)	Density (g/cm ³)	Total No. Samples
BaK-4	577/587	BA	331904/X, LK9056	0.16	3.10	20
BK-7	520/642	CA	G1129/I, LK584	0.20	2.51	10
BK-7	520/642	CV	G1110/I, LK536	0.20	2.51	10
BK7-G14	520/642	TA	362672/I, LK20959	0.21	2.53	12
KzFS-N4	613/443	KA	700470/3-5, LK9242	0.16	3.20	10
KzFS-N4	613/443	KV	700473/5, LK9242	0.16	3.20	10
LaK-10	720/504	LA	B499, LK463	0.13	3.81	10
LaK-10	720/504	LV	B128, LK116	0.13	3.81	10
SF-10	728/284	FA	F175, LK33	0.11	4.28	10
SF-10	728/284	FV	351554/III, LK9091	0.11	4.28	10
SF-11	785/258	VA	G167/III, LK127	0.10	4.74	11
SF-11	785/258	VV	G168, LK127	0.10	4.74	9
SK-7	607/595	XA	F578, LK181	0.14	3.51	10
SK-7	607/595	XV	332773/IV, LK20223	0.14	3.51	10
SK-14	603/606	NA	312930/II, LK21088	0.14	3.44	10
SK-14	603/606	NV	B310, LK262	0.14	3.44	10
UBK-7	517/643	HA	322526/I, LK9215	0.20	2.51	10
UBK-7	517/643	HV	13988	0.20	2.51	10
Quartz, Z-cut	599/-	OA	-	0.20	2.65	6
Sapphire	702/-	SA	-	0.20	4.00	6
Supra- sil 2	419/-	UA	T-20	0.32	2.19	6

^aCode key: B A 07

Individual sample number
Melt reference
Sample type reference

^bAll samples 2.54 cm high x 3.81 cm wide; dimensional tolerance ± 0.01 cm.

2.2 OPTICAL SYSTEM

The short-wavelength limit to which optical measurements can be made in air is limited by the oxygen absorption band at 1400 \AA (Ref. 6). Excited oxygen molecules resulting from absorption of light in this band have a significant cross section for the formation of ozone. Consequently, if a light source is sufficiently UV-rich, the short-wavelength limit is shifted to nearly 3000 \AA due to the broad ozone absorption band at 2600 \AA . Therefore, to make optical measurements in the $1400\text{-}2000 \text{ \AA}$ region, it is necessary to enclose the optical path in a vacuum. Typically, vacuums better than 10^{-4} torr are required (Ref. 7).

In situ and ultraviolet measurements were made using the optical system shown in Figure 1. Since many of these measurements were made below 2000 \AA , the system was evacuated to 10^{-4} to 10^{-5} torr. The system consisted of three elements: sample chamber, vacuum ultraviolet monochromator, and detector assembly.

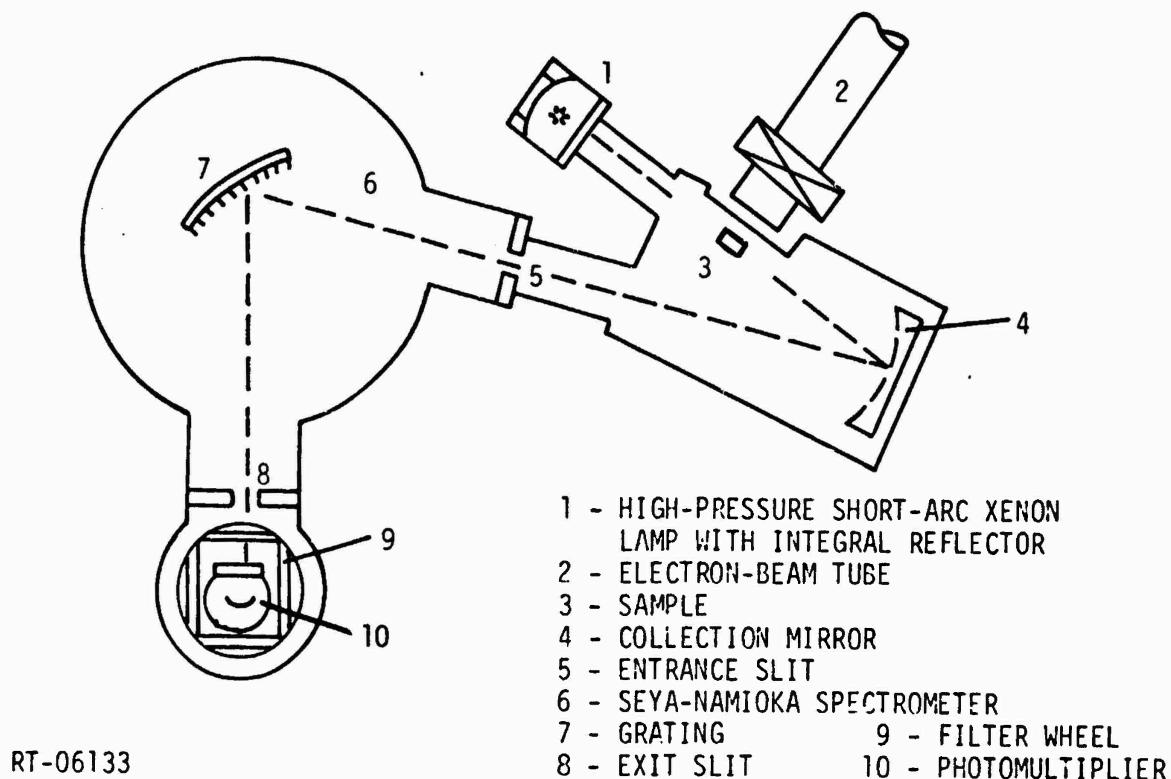


Figure 1. Schematic of *in situ* optical system

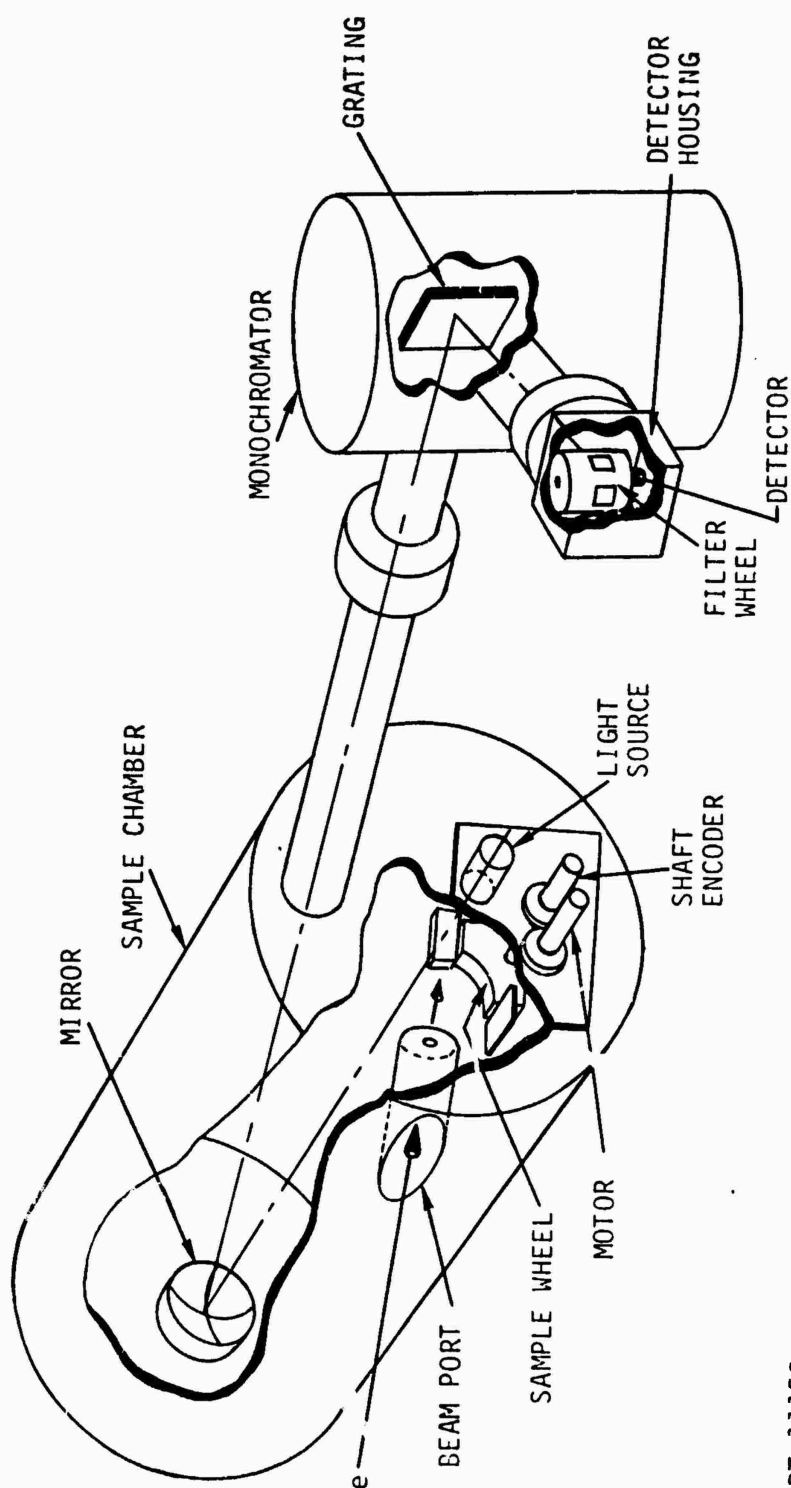


Figure 2. Cutaway drawing of sample chamber

RT-11158

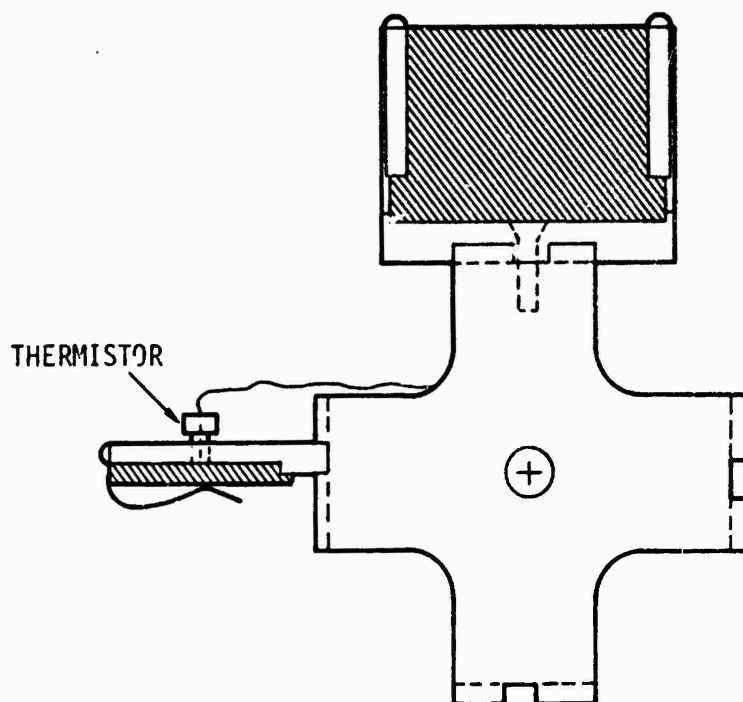
2.2.1 Sample Chamber

A cutaway drawing of the sample chamber is shown in Figure 2. The light source, sample wheel, position encoder, and drive motor were mounted on a single removable O-ring sealed plate. The source was a high-pressure xenon arc lamp, model VIX150 UV (12.5 V dc, 12 amp) produced by Eimac Corporation. This model is a 150-watt dc short-arc (0.040-inch), high-pressure (20 to 40 atm) lamp with a sapphire window and silver-plated aluminized parabolic reflector. The lamp has a UV-rich output and "closely matched a 5100°K source over the visible spectrum" (Ref. 8). The light was focused onto the sample by means of a quartz lens (focal length 8.9 cm) which defined the short-wavelength cutoff of absorption measurements to be about 1800 Å. We originally intended to use a similar lamp with a hyperbolic reflector which did not require the use of a lens. Such a lamp is usable to the sapphire cutoff at ~1500 Å. Unfortunately, the manufacturer no longer produces these lamps.

The sample wheel and sample holders are shown in Figure 3. This arrangement allowed four samples to be mounted in the chamber with the sample long axis either parallel or perpendicular to the optical axis and in both cases at 45° to the electron-beam direction. Each sample could be irradiated and investigated separately *in situ*, thus reducing the time spent changing samples and pumping down the chamber. The sample wheel was connected via a Ferrofluidic Rotary feedthrough to a position encoder which was, in turn, connected via a 1:1 gear arrangement to a 24 V dc Globe motor. The sample wheel position could be determined within 1.5° of rotation via an 8-bit Grey code output from the rotary encoder, Electro-Mec model DISPG-2 obtained from American Design Components, New York.

The thermistor arrangement in Figure 3 was to be used to measure sample temperature after irradiations, but did not prove to be a useful method due to mounting problems. As a result, no measurements were made of sample temperatures; however, the sample holders were constructed to allow for thermal expansion of the samples in the event that the heating became excessive.

Light signals were focused onto the entrance slits of the monochromator by a front-surface concave mirror obtained from Oriel Corporation.



RT-09271

Figure 3. Sample wheel and sample holders

The mirror was 108 mm in diameter with a radius of curvature of 46 cm. The aluminized reflecting surface was overcoated with magnesium fluoride to reduce degradation resulting from exposure to the atmosphere.

The sample chamber was constructed of aluminum which was hard anodized flat black to reduce the amount of stray light entering the monochromator. A cylinder, closed at one end, was welded into the side of the sample chamber to accept the end of the Dynamitron beam tube. This arrangement minimized the air path which the electrons had to travel before entering the sample chamber via a 2-mil aluminum window. A 3-cm-thick graphite collimator with a 2.54-cm aperture was placed between this window and the beam tube.

2.2.2 Vacuum Ultraviolet Monochromator

The monochromator was a Jerrell-Ash Seya-Namioka vacuum, ultraviolet, grating monochromator. This is a 0.5-m instrument with a 15,000-line/inch concave grating blazed at 2500 \AA and overcoated with MgF_2 . The grating drive was instrumented with Selsyn motors and was driven remotely.

2.2.3 Detector Assembly

An RCA C-30125J photomultiplier was located at the exit slit of the monochromator. This tube is equipped with a UV-grade sapphire window which determines the short-wavelength cutoff of the tube, while the long-wavelength cutoff is determined by the photocathode material. The quantum efficiency and absolute and relative sensitivities are shown in Figure 4.

One problem with any grating monochromator is that light from multiple orders falls on the exit slit at the same time. To separate the first-order light from the higher orders, a series of remotely operated filters was inserted between the exit slits and the photomultiplier tube: between 1400 and 2500 Å, no filter was necessary; between 2500 and 3000 Å, a quartz filter; between 3800 and 6000 Å, a glass filter; between 6000 and 9000 Å, a KRS-5 filter. The transmission spectra for these filters are shown in Figure 5. The filters were mounted on a cylinder which surrounded the photomultiplier tube, and the entire assembly was evacuated.

2.2.4 Calibration

The National Bureau of Standards has adopted tungsten as the standard source for spectral irradiance down to 2600 Å (Ref. 9), and other than synchrotron radiation, no standard source exists below 2600 Å.

Absolute intensity calibration of the optical system — sample chamber, monochromator, and photomultiplier — was accomplished by placing a 650-watt tungsten-halogen projection lamp (Sylvania model DVY) at the sample position. Such lamps can be used for absolute intensity standards from 0.25 to 2.6 μm (Ref. 10). The calibration was extended below 0.25 μm by using a Hg:Ne low-pressure line-source lamp. The relative intensities of the lines given off by Hg:Ne lamps are listed in the AIP Handbook (Ref. 11). The absolute intensity of the lines may vary from lamp to lamp. However, by normalizing the emission intensity of several lines for our lamp in the visible where the system had previously been absolutely calibrated against a tungsten source, the calibration of the system could be extended in the UV region to ~0.20 μm, where the quartz envelope of the Hg:Ne lamp became severely attenuating. This was done by comparing the published relative intensities with the measured photomultiplier tube signals.

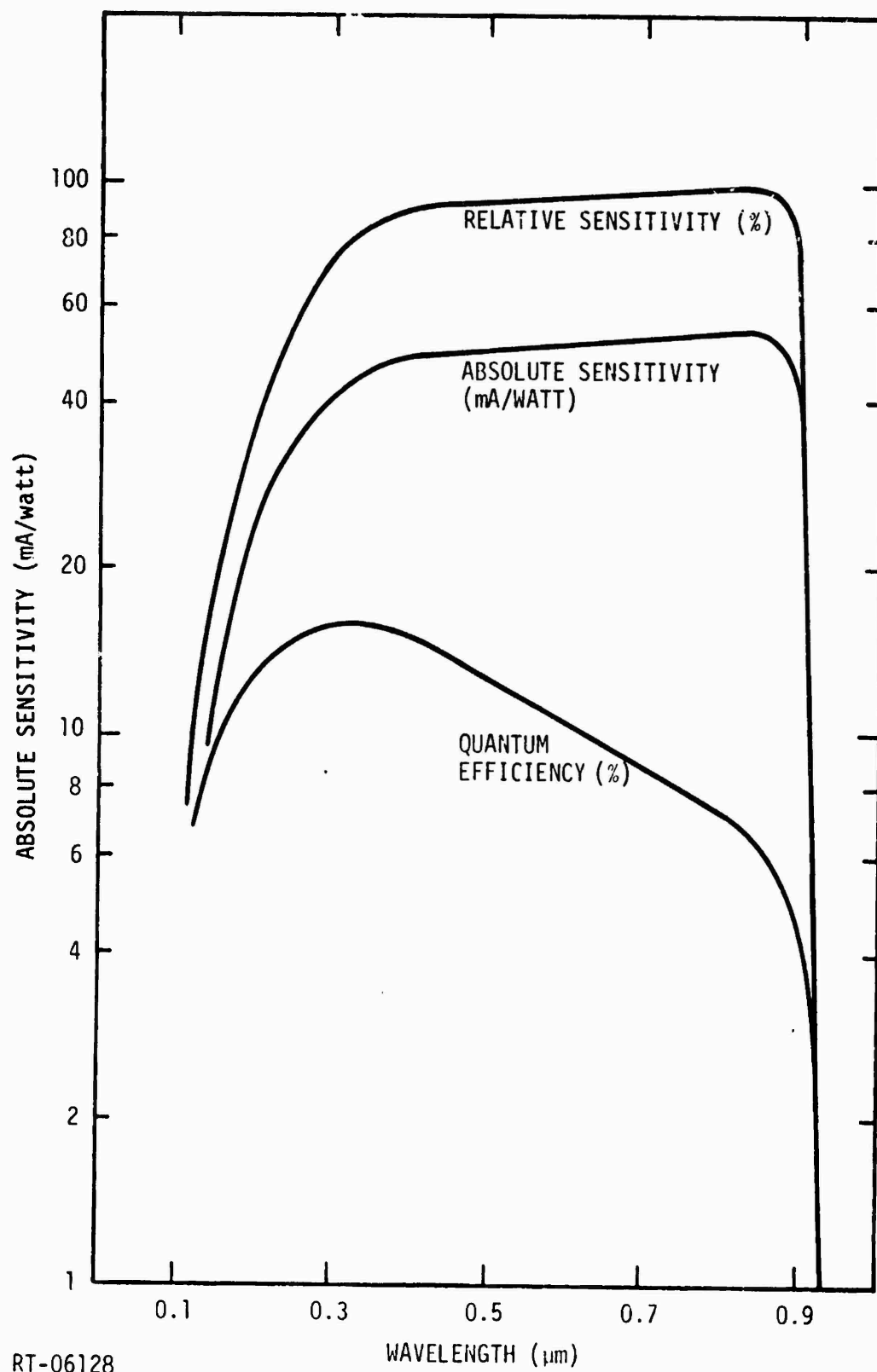


Figure 4. Typical photomultiplier response characteristics

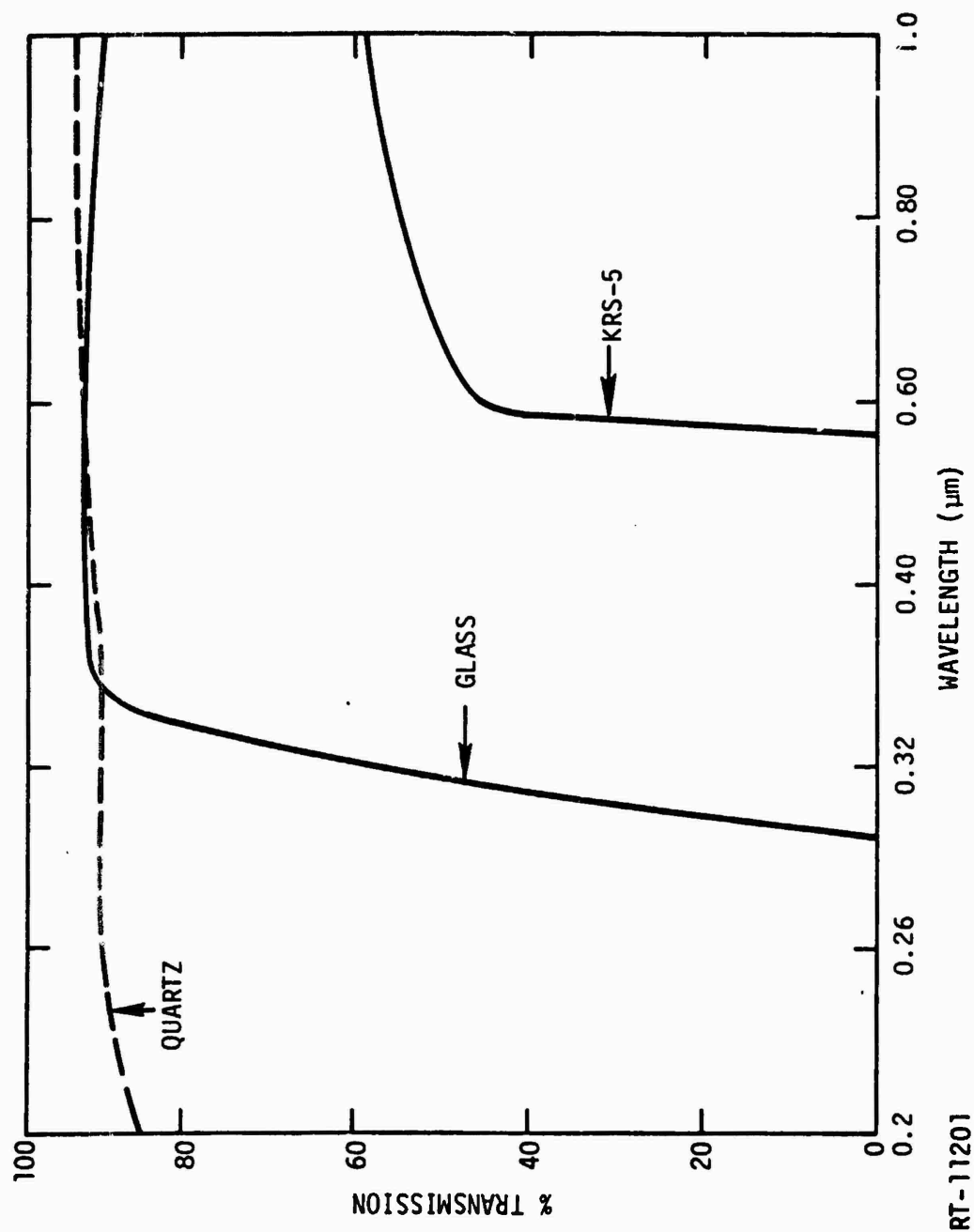


Figure 5. Transmission spectra for quartz, glass, and KRS-5 filters

The basic requirement for absolute calibration is to put an object of known spectral radiance, $R(\lambda)$, at the sample position and then measure the spectral dependence of the detector output current, $I(\lambda)$, to determine the spectral throughput characteristics of the optical system, $\kappa(\lambda)/\pi = I(\lambda)/R(\lambda)$.

The spectral radiance emittance of a tungsten filament lamp at several temperatures is shown in Figure 6. The spectral radiance emittance of tungsten is the blackbody emittance times the spectral emissivity of tungsten at that temperature and wavelength (Ref. 12). The observed photomultiplier current for this lamp (subject to a number of conditions, including lamp temperature, PM tube voltage, and monochromator slit width) was recorded as a function of wavelength. Dividing the data in Figure 6 by the photomultiplier current point by point results in a calibration versus wavelength such as that shown in Figure 7. The calibration factor in Figure 7 is subject to a number of constraints including PM tube voltage, monochromator slit width, and duration of illumination. However, the spectral radiant emittance $M(\lambda)$ of an unknown sample is related to the emittance of the standard by the sample ratio

$$M(\lambda) = \frac{I \cdot M(\lambda)_{\text{STD}}}{I(\text{STD})} \quad (1)$$

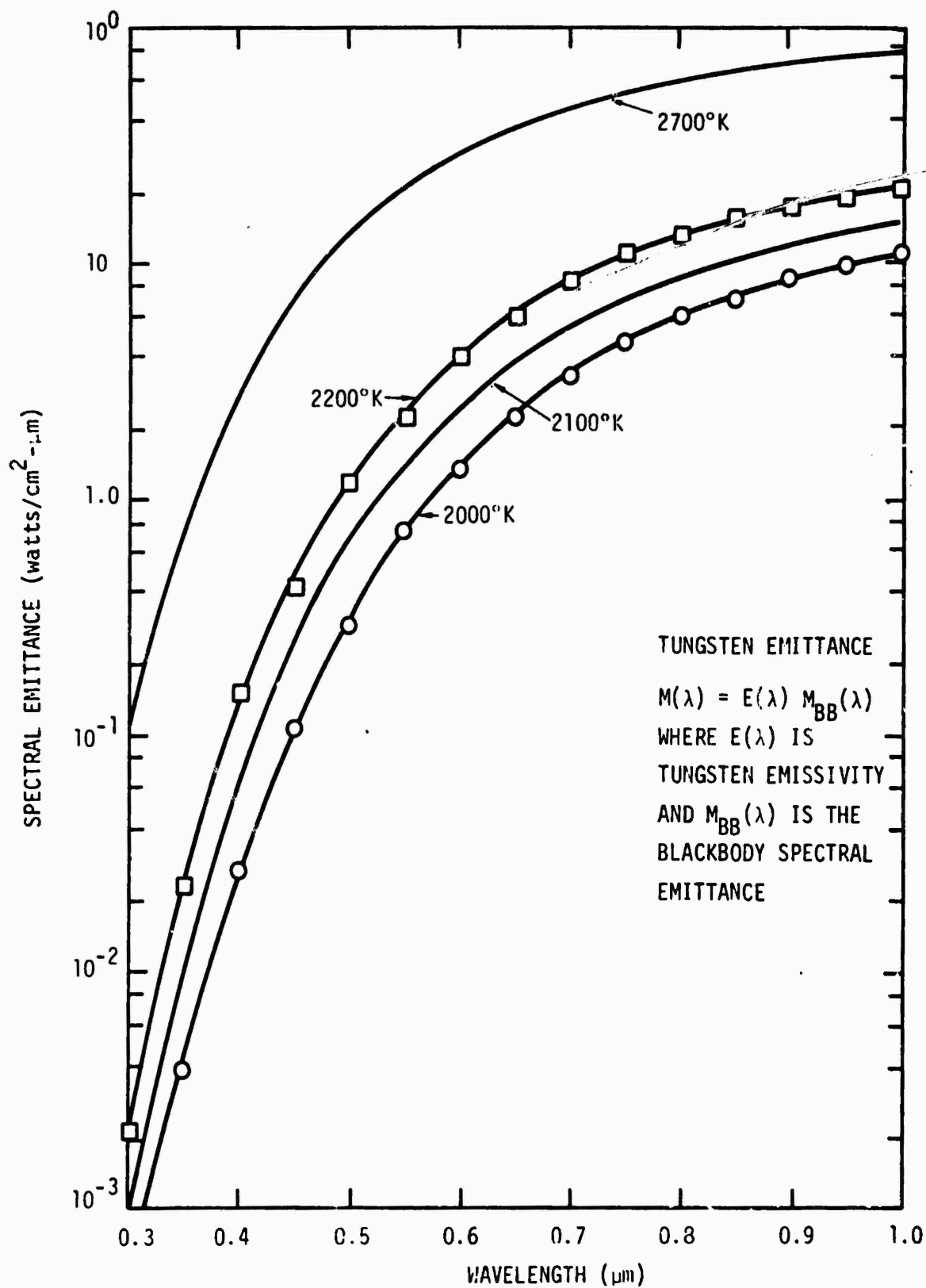
Likewise, the radiance $R(\lambda)$ of an unknown is related to the radiance of the standard $R_{\text{S D}}(\lambda)$ as

$$R(\lambda) = \frac{I R_{\text{S D}}(\lambda)}{I_{\text{S D}}} \quad (2)$$

Implicit in this calibration is the assumption that the radiation patterns for the standard source and the unknown are the same. A more detailed account of the calibration procedure is included in Appendix C.

2.2.5 Wavelength Calibration

The wavelength readings of the *in situ* optical system were calibrated against a low-pressure Cenco helium line source. The He source is a convenient calibration lamp because of the isolated intense yellow line at 5876 Å which provides an easily identified starting point, and because the remaining lines are well spaced. The prominent lines and their relative intensities are listed in Table 2.



RT-07367

Figure 6. Tungsten spectral radiant emittance at several temperatures

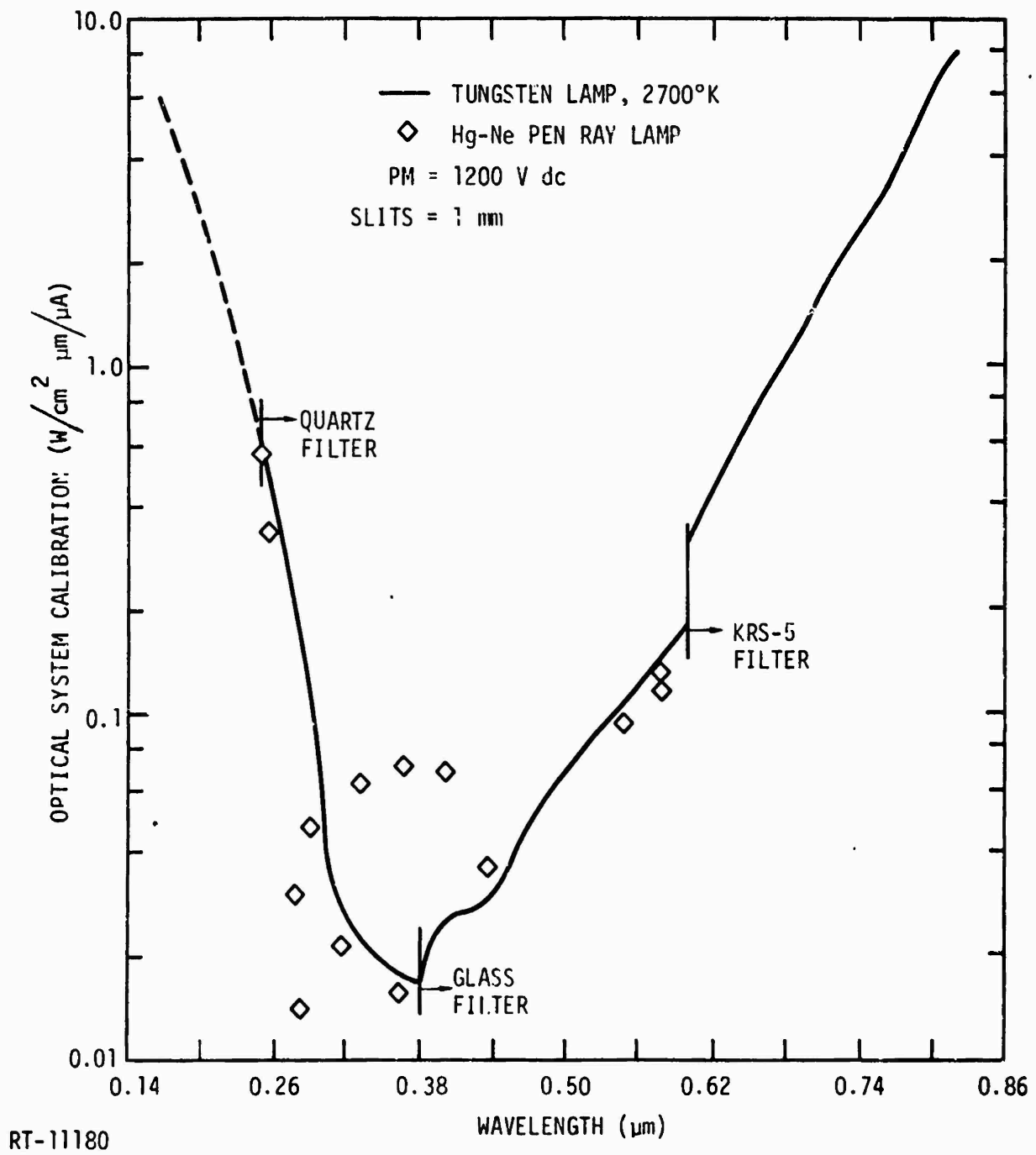


Figure 7. Absolute intensity calibration of *in situ* optical system

Table 2
 PROMINENT He LINES

Wavelength (Å)	Strength
3889	M
3965	M
4388	W
4471	M
4713	M
4922	M
5015	S
5048	W
5876	VS
6678	S
7065	M
7281	M

VS = very strong

S = strong

M = medium

W = weak

The line source could not be placed at the sample position due to the size of the lamp; therefore, calibration was performed by placing the He source at the entrance slit of the monochromator. Initial adjustments were made by visually observing the lines appearing at the exit slit, while finer adjustments were made by placing the photomultiplier at the exit slit.

2.3 SPECIAL ELECTRONICS FOR *IN SITU* MEASUREMENTS

Two electronic systems were constructed to facilitate the *in situ* measurements: (1) The positioning and ratioing system was used to determine the sample position for luminescence measurements and to accept and ratio PM tube signals during relative absorption measurements. (2) The beam steering system was used to divert the Dynamitron beam for making transient absorption and luminescence measurements.

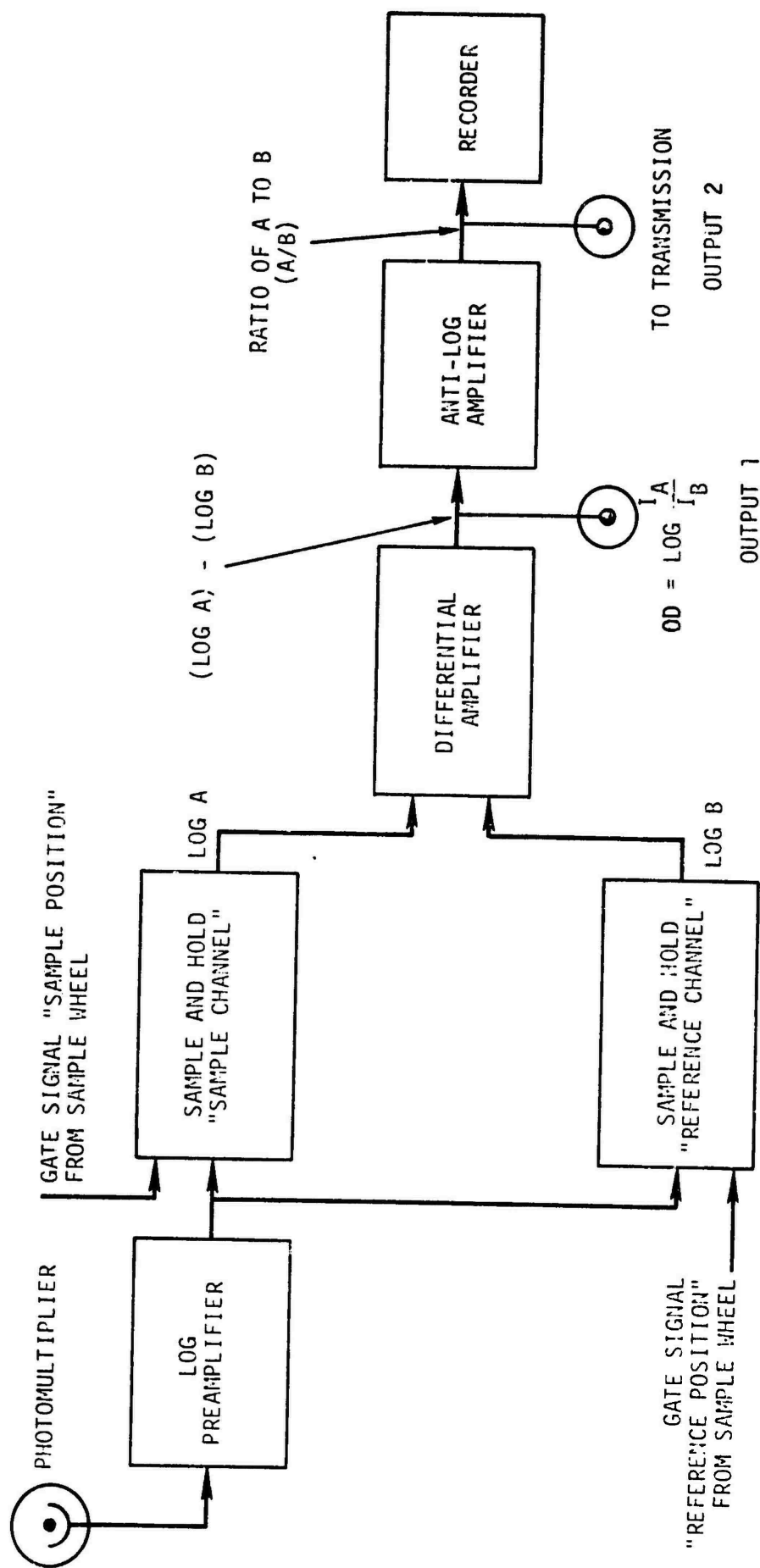
2.3.1 Sample Positioning

As mentioned in Section 2.2.1, four samples were mounted simultaneously in the sample chamber. The sample wheel could be rotated and its position determined by means of an analog-to-digital, mechanical shaft encoder. The encoder output (an 8-bit Grey code) was connected to a reader and indicator circuit. This circuit performed the following functions. (1) It displayed the encoder binary output by means of eight LEDs; (2) it allowed any encoder output to be exclusively designated as sample wheel positions 1 through 8 (four sample positions and four reference positions); (3) it displayed which, if any, of the eight sample wheel positions was in the optical path. As mentioned earlier, the sample wheel was driven remotely; therefore, any sample wheel position could be placed in the optical path within the resolution of the encoder output (256 bits for 360° of rotation).

2.3.2 Ratioing Electronics

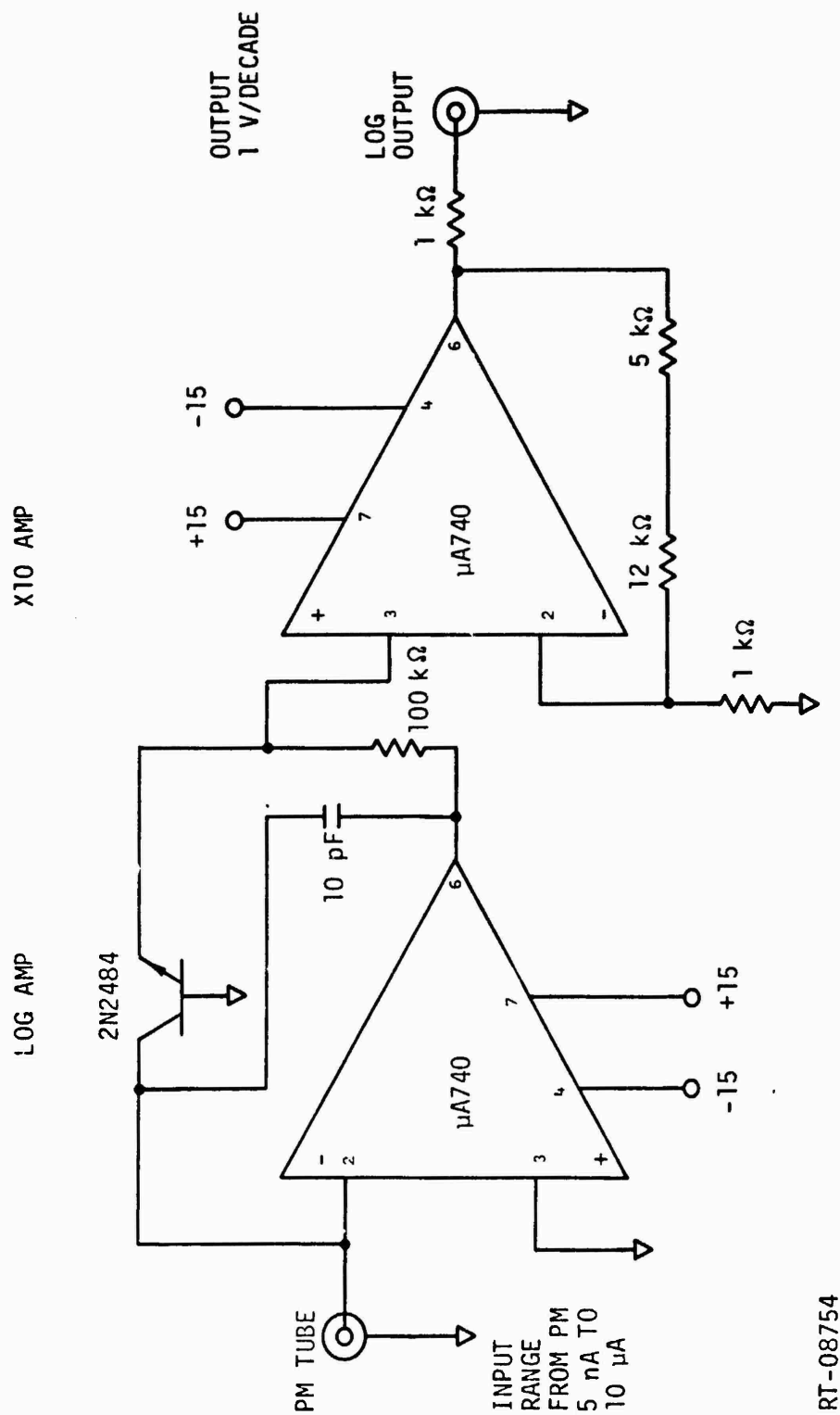
When making relative absorption measurements, two identical optical paths are normally used. This method has two significant drawbacks: (1) it requires that the optical components in the reference and sample paths be closely matched — i.e., that the spectral response of the reflectivity be closely matched, which is difficult and expensive; (2) in the VUV, reflectivities can easily be down in the 70 to 80% range even for good optical surfaces, and since the dual-beam method requires at least two reflecting surfaces, this introduces a reduction of the UV signals not found in a one-mirror system.

To circumvent these difficulties, we developed a single-beam method to make relative absorption measurements. Instead of two optical paths, the sample was rotated in and out of a single optical path (shown in Figure 2). The electronics used to make these measurements are shown diagrammatically in Figure 8 and schematically in Figures 9 and 10. The sample wheel was rotated at 110 RPM with as many as four samples mounted. The photomultiplier output was presented to the log amplifier, the output



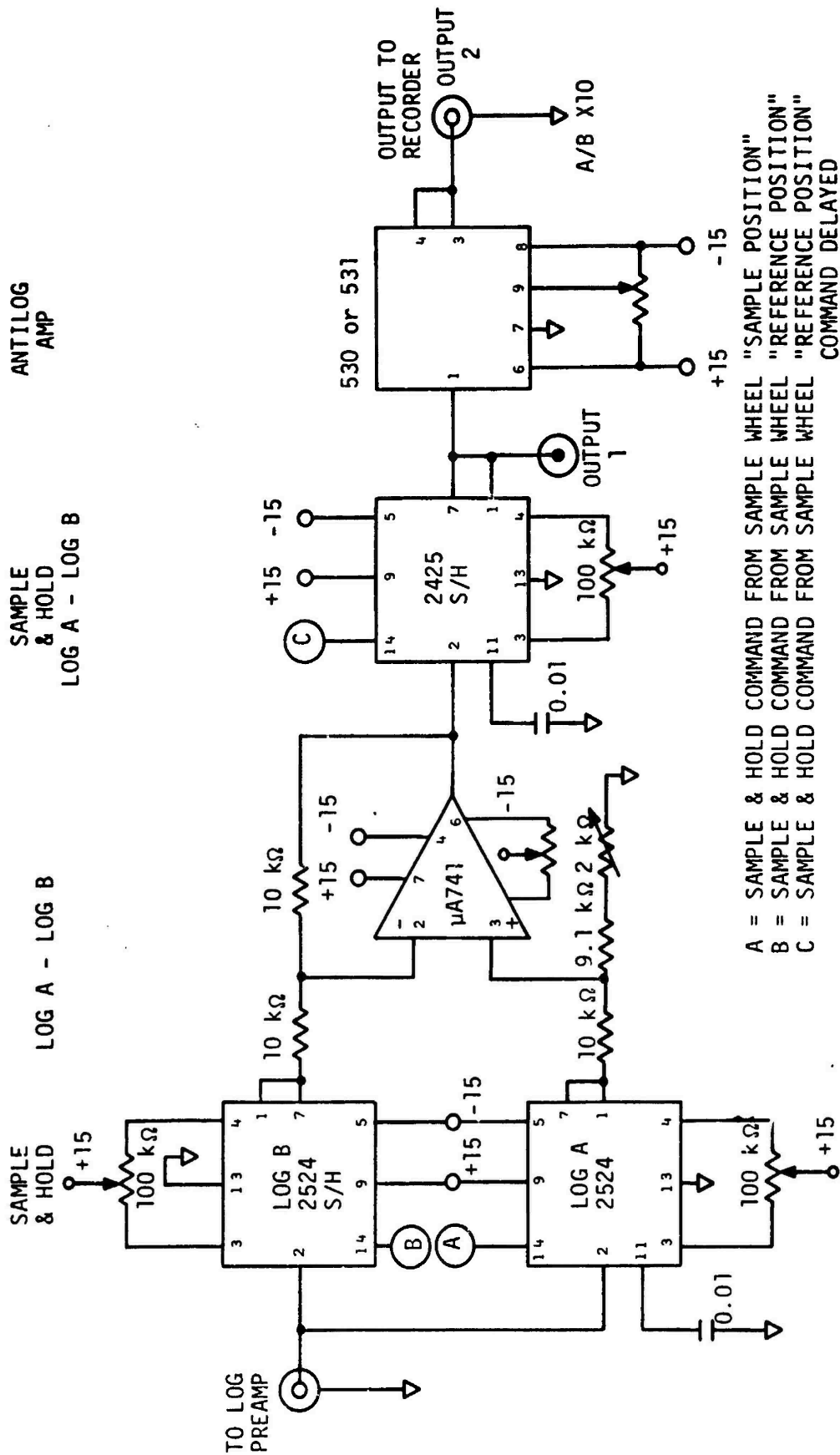
RT-08744

Figure 8. Block diagram of ratioing electronics



RT-08754

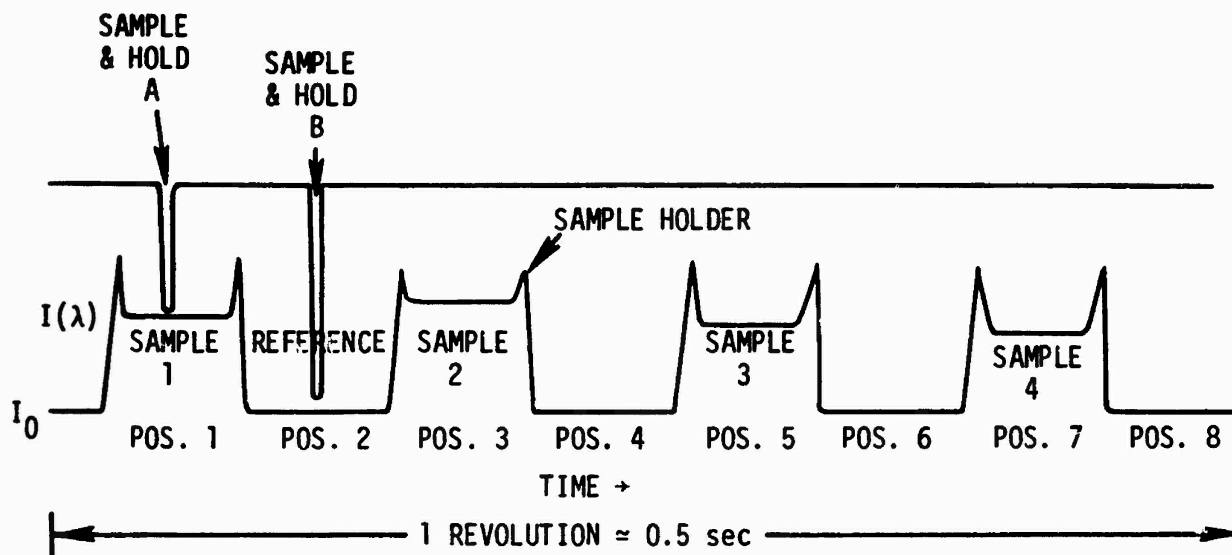
Figure 9. Schematic diagram of log amplifier designed for 10 mA to 10 μ A signals



RT-08755

Figure 10. Schematic diagram of sample-and-hold, ratioing, and antilog circuitry

of which was presented to the ratioing electronics. The diagram below is exemplary of the log amplifier output.



Ratioing was accomplished by means of two sample-and-hold circuits, one which sampled the log amplifier output [$\log I_A(\lambda)$] at the center of a preset sample position and one which sampled at a preset reference position, as shown in the diagram.

For each rotation of the wheel, the following chain of events occurred.

1. Sample and hold $\log I_A$ (I_A = sample signal).
2. Sample and hold $\log I_B$ (I_B = reference signal).
3. Present S/H $\log A$ and S/H $\log B$ to the inputs of the differential amplifier (plus and minus, respectively).
4. Sample and hold the differential amplifier output ($\log A - \log B$) = $\log (I_A/I_B)$ = output 1 (optical density).
5. Present ($\log A - \log B$) to output 1 (Fig. 8).
6. Simultaneously present antilog ($\log A/B$) to output 2 (percent transmission, Fig. 8).

The positions which actuated the sample-and-hold circuits were preset by means of thumbwheels, one for the sample channel (A) and one for the reference channel (B). Each thumbwheel could be set for any of the eight sample wheel positions. The sample-and-hold in Event 4 was triggered by a delayed B sample-and-hold command.

Figure 11 shows a transmission spectrum taken using the above apparatus compared to a spectrum of the same sample obtained using the Beckman DK-1A.

2.3.3 Beam Steering System

To make measurements of the transient absorption and radioluminescence, it was necessary to pulse the Dynamitron beam onto the samples for times on the order of 10 to 15 msec with rise and fall times less than 1 msec. This was accomplished by placing Helmholtz coils on the Dynamitron beam tube ~10 feet from the sample chamber. The coils were 6 inches in diameter and separated by 3 inches, with 80 turns per coil, and were operated at 1 amp, which produced a field strength of 9 gauss. When power was supplied to the coils, the beam was diverted from the sample, and when the power was removed, the beam was again incident upon the samples. Figure 12 shows the electronics used to pulse the magnet. After tuning the Dynamitron, the magnet power was turned on, thus diverting the electron beam. By applying a positive-going pulse of >10 volts, the magnet could be driven off, thereby allowing the beam to strike the samples. When the beam was diverted, the beam current as measured behind the sample position dropped below measurable values (a drop of more than 3 orders of magnitude). The response time of this system was less than 1 msec.

2.4 DK-1A

Of the samples listed in Table 1, the Schott samples did not transmit light at wavelengths shorter than 2600 Å. Measurements of the long-term (>90 sec) absorption of the Schott glasses could then be made in air. These measurements were performed on a Beckman DK-1A spectrophotometer. The optical system of the DK-1A is shown in Figure 13 (Ref. 13).

2.5 DOSIMETRY

Beam current measurements were made by two methods: for irradiations in air, a Faraday cup, provided by the Jet Propulsion Laboratory Dynamitron facility, was used; for irradiation of samples in a vacuum, a stopping block was used. Correlation of fluence (e/cm^2) and ionizing dose (rads) was accomplished by means of cobalt-glass dosimeters.

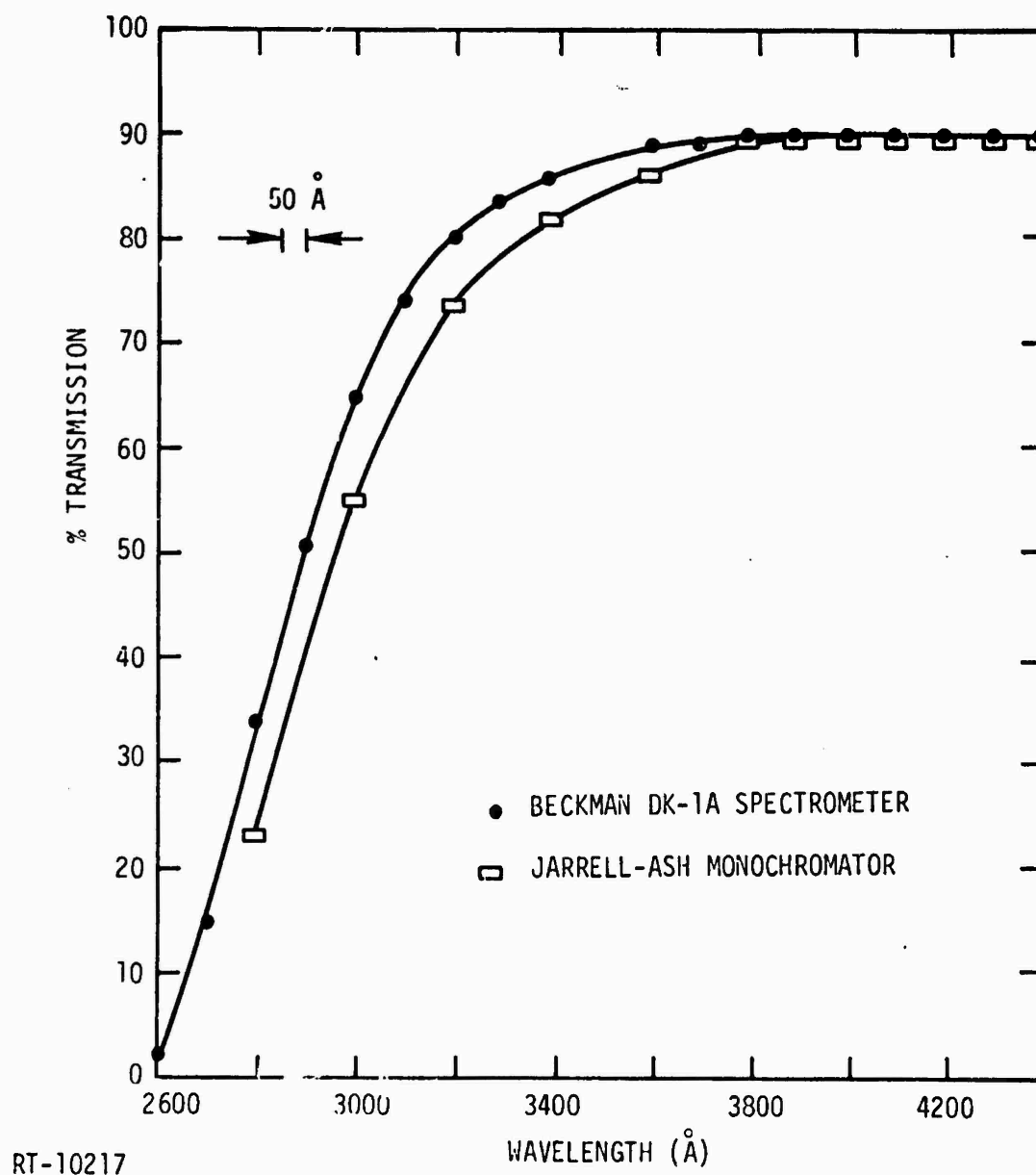


Figure 11. Transmission spectra of Schott SK-7 glass taken with two different instruments. Differences were traced to 50 Å difference in wavelength calibration of two systems

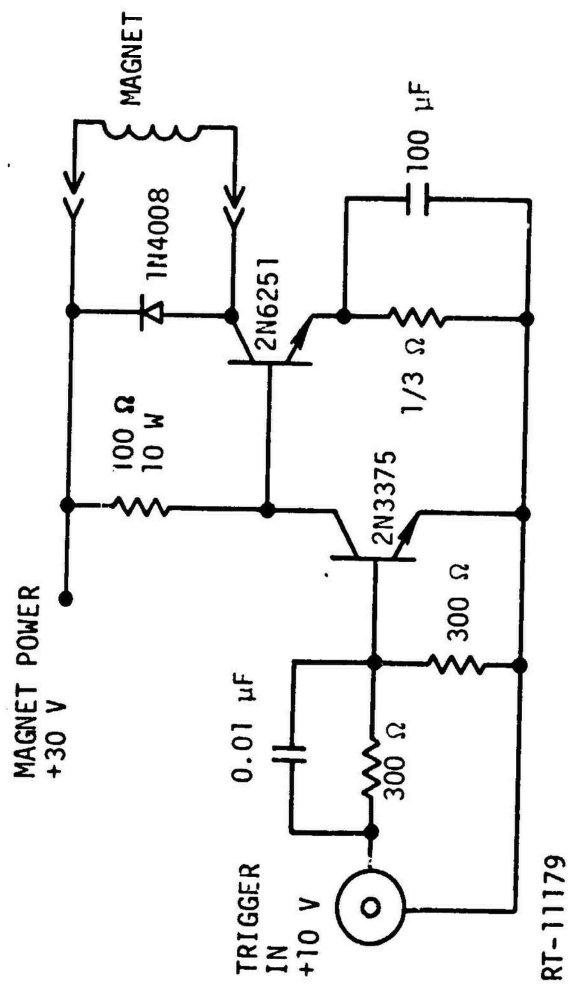


Figure 12. Pulsing electronics for steering magnet

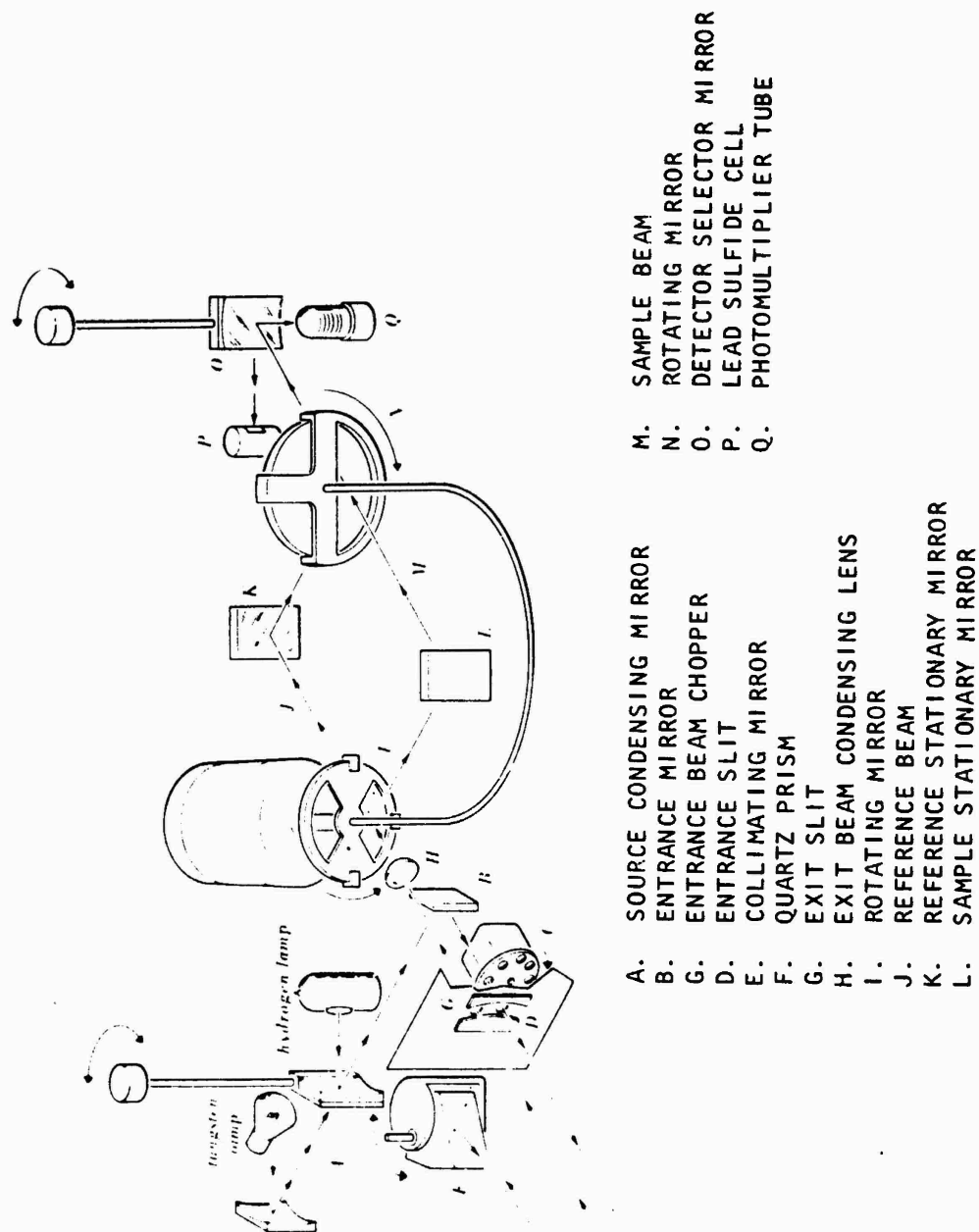


Figure 13. Optical diagram of DK-1A spectrophotometer (from Beckman Instruments, Inc., DK-1A Spectrometer Manual, January 1967)

2.5.1 Faraday Cup

The Faraday cup is simply a device consisting of a stopping block of low-Z material mounted in a special vacuum chamber, as shown in Figure 14. The chamber is designed to avoid the collection of secondary electrons emitted from the foil window and to collect the back-scattered and secondary electrons emitted from the stopping block.

The current from the Faraday cup was measured with an Elcor current meter. From the instantaneous and integrated current and knowledge of the area of the Faraday cup aperture (1 cm^2), the flux and fluence were determined.

2.5.2 Cobalt-Glass Dosimetry

Cobalt-glass dosimeters were used to correlate the fluence (e/cm^2) and the ionizing dose (rads). The cobalt dosimeters were mounted on the face plate of the Faraday cup, with a 1-inch layer of styrofoam and a 1/2-inch-thick piece of aluminum between the two to avoid dose enhancement from back-scattered electrons. The transmission of the cobalt glass was measured before and after irradiation to a known fluence (as measured with the Faraday cup). From the change in transmission and previously existing calibration curves, the ionizing dose was determined. It was found that

$$1 \text{ rad(glass)} = 2.2 \times 10^7 \text{ e/cm}^2 \pm 12\% \quad (E = 2.5 \text{ MeV}) \quad (3)$$

This is dependent upon the thickness of the sample and is valid where the thickness is less than the electron range.

2.5.3 Stopping Block

The stopping block was mounted on an insulated standoff on the removable back plate of the *in situ* apparatus described in Section 2.2.1. The stopping block was positioned $\sim 4.2 \text{ cm}$ from the center of the sample position and was centered on a line defined by the axis of the beam tube. The block was an aluminum disk 1.9 cm in diameter and 0.5 cm thick, and was oriented at a 45° angle to the beam-tube axis. The current from the stopping block was measured with an Elcor current meter and integrator. The flux measured at the stopping block was approximately half that which would have been

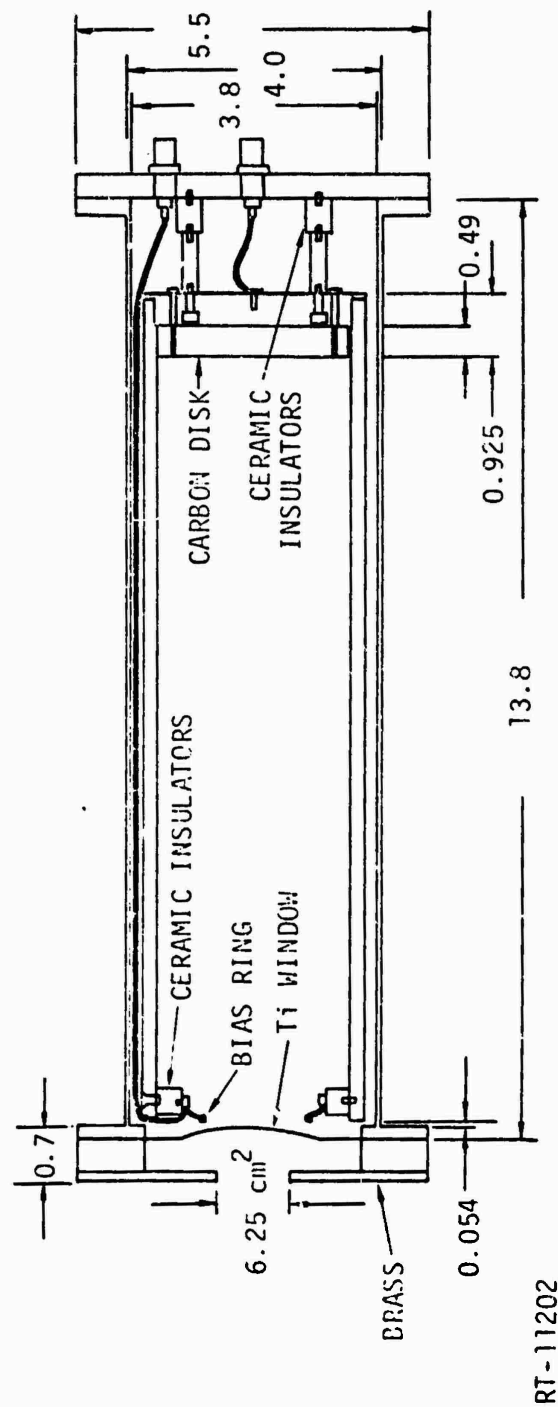


Figure 14. Schematic of Faraday cup

measured at the sample position due to beam spreading. To correlate the flux at these two positions, cobalt-glass dosimeters were placed in the sample wheel and rotated out of the path of the beam. The Dynamitron was tuned and allowed to stabilize at some current, I_{SB} , as determined from the stopping block. The cobalt glasses were then rotated into the beam and irradiated for some time, t , and again rotated out of the beam. At this time, the stopping block current was checked to make sure that the beam current had not changed. The dose accumulated at the sample position was determined from the cobalt glasses, and the dose was related to the flux at the sample position by Eq. 3. Comparison of this flux to the current measured at the stopping block gave the desired calibration factor:

$$\frac{\dot{\phi}_e}{I_{SB}} = 6 \times 10^{18} \frac{e}{\text{cm}^2\text{-sec}} / \mu\text{A} \pm 12\% , \quad (4)$$

where $\dot{\phi}_e$ is the electron flux at the sample position and I_{SB} is the current measured at the stopping block.

Since the beam current could not be quantitatively measured when samples were in place, the stopping block current was measured before and after each irradiation. For very long irradiations, the samples were periodically rotated out of the beam and the current checked, and then the irradiation was continued. In addition, although the stopping block current was reduced when samples were being irradiated, a current signal could still be read, and this signal was continually monitored for drift, providing an additional means of ensuring current stability.

3. ABSORPTION MEASUREMENTS

This chapter describes the procedure used for making absorption measurements and the results of these measurements. We have attempted to include as much of the data in "raw" form as possible.

The measurements were divided into three categories — permanent, intermediate, and transient. Absorption centers which persisted longer than 90 sec were referred to as long-term or permanent. Intermediate centers are those which persisted for less than 90 sec, and transient centers are those which lasted for less than 1 sec.

Measurements of the induced absorption were made over a wide range of flux, fluence, and time. The results are presented in apparent absorption coefficient as defined by

$$\alpha = \frac{1}{X} \ln \frac{I_0}{I}, \quad (5)$$

where α is the apparent absorption coefficient (cm^{-1}), X is the sample thickness (cm), I_0 is the light intensity incident on the sample, and I is the light intensity transmitted (I_0 and I need only be in equivalent units). This quantity is most directly related to the measured quantities I and I_0 and differs from the true absorption coefficient, α_0 , by a quantity $R = \alpha - \alpha_0$.

$$R = \frac{2}{X} \ln \left(\frac{1}{1-r} \right) \quad (6)$$

where r is the reflection coefficient at a dielectric-air interface,

$$r = \left(\frac{n-1}{n+1} \right)^2$$

where n = index of refraction. In this study we did not measure the reflection coefficient of our samples, but the quantity R is calculated for each sample type in Table 3, for typical published refractive indices.

Table 3
DIFFERENCE BETWEEN TRUE ABSORPTION AND APPARENT ABSORPTION

Material	Index of Refraction at 5876 Å°	Sample Thickness (cm)	$R = (\alpha - \alpha_0)$ (cm ⁻¹)
BaK4	1.569	0.16	0.69
Bk7	1.520	0.20	0.48
Bk7-G14	1.520	0.21	0.46
KZFS-N4	1.613	0.16	0.77
LaK10	1.720	0.13	1.2
SF10	1.728	0.12	1.3
SF11	1.785	0.11	1.6
SK7	1.607	0.14	0.86
SK14	1.603	0.14	0.86
UBK7	1.517	0.20	0.47
SiO ₂ (Fused)	1.57	0.32	0.31
Al ₂ O ₃	1.73 ± 0.03	0.20	0.75
SiO ₂ (Z)	1.44	0.20	0.33

This quantity is also indicated as a horizontal line on all the figures of optical absorption.

Since radiation-induced changes in the index of refraction are small, this component has no effect on displays of radiation-induced absorption, in which the preirradiation optical absorption has been subtracted from the observed absorption to find the radiation-induced absorption.

The apparent absorption coefficient can be related to the optical density, OD, which is a dimensionless quantity dependent upon the thickness of the particular sample by

$$OD = \log \frac{I_0}{I} \quad n = \frac{\alpha x}{2.3} \quad (7)$$

3.1 PERMANENT ABSORPTION MEASUREMENTS

Absorption measurements on sapphire, Suprasil 2, and crystalline quartz samples were first made using the *in situ* optical system, and after exposure to 10^{16} e/cm², no induced absorption was observed.* Since this was contrary to the results of previous work (Ref. 14), subsequent irradiation of these samples was performed in air and absorption measurements made using the DK-1A. The results of these measurements are shown in Figures 15, 16, and 17. The well known quartz absorption band between 2000 and 2200 Å was observed in both crystalline quartz (at 2000 Å) and Suprasil 2 (at 2080 Å). Previous work (Ref. 15) has shown that the exact peak of this band is dependent upon the composition of the particular sample. Sapphire displayed a small increase in absorption, centered near 2300 Å. It should be noted that these samples were irradiated at a high flux and at the end of the irradiation were so hot they could not be held with bare hands. In addition, as a result of the extreme heating of the samples, the crystalline quartz sample was dislodged from the irradiation position and fell well out of the beam path at some unknown time; therefore, no fluence is noted for this sample.

Since the quartz, Suprasil 2, and sapphire samples proved to be particularly radiation-hard, the remainder of the permanent absorption investigation was limited to the Schott glasses. The Schott glasses are opaque at wavelengths shorter than 2600 Å; consequently, absorption measurements of these samples could be made in air using the Beckman spectrophotometer. The samples were mounted in envelopes on the aperture plate of the Faraday cup on the side facing the beam tube. Two or three samples were exposed simultaneously, with the samples arranged symmetrically around the aperture. Care was taken to ensure that the samples were irradiated uniformly. To avoid dose enhancement from electrons back-scattered from the brass aperture plate, a 0.5-cm sandwich of glass plates was placed between the samples and the brass.

*It is not unreasonable to assume that the absorption was bleached by the high-intensity x-ray source. A high degree of bleaching in Corning fused silica has been reported by Palma and Gagosz (Ref. 6).

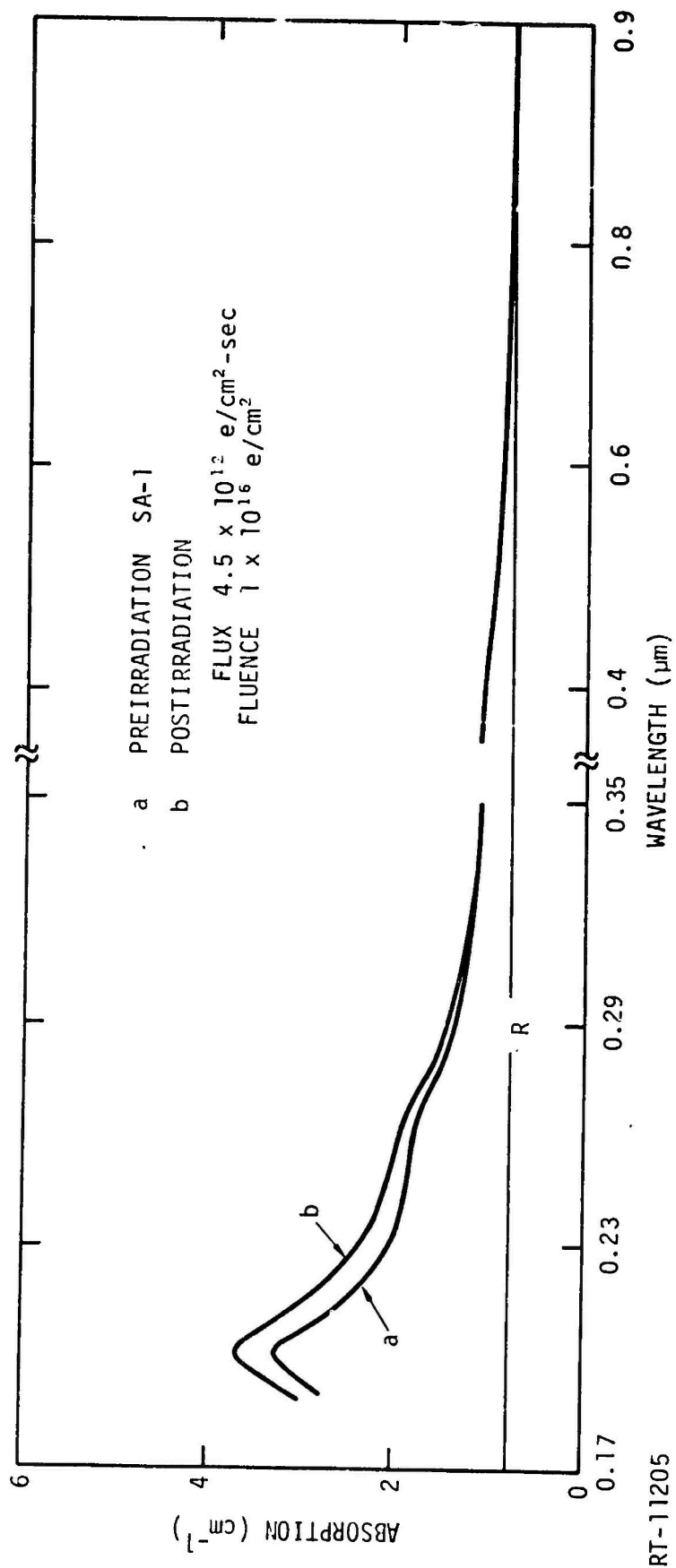


Figure 15. Absorption spectra of irradiated sapphire

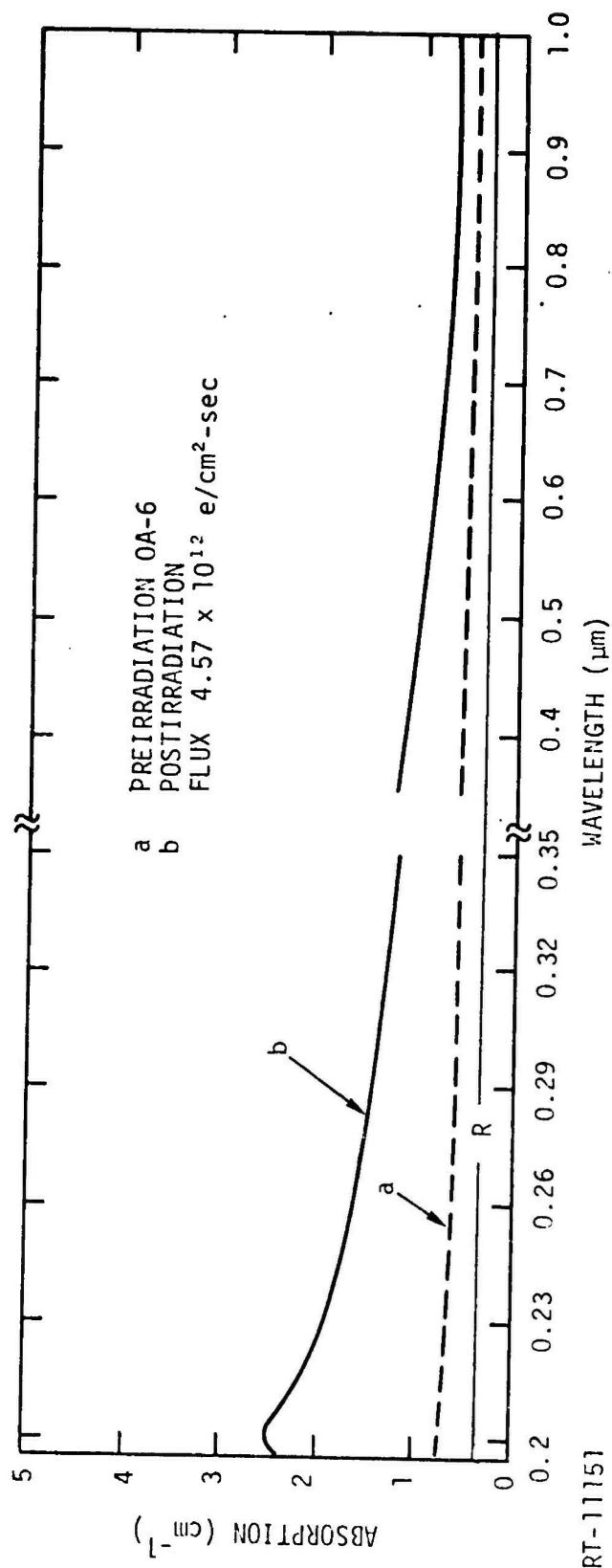


Figure 16. Absorption spectra of irradiated crystalline quartz

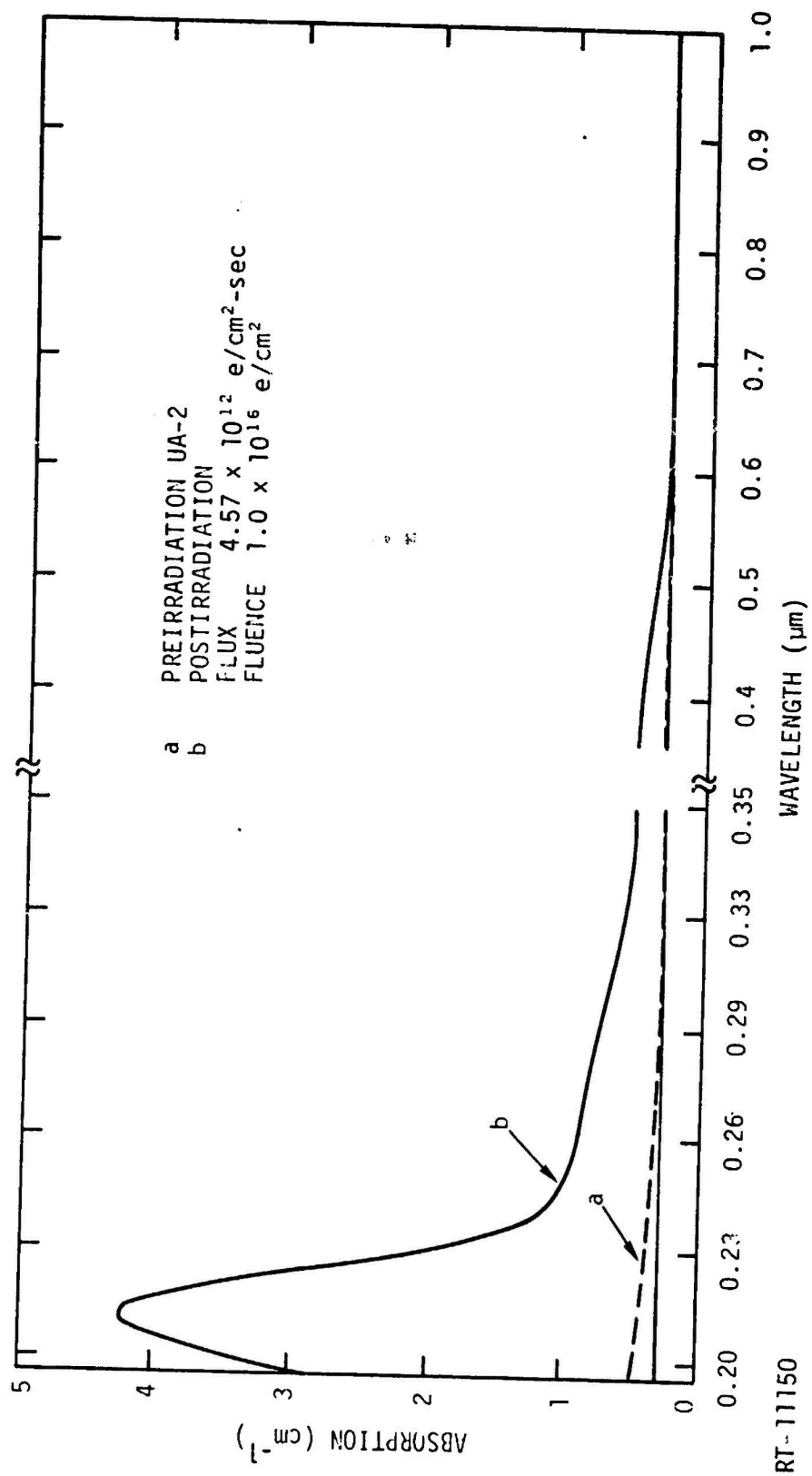


Figure 17. Absorption spectra of irradiated Suprasil 2

Flux and fluence were determined by means of the Faraday cup and Elcor current integrator and by recording the exposure time. The exposure times ranged from 6 to 600 sec. At the end of the irradiations, the Dynamitron was shut down and the samples were removed from the radiation room and placed in the DK-1A (average time for this procedure was 90 sec). The time to make a spectral scan was 120 sec maximum, and the time necessary to remove a sample and begin the next spectral scan was typically 10 to 20 sec maximum.

Schott BK7-G14, which is a radiation-hard, cerium-doped glass, showed no change in transmission after exposure to 10^{16} e/cm². The spectrum of BK7-G14 is included in Appendix A.

3.1.1 Melt-to-Melt Variation of the Induced Absorption

Measurements were made on samples of the same glass type obtained from different melts to determine if the darkening rates were significantly different. The samples were irradiated in pairs, one from each melt, to a fluence of 8×10^{13} e/cm² at a flux of $\sim 5.5 \times 10^{12}$ e/cm²-sec. Schott SK-14 was the only sample that displayed any significant melt-to-melt variation, as shown in Figure 18. Note the difference in the preirradiation spectra, particularly at the band edge, which was observed only in SK-14. A check of other SK-14 samples showed that the difference in preirradiation spectra was consistent throughout all the SK-14 samples. The difference in darkening for the SK-14 samples is so severe that this can be attributed only to a melt-to-melt variation in the darkening rate.

The LaK-10 samples also appear to darken at a slightly different rate, as shown in Figure 20; however, given the reproducibility of the Beckman spectrophotometer and the accuracy of the dosimeter, it is difficult to unquestionably attribute this difference to a melt-to-melt variation in darkening rate.

3.1.2 Temporal Bleaching

It is well known (Refs. 6,15) that radiation-induced darkening in most glasses will "fade" with time. The rapidity of the fading is dependent upon the particular material and wavelength. This phenomenon is

described as bleaching if the color center is simply depopulated; i.e., a trapped electron or hole is thermally activated out of the center or as annealing if the defect center is removed by rearrangement of the ions surrounding the defect. No such distinction shall be made in this report and the fading process will be referred to as bleaching.

To determine the magnitude of the bleaching effects, spectral scans were made over a period of time of the samples irradiated for the melt-to-melt variation investigation. These spectra are shown in Figures 18 through 26. All of the Schott glasses displayed significant bleaching over a period of 1000 min, and some displayed noticeable bleaching within 10 min of the irradiation. Note that, although the SK-14 samples from different melts darken at different rates, the degree and rate of the bleaching are not noticeably different.

It was found that the bleaching behavior could be described by an equation of the form

$$\frac{\alpha(t, \lambda)}{\alpha_0(\lambda)} = A - B \ln t \quad (8)$$

where $\alpha(t, \lambda)$ is the absorption at some wavelength λ at time t , and $\alpha_0(\lambda)$ is the absorption as measured 90 to 100 seconds after irradiation. A and B are positive constants which are dependent on wavelength and glass type. Equation 8 is indicative of a system in which color centers are not all in similar environments but are distributed in a large number of environments. As a result of the varying environments, the rate of decrease of the color center population cannot be described by a single activation energy but by a distribution of activation energies (Ref. 16). Values of A and B were calculated from the spectra shown in Figures 18 through 26 and these values are listed in Table 4.

A significant variation in the bleaching rates of SF-10 and SF-11 was observed for samples irradiated at a lower flux. These results are included in the discussion of flux dependencies presented in Section 3.1.4.

Table 4
BLEACHING PARAMETERS

Sample	Wavelengths (μm)	A	B
BaK4	0.6	1.3	0.088
	0.8	1.2	0.069
BK7	0.5	1.3	0.063
	0.6	1.3	0.063
UBK7	0.5	1.3	0.056
	0.6	1.2	0.048
LaK10	0.5	1.5	0.096
	0.6	1.5	0.091
	0.8	1.4	0.076
KZFS-N4	0.5	1.5	0.091
	0.6	1.5	0.093
	0.8	1.3	0.074
SK7	0.4	1.3	0.069
	0.5	1.4	0.084
	0.6	1.4	0.084
SK14	0.5	1.4	0.074
	0.6	1.4	0.074
SF10	0.4	1.5	0.091
SF11	0.4	1.4	0.087

A: $\pm 5\%$ } A and B were calculated from Eq. 8 where
 B: $\pm 8\%$ } time was expressed in seconds.

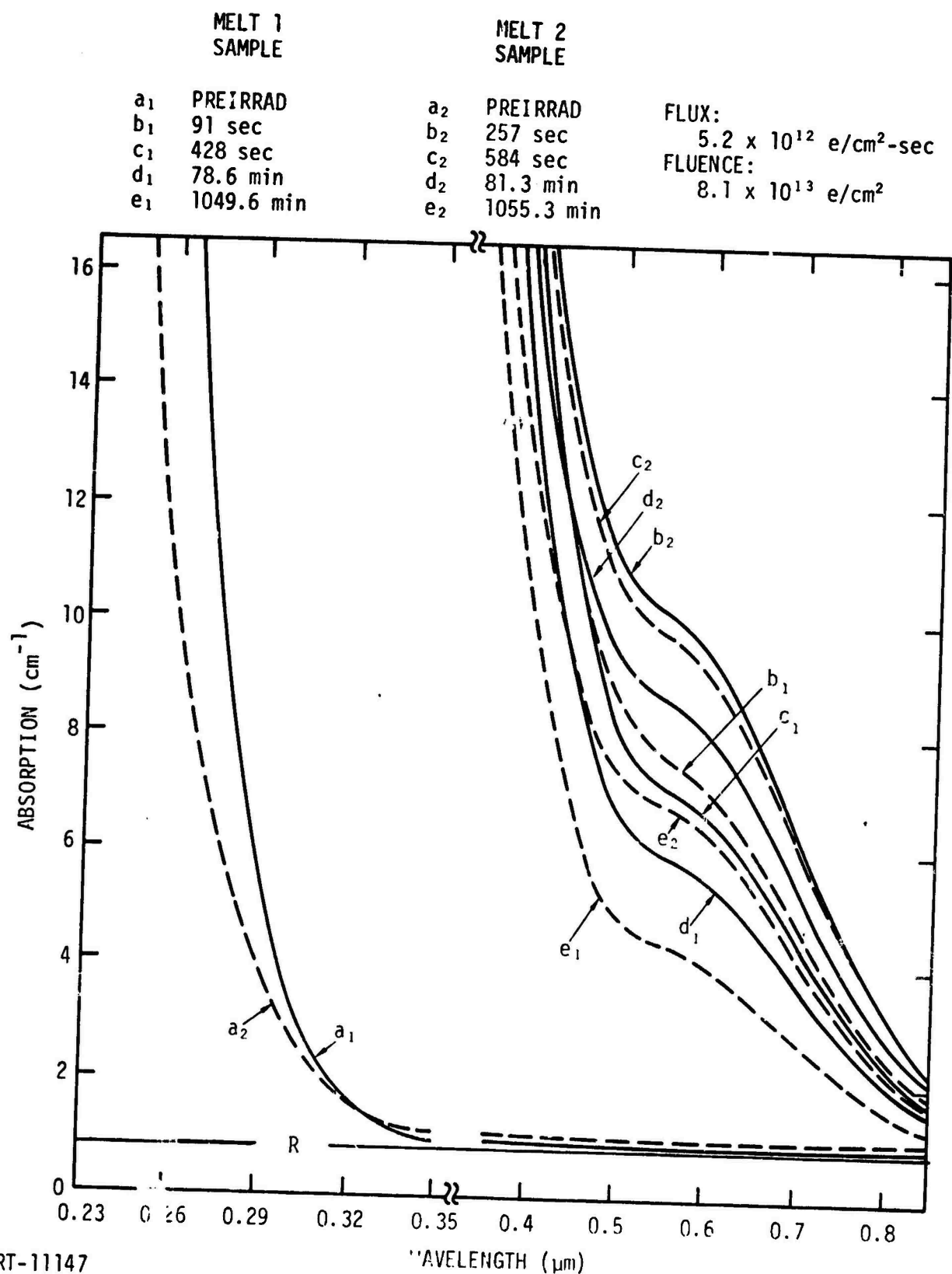


Figure 18. Bleaching of SK-14 absorption spectra

TIME AFTER IRRAD

a PREIRRAD
b 78 sec
c 376 sec
d 52.2 min
e 1030.7 min

FLUX $5.8 \times 10^{12} \text{ e/cm}^2\text{-sec}$
FLUENCE $8.1 \times 10^{13} \text{ e/cm}^2$
SAMPLE XA-8

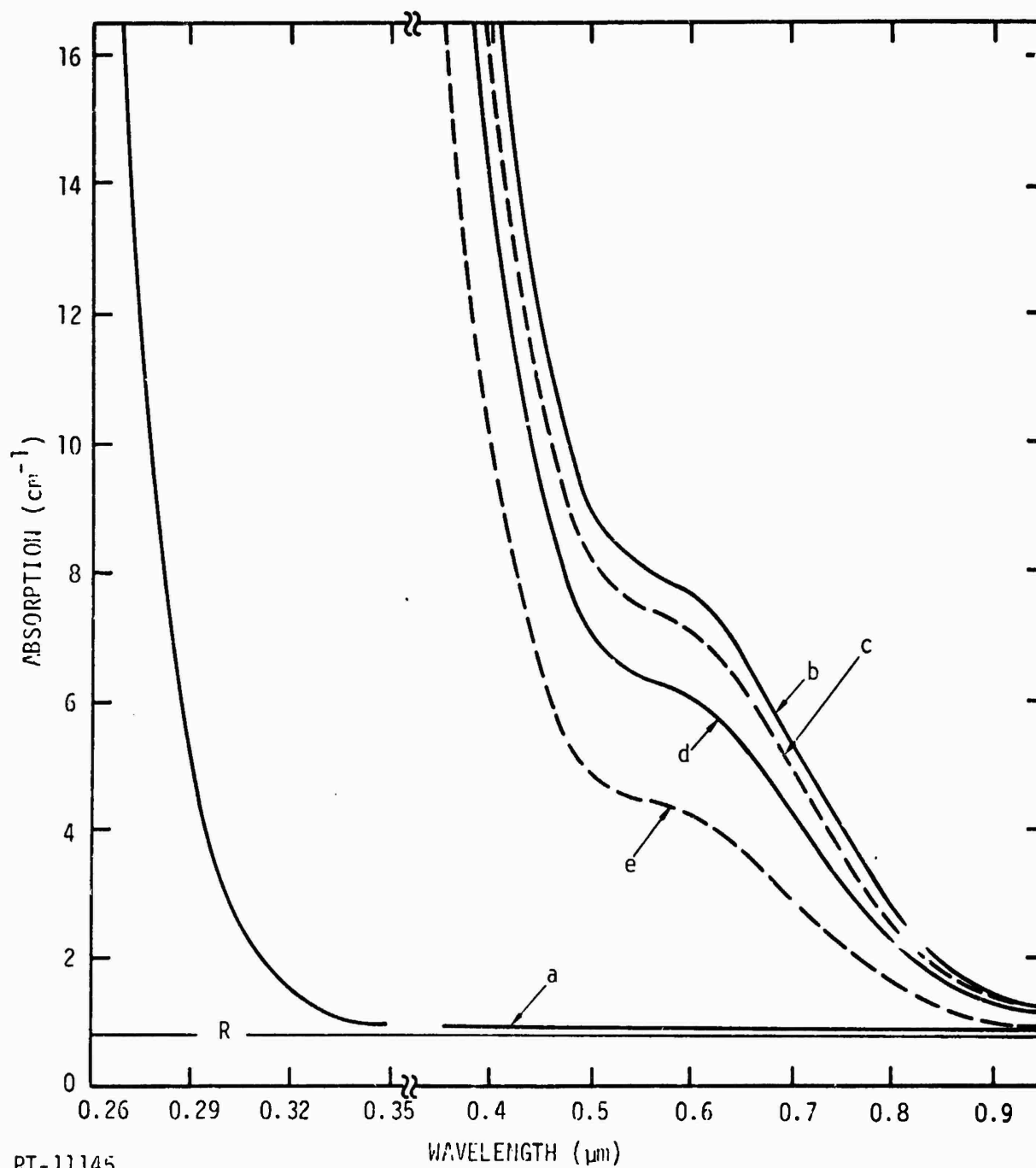


Figure 19. Bleaching of SK-7 absorption spectra

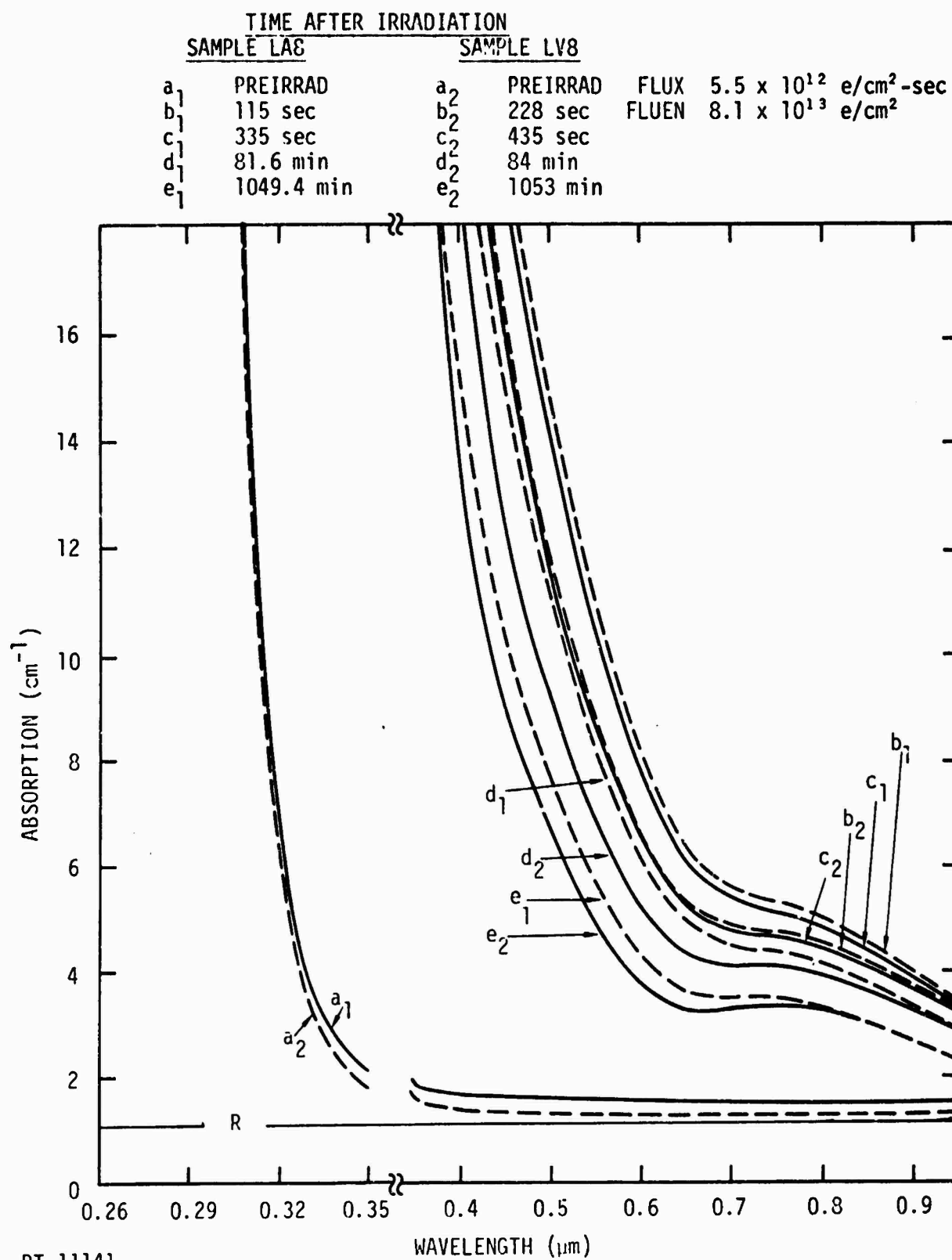


Figure 20. Bleaching of LaK-10 absorption spectra

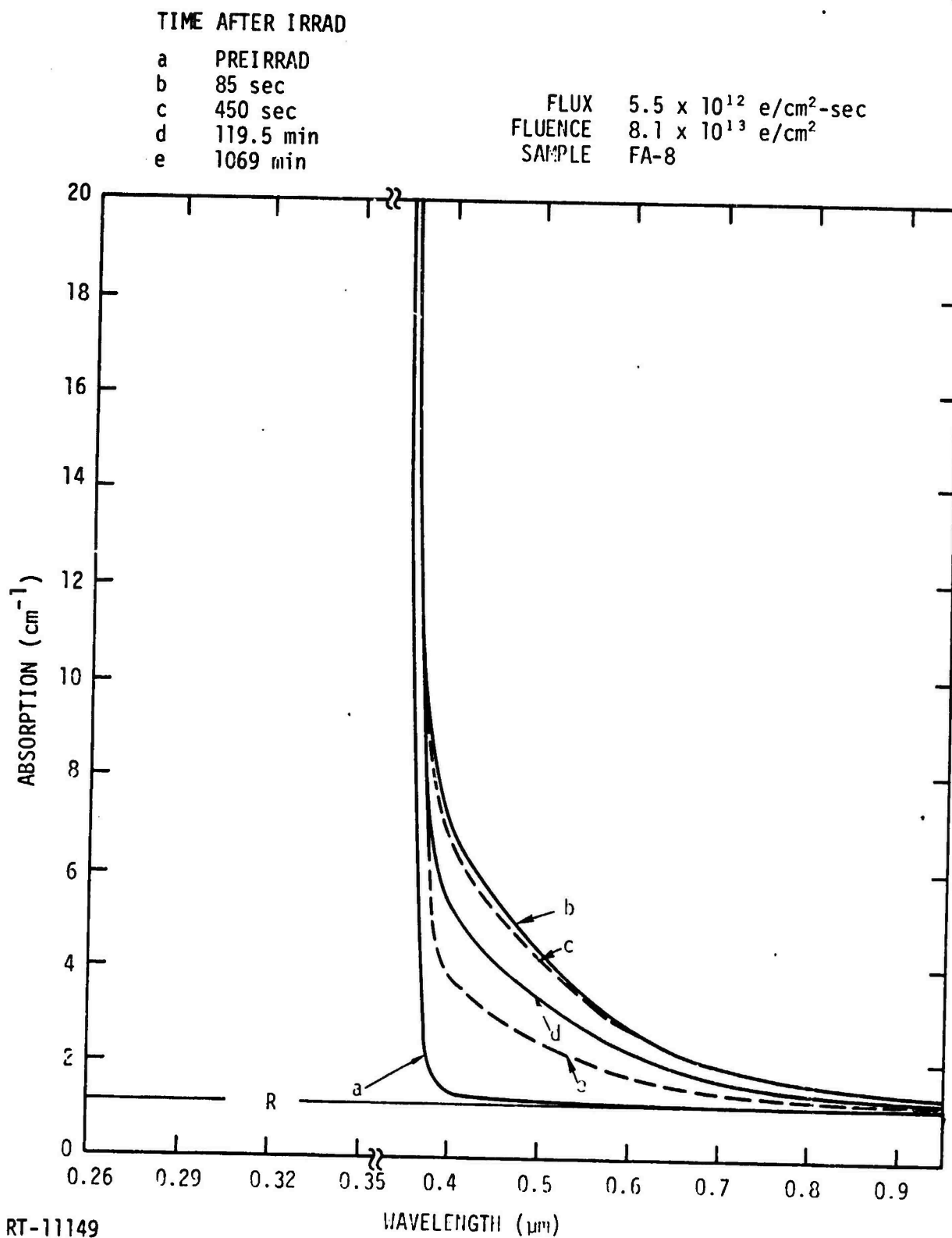
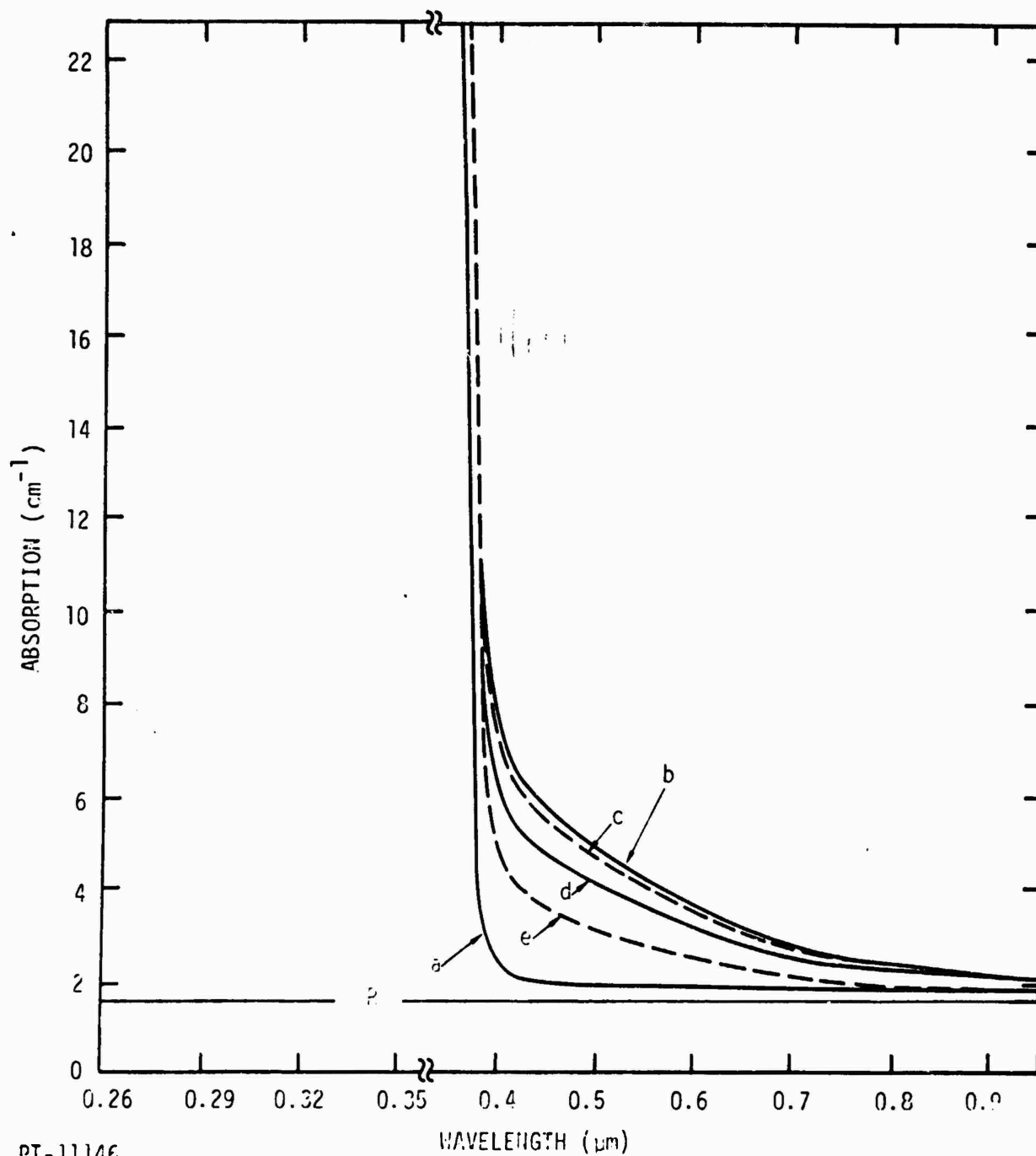


Figure 21. Bleaching of SF-10 absorption spectra

TIME AFTER IRRAD

a PREIRRAD
b 85 sec
c 412 sec
d 73.5 min
e 1041.1 min

FLUX 5.3×10^{12} e/cm²-sec
FLUENCE 8.1×10^{13} e/cm²
SAMPLE VA-8



RT-11146

Figure 22. Bleaching of SF-11 absorption spectra

TIM₂ AFTER IRRAD

a PREIRRAD
b 95 sec
c 475 sec
d 160 min
e 1108 min

FLUX $5.4 \times 10^{12} \text{ e/cm}^2\text{-sec}$
FLUENCE $8.1 \times 10^{13} \text{ e/cm}$
SAMPLE CA-8

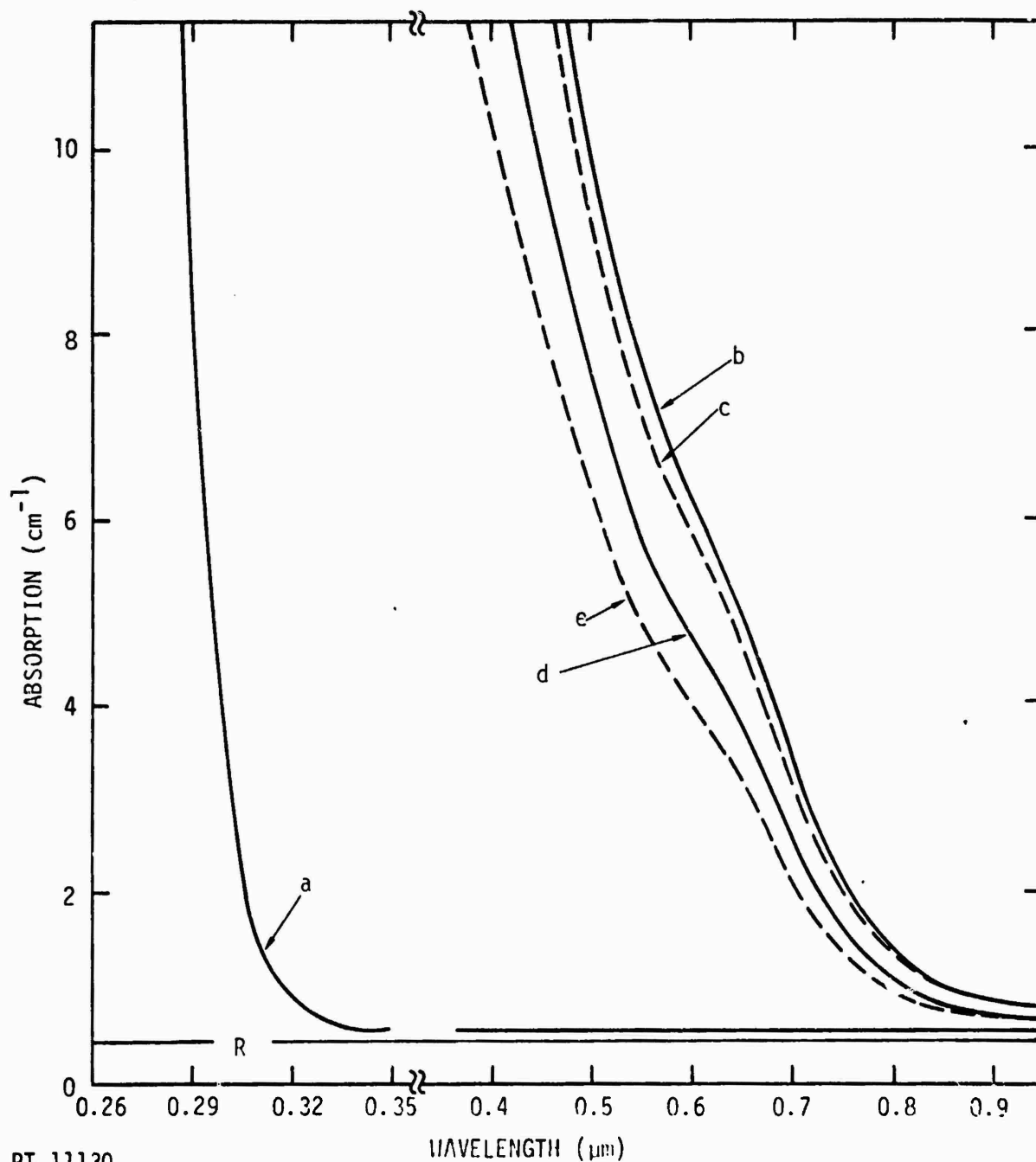
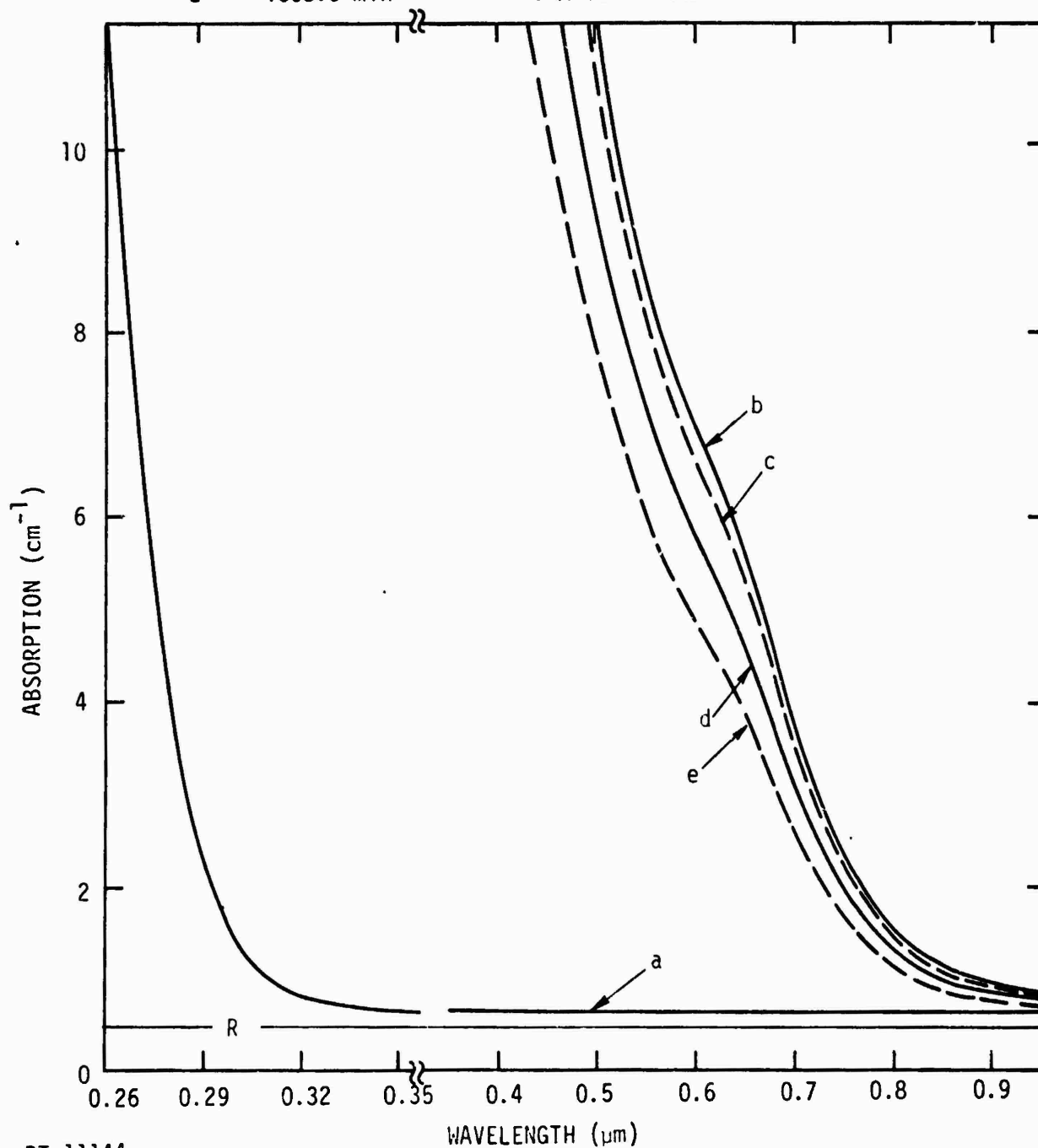


Figure 23 Bleaching of BK-7 absorption spectra

TIME AFTER IRRAD

a PREIRRAD
b 94 sec
c 399 sec
d 106.3 min
e 1058.3 min

FLUX 5.3×10^{12} e/cm²-sec
FLUENCE 8.1×10^{13} e/cm
SAMPLE HA8



RT-11144

Figure 24. Bleaching of UBK-7 absorption spectra

TIME AFTER IRRAD

a PREIRRAD
b 71 sec
c 156 sec
d 456 sec
e 51.3 min
e 955 min

FLUX 5.8×10^{12} e/cm²-sec
FLUENCE 8.1×10^{13} e/cm²
SAMPLE BA-8

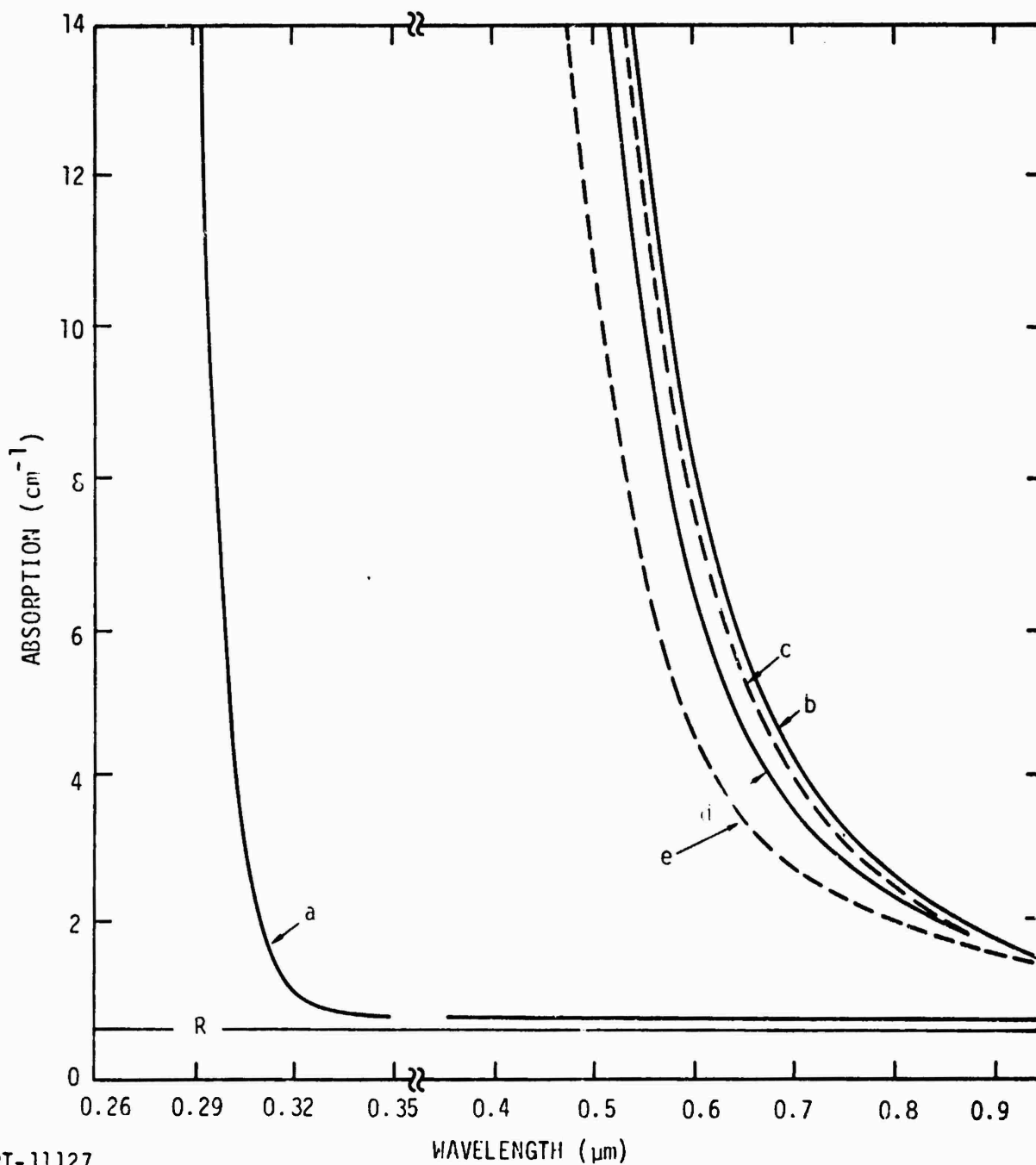


Figure 25. Bleaching of BaK-4 absorption spectra

TIME AFTER IRRAD

a PREIRRAD

b 90 sec

c 433 sec

d 95 min

e 1049.5 min

FLUX $5.5 \times 10^{12} \text{ e/cm}^2\text{-sec}$

FLUENCE $8.1 \times 10^{13} \text{ e/cm}^2$

SAMPLE KA-8

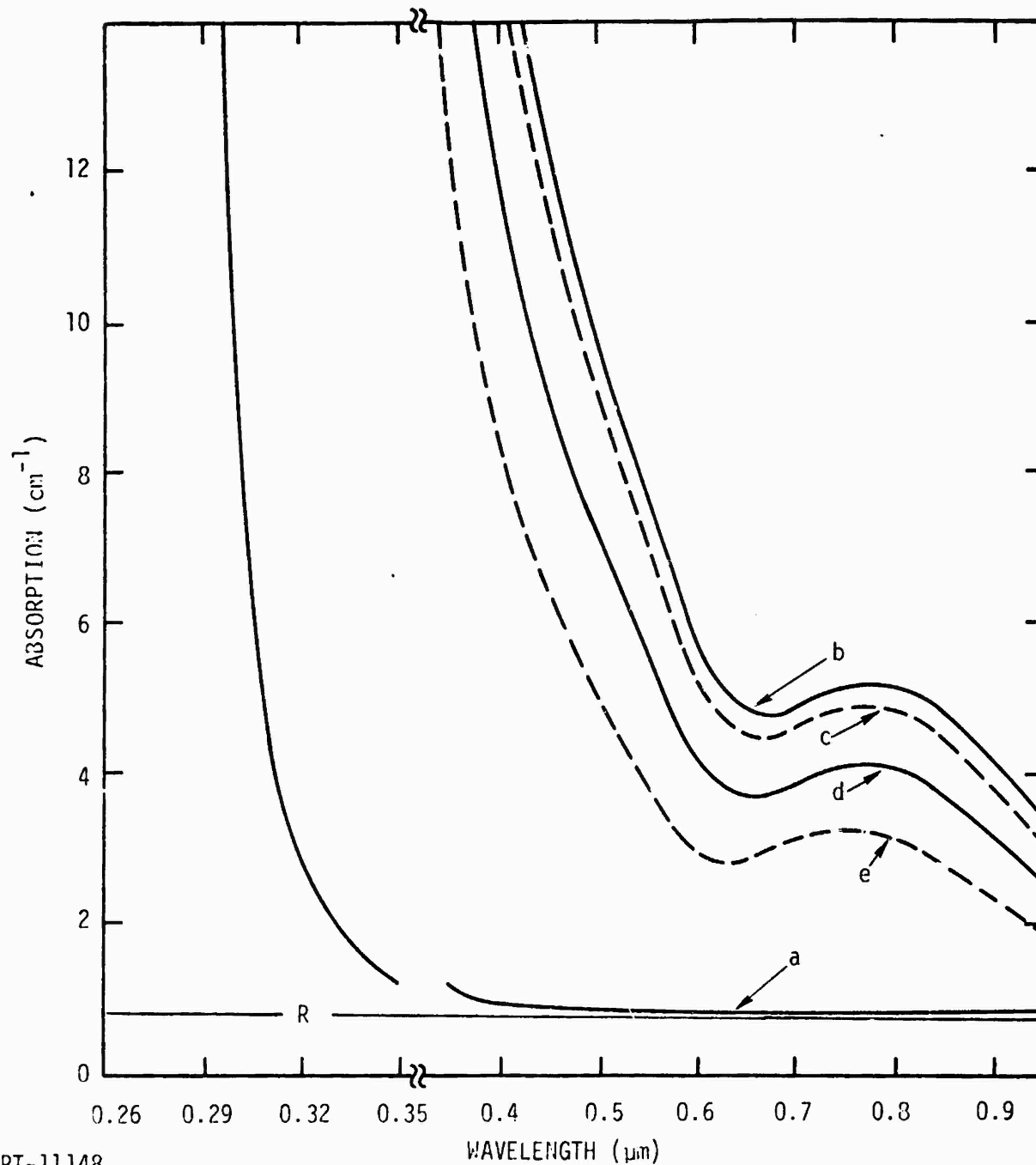


Figure 26. Bleaching of KzFS-N4 absorption spectra

3.1.3 Absorption as a Function of Fluence

Full spectral scans of all the Schott glasses were made after exposure to a range of fluences from 5.6×10^{10} to 5.6×10^{14} e/cm². Three glass types were irradiated simultaneously at a flux of $\sim 1 \times 10^{10}$ e/cm²-sec to a fluence of 5.6×10^{10} e/cm². These samples were removed from the radiation room and spectral scans were made while the next three samples were irradiated similarly. After all nine samples were irradiated to a fluence of 5.6×10^{10} e/cm², the above procedure was repeated to a fluence of 5.6×10^{11} e/cm² and then to 5.6×10^{12} e/cm². Then new samples were irradiated similarly at $\sim 1 \times 10^{12}$ e/cm²-sec to fluences of 5.6×10^{12} , 5.6×10^{13} , and 5.6×10^{14} e/cm². The main points to realize from the above description are:

1. At a given flux, the duration of the irradiations became longer as the fluence levels increased.
2. As a result of the longer irradiation times, the time between successive irradiations of the same sample increased.
3. For long irradiations, the bleaching of the induced absorption during and between irradiations could not be ignored.

The spectra obtained by the above procedure are shown in Figures 27 through 35.* Except for SF-10 and SF-11, these spectra have been corrected for bleaching which occurred between irradiations. The procedure used to correct the spectra and the uncorrected spectra are included in Appendix D. As mentioned in Section 3.1.4, the Schott SF-10 and SF-11 displayed flux-dependent bleaching rates which makes correction of the spectra of these samples by the method outlined in Appendix A inappropriate. The fact that such a straightforward correction was applicable to the remainder of the samples was in itself surprising.

Examination of Figures 27 through 35 reveals that the darkening does not proceed as a linear function of fluence over the entire range of fluences. The induced absorption at several wavelengths was plotted as a

*It became apparent that subsequent irradiations of samples to intermediate fluences would yield useful data. These irradiations were carried out as described above, and the results are included in Figures 27-35.

a PREIRRAD
 a 5.6×10^{10} e/cm²
 b 5.6×10^{11} e/cm²
 c 5.6×10^{12} e/cm²
 d 2.5×10^{13} e/cm²
 e 5.6×10^{13} e/cm²
 f 8.1×10^{13} e/cm²
 g 5.6×10^{14} e/cm²

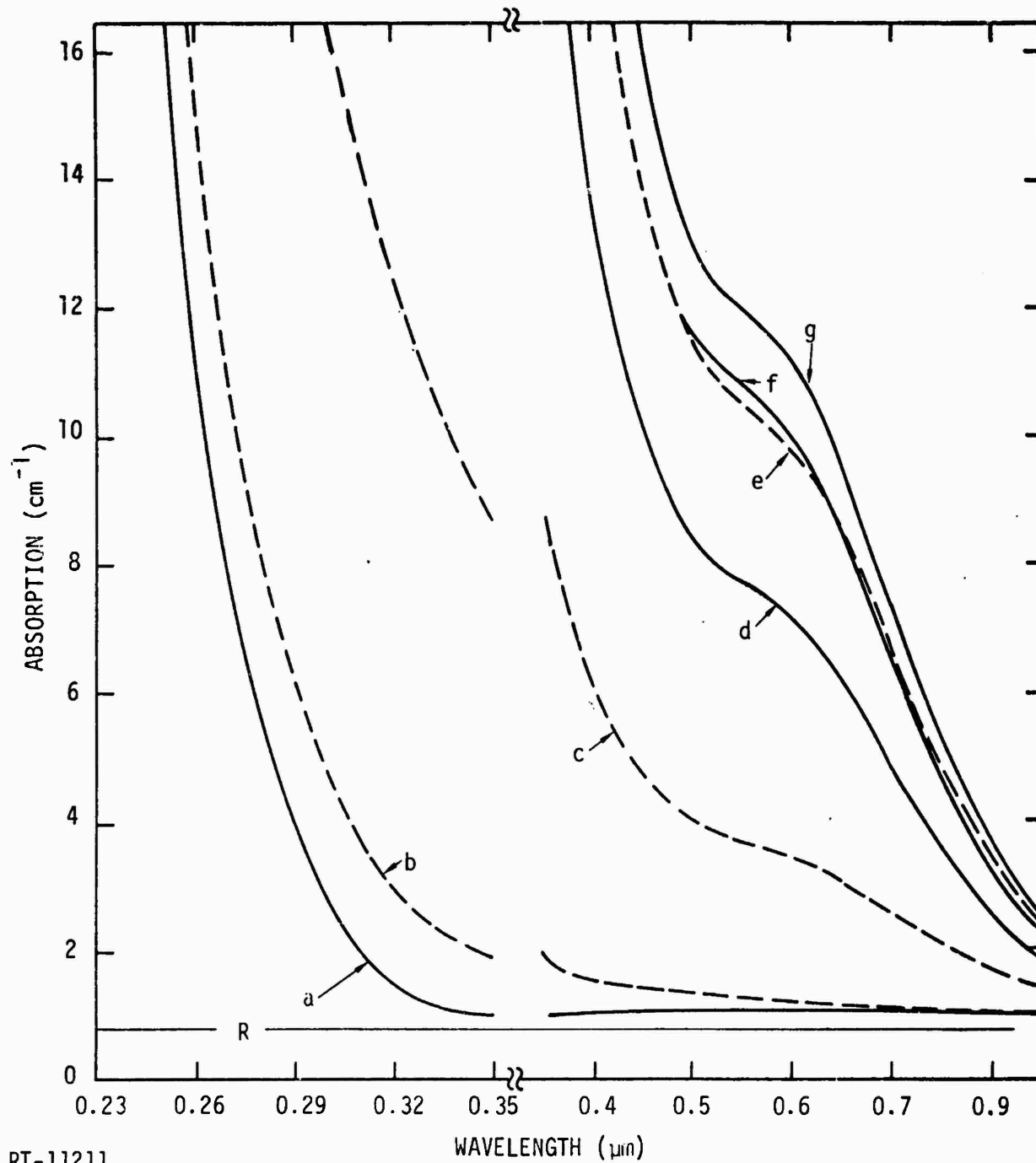
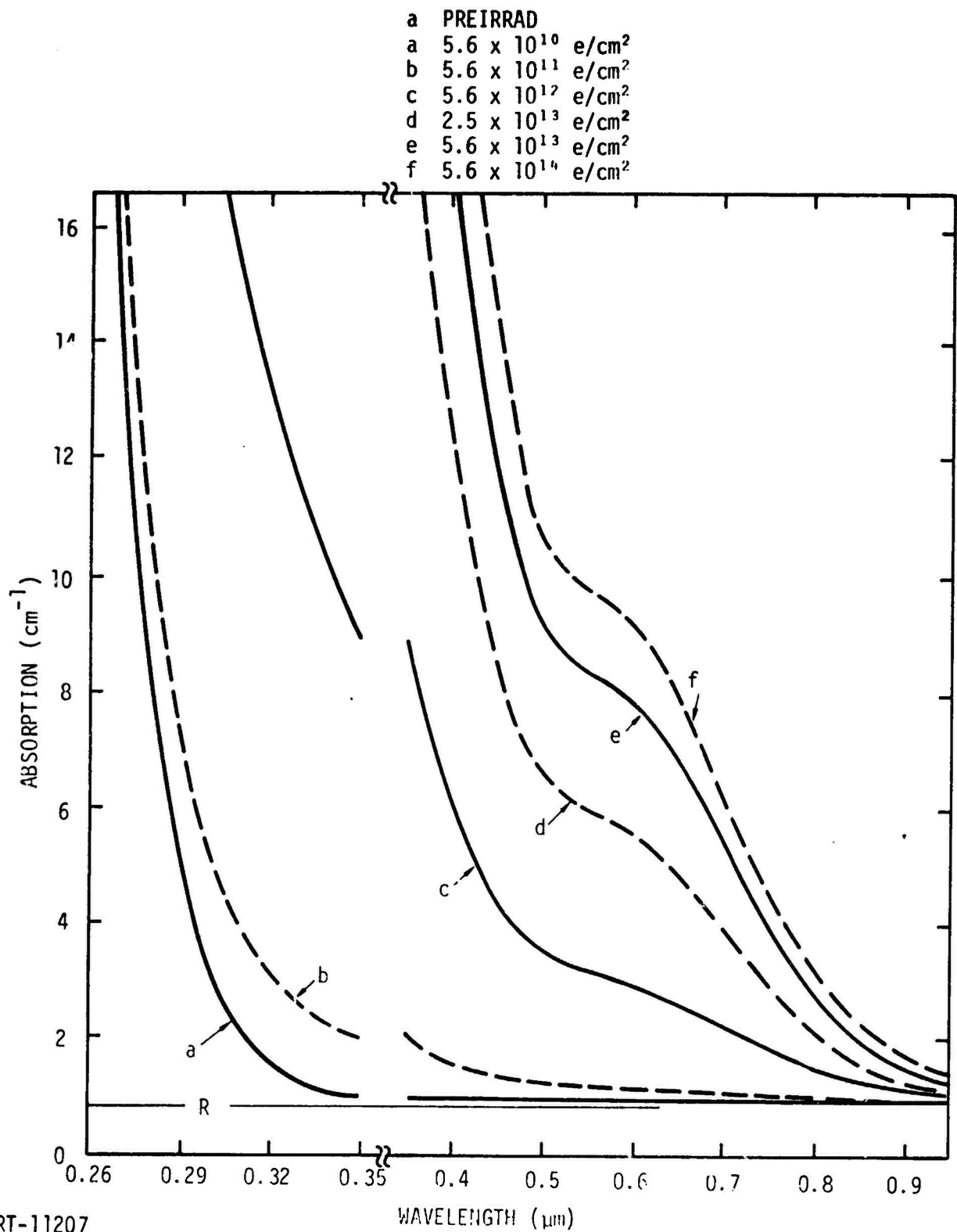


Figure 27. SK-14 absorption spectra at several fluences



RT-11207

Figure 28. SK-7 absorption spectra at several fluences

a	PREIRRAD
b	$5.6 \times 10^{10} \text{ e/cm}^2$
c	$5.6 \times 10^{11} \text{ e/cm}^2$
d	$5.6 \times 10^{12} \text{ e/cm}^2$
e	$2.5 \times 10^{13} \text{ e/cm}^2$
f	$5.6 \times 10^{13} \text{ e/cm}^2$
g	$8.1 \times 10^{13} \text{ e/cm}^2$
h	$5.6 \times 10^{14} \text{ e/cm}^2$

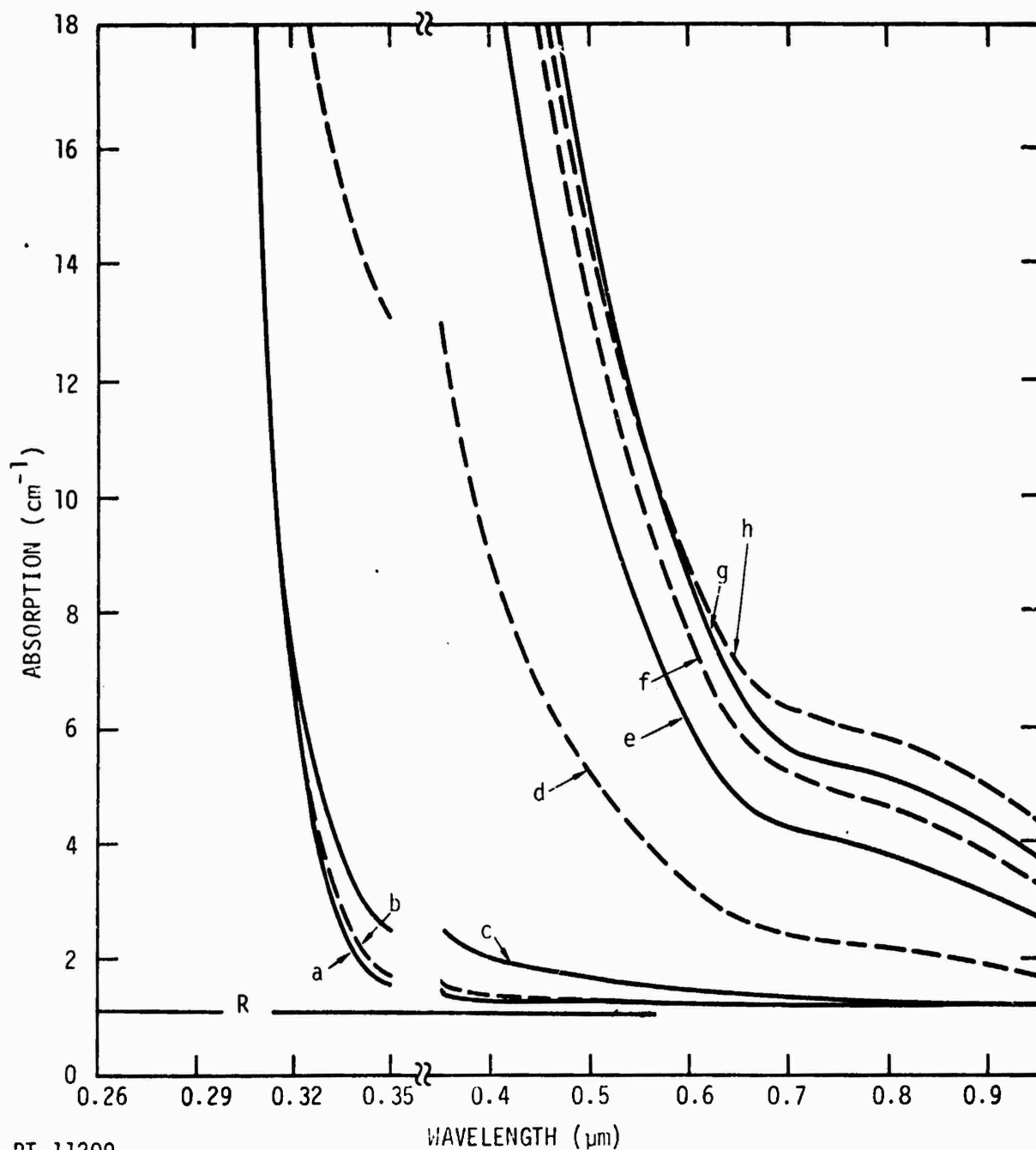
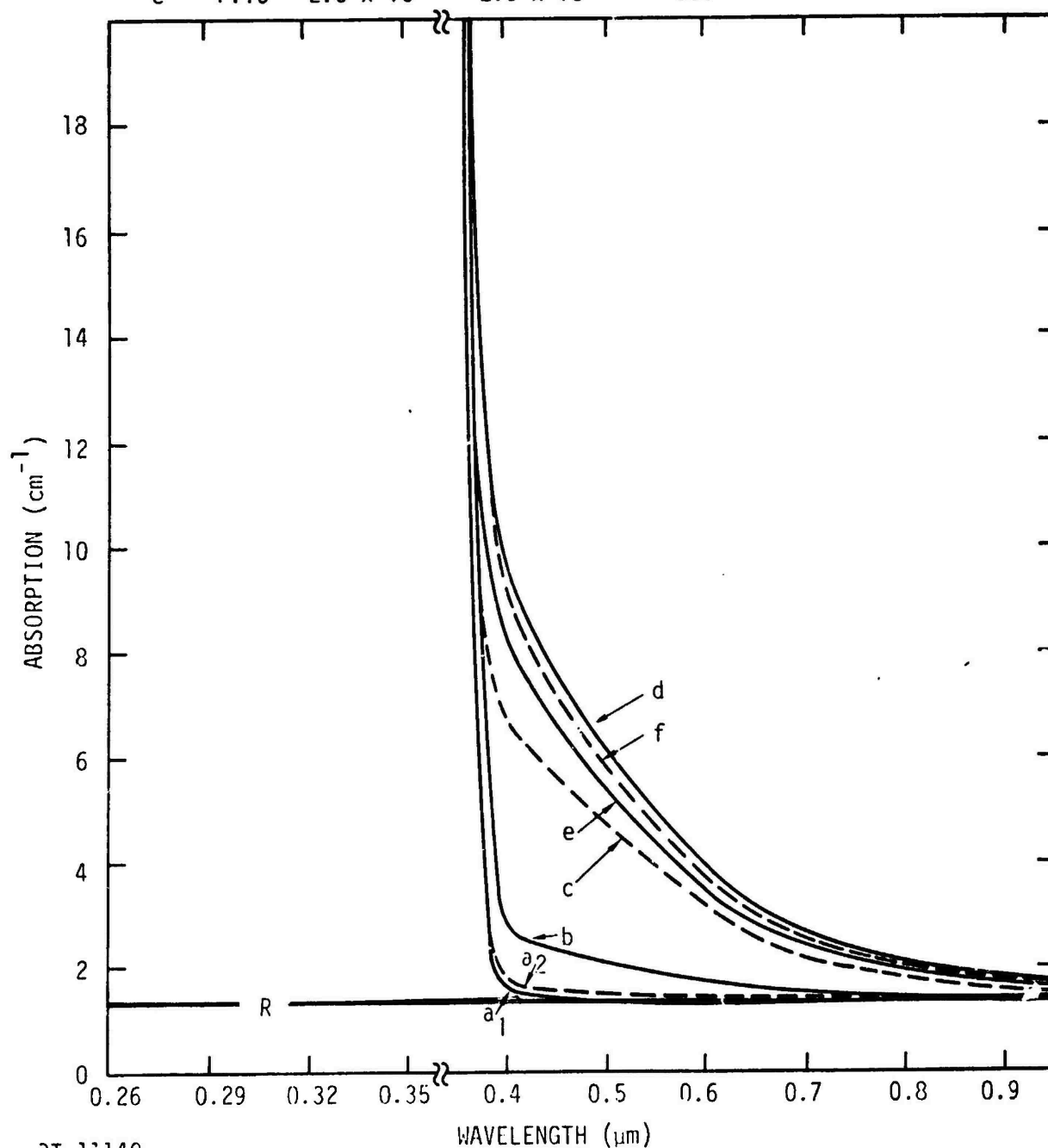


Figure 29. LaK-10 absorption spectra at several fluences

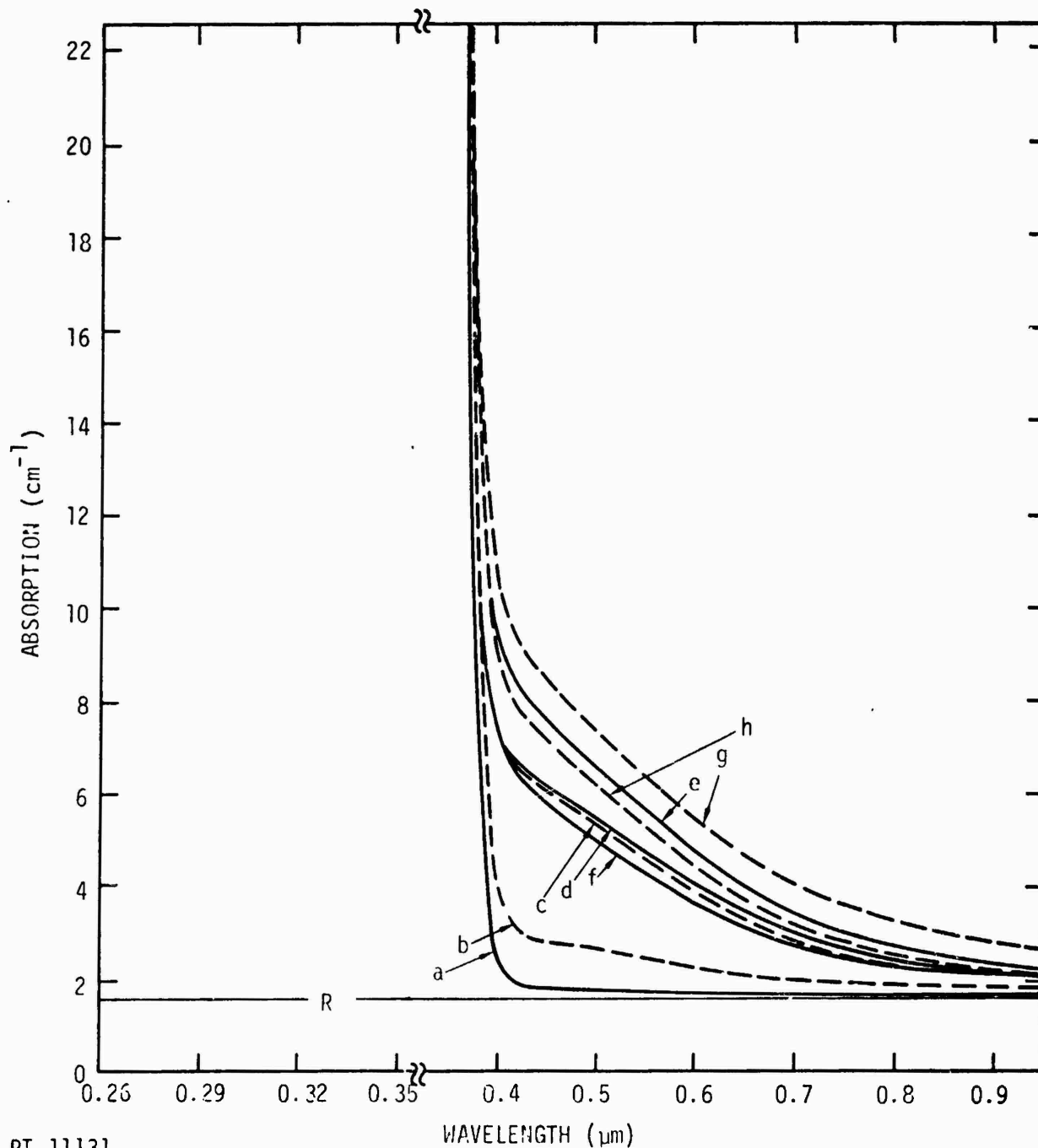
SAMPLE NO.	FLUX (e/cm ² -sec)	FLUENCE (e/cm ²)	TIME AFTER IRRAD (sec)	TIME BETWEEN DATA (min)	
a ₁	FV6,FV9,FV10	PREIRRAD	-	-	
a ₂	FV7	PREIRRAD	-	-	
a ₂	FV7	7.5 x 10 ⁹	5.6 x 10 ¹⁰	535	
b	FV7	9.6 x 10 ⁹	5.6 x 10 ¹¹	497	38.1
c	FV7	1.0 x 10 ¹⁰	5.6 x 10 ¹²	464	65.4
c	FV6	8.6 x 10 ¹¹	5.6 x 10 ¹²	383	-
d	FV6	1.0 x 10 ¹²	5.6 x 10 ¹³	302	35.4
e	FV6	1.0 x 10 ¹²	5.6 x 10 ¹⁴	276	44.2
f	FV9	1.1 x 10 ¹¹	8.1 x 10 ¹³	504	-
d	FV10	2.5 x 10 ¹¹	2.5 x 10 ¹³	311	-
e	FV10	2.5 x 10 ¹¹	2.5 x 10 ¹³	365	-



RT-11140

Figure 30. SF-10 absorption spectra at several fluences

	SAMPLE NO.	FLUX ($\text{e}/\text{cm}^2\text{-sec}$)	FLUENCE (e/cm^2)	TIME AFTER IRRAD (sec)	TIME BETWEEN DATA (min)
a	PREIRRAD	-	-	-	-
a	VV7	8.7×10^3	5.6×10^{10}	283	-
b	VV7	9.5×10^9	5.6×10^{11}	296	44.5
c	VV7	1.0×10^{10}	5.6×10^{12}	283	73.8
d	VV6	9.8×10^{11}	5.6×10^{12}	251	-
e	VV6	9.8×10^{11}	5.6×10^{13}	198	33.6
f	VV6	1.0×10^{12}	5.6×10^{14}	343	107.9
g	VV9	1.1×10^{11}	8.1×10^{13}	197	-
h	VV1	2.5×10^{11}	2.5×10^{13}	304	-



RT-11131

Figure 31. SF-11 absorption spectra at several fluences

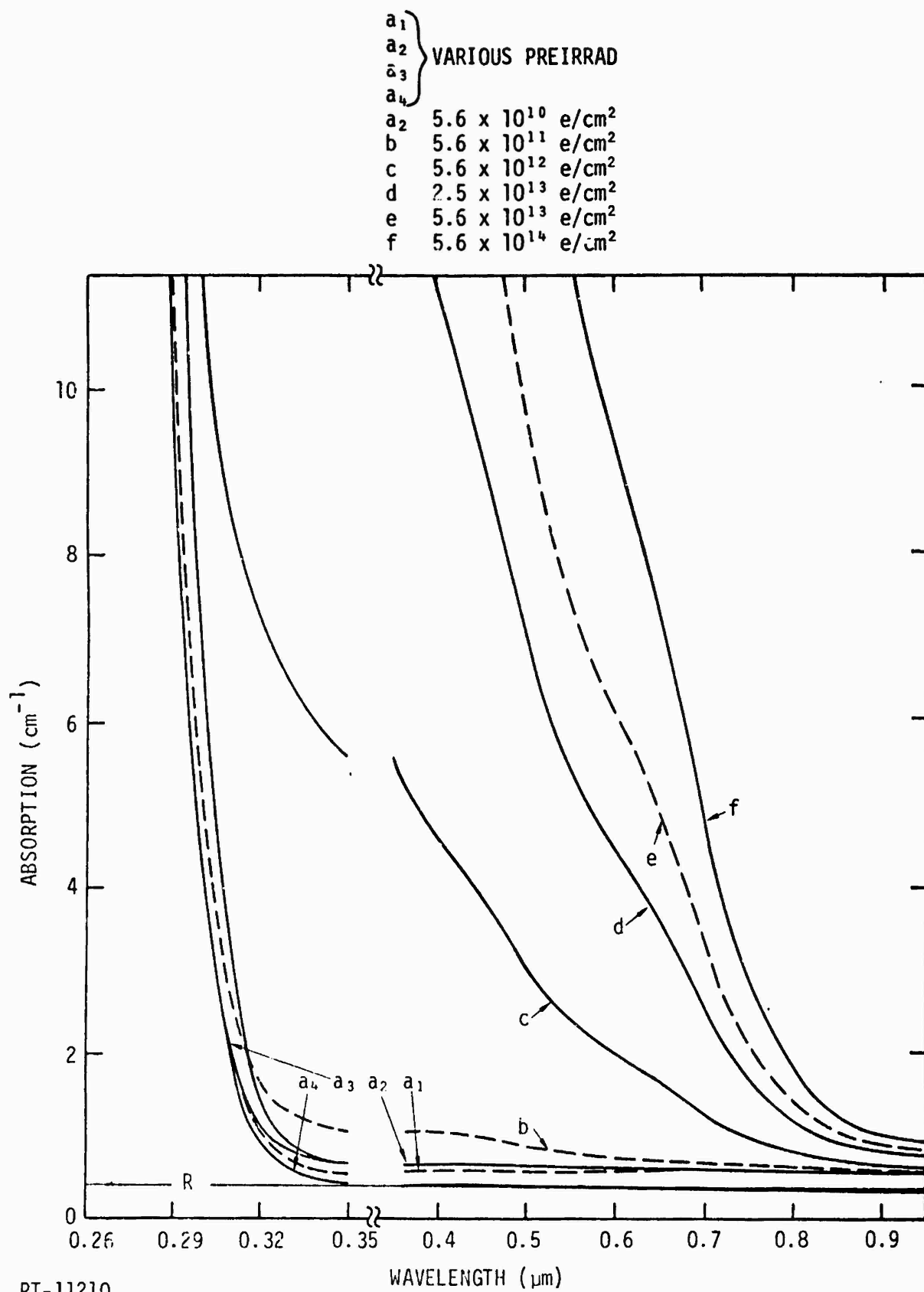
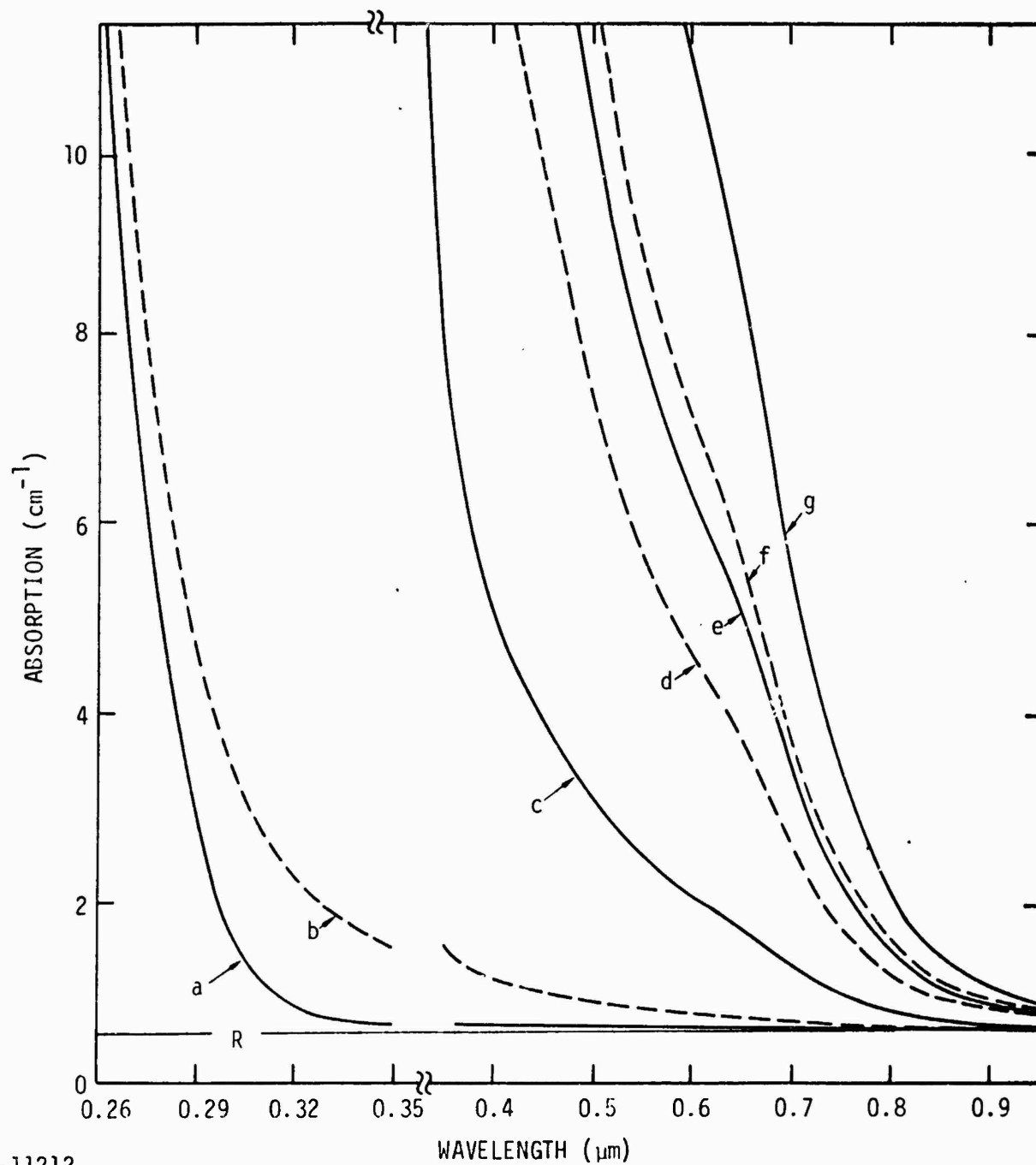


Figure 32. BK-7 absorption spectra at several fluences

a	PREIRRAD
a	$5.6 \times 10^{10} \text{ e/cm}^2$
b	$5.6 \times 10^{11} \text{ e/cm}^2$
c	$5.6 \times 10^{12} \text{ e/cm}^2$
d	$2.5 \times 10^{13} \text{ e/cm}^2$
e	$5.6 \times 10^{13} \text{ e/cm}^2$
f	$8.1 \times 10^{13} \text{ e/cm}^2$
g	$5.6 \times 10^{14} \text{ e/cm}^2$



RT-11212

Figure 33. UBK-7 absorption spectra at several fluences

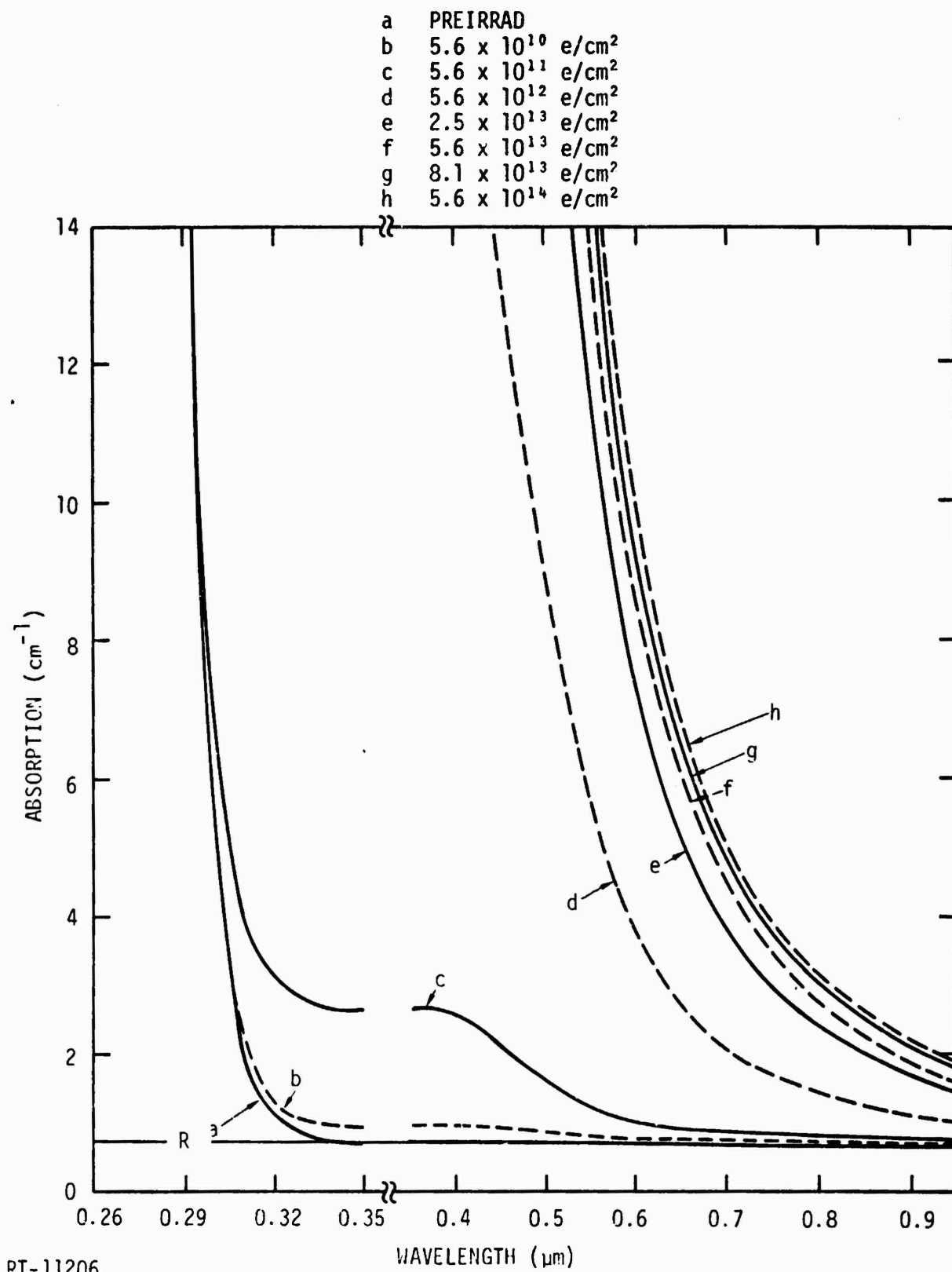
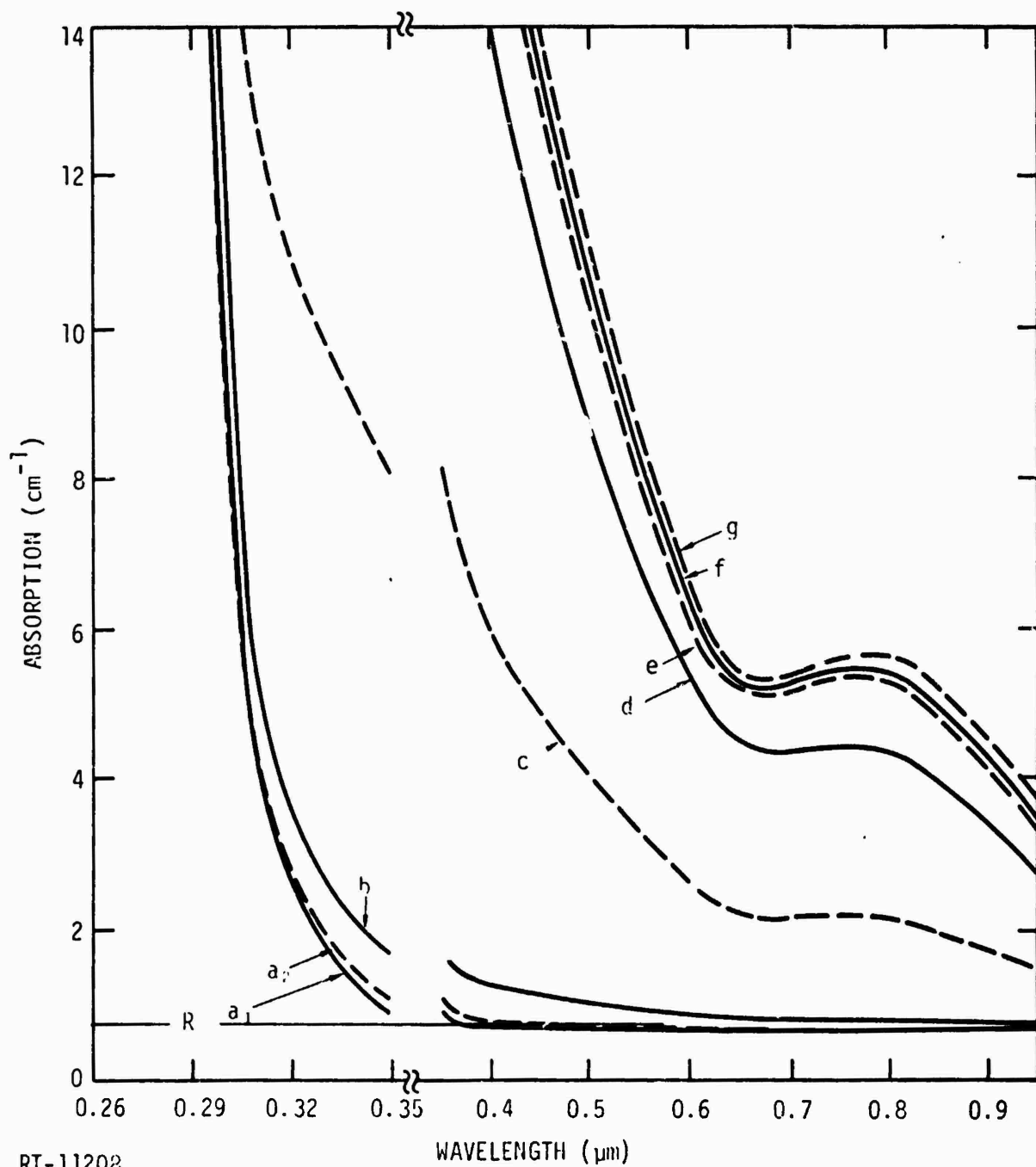


Figure 34. BaK-4 absorption spectra at several fluences

a_1	} VARIOUS PREIRRAD	
a_2		
a_1		$5.6 \times 10^{10} \text{ e/cm}^2$
b		$5.6 \times 10^{11} \text{ e/cm}^2$
c		$5.6 \times 10^{12} \text{ e/cm}^2$
d		$2.5 \times 10^{13} \text{ e/cm}^2$
e		$5.6 \times 10^{13} \text{ e/cm}^2$
f		$8.1 \times 10^{13} \text{ e/cm}^2$
g		$5.6 \times 10^{14} \text{ e/cm}^2$



RT-11208

Figure 35. KzFS-N4 absorption spectra at several fluences

function of fluence for each sample, and these results are shown in Figures 36 through 44. Note that the absorption proceeds as a linear function of the fluence for fluences up to about 10^{13} e/cm², while at larger fluences the induced absorption rapidly approaches a quasi-saturation level, after which the growth proceeds at a much slower rate.

It has been reported (Refs. 17,18) that the induced darkening in glasses can be parametrized by an equation of the form

$$\alpha(\phi) = \alpha_S [1 - \exp(-B\phi)] + \alpha_L \phi, \quad (9)$$

where $\alpha(\phi)$ is the radiation-induced absorption coefficient at some wavelength λ after exposure to a fluence ϕ and is determined by subtracting the preirradiation spectra from the post-irradiation spectra. The α_S , B , and α_L are constants dependent on wavelength and glass type. At very high fluences, where $\phi \gg 1/B$,

$$[1 - \exp(-B\phi)] \approx 0,$$

and Eq. 9 can be written as

$$\alpha(\phi) \approx \alpha_S + \alpha_L \phi \quad \phi \gg 1/B.$$

At low fluences, $[\exp(-B\phi)]$ can be expanded and Eq. 9 can be written as

$$\begin{aligned} \alpha(\phi) &\approx \alpha_S B\phi + \alpha_L \phi & \phi \ll 1/B, \\ &\approx \alpha_S B\phi & \text{if } \alpha_S B \gg \alpha_L. \end{aligned}$$

At intermediate fluences, the darkening proceeds as a saturating exponential. This behavior is consistent with the data in Figures 36 through 44.

As can be seen from Figures 36 through 44, for the range of fluences used in this investigation, the linear term ($\alpha_L \phi$) in Eq. 9 can effectively be set equal to zero. Therefore, the darkening growth in this fluence range can be described accurately by α_S and B for those curves which saturate and for those curves which appear linear by $\alpha_S B$. Values of α_S , B , and $\alpha_S B$ obtained for the Schott glasses are listed in Table 5. Note that the darkening for SF-10 and SF-11 apparently decreases at the highest fluence. This results from the fact that corrections for bleaching in these samples were not made. Notice that, for the most part, the darkening curves at various

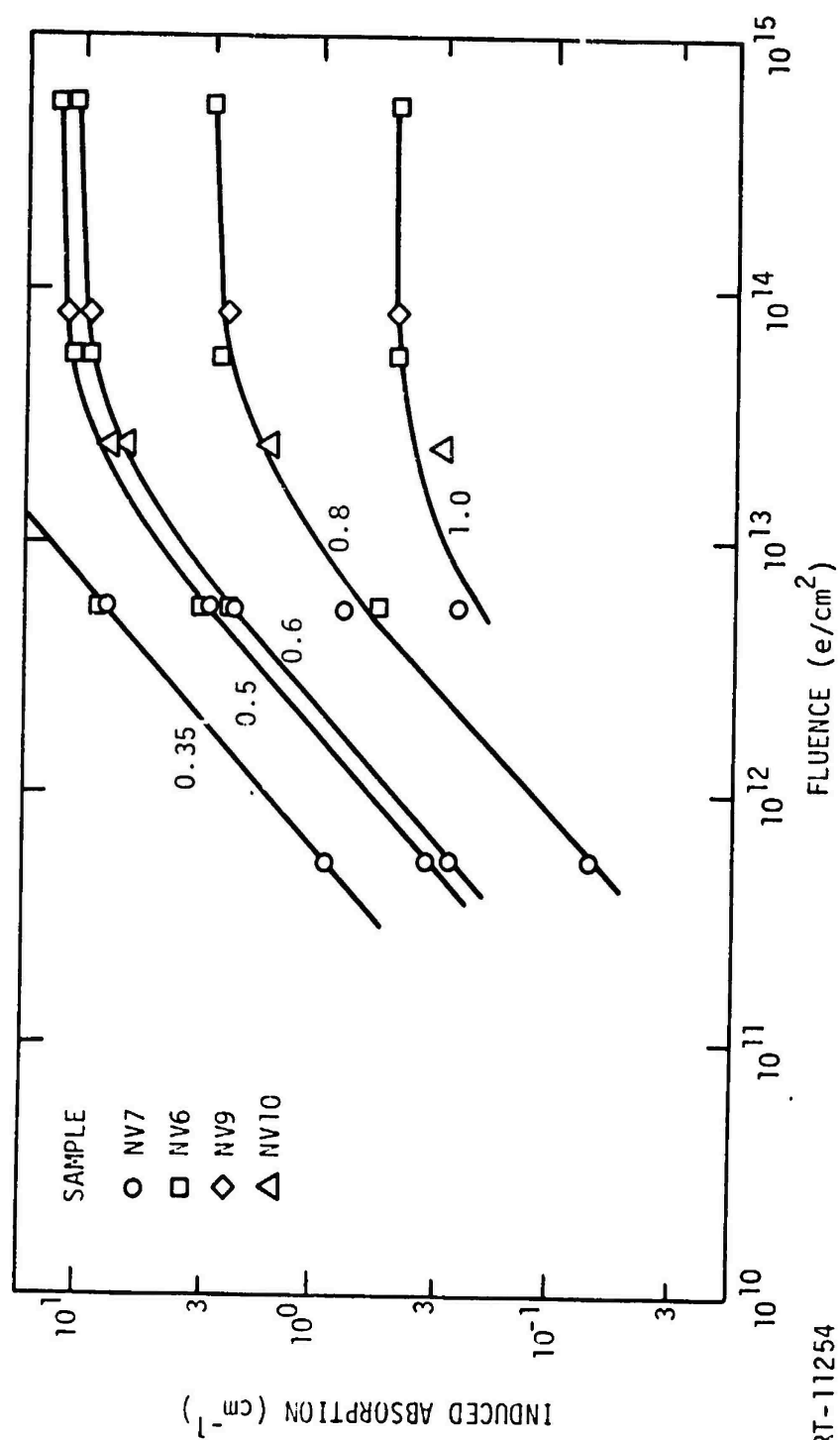


Figure 36. SK-14 absorption growth curves

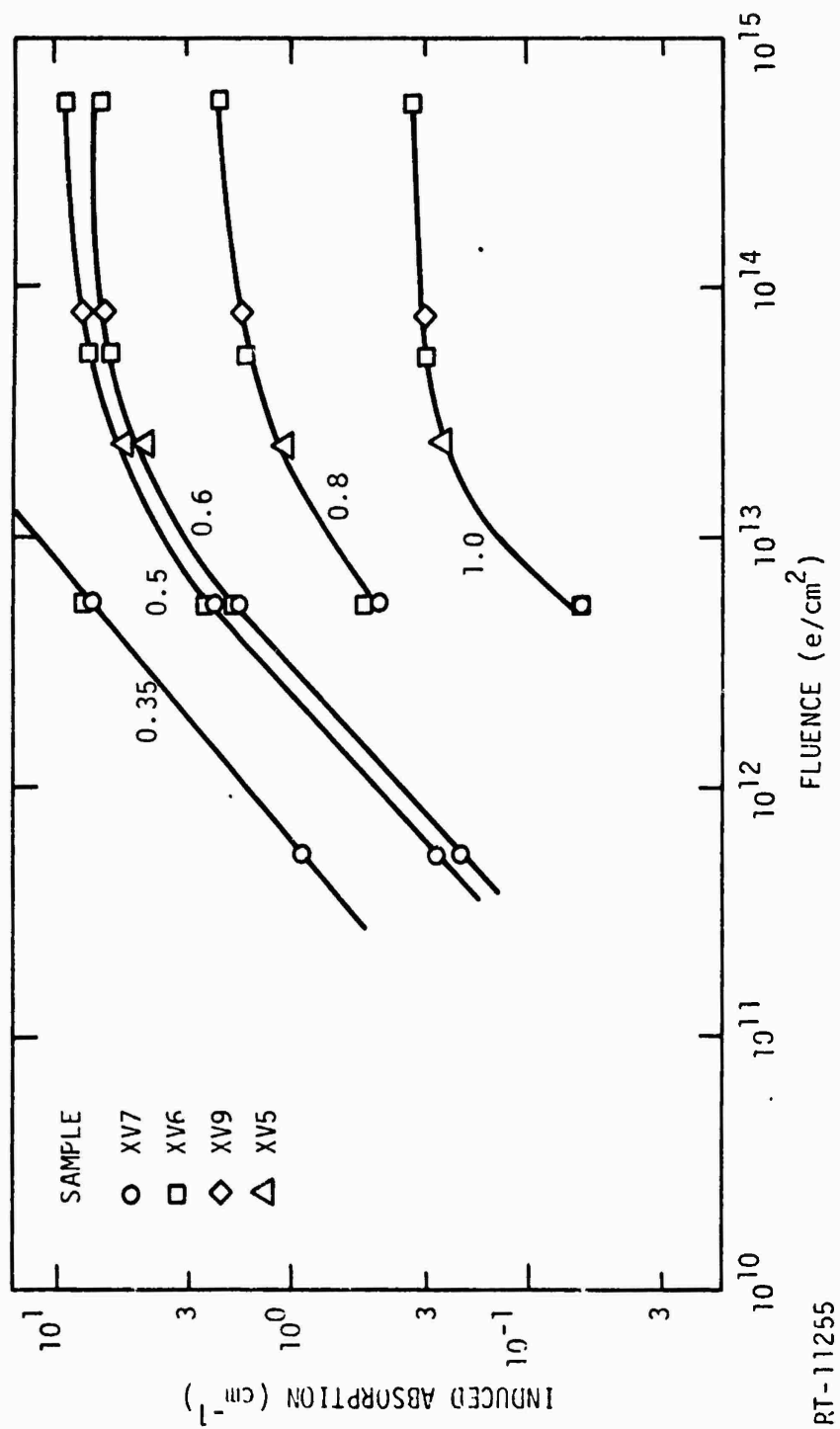


Figure 37. SK-7 absorption growth curves

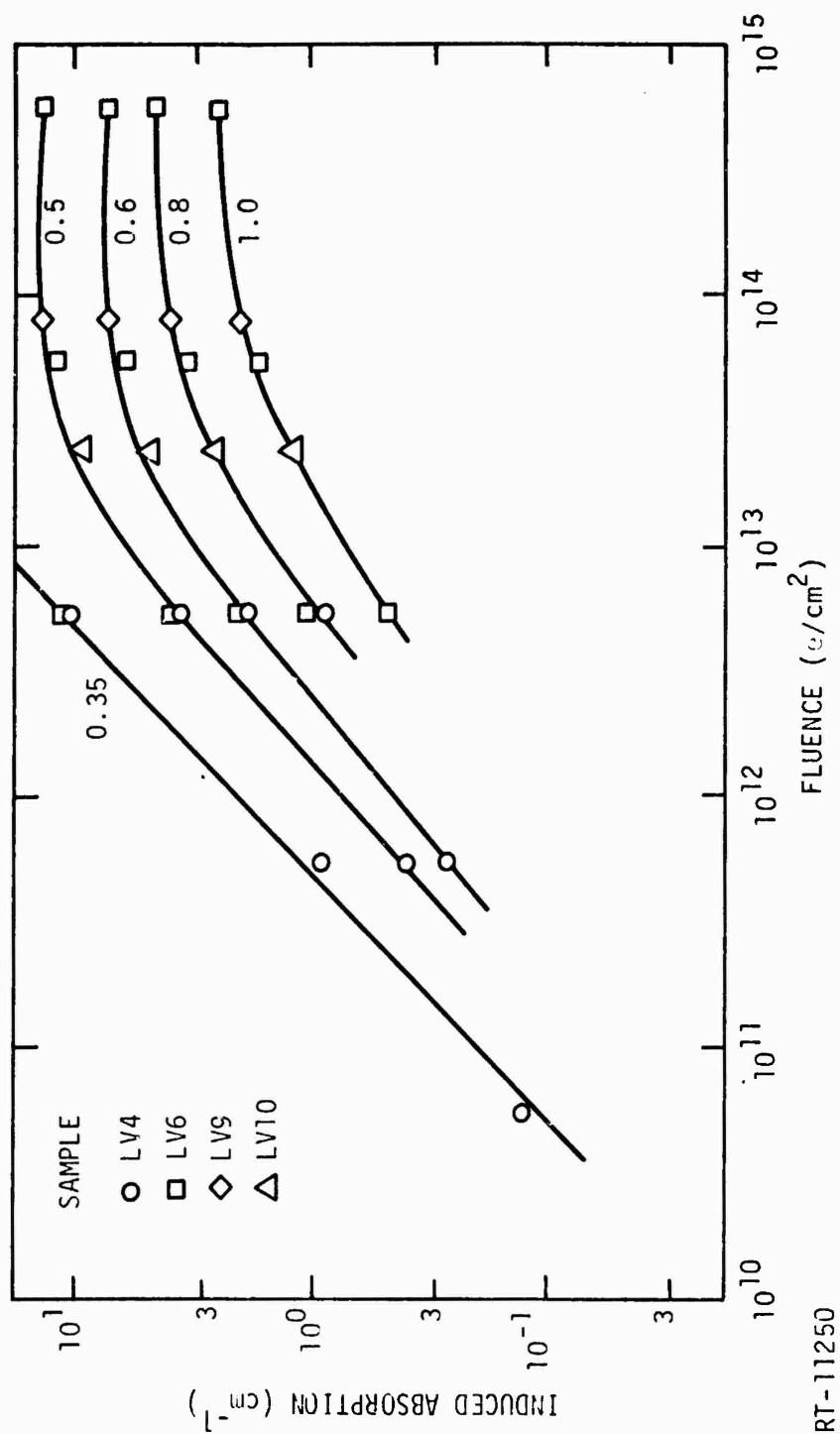


Figure 38. LaK-10 absorption growth curves

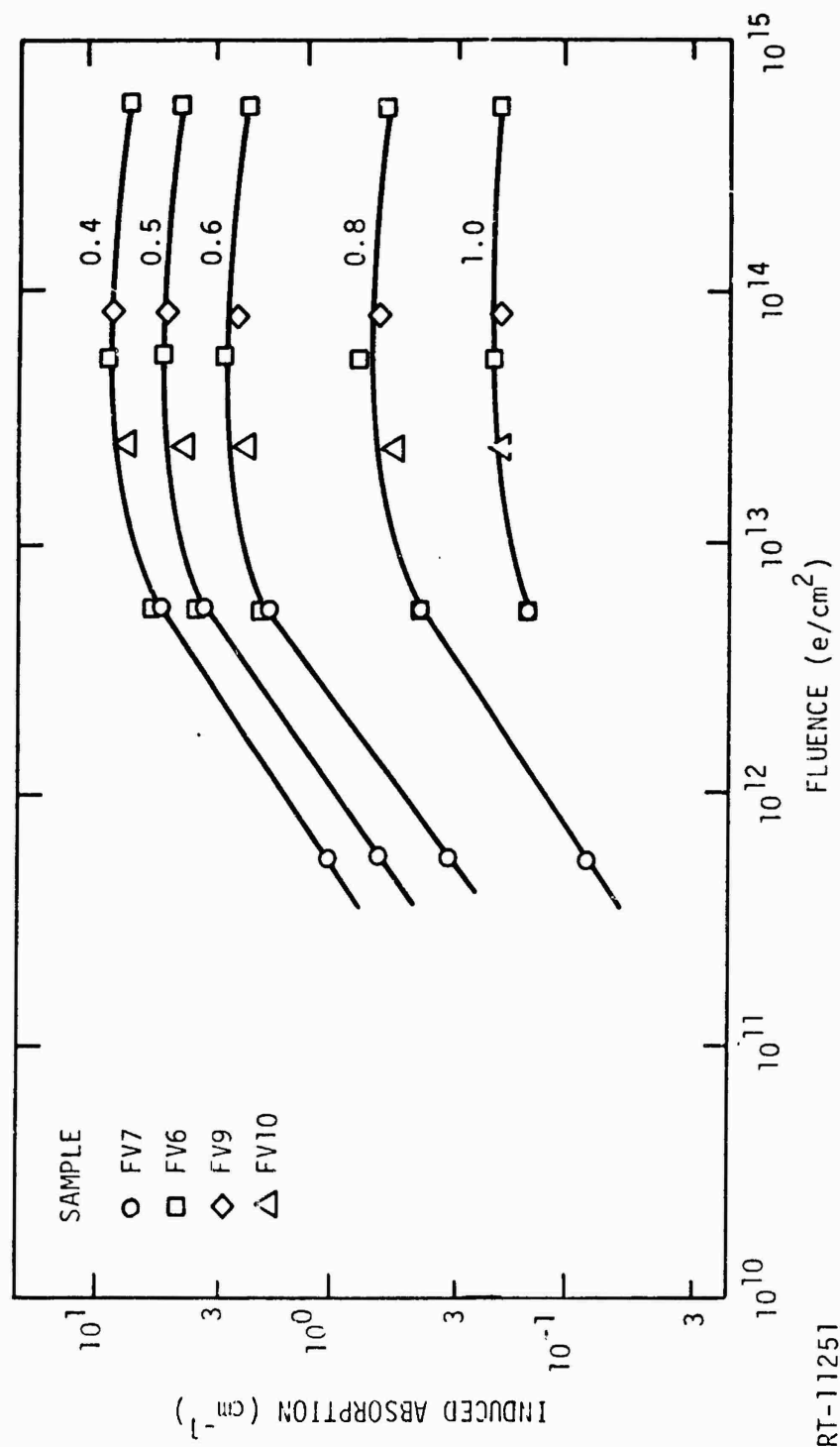


Figure 39. SF-10 absorption growth curves

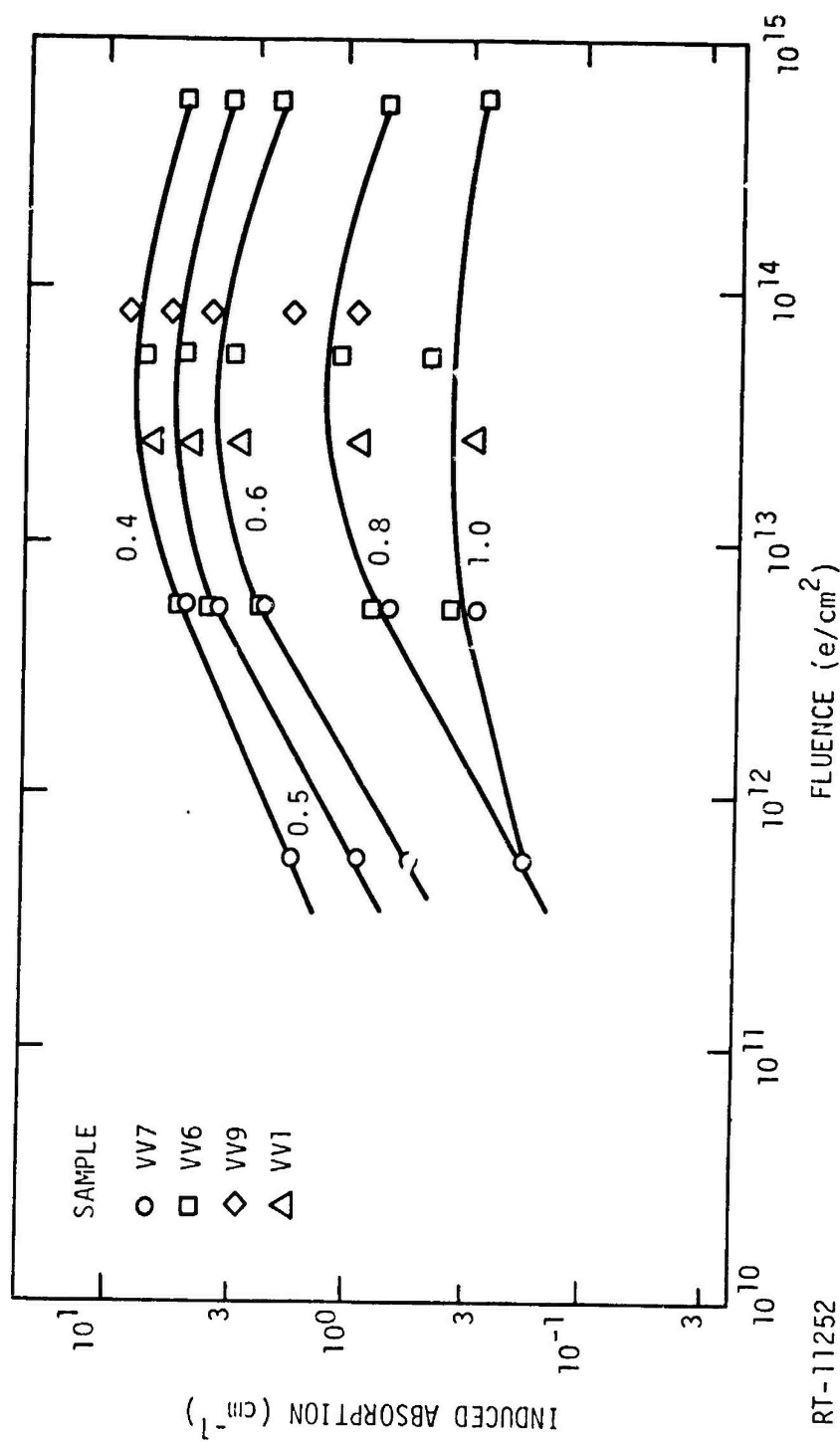


Figure 40. SF-11 absorption growth curves

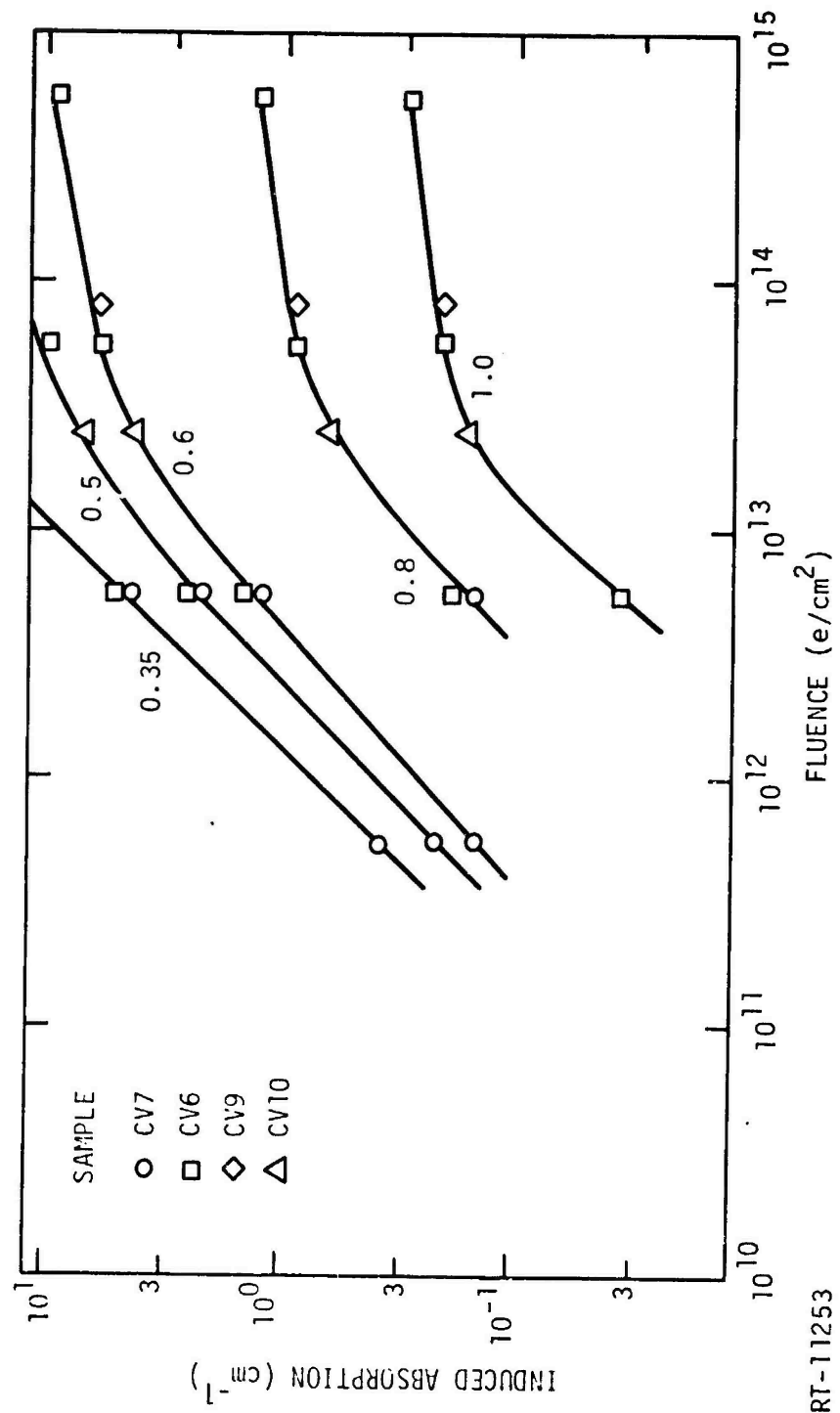


Figure 41. BK-7 absorption growth curves

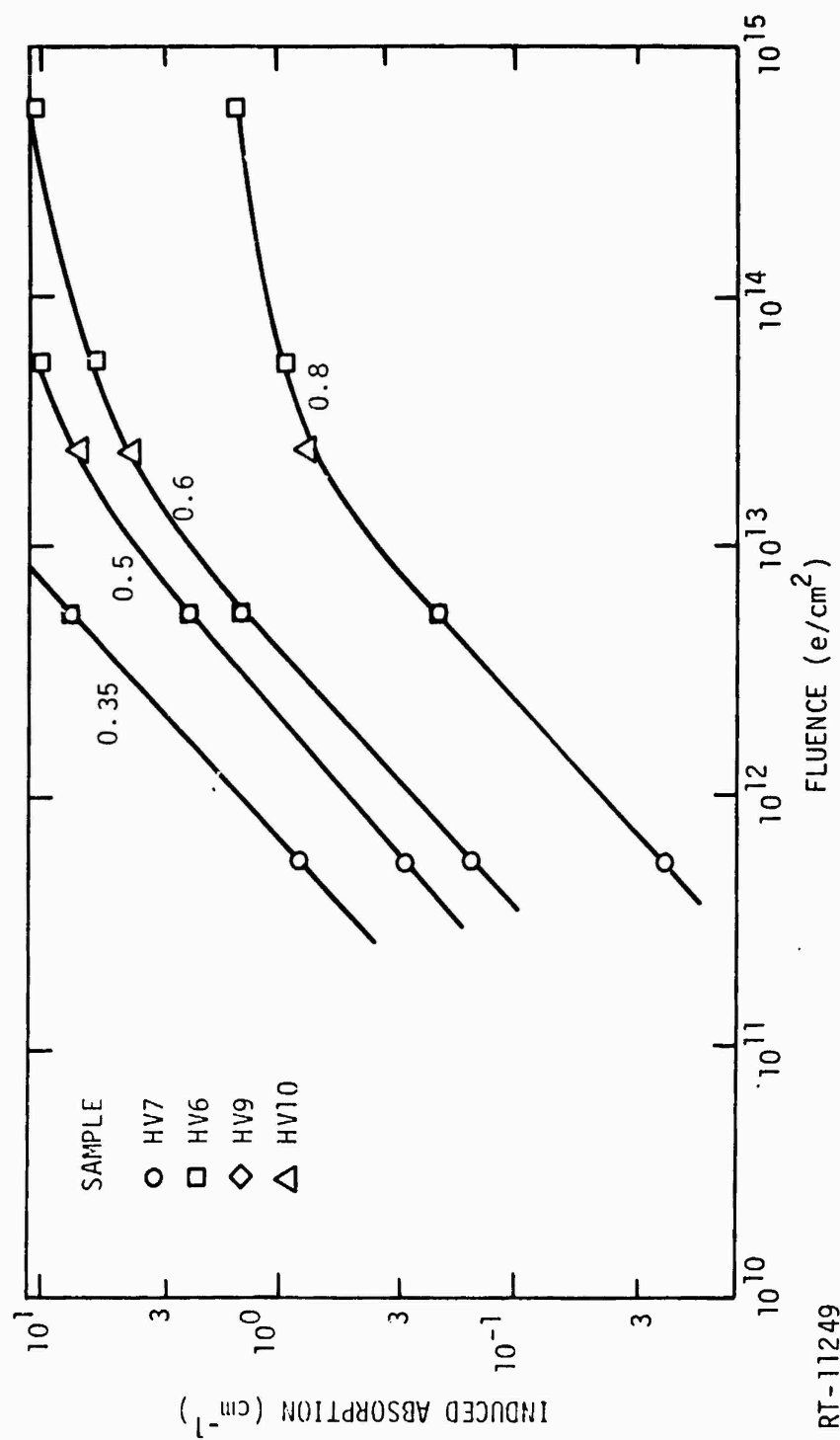


Figure 42. UBK-7 absorption growth curves

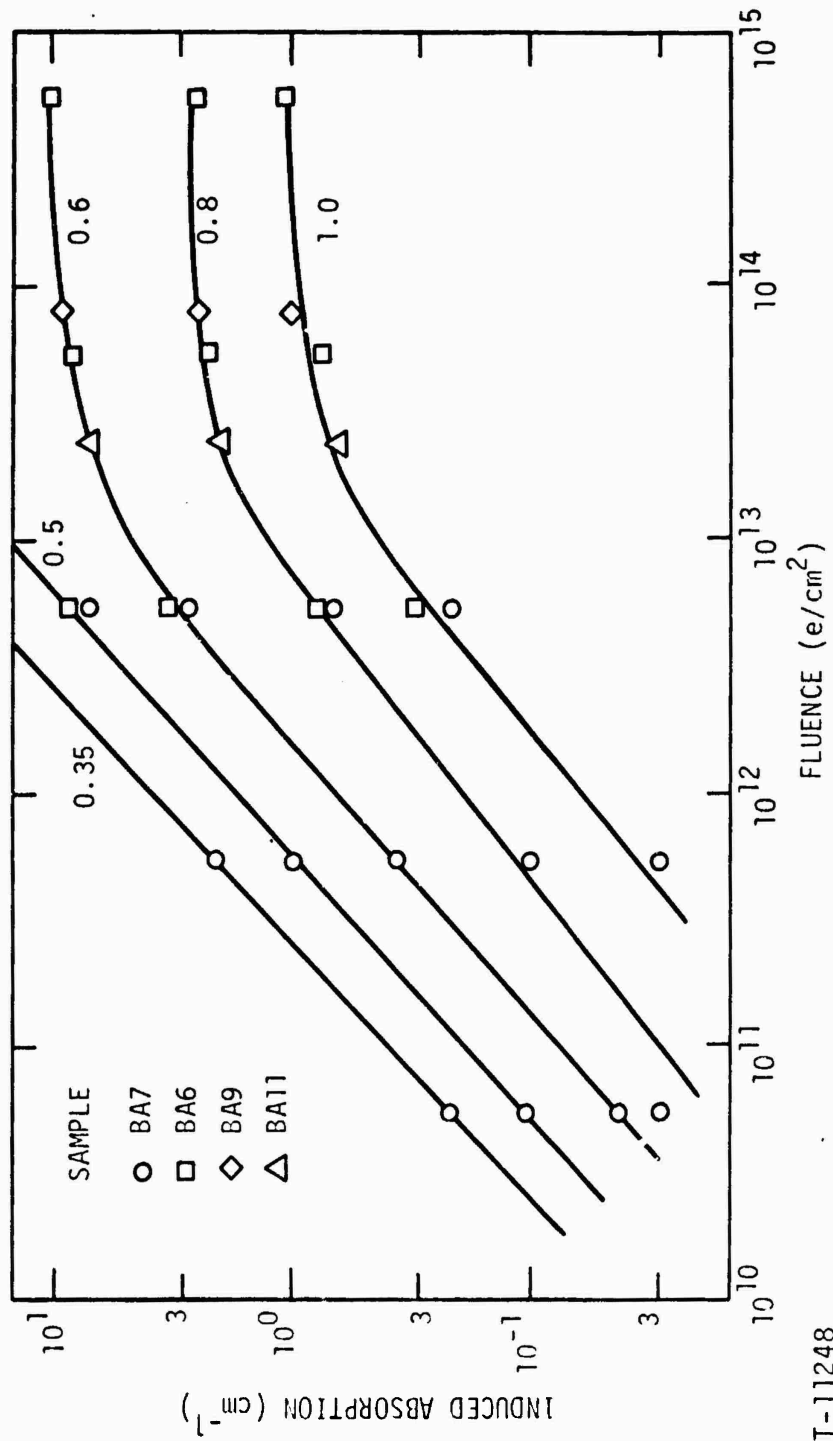


Figure 43. BaK-4 absorption growth curves

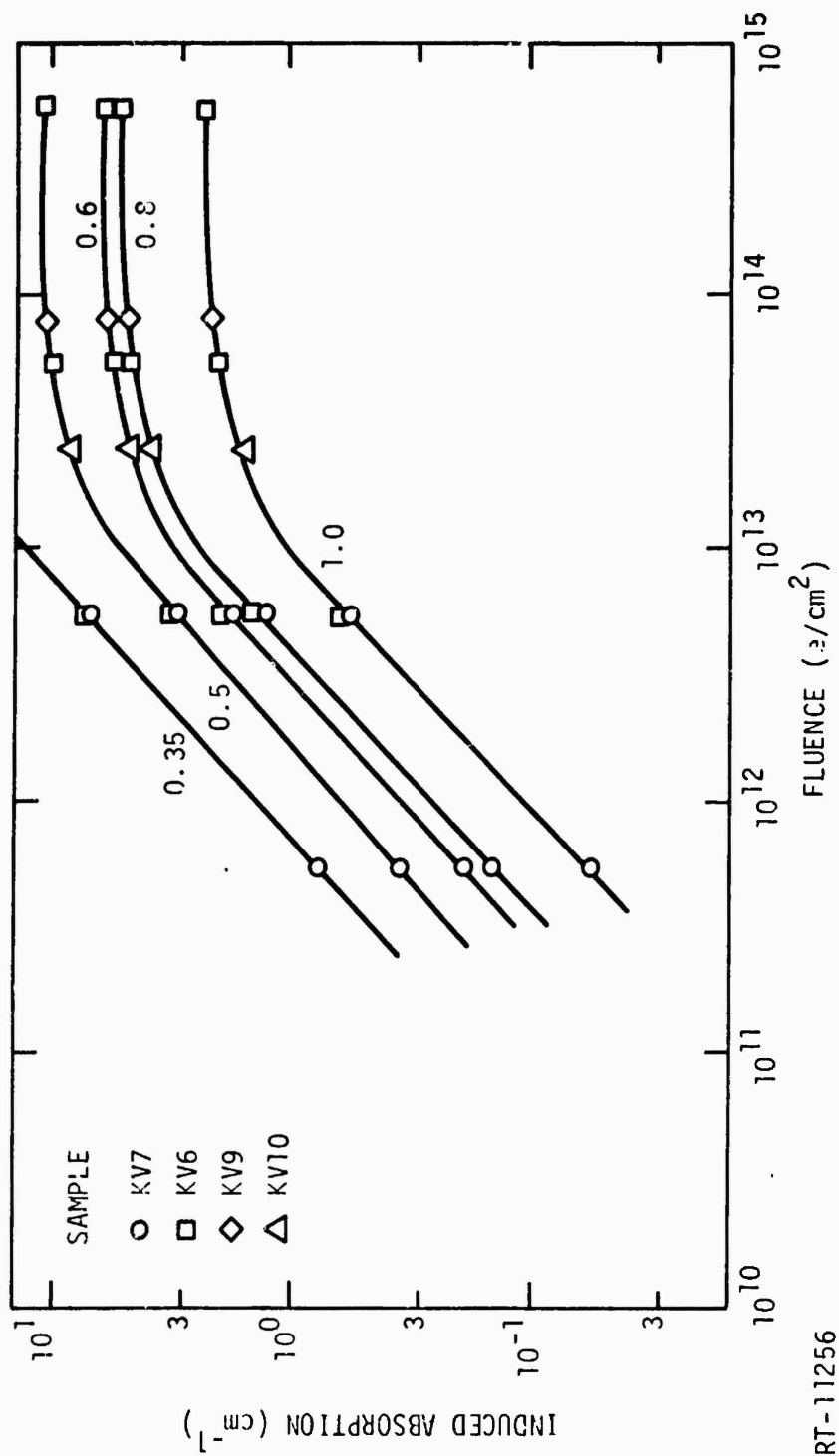


Figure 44. KzFS-N4 absorption growth curves

Table 5

ABSORPTION GROWTH PARAMETERS

Sample Type	1.0 μm		0.8 μm		0.6 μm		0.5 μm		0.35 μm	
	α_s (cm^{-1})	B (rad^{-1})	α_s (cm^{-1})	B (rad^{-1})	α_s (cm^{-1})	B (rad^{-1})	α_s (cm^{-1})	B (rad^{-1})	α_s (cm^{-1})	B (rad^{-1})
BaK-4	1.0	1.0×10^{-6}	2.7	1.1×10^{-6}	10.4	1.2×10^{-6}	3.1×10^{-5}		8.1×10^{-5}	
UBK-7			1.6	4.9×10^{-7}	10.9	5×10^{-7}	9.0×10^{-6}		3.1×10^{-5}	
BK7	0.31	5.8×10^{-7}	1.3	4.3×10^{-7}	9.2	5.1×10^{-7}	7.3×10^{-6}		1.8×10^{-5}	

	1.0 μm		0.8 μm		0.6 μm		0.5 μm		0.35 μm	
	α_s (cm^{-1})	B (rad^{-1})	α_s (cm^{-1})	B (rad^{-1})	α_s (cm^{-1})	B (rad^{-1})	α_s (cm^{-1})	B (rad^{-1})	α_s (cm^{-1})	B (rad^{-1})
SK14	0.48	1.8×10^{-6}	2.8	8.5×10^{-7}	10.7	8.8×10^{-7}	12.8	8.5×10^{-7}	3.1×10^{-5}	
SK7	0.36	1.1×10^{-6}	2.3	6.3×10^{-7}	7.4	1×10^{-6}	10.2	9.2×10^{-7}	2.9×10^{-5}	
LaK10	2.7	4.1×10^{-7}	4.8	6.3×10^{-7}	7.6	8.8×10^{-7}	14.2	1.0×10^{-6}	4.6×10^{-5}	
KZFS-N4	2.4	9.6×10^{-7}	5.5	9.6×10^{-7}	6.2	1.2×10^{-6}	11.2	1.0×10^{-6}	2.6×10^{-5}	

wavelengths could be superimposed by a simple vertical translation (on a logarithmic scale), which implies that the spectral shape of the radiation-induced absorption does not depend on fluence.

The growth of the induced absorption predicted by Eq. 9 may be understood if one considers that $\alpha_s[1 - \exp(-B\phi)]$ may represent the absorption due to centers which are initially present but not populated. Such centers rapidly become populated, and thus, the absorption due to these centers saturates, reaching a limiting value of α_s . Then any additional darkening occurs only through the creation of new centers, which proceeds as a linear function of the fluence.

3.1.4 Flux Dependence of the Induced Absorption

To expose samples to the equivalent of one day's to several years' accumulated fluence, it was necessary to radically accelerate the flux due to the cost of operating a radiation facility. In any accelerated test such as this, consideration must be given to the effects of the accelerated testing on the results. In this study, measurements were made to determine if the induced absorption was affected by the flux level of the irradiations:

Comparison of the absorption spectra of identical Schott glass samples taken after exposure to equivalent fluences at two different fluxes showed a significant difference in the darkening of SF-10 and also SF-11. The samples were exposed to a fluence of $8 \times 10^{13} \text{ e/cm}^2$ at fluxes of 1.2×10^{11} and $5.5 \times 10^{12} \text{ e/cm}^2\text{-sec}$. These spectra are shown in Figures 45 and 46, and definitely indicate a flux dependence of the darkening of these two glasses. Further study showed that this flux dependence is not observed for fluxes up to $1 \times 10^{12} \text{ e/cm}^2\text{-sec}$, which can be considered an upper bound of flux levels for testing these samples. Several points should be noted: first, SF-10 and SF-11 are similar glass types; second, the samples exposed at higher flux exhibit the least amount of darkening; third, note the difference in magnitude of the observed bleaching — the sample exposed at the highest flux appears to bleach less. This last observation could be quite deceptive. It is conceivable that the sample exposed at the higher

flux bleached very fast initially and had reached a stable absorption level before our measurements were made.*

These latter two points can be explained by either the action of a true radiation bleaching effect at high flux levels or an apparent radiation bleaching effect. The apparent radiation bleaching would result from an increase in the thermal bleaching rate due to radiation heating of the sample. Ignoring cooling, exposure to 8×10^{13} e/cm² would result in a temperature rise of 60 to 70°C; however, this energy deposition at a flux of 1.2×10^{11} e/cm²-sec is accomplished in 667 sec, as compared to 15 sec at a flux of 5.5×10^{12} e/cm²-sec. Therefore, the sample exposed at the higher flux would suffer a greater temperature rise. The temperature of the samples was not monitored; therefore, we do not know how large this difference was. However, the possibility of a temperature rise in one case of as much as 60 to 70°C is important in view of the results of isochronal anneal data. After exposure to ⁶⁰Co gamma irradiation, it was observed that the absorption of SF10 and SF11 began to bleach at a noticeably accelerated rate at temperatures as low as 40 to 60°C. The remaining glasses displayed an increase in bleaching only above 100 to 120°C. In view of this, it is possible that the "flux" dependence of the absorption growth resulted solely from sample heating.

3.2 INTERMEDIATE ABSORPTION MEASUREMENTS

This section describes absorption measurements made in the time regime of 1 to 90 sec after irradiation. These measurements were made on the Schott glass samples, except BK7-G14, to determine if the induced absorption changed significantly before permanent absorption measurements could be made using the DK-1A as described in the previous sections.

The *in situ* optical system was used to make these measurements. The light transmission at some wavelength λ was monitored before, during, and for 90 sec after irradiation. Irradiation times varied but were typically 15 to 25 sec. The xenon light source was replaced by a 650-watt tungsten halogen lamp, and the photomultiplier current was recorded on a Texas

* In the next section, it is pointed out that in the 1- to 90-sec time regime, SF-10 and SF-11 exhibit a significantly greater degree of bleaching than the other glasses.

SAMPLE		TIME AFTER IRRAD	FLUX ($\text{e}/\text{cm}^2\text{-sec}$)	FLUENCE (e/cm^2)
a ₁	FV9	194 sec	1.1×10^{11}	8.1×10^{13}
a ₂	FV9	504 sec		
a ₃	FV9	804 sec		
b ₁	FA8	85 sec	5.5×10^{12}	8.1×10^{13}
b ₂	FA8	450 sec		
b ₃	FA8	119 min		

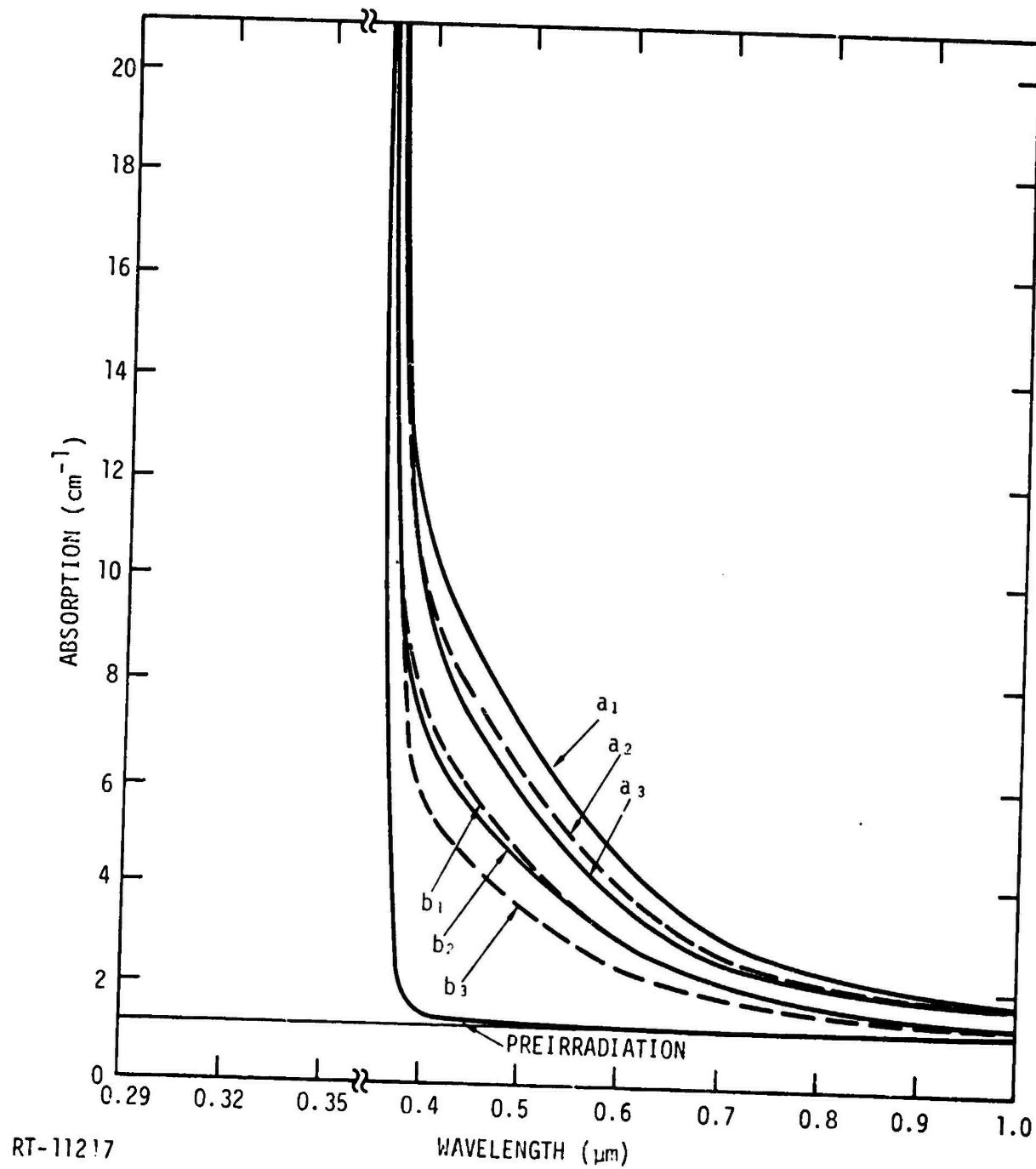


Figure 45. SF-10 absorption spectra at two fluxes

SAMPLE		TIME AFTER IRRAD	FLUX ($e/cm^2\text{-sec}$)	FLUENCE (e/cm^2)
a ₁	VV9	198 sec	1.1×10^{11}	8.1×10^{13}
a ₂	VV9	496 sec		
a ₃	VV9	724 sec		
b ₁	VA8	85 sec	5.3×10^{12}	8.1×10^{13}
b ₂	VA8	412 sec		
b ₃	VA8	73.5 min		

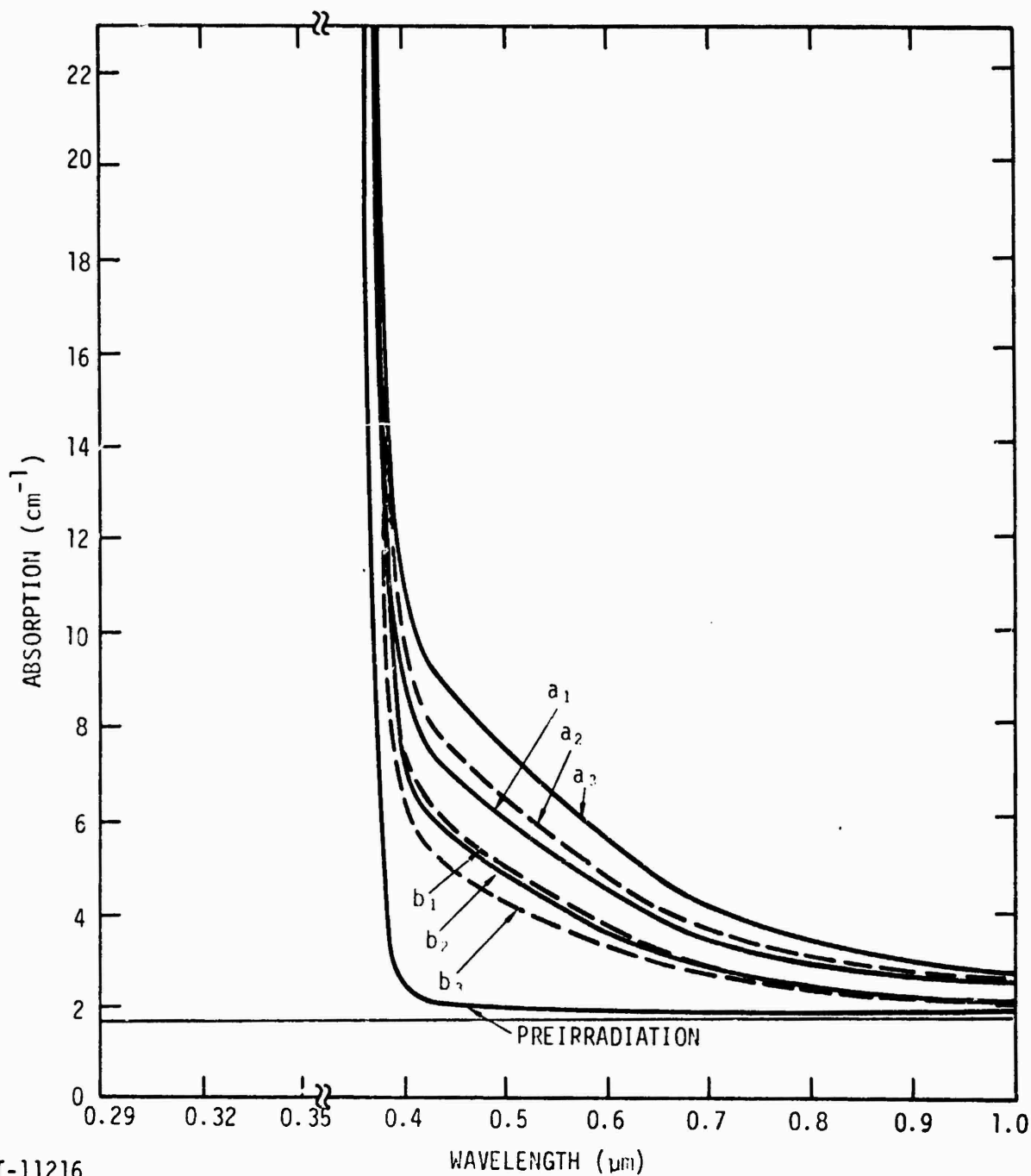
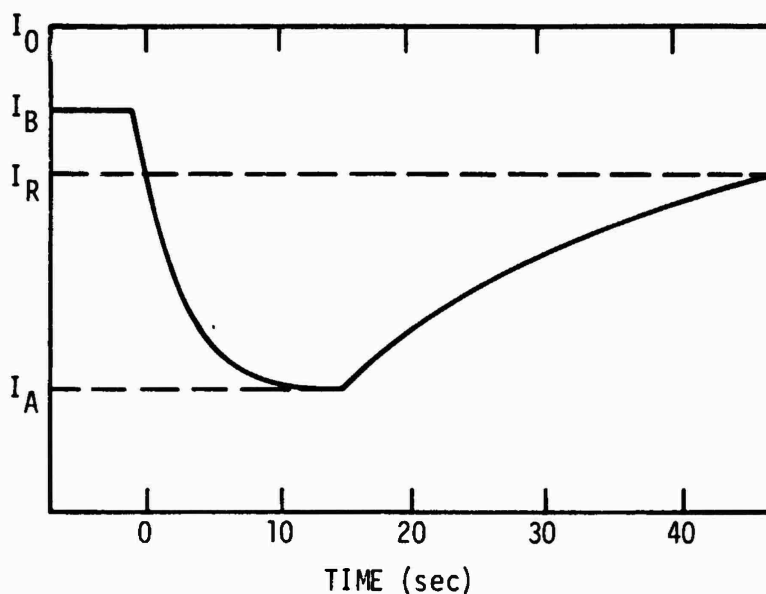


Figure 46. SF-11 absorption spectra at two fluxes

Instruments strip-chart recorder by using the analog output of a Boonton vacuum-tube voltmeter.

With the initiation of the irradiation, the samples began to darken and eventually approached some saturation level, I_A , as shown in the example below. With cessation of irradiation, the samples began to recover asymptotically, approaching some recovery level I_R , where I_R was less than the initial transmission I_B . This indicated that at least two types of absorption centers were being introduced — one with a lifetime on the order of tens of seconds and the other with a much longer lifetime.



To understand the time dependence of the short-lived absorption, consider the absorption, $\alpha_A(t)$, after irradiation to be the sum of the short-lived absorption, $\alpha_S(t)$, and the "permanent" absorption, α_p :

$$\alpha_A(t) = \alpha_S(t) + \alpha_p \quad t > t_{\text{irrad}} \quad (10)$$

If $\alpha_S(t)$ is assumed to decay by a first-order kinetic process (i.e., the parameter determining the rate of change of the absorption is only the

instantaneous magnitude of the absorption), the time rate of change of the absorption can be written as

$$\frac{d\alpha_S(t)}{dt} = -\frac{1}{\tau} \alpha_S(t) \quad t > t_p \quad (11)$$

Integrating yields

$$\alpha_S(t) = \alpha_S(0) \exp[-(t/\tau)] ,$$

and Eq. 10 can be written now as

$$\alpha_A(t) = \alpha_S(0) \exp(-t/\tau) + \alpha_p \quad (12)$$

Rearranging Eq. 12 and taking the natural log of both sides yields

$$\ln \left[\frac{\alpha_A(t) - \alpha_p}{\alpha_S(0)} \right] = -\frac{t}{\tau} \quad (13)$$

Plotting the left-hand side of Eq. 13 versus time will then yield a straight line, the slope of which will be $-1/\tau$, where τ is the lifetime of the short-lived absorption.

To characterize the short-lived absorption, it is necessary to determine the generation rate of the short-lived absorption centers as well as the lifetime. To determine the generation rate required repeating the measurements described above at a number of fluxes and fluences. This was not done simply due to time restrictions and a lack of virgin samples. We were able to determine the percent recovery -- i.e., what percentage of the absorption was due to the short-lived absorption centers. Although the flux and fluence dependence of this recovery has not been determined, these data give important systems design information on the magnitude of the absorption introduced by the short-lived centers.

Referring to the example diagram and recalling that

$$\alpha x = \ln \frac{I_0}{I} - 2 \ln \left(\frac{1}{1-r} \right) ,$$

the total increase in absorption as a result of the irradiation is given by

$$\frac{1}{x} \ln \frac{I_0}{I_A} - \frac{1}{x} \ln \frac{I_0}{I_B} = \frac{1}{x} \ln \frac{I_B}{I_A} ,$$

and the increase in permanent absorption is given by

$$\frac{1}{x} \ln \frac{I_0}{I_R} - \frac{1}{x} \ln \frac{I_0}{I_B} = \frac{1}{x} \ln \frac{I_B}{I_R} .$$

Therefore, the percentage recovery is given by

$$\frac{\ln \frac{I_B}{I_A} - \ln \frac{I_B}{I_R}}{\ln \frac{I_B}{I_A}} \times 100 = \frac{\ln \frac{I_R}{I_A}}{\ln \frac{I_B}{I_A}} \times 100 \quad (14)$$

By making use of Eqs. 13 and 14, the lifetime and percentage recovery of the short-lived absorption were determined for each sample. These results are listed in Table 6. Note that the absorption in most cases shows greater recovery at 5000 Å than at 3800 Å. Also note that the SF-10 and SF-11 samples exhibit the greatest percent recovery, which is interesting in light of Figures 30 and 31 which indicate that these samples exhibit the least amount of permanent absorption. From this it can be concluded that the SF-10 and SF-11 samples are not necessarily more radiation-hard than the other glasses but only that they recover more in the intermediate time regime ($t < 90$ sec). In addition, since the recovery could be described by Eq. 13, this identifies the kinetics of the short-term bleaching as first-order.

3.3 TRANSIENT ABSORPTION MEASUREMENTS

To make absorption measurements in the 1-msec to 1-sec time regime, the Dynamitron beam was pulsed onto the samples for ~15 msec while the light transmitted by the sample was monitored.

Figure 47 shows the apparatus used to make these measurements. The dc photomultiplier output was monitored with the Boonton meter, while the transient changes in the photomultiplier output during a pulse were measured on the oscilloscope. With this arrangement, transmission changes

Table 6

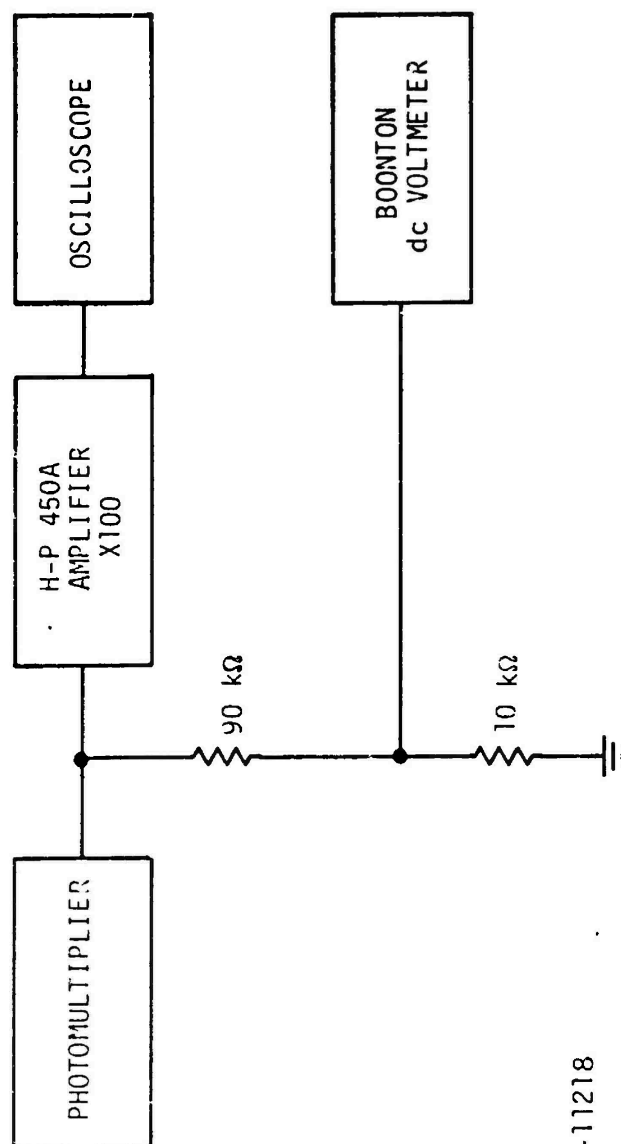
INTERMEDIATE ABSORPTION LIFETIMES AND PERCENT RECOVERY

Schott Glass	3800 Å		5000 Å	
	τ (sec)	Percent Recovery	τ (sec)	Percent Recovery
BaK-4	†		30	75%
BK-7	†		28	45%
SF-10	†		25	60%
UBK-7	30	21%	30	10%
KZFS-N4	44	21%	30	21%
LaK-10	30	16%	26	19%
SK-14	20	18%	24	36%
SF-11	30	32%	27	74%
SK-7	28	15%	24	27%

† At the time that these measurements were made, there were no remaining virgin samples. The amount of absorption that we could induce in these samples in 10-15 sec was then severely reduced due to the saturation effect discussed in Section 3.1.3. Where no values are listed, a change in transmission could not be measured.

as small as a few percent could be measured. Each sample was investigated in 100 Å increments from 9000 Å to the band edge transmission cut-off of the particular sample. The electron pulses were ~13 msec.

At a flux of 1×10^{13} e/cm²-sec, only sapphire and Schott BaK-4 displayed measurable transient absorption. The lifetime of the transient absorption was determined directly from the oscilloscope traces to be 44 msec for sapphire and 50 msec for BaK-4. The spectral dependence of the induced absorption (as measured at the maximum of the transient signal) for these samples is shown in Figures 48 and 49.



R²-11218

Figure 47. Apparatus for making transient absorption measurements

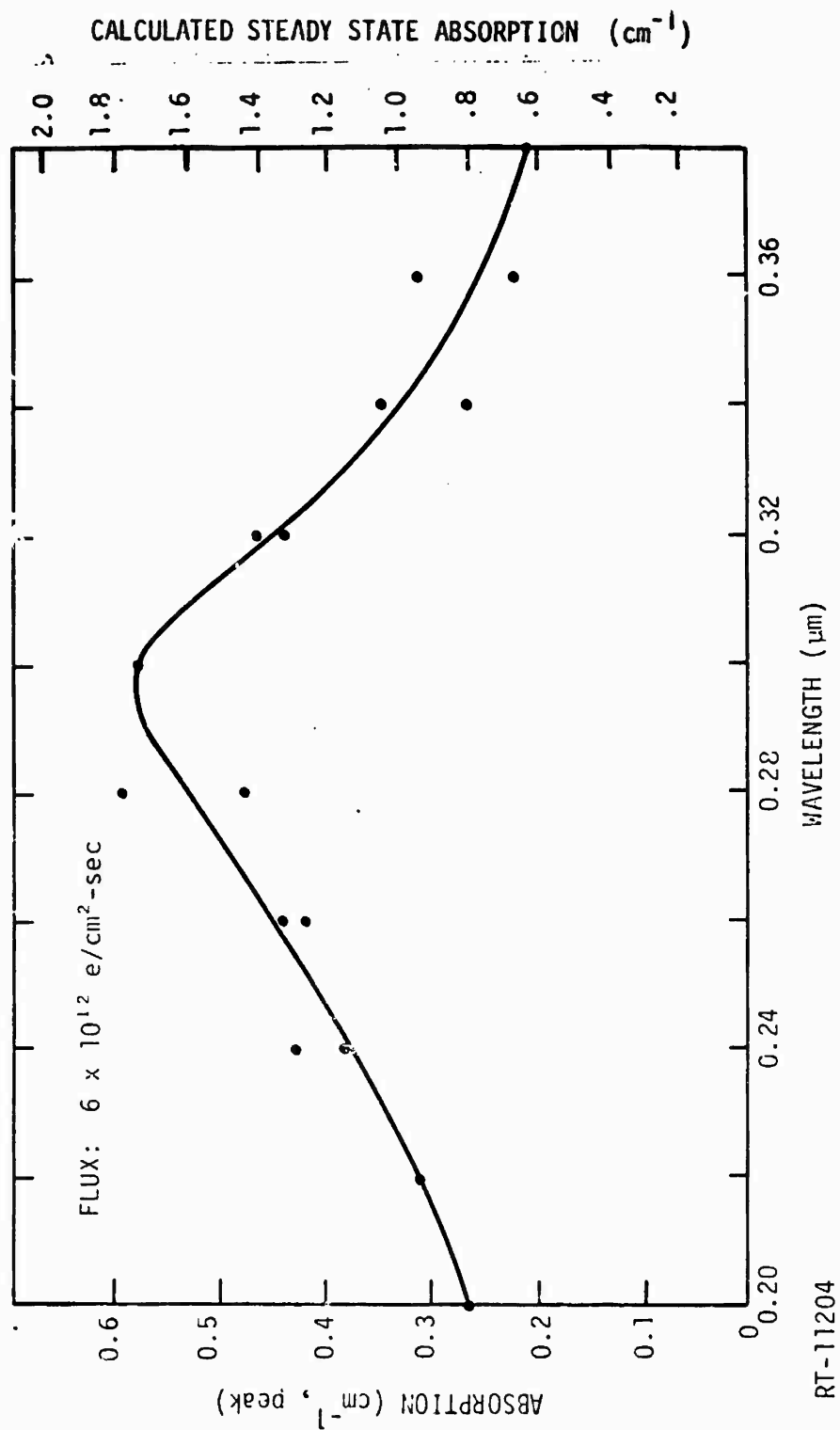


Figure 48. Transient absorption spectrum of sapphire

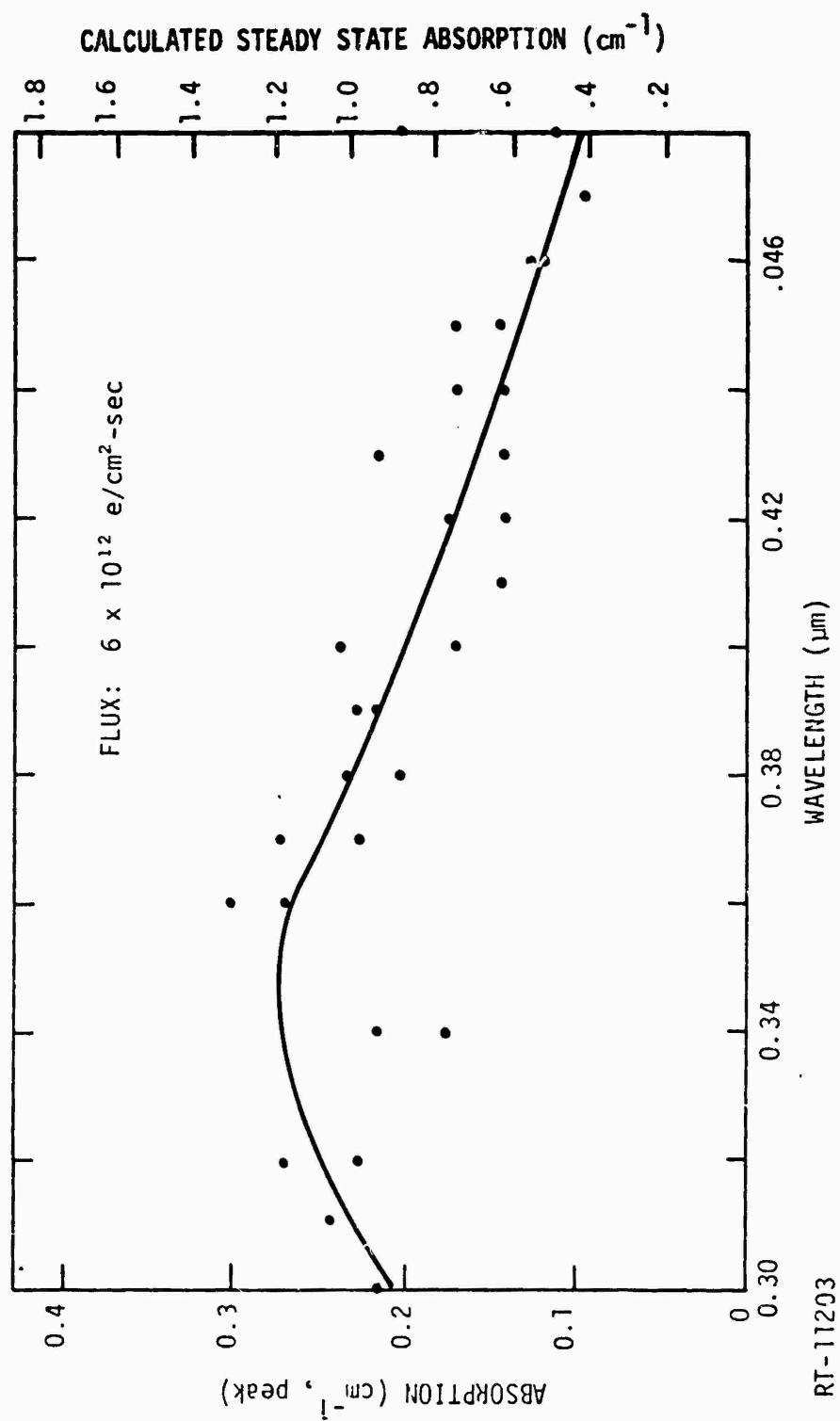


Figure 49. Transient absorption spectrum of Bak-4

The peak values measured are a function of the flux, the generation rate of absorbing centers, the lifetime of the centers, and the irradiation time. The latter results from the fact that the absorbing center lifetimes (40 to 50 msec) are longer than the pulse width (13 msec); however, this dependence can be removed. If $g\dot{\phi}$ is the generation rate of the absorbing center and τ the lifetime, the growth of the absorbing center population during irradiation can be written as

$$\frac{dn(t)}{dt} = g\dot{\phi} - \frac{1}{\tau} n(t) \quad .$$

This can be integrated to yield

$$n(t) = g\dot{\phi}\tau [1 - \exp(-\frac{t}{\tau})] \quad (15)$$

during irradiation. As the irradiation time t_p becomes long compared to τ , $n(t)$ will approach an equilibrium value:

$$n(t) = g\dot{\phi}\tau \quad t \gg \tau \quad .$$

In our experiments, t_p was not much greater than the absorbing center lifetimes, and therefore, at the end of the irradiation the population was

$$n(t_p) = g\dot{\phi}\tau [1 - \exp(-t_p/\tau)] \quad (16a)$$

The absorption measured at the end of the pulse is directly proportional to the center population; therefore, the steady-state absorption value can be calculated from Eq. 16a by

$$\frac{\alpha(t_p)}{[1 - \exp(-t_p/\tau)]} = \alpha_{\text{Steady-State}} \quad (16b)$$

The values obtained by using Eq. 16b are indicated by the right-hand scale in both Figures 48 and 49.

It is quite possible that the measured lifetimes were influenced by our measurement technique, specifically by the intensity of the light source. Previous work (Ref. 6) has shown that the bleaching rate of the permanent absorption can be greatly accelerated by exposing the samples to light and

that this accelerated bleaching rate is directly proportional to the light intensity at the sample. If $g\dot{\phi}$ is the generation rate of defects, νI is the optical bleaching rate, and τ is the lifetime of the centers, then the rate of darkening can be written as

$$\frac{1}{\sigma} \frac{d\alpha}{dt} = \frac{dn}{dt} = g\dot{\phi} - \nu I n - \frac{1}{\tau} n, \quad (17)$$

where $\dot{\phi}$ is the dose rate, I is the light intensity at the sample, σ is the absorption cross section of the centers, and n is the number of centers per unit volume. Eq. 17 can be integrated to yield

$$n = \frac{g\dot{\phi}}{C} [1 - \exp(-Ct)] \quad t < t_p,$$

where t_p is the radiation pulse width, and after the pulse,

$$n = n(t_p) \exp[-(t-t_p)C] \quad t > t_p \quad (\text{i.e., } g = 0) \quad (18)$$

where $C = \nu I + 1/\tau$. C can then be determined by measuring the time after the end of the pulse necessary for the induced absorption to fall to $1/e$ of its value at the end of the pulse. This is the method used to obtain the lifetimes given above. If $\nu I \gg 1/\tau$, the "measured lifetime" is not the lifetime of the transient centers but is indeed the optical bleaching rate of the centers. Since our light source was very intense, this may have been the case.

4. RADIOLUMINESCENCE MEASUREMENTS

This section describes the procedure used in making radioluminescence measurements and the results of these measurements. The intensity of the observed radioluminescence is presented in $\text{mW/cm}^2\text{-}\mu\text{m}$ and mW/cm^2 , as determined from the calibration procedures described in Section 2.2.4 and Appendix C. All radioluminescence measurements were made using the *in situ* apparatus, which was designed to minimize the collection of Cerenkov radiation.

4.1 SPECTRAL DISTRIBUTION

Measurement of the spectral distribution of the luminescence of the various samples was made by rotating a sample into the optical path and irradiating the sample while scanning the monochromator. The photomultiplier signal was measured with a Boonton sensitive dc meter, the analog output of which was recorded on a Texas Instruments strip-chart recorder.

In a measurement of this type, a trade-off must be made in selecting the flux, since the luminescence intensity and the darkening rate increase as the flux increases. Since the Schott glasses, except BK7-G14, darkened significantly in the time necessary to scan the monochromator, determination of the spectral dependence of the radioluminescence from these samples could not be made with our apparatus.

Spectral scans of the radioluminescence from sapphire, crystalline quartz, Suprasil 2, and BK7-G14 were obtained and are shown in Figures 50 through 54. Crystalline quartz displayed one intense band peaking near 1850 \AA and a weaker band peaking near 2850 \AA . The radioluminescence spectrum of Suprasil 2 (fused quartz) is almost identical to that of crystalline quartz, with the intense band at 1850 \AA being somewhat broader for crystalline quartz than for Suprasil 2. Schott BK7-G14 displayed one very broad band which peaked at 4200 \AA and has a shoulder at 4800 \AA .

*Even operating at the highest available flux and in a pulsed mode, the radioluminescence from the Schott samples was too weak to be detected. It is felt by the authors, however, that these spectra can easily be determined by utilizing a linear accelerator which is capable of operating at much higher fluxes and short pulses.

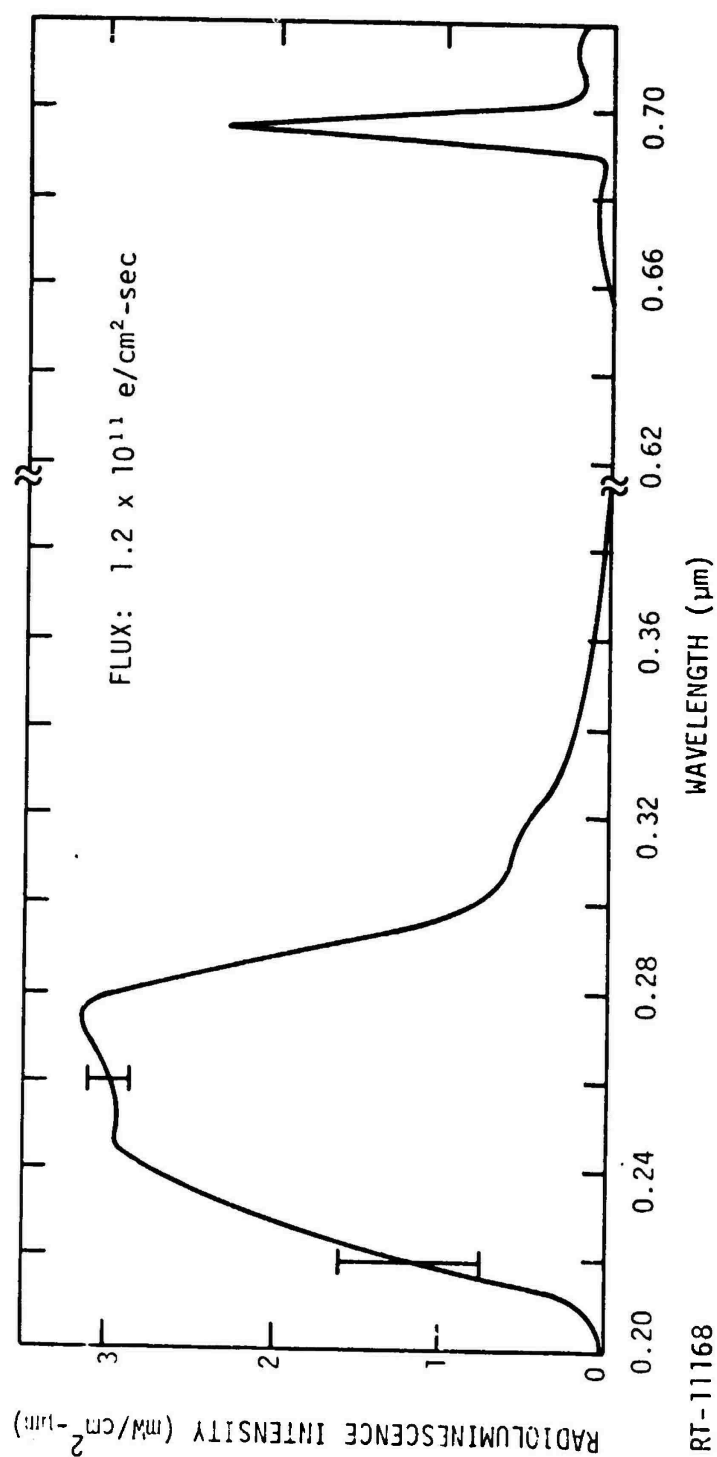


Figure 50. Sapphire radioluminescence spectrum at 10^{11} e/cm²-sec

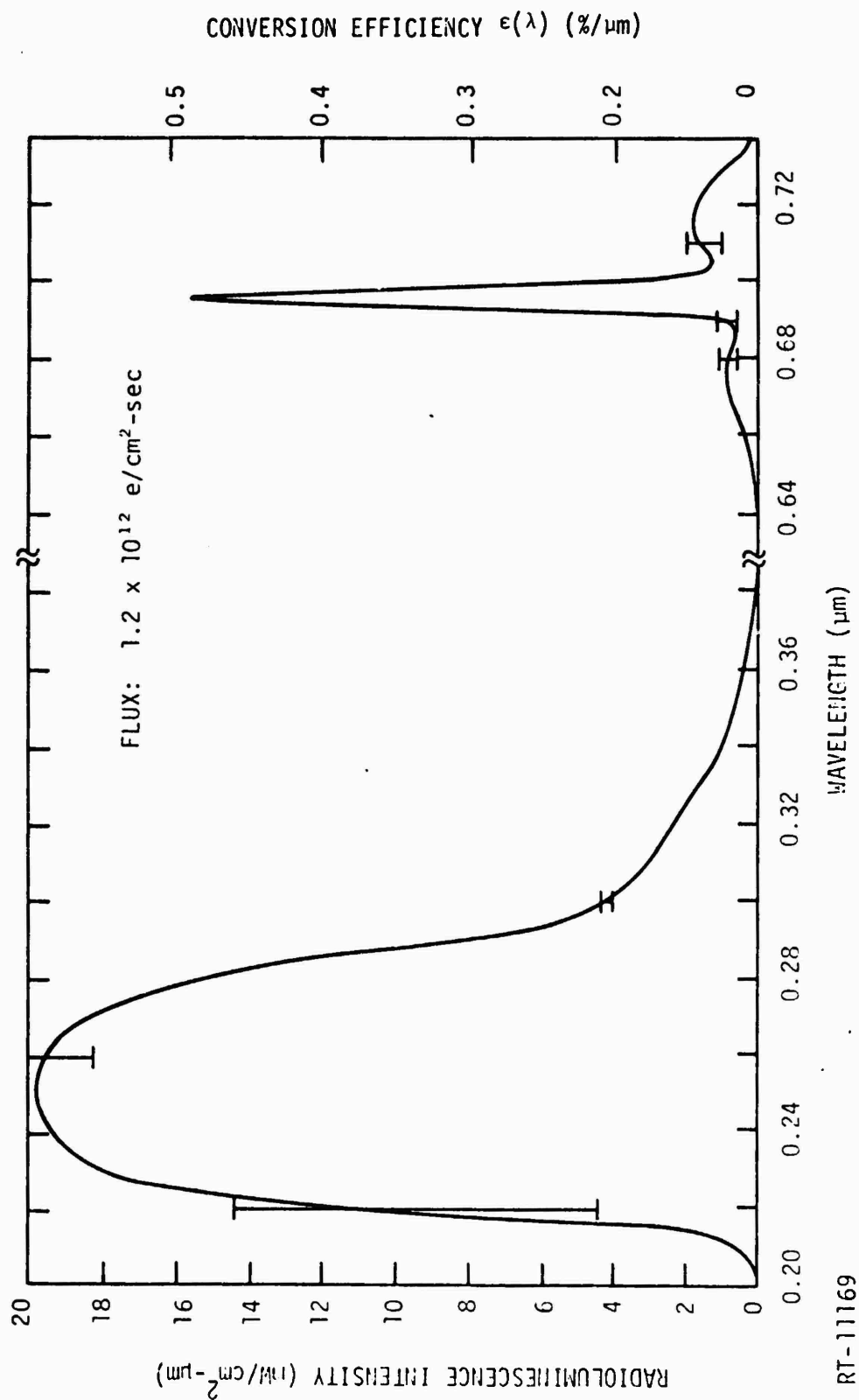


Figure 51. Sapphire radioluminescence spectrum at $10^{12} \text{ e}/\text{cm}^2\text{-sec}$

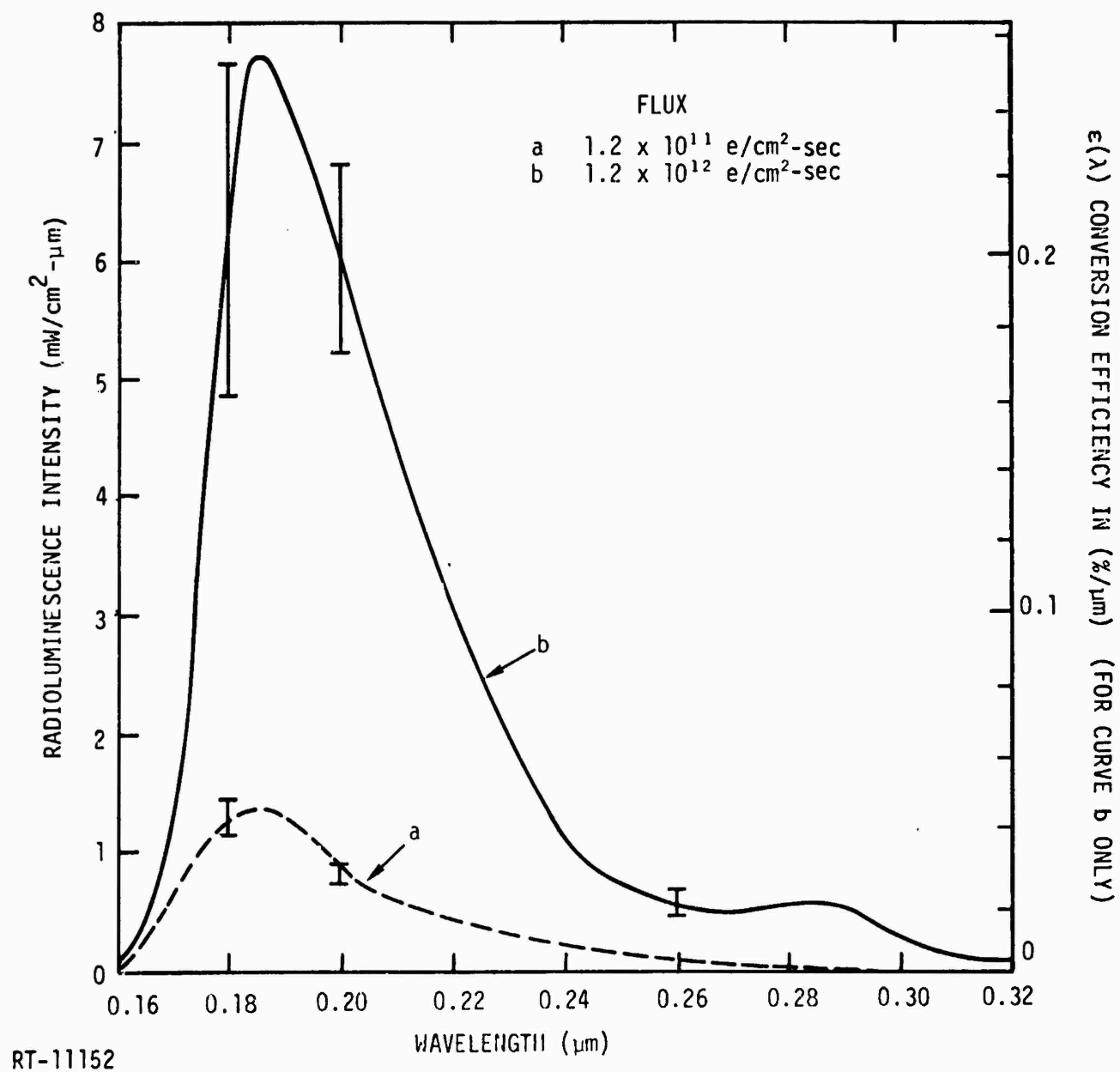


Figure 52. Crystalline quartz radioluminescence spectra

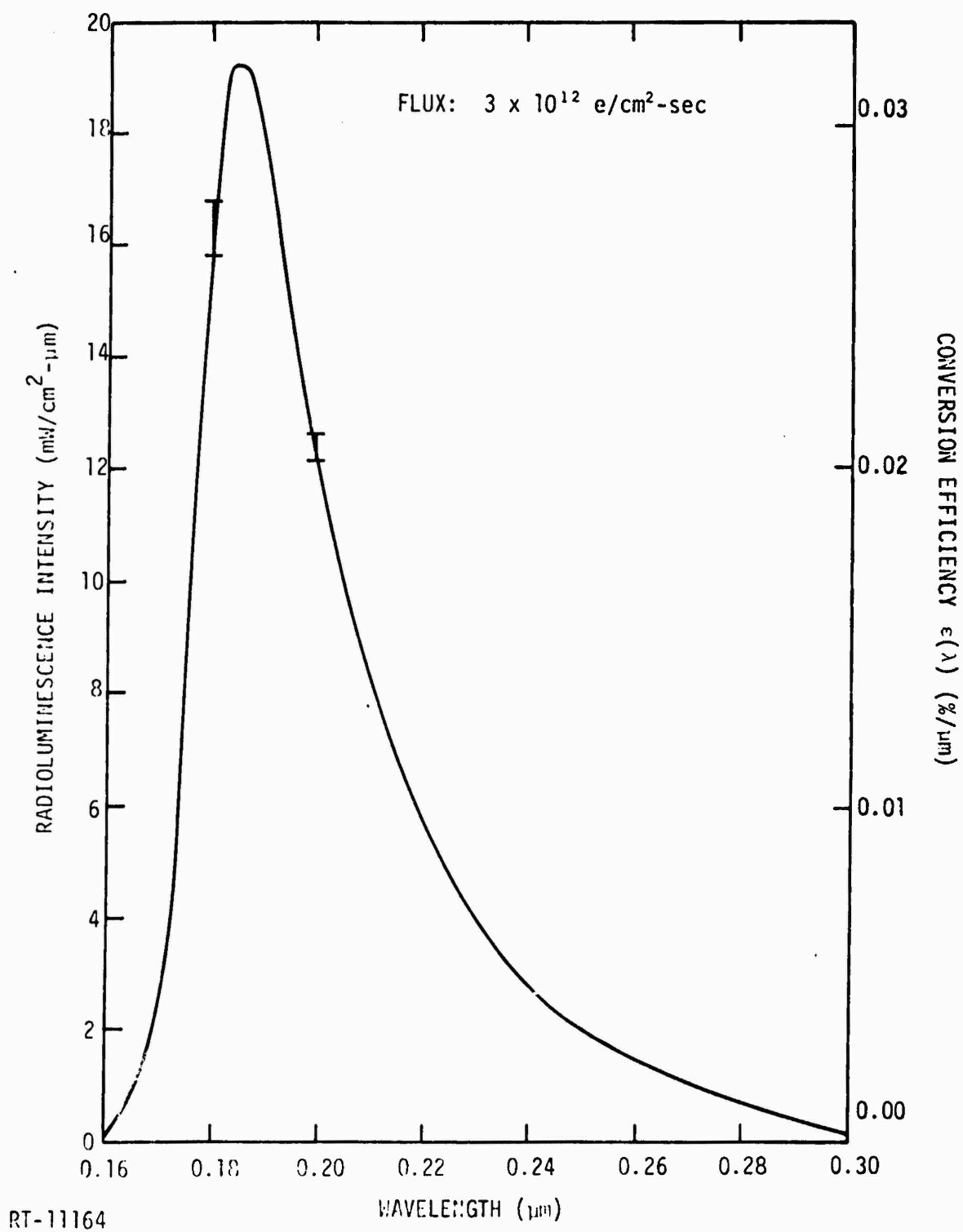


Figure 53. Suprasil 2 radioluminescence spectrum

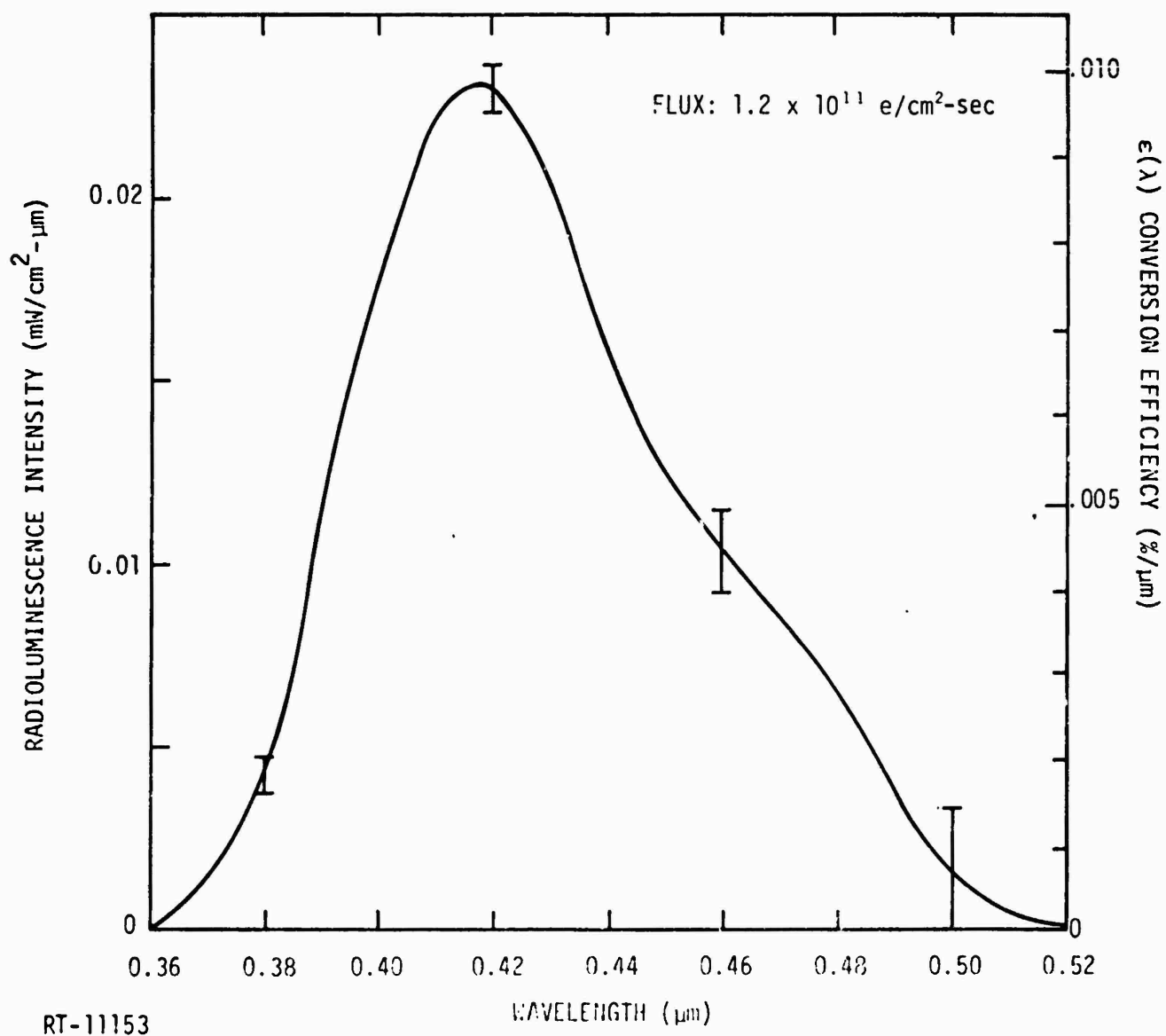


Figure 54. BK7-G14 radioluminescence spectrum

Comparison of this spectrum with free-ion energy levels strongly suggests that the radioluminescence from BK7-G14 is predominantly from the cerium impurity (BK7-G14 contains 1.4% cerium) (Ref. 19). Sapphire displayed a broad band peaking near 2500 Å and another sharp intense band at 6960 Å. Since pure sapphire and chromium-doped sapphire are grown in the same crucible (due to the crucible cost), the 6960 Å luminescence is undoubtedly due to chromium impurities. On both sides of the chromium line is a weak band at 6760 and 7140 Å. The difference in the 2500 Å sapphire peak for 1.2×10^{11} and 1.2×10^{12} e/cm²-sec could quite possibly be artificial, resulting from beam drift. The error bars in Figures 50 through 54 reflect the accuracy to which we could measure the photomultiplier current as convoluted by the correction curve shown in Figure 7.

4.2 TEMPORAL DISTRIBUTION

The luminescence intensity observed from a sample exposed to ionizing radiation varies with the radiation exposure rate and the wavelength. In addition, the duration of the exposure can affect the observed luminescence intensity in the following manner.

Consider a sample exposed to ionizing radiation at a rate $\dot{\gamma}$ which results in the formation of luminescence centers at a rate $G\dot{\gamma}$. If these centers decay with a lifetime τ , the rate of change of the center population can be written as

$$\frac{dn}{dt} = G\dot{\gamma} - \frac{n}{\tau}.$$

Integrating yields

$$n = G\dot{\gamma}\tau [1 - \exp(-t/\tau)] \quad \text{during the pulse } (t < t_p)$$

and

$$\begin{aligned} n &= G\dot{\gamma}\tau [1 - \exp(-t_p/\tau)] \exp[-(t-t_p)\tau] \\ &= n(t_p) \exp[-(t-t_p)\tau] \quad \text{after the pulse } (t > t_p) \end{aligned}$$

where t_p is the duration of the irradiation and $n(t_p)$ is the luminescent center population at the end of the pulse.

The luminescence intensity is related to the population of luminescent centers by the radiative decay rate (τ_{rad}^{-1}), and the intensity can be written as

$$I = \frac{G\dot{\gamma}\tau}{\tau_{\text{rad}}} [1 - \exp(-t/\tau)] \quad t < t_p \quad (19a)$$

and

$$I = I_{\text{MAX}} \exp[-(t-t_p)/\tau] \quad t > t_p \quad (19b)$$

where τ_{rad} is the radiative decay time of the centers. Two special cases can be considered.

Case 1

The luminescence lifetime is much smaller than the pulse length. Then Eq. 19a becomes

$$I_{\text{SS}} = \frac{G\dot{\gamma}\tau}{\tau_{\text{rad}}} \quad (20)$$

This predicts that by the end of the pulse the luminescence intensity will have reached some steady-state value ($G\dot{\gamma}\tau/\tau_{\text{rad}}$) and will remain at that level until the end of the pulse. In this case, the luminescence for each material can be characterized by $G\dot{\gamma}\tau/\tau_{\text{rad}} = I_{\text{SS}}/\dot{\gamma}$, where τ and τ_{rad} are wavelength-dependent. Therefore, to characterize the luminescence, one needs to know only I_{SS} and $\dot{\gamma}$, and the result is not dependent upon the pulse width as long as $\tau \ll t_p$.

Case 2

If the pulse width is not much greater than the lifetime, the luminescence does not reach a steady-state value during the pulse, and the observed luminescence intensity I_{MAX} will depend upon the length of the

pulse. At the end of the pulse, the intensity will be

$$I_{MAX} = \frac{G\dot{\gamma}\tau}{\tau_{rad}} [1 - \exp(-t_p/\tau)] . \quad (21a)$$

To uniquely characterize the luminescence in this case, it is necessary to know τ so that $G\dot{\gamma}\tau/\tau_{rad}$ can be determined:

$$\frac{G\dot{\gamma}\tau}{\tau_{rad}} = \frac{I_{MAX}}{[1 - \exp(-t_p/\tau)]} , \quad (21b)$$

where $G\dot{\gamma}\tau/\tau_{rad}$ is the intensity that would have been observed if the pulse were much longer as in case 1.

Measurements of luminescence lifetimes were made by pulsing the Dynamitron beam onto a sample and observing the time history of the photomultiplier tube output on an oscilloscope. To reduce the RC integration constant resulting from the inherent capacitance of coaxial cable and resistance of the measuring circuitry, a cathode-follower was placed between the photo-tube and oscilloscope with less than five feet of coaxial cable between the cathode-follower and the photomultiplier. With this arrangement, luminescence lifetimes on the order of 1 msec could easily be measured.

Only sapphire displayed a lifetime greater than 1 msec. The luminescence lifetime was determined from the oscilloscope traces to be 4 msec at 3000 Å and 6 msec at 6930 Å. During the ~12-msec pulse width, the sapphire luminescent intensity did not reach a steady-state value, and thus, intensity values obtained by pulsing the Dynamitron beam in 15-msec pulses were corrected by using Eq. 20. The correction was only 4%.

4.3 FLUX DEPENDENCE OF THE RADIOLUMINESCENCE YIELD

To predict the luminescence intensity from a sample exposed to some flux, Φ , it is necessary to determine the rate of change of the luminescence intensity with flux.

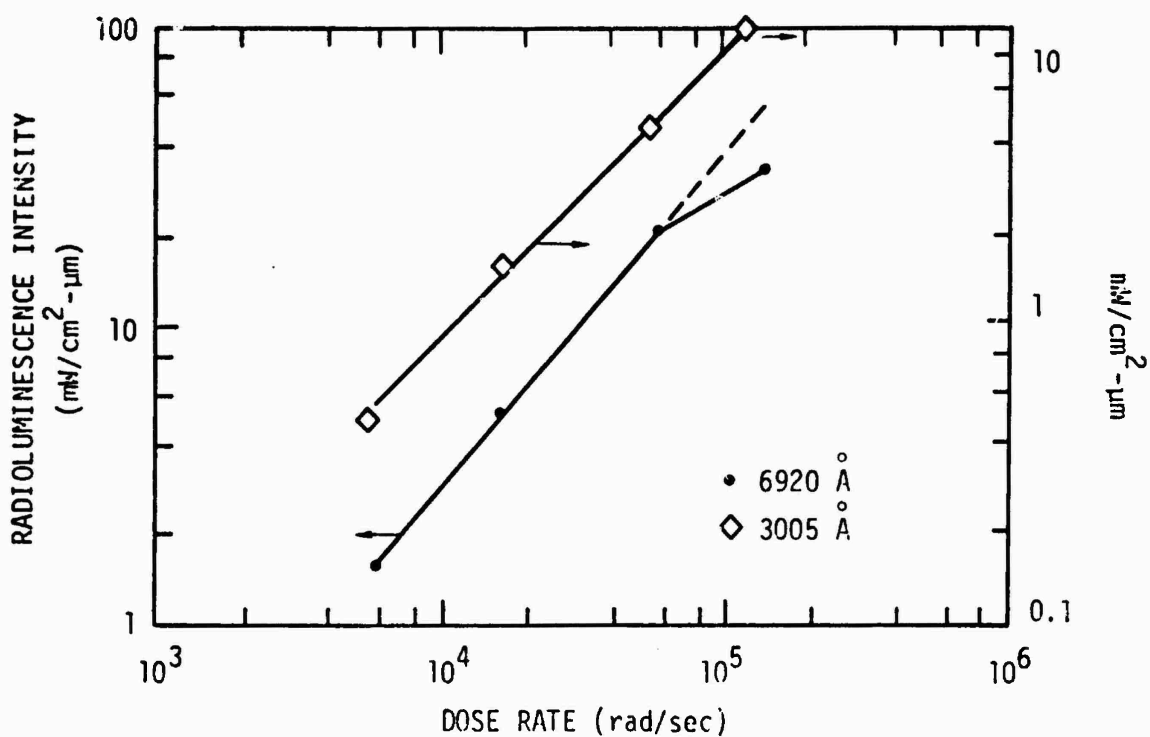
Measurements of the flux dependence of the intensity of various luminescence peaks were made by rotating a sample into the electron beam and

simultaneously measuring the photomultiplier signal with the Boonton meter. The flux was measured before and after each luminescence measurement. The results of these measurements for sapphire, crystalline quartz, and Schott BK7-G14 are shown in Figures 55, 56, and 57. The slopes are all unity within 10%. The deviation from a straight line observed for BK7-G14 was a reproducible effect verified by exposing a BK7-G14 sample at a dose rate of 1.4×10^5 rad/sec and observing the 4200 Å luminescence as a function of time. The luminescence was observed to decrease with time, which possibly indicated darkening of the sample, although an absorption measurement made on this sample after the irradiation indicated no measurable absorption (in agreement with results described in Section 3.1). Perhaps this indicates that BK7-G14 does darken but that the darkening bleaches rapidly upon exposure to room light.

The deviation from a straight line observed for sapphire at 6920 Å (Figure 55) was also a reproducible effect. Similar to BK7-G14, the sapphire 6920 Å luminescence decreased with exposure time although no absorption was observed for sapphire at 6920 Å in any time regime.

As mentioned in Section 3.1, luminescence signals at selected wavelengths for the Schott glasses, except BK7-G14, were too weak to be detected by our apparatus; however, by setting the monochromator on the "zero order," the spectrally integrated luminescence from the samples could easily be detected. Absolute intensity calibration of the optical system for spectrally integrated luminescence is described in Appendix C. To avoid severely darkening these samples, the electron beam was single-pulsed in 15-msec pulses and the luminescence intensity was measured on an oscilloscope.

The flux dependence of the spectrally integrated luminescence intensity for sapphire, crystalline quartz, Suprasil, and BK7-G14 is shown in Figure 58. The slopes, as for the flux dependence of the luminescence peaks, are again nearly unity, with sapphire exhibiting the greatest deviation from unity slope. It is interesting to note that, while Figures 55, 56, and 57 indicated that the sapphire spectral radioluminescence intensity is twice that of crystalline quartz, which is almost two orders of magnitude greater than that of BK7-G14, when one considers the spectrally integrated intensity



RT-11379

Figure 55. Sapphire radioluminescence intensity versus dose rate at 6920 and 3005 Å

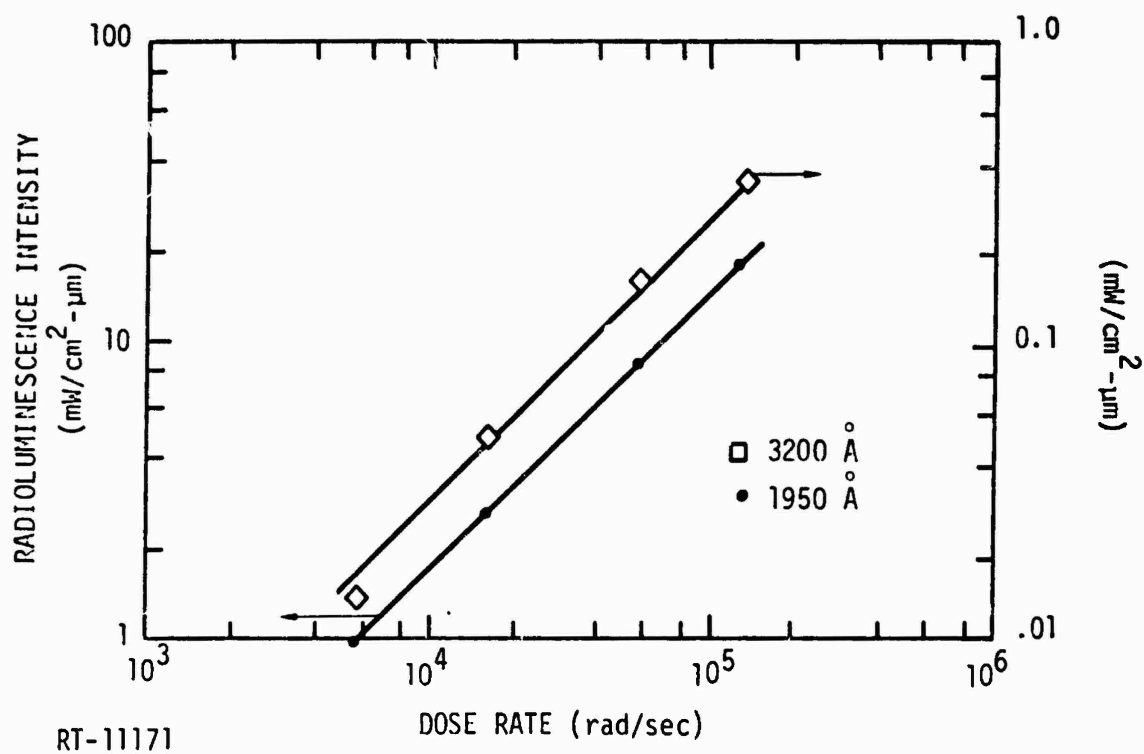


Figure 56. Crystalline quartz radioluminescence intensity versus dose rate at 3200 and 1950 Å

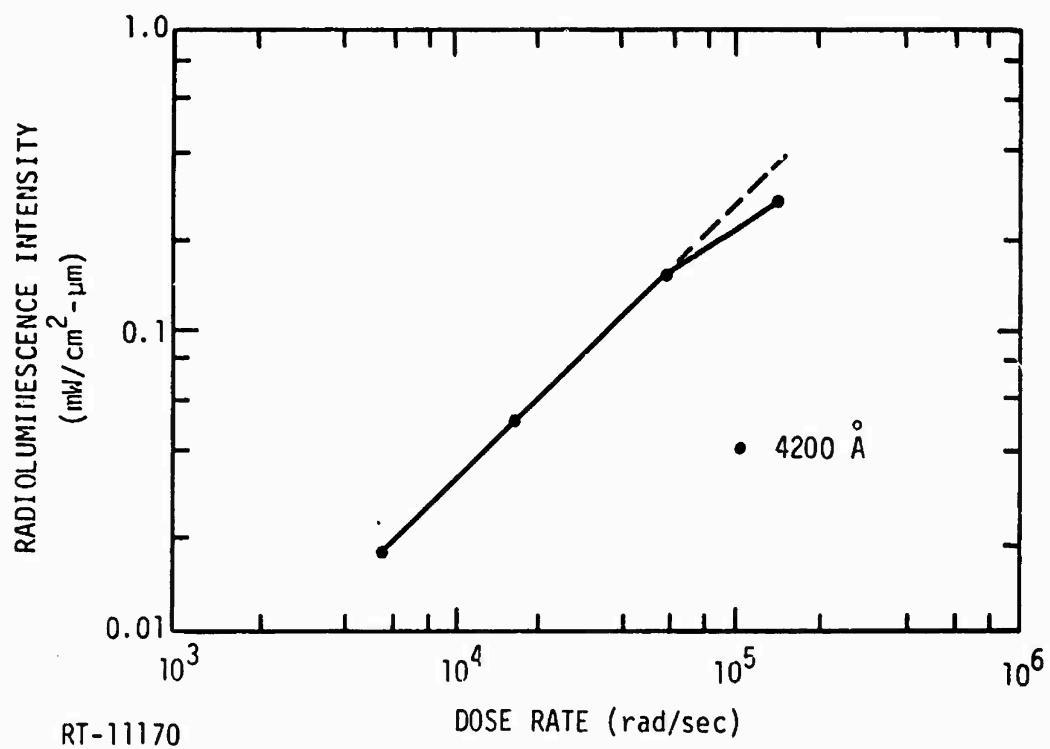


Figure 57. BK7-G14 radioluminescence intensity versus dose rate at 4200 Å

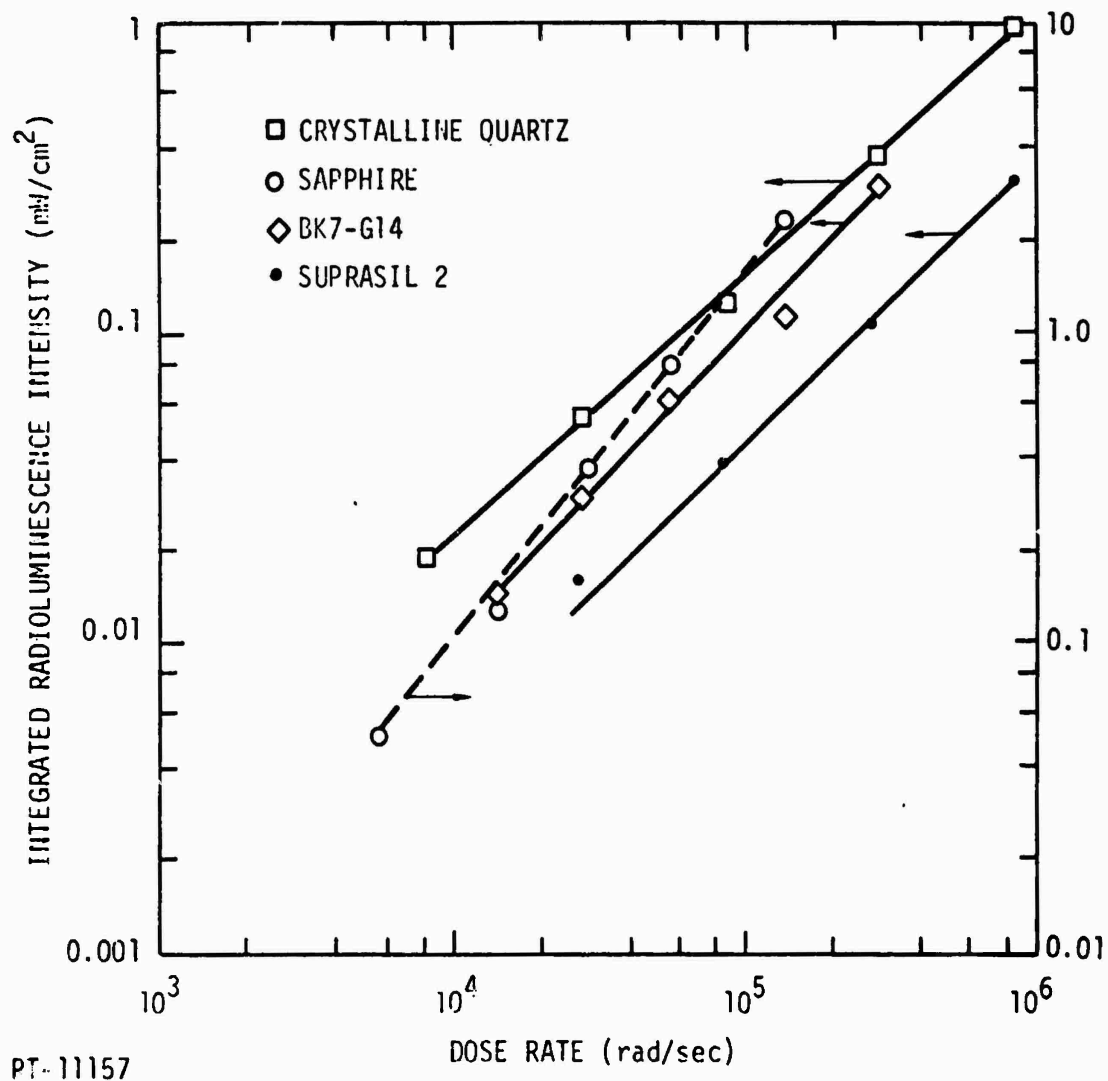


Figure 58. Spectrally integrated radioluminescence intensity versus dose rate: crystalline quartz, sapphire, Suprasil 2, BK7-G14

it is found that the sapphire intensity is five times greater than that of quartz which is, in turn, only twice the intensity of BK7-G14. This demonstrates the importance of considering the spectrally integrated intensity when planning a systems application.

The flux dependence of the spectrally integrated luminescence intensity for the remaining samples is shown in Figures 59, 60, and 61. It must be remembered that these samples darken readily, and consequently, the observed luminescence intensity is somewhat lower than the actual intensity due to absorption in the sample. To minimize the effect of this self-absorption upon the results, the samples were exposed at the highest dose rate first and then at continually decreasing dose rates. In this manner, about 88% of the absorption present at the end of the measurements was introduced while making the first measurement (i.e., at the highest dose rate). The induced absorption, then, does not affect the linearity or the slope of the lines shown in Figures 59, 60, and 61, but does shift each line down by a multiplicative factor.

Since the Schott glass sample thicknesses were chosen such that exposure to equivalent fluences results in equivalent energy deposition, Figures 55 through 61 can be used to determine the relative radioluminescence efficiencies of these samples. These results are presented in the next section.

4.4 CONVERSION EFFICIENCY AND CORRECTIONS FOR SELF-ABSORPTION

In this investigation, the optical system was calibrated by inserting a lamp of known spectral radiant emittance in the sample location. For known and reproducible conditions (e.g., wavelength, slit width, PM tube voltage), we recorded the detector output. Then, when the radioluminescent output from a sample was recorded (under the same experimental conditions), what we really had was a measure of the spectral radiant emittance (in $\text{W}/\text{cm}^2\text{-}\mu\text{m}$) of the sample surface facing the collection optics.

If a number of specific conditions are met, one can calculate a conversion efficiency of energy in the form of radiation deposited in the sample to energy emitted by the sample in the form of optical photons (light). In the present investigation, the conditions necessary to make this calculation include the following.

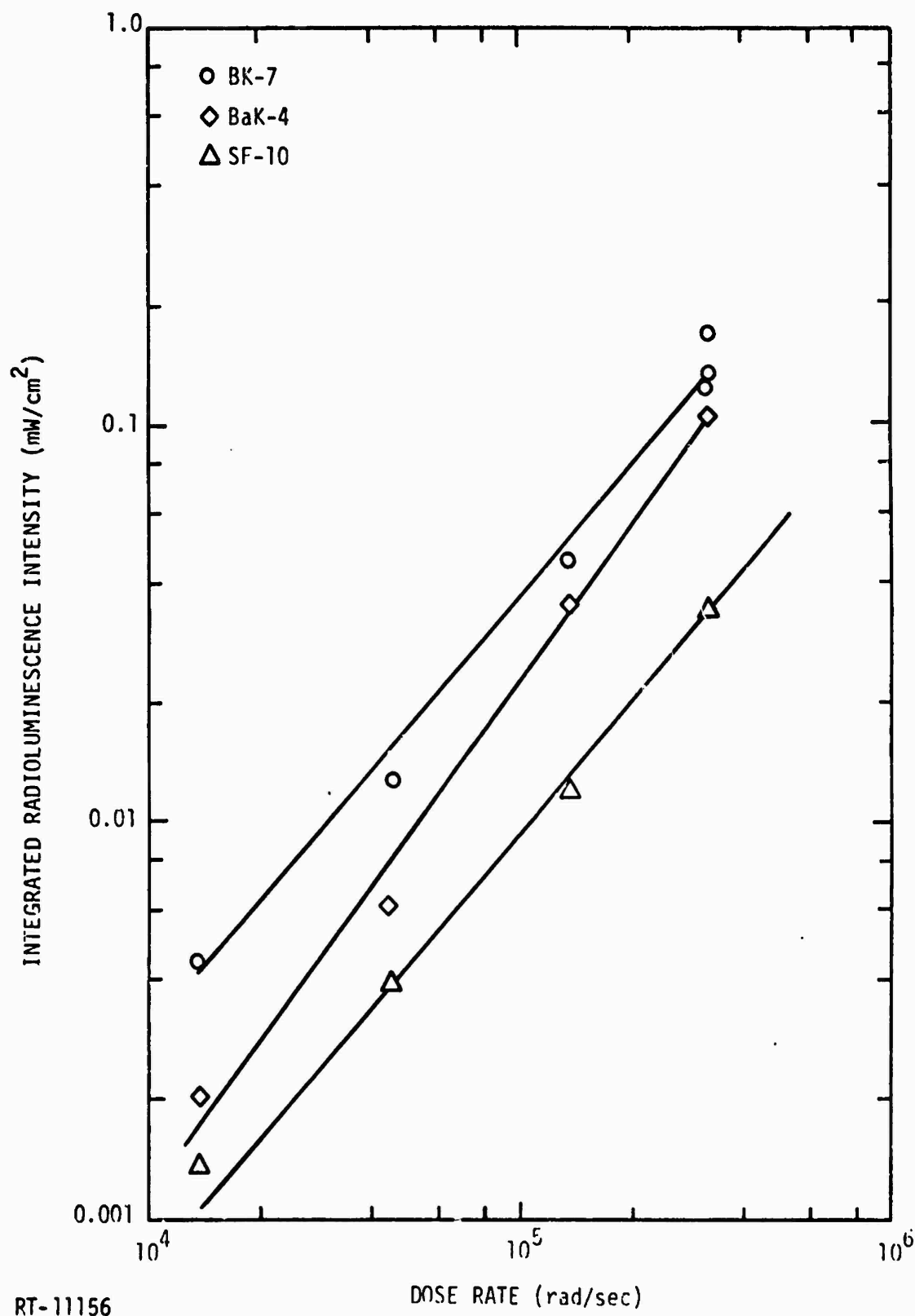
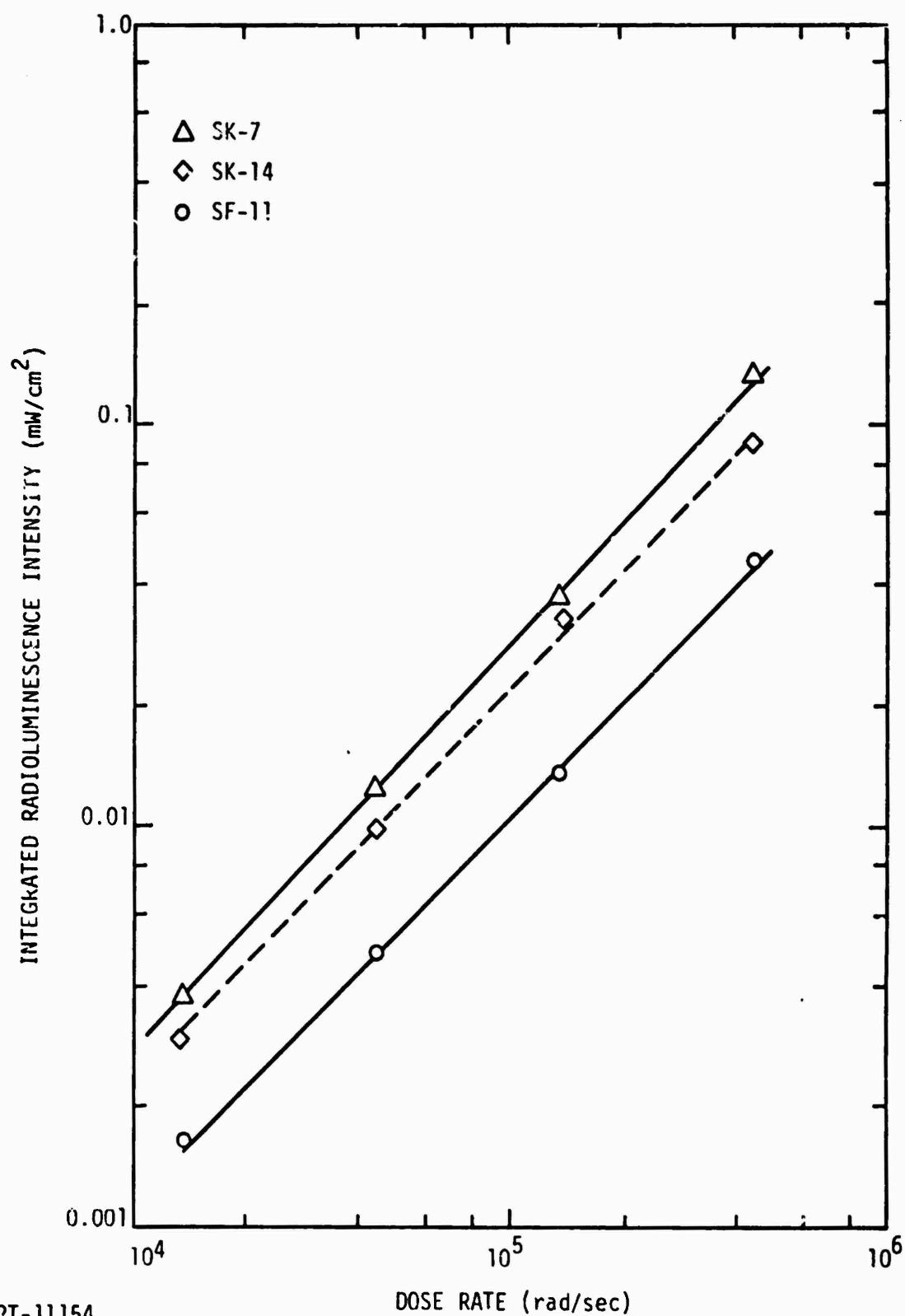
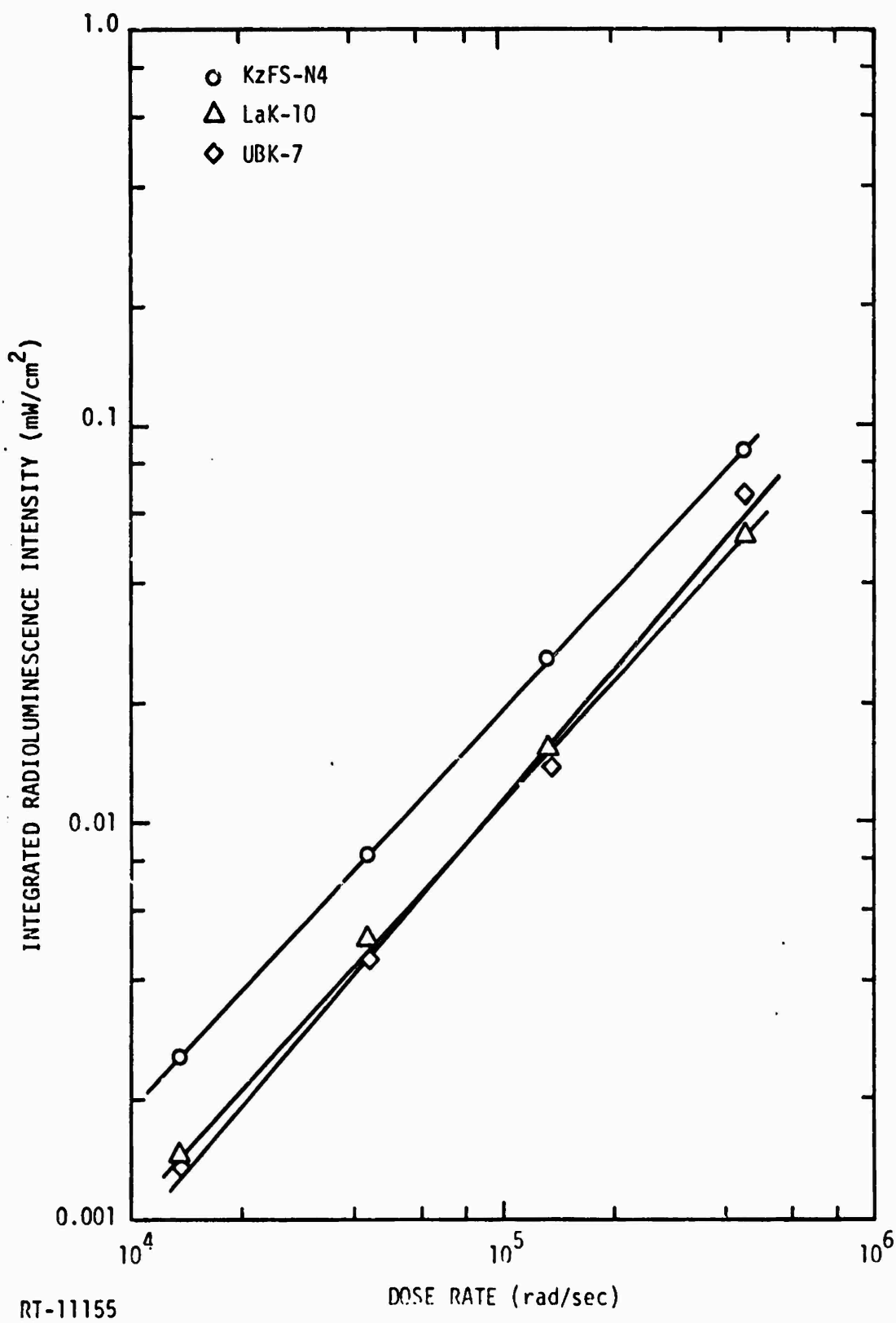


Figure 59. Spectrally integrated radioluminescence intensity versus dose rate: Schott BK-7, BaK-4, SF-10



RT-11154

Figure 60. Spectrally integrated radioluminescence intensity versus dose rate: Schott SK-7, SK-14, SF-11



RT-11155

Figure 61. Spectrally integrated radioluminescence intensity versus dose rate: Schott KzFS-N4, LaK-10, UBK-7

1. That the sample be uniformly irradiated (this condition was reasonably well satisfied and verified experimentally).
2. That the luminescence lifetime be short and that the luminescence be directly proportional to the dose rate. (See Sections 4.2 and 4.3 to establish the degree to which this is true for any given sample).
3. That the luminescence is isotropic and that the radiation pattern from a sample is the same as that from the calibration source. This implies that Cerenkov radiation (which is directional) is excluded. This condition was satisfied by the geometry of the optical system. Whether the radiation pattern from a sample is identical to that of a source is unknown, and constitutes the major uncertainty in the calculation. For this document, we have assumed the samples radiate according to Lambert's law. This is also a good approximation for a flat (large-area) filament lamp such as the G.E. 30A/T24/17. The difference between a Lambertian and a spherical or cylindrical radiator would alter the calibration by a factor of 4 or π , respectively.

The definition of dose rate, $\dot{\gamma}$, is energy, Q , deposited per unit mass, m , per unit time, t :

$$\dot{\gamma} = \frac{Q}{mt} = \frac{Q}{\rho vt} ,$$

where ρ is density and v is sample volume. If one assumes that a fraction ϵ is converted to optical radiation which is isotropically emitted from the sample, the radiant emittance (power, P , per unit area) should be (assuming negligible optical self-absorption)

$$\frac{P}{A} = \frac{\epsilon Q}{At} = \frac{\epsilon \rho v \dot{\gamma}}{A} = \frac{\epsilon \rho \dot{\gamma} L}{2} , \quad (22)$$

where L is the sample dimension normal to the emitting surface. The factor of two in the denominator accounts for the fact that half the photons generated are directed away from the collection cone. Thus, for a sample of known geometry and density, the conversion efficiency ϵ is obtained from the observed radiant emittance by

$$\epsilon = \frac{2(P/A)}{\rho \dot{\gamma} L} ,$$

and the spectral conversion efficiency $\epsilon(\lambda)$ is obtained from the spectral radiant emittance $P(\lambda)/A$ by

$$\epsilon(\lambda) = \frac{2[P(\lambda)/A]}{\rho \dot{\gamma} L} . \quad (23)$$

Care was taken to keep the radiation exposure to a minimum during luminescence measurements, so that $\alpha L < 1$; therefore, correction for optical self-absorption could be neglected. However, should one care to calculate the luminescence expected from a sample which has a previous radiation history such that $\alpha L > 0$, one would have to recognize that light of wavelength λ originating a distance x beneath the surface of the sample would be attenuated as

$$I(\lambda) = I_0 \exp[-\alpha(\lambda)x] ,$$

where $\alpha(\lambda)$ could be taken from a figure in this report. Thus, the radiant emittance from an absorbing slab of thickness L would be

$$\frac{P}{A} = \frac{\epsilon \rho \dot{\gamma}}{2} \int_0^L \exp[-\alpha(\lambda)x] dx = \frac{\epsilon \rho \dot{\gamma}}{2\alpha} \{1 - \exp[-\alpha(\lambda)L]\} ,$$

and the spectral radiant emittance $P(\lambda)/A$ would be related to the spectral conversion efficiency $\epsilon(\lambda)$ and spectral absorption as

$$P(\lambda)/A = \frac{\epsilon(\lambda) \rho \dot{\gamma}}{2\alpha(\lambda)} \{1 - \exp[-\alpha(\lambda)L]\} .$$

This expression may become quite complicated if there is significant transient absorption since then both $\epsilon(\lambda)$ and $\alpha(\lambda)$ may be functions of previous radiation history, temperature, dose rate, and time, as well as of wavelength.

Because these complications were clearly recognized, pains were taken to measure luminescence on samples with no previous radiation history, and to complete the measurements with as little accumulated dose as possible so that conversion efficiencies could be calculated adequately from the simplest expression. Consider sapphire, for example:

$$\rho = 3.9 \text{ g/cm}^3 ;$$

for all our samples, $L = 3.82 \text{ cm}$, (other sample densities are as given in Table 1) then from Figure 58,

$$\frac{P}{A} \approx 10^{-4} \text{ W/cm}^2 \text{ at } \dot{\gamma} = 10^4 \text{ rad/sec (1 rad/sec} = 10^{-5} \text{ W/g)} ;$$

so from

$$\begin{aligned} \epsilon &= \frac{2(P/A)}{\rho \dot{\gamma} L} \\ &= \frac{2 \times 10^{-4} \text{ W/cm}^2}{3.9 \text{ g/cm}^3 [10^{-1} \text{ W/g}] 3.82 \text{ cm}} = 0.0134\% . \end{aligned}$$

Alternatively, one may integrate the area under Figures 50 and 51 (remembering that $1 \text{ rad} \approx 2.2 \times 10^7 \text{ e/cm}^2$) to obtain

$$\epsilon = 0.04 \pm 0.01\% .$$

The major discrepancy between these two values is thought to result from the fact that an "average" optical throughput (related to system sensitivity, Figure 7) was used to generate Figure 58. The values obtained

from integration of the spectral curves are more accurate for materials such as sapphire and quartz, which are rich in UV emissions.

Using the prescription indicated here, we find the conversion efficiency of the materials studied as given in Table 7.

Table 7

EFFICIENCY OF CONVERTING ENERGY DEPOSITED AS IONIZING RADIATION
TO RADIOLUMINESCENCE IN UNITS OF PERCENT

Sample Type	ϵ (%)
BaK-4	3.4×10^{-4}
BK-7	7×10^{-4}
BK7-G14	2×10^{-3}
LaK-10	1.4×10^{-4}
SF-10	1.2×10^{-4}
SF-11	1.2×10^{-4}
SK-7	4.5×10^{-4}
SK-14	3.4×10^{-4}
UBK-7	2.1×10^{-4}
SiO ₂ (Z-cut)	3×10^{-3}
SiO ₂ (Fused)	9×10^{-4}
Al ₂ O ₃	1×10^{-2}

REFERENCES

1. P. L. Mattern et al., IEEE Trans. Nucl. Sci. NS-21, 81, December 1974.
2. B. D. Evans and G. H. Sigel Jr., IEEE Trans. Nucl. Sci. NS-21, 113, December 1974.
3. J. I. Vette et al., NASA SP-3024 (1967).
4. D. D. Davis Jr., NASA SP-27, December 1962.
5. J. H. Trainor et al., Goddard Space Flight Center X66074-198, June 1974.
6. G. E. Palma and R. M. Gagosz, United Aircraft Research Laboratories, "Optical Absorption in Transparent Materials During 1.5-MeV Electron Irradiation," J-990929-1, NASA contract SNPC-70.
7. J. A. Samson, Techniques of Vacuum Ultraviolet Spectroscopy, Wiley & Sons, New York (1967).
8. Data Sheet, Eimac Division of Varian, San Carlos, California.
9. R. Spair et al., J. Research NBS-A-64A, 291 (1960).
10. R. L. Christensen and I. Avila, J. Opt. Soc. of America 51, 224 (1961).
11. American Institute of Physics Handbook, Section 7, McGraw Hill, New York (1957).
12. L. Levi, Applied Optics, John Wiley & Sons, New York (1968).
13. Beckman DK-1A Operation Manual, Beckman Scientific and Process Instruments Division, Fullerton California (1962).
14. D. Heath and P. Sacker, Applied Optics, Vol. 5, p. 937, June 1966.
15. E. Lell et al., Progress in Ceramic Science, Vol. 4, Pergamon Press (1966).
16. W. Primak, Physical Review 100, 1677, December 1955.
17. M. Goldberg et al., Nuclear Instruments and Methods 108, p. 119 (1973).
18. P. W. Levy et al., Solid-State Commun. 9, 1907 (1971).
19. K. Patek, Glass Lasers, The Chemical Rubber Co., Cleveland (1970).

APPENDIX A

^{60}Co GAMMA IRRADIATION AND OPTICAL BLEACHING MEASUREMENTS

Palma and Gagosz* reported that radiation-induced absorption in Corning grade 7940 fused silica can be optically bleached. In an attempt to determine the importance of this effect on the samples considered in this investigation, and to obtain preliminary data to aid in directing our efforts at the Dynamitron facility, preliminary measurements were made on one sample of each type listed in Table A-1. These samples had dimensions of 0.2 x 0.4 x 0.8 inch except BK7-Gi4, which was 1 x 1 x 0.25 inch, and were obtained from Dr. P. Schall of Aerospace Corporation, El Segundo, California. Absorption measurements were made through the 0.2-inch thickness.

The samples were irradiated at the Salk Institute's ^{60}Co gamma-ray source at a rate of 0.25 Mrad/hr to a dose of 0.5 Mrad (equivalent to $\sim 10^{13}$ e/cm², E = 2.5 MeV). The samples were shielded from room light at all times. All irradiation and transmission measurements were performed at room temperature. Changes in transmission as a result of making a transmission measurement were not observed. The horizontal lines drawn on each figure (near 90%) represent the transmission losses due to reflectances at the surfaces.

Comparison of the transmission spectra before and after irradiation showed that the cerium-doped Schott glass BK7-Gi4 did not darken, the quartz, sapphire, and Suprasil 2 samples darken very little, and the remaining Schott glasses darkened severely. Attention was focused on the latter group.

After irradiation, the transmission spectra of the samples were taken. The samples were then placed in a vacuum to avoid the production of ozone, and exposed to the output of the Eimac 150-watt xenon lamp. The light flux at the samples, integrated over the spectral range, was ~ 100 mW/cm². Such

*G. E. Palma and R. M. Gagosz, "Optical Absorption in Transparent Materials during 1.5-MeV Electron Irradiation," United Aircraft Research Labs report J-990929-1 under NASA contract SNPC-70, October 1970.

a light flux is a reasonable approximation of one sun (air mass zero). Thermistors were used to monitor the sample temperature to ensure that any change in transmission was not the result of heating of the sample by the light source. Transmission spectra were obtained after 5, 10, 20, and 40 minutes' total exposure to the light source, and the results are shown in Figures A-1 through A-10. These measurements were made using the DK-1A.

Comparison of the results of these measurements to optical bleaching theories indicates that (1) all of the samples considered bleach, (2) the bleaching can be expressed in terms of a bleaching rate, and (3) the darkening of at least some samples is the result of two types of defects, one of which bleaches and one which does not. After 40 minutes of bleaching, the samples were bleached for an additional hour and transmission spectra again were taken. The results of this measurement indicate the absorption which results from the nonbleaching centers.

The absorption at some wavelength λ can be written as

$$\alpha = \alpha_p + \alpha_R \quad (1)$$

where

- α = total absorption (cm^{-1}),
- α_R = radiation-induced absorption (cm^{-1}),
- α_p = absorption present before irradiation; includes reflection losses (cm^{-1}).

The spectra shown in Figures A-1 through A-10 are in percent transmission which can be related to the absorption coefficient (cm^{-1}) by

$$-\frac{1}{x} \ln T = -\alpha,$$

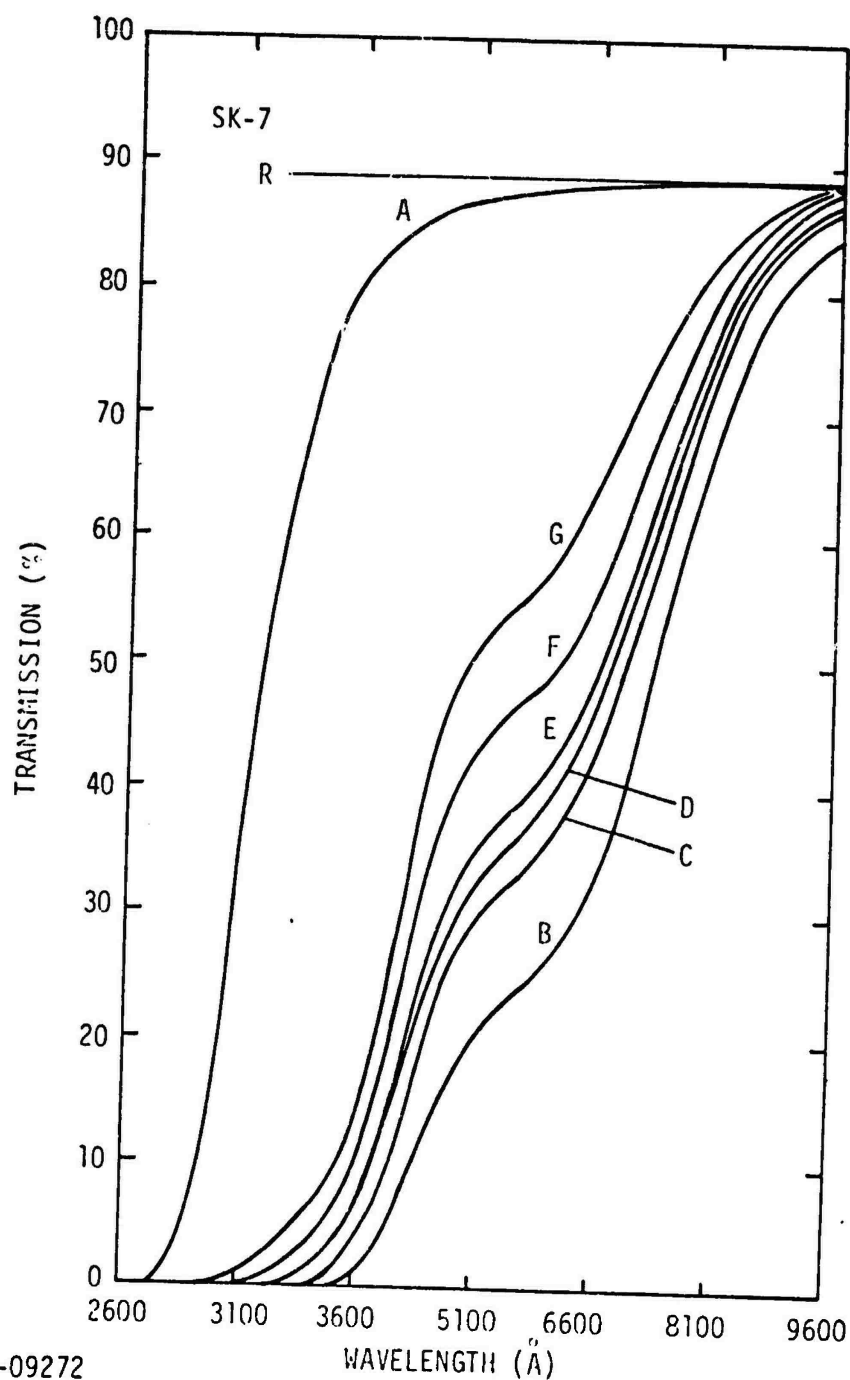
where $T = \% \text{ transmission}/100$.

Equation 1 can be written as

$$-\frac{1}{x} \ln T = -\frac{1}{x} \ln T_p + \alpha_R. \quad (2)$$

Therefore,

$$\alpha_R = -\frac{1}{x} \ln T + \frac{1}{x} \ln T_p = \frac{1}{x} \ln \frac{T_p}{T}. \quad (3)$$



RT-09272

Figure A-1. Optical transmission of Schott glass SK-7 versus wavelength; A = preirradiation, B = 24 hours after irradiation to 0.5 Mrad (^{60}Co , room temperature, in dark), C = after 5 days at room temperature +5 hours room light, D = after 5 minutes of xenon light, 100 mW/cm², E = after 10 minutes of xenon light, F = after 20 minutes of xenon light, G = after 40 minutes of xenon light

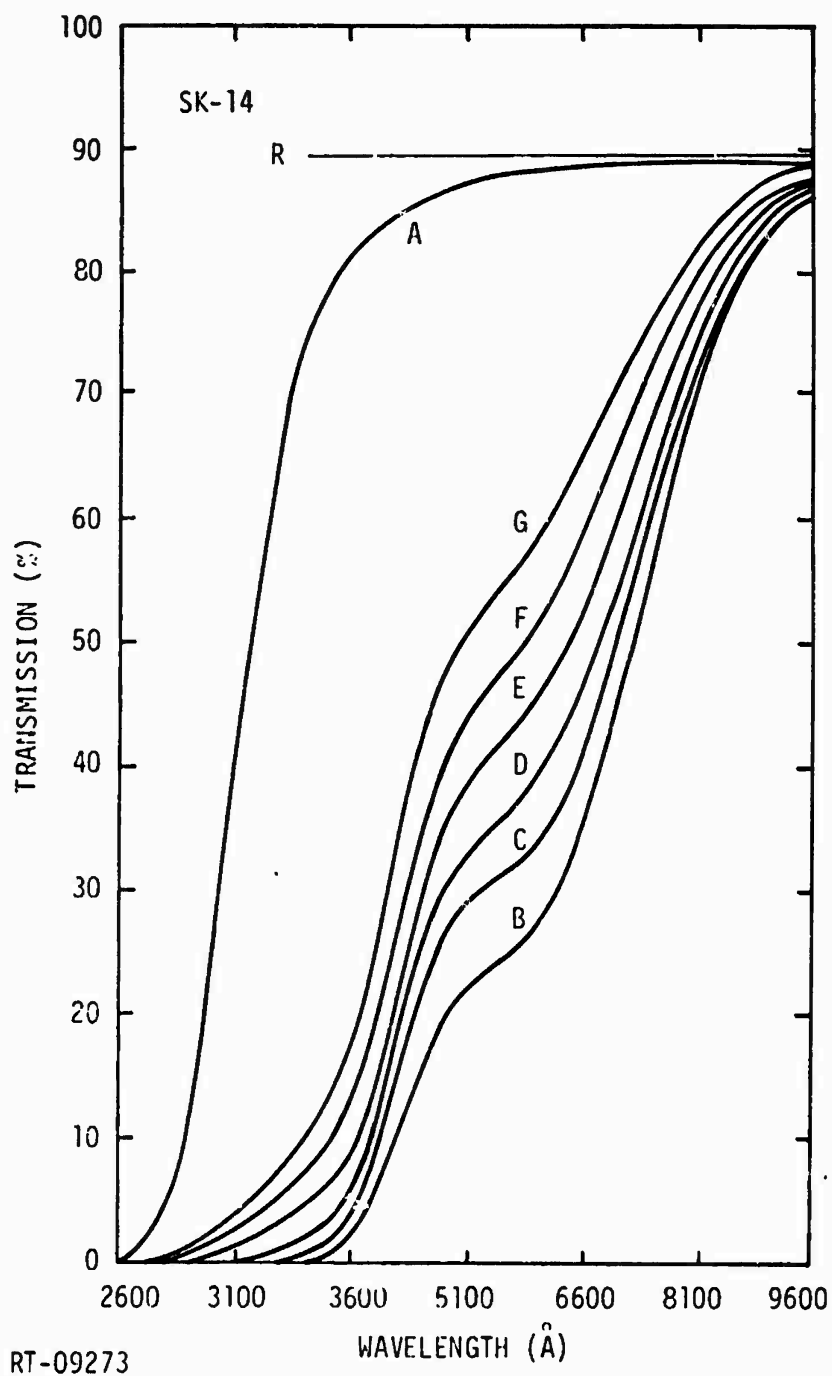
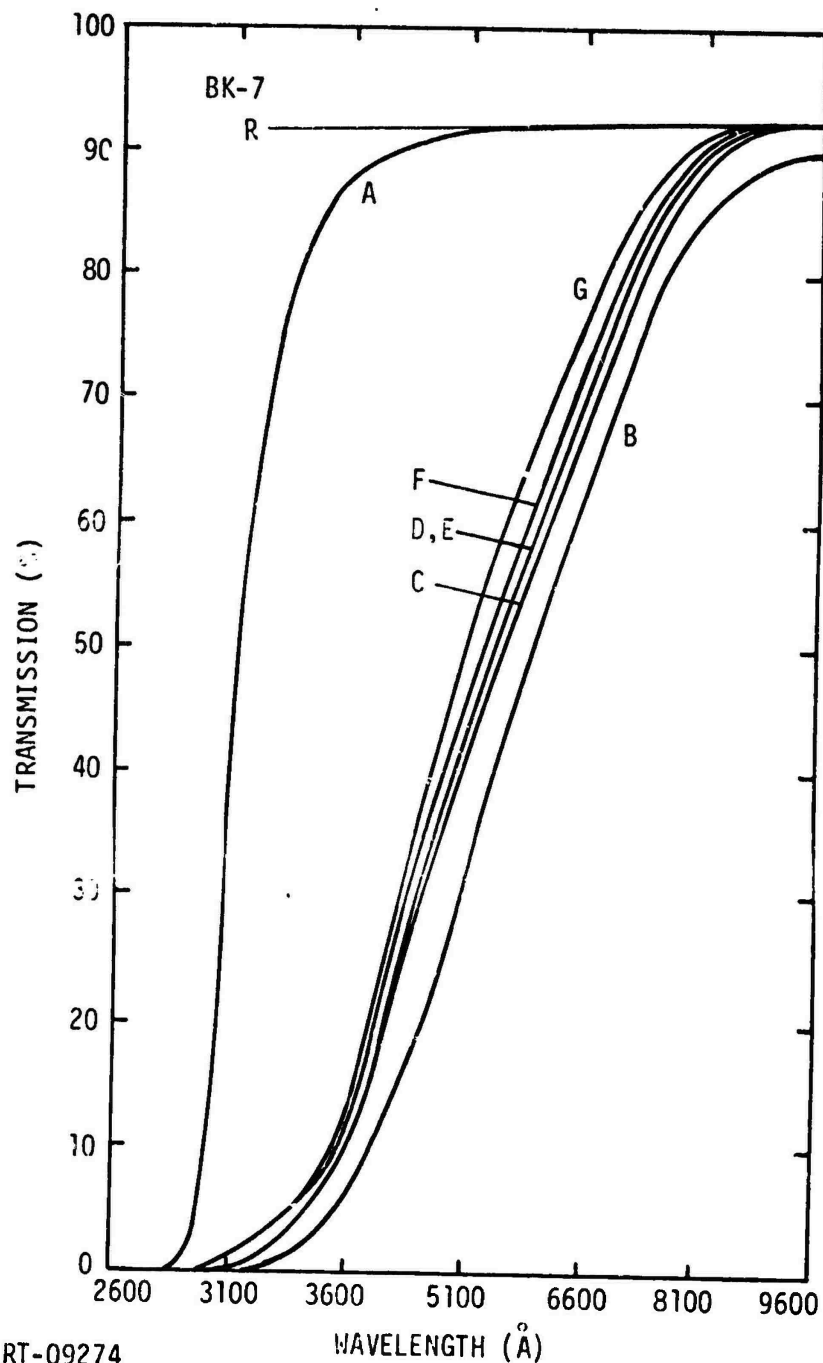
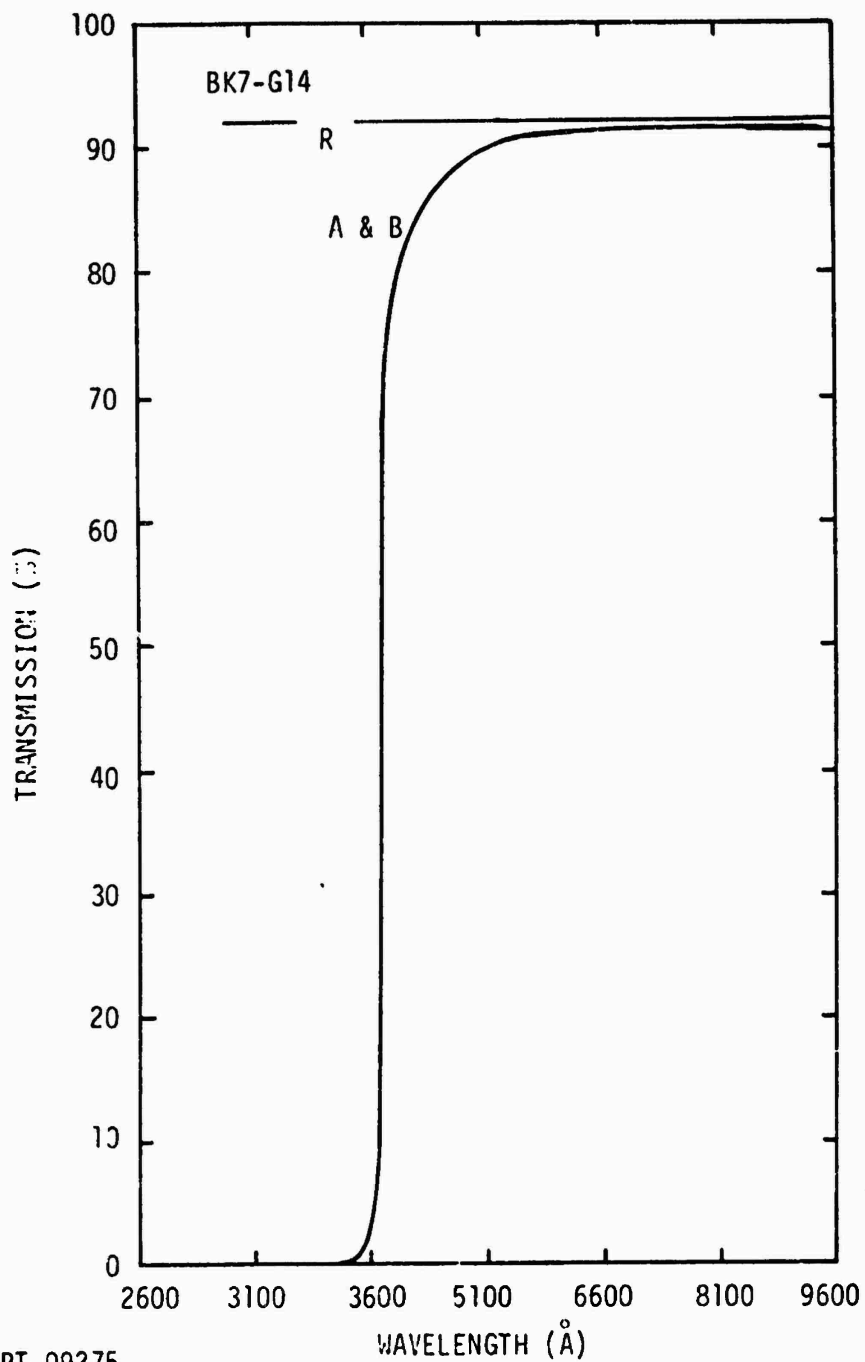


Figure A-2. Optical transmission of Schott glass SK-14 versus wavelength; A = preirradiation, B = 24 hours after irradiation to 0.5 Mrad (^{60}Co , room temperature, in dark), C = after 5 days at room temperature +5 hours room light, D = after 5 minutes of xenon light, 100 mW/cm², E = after 10 minutes of xenon light, F = after 20 minutes of xenon light, G = after 40 minutes of xenon light



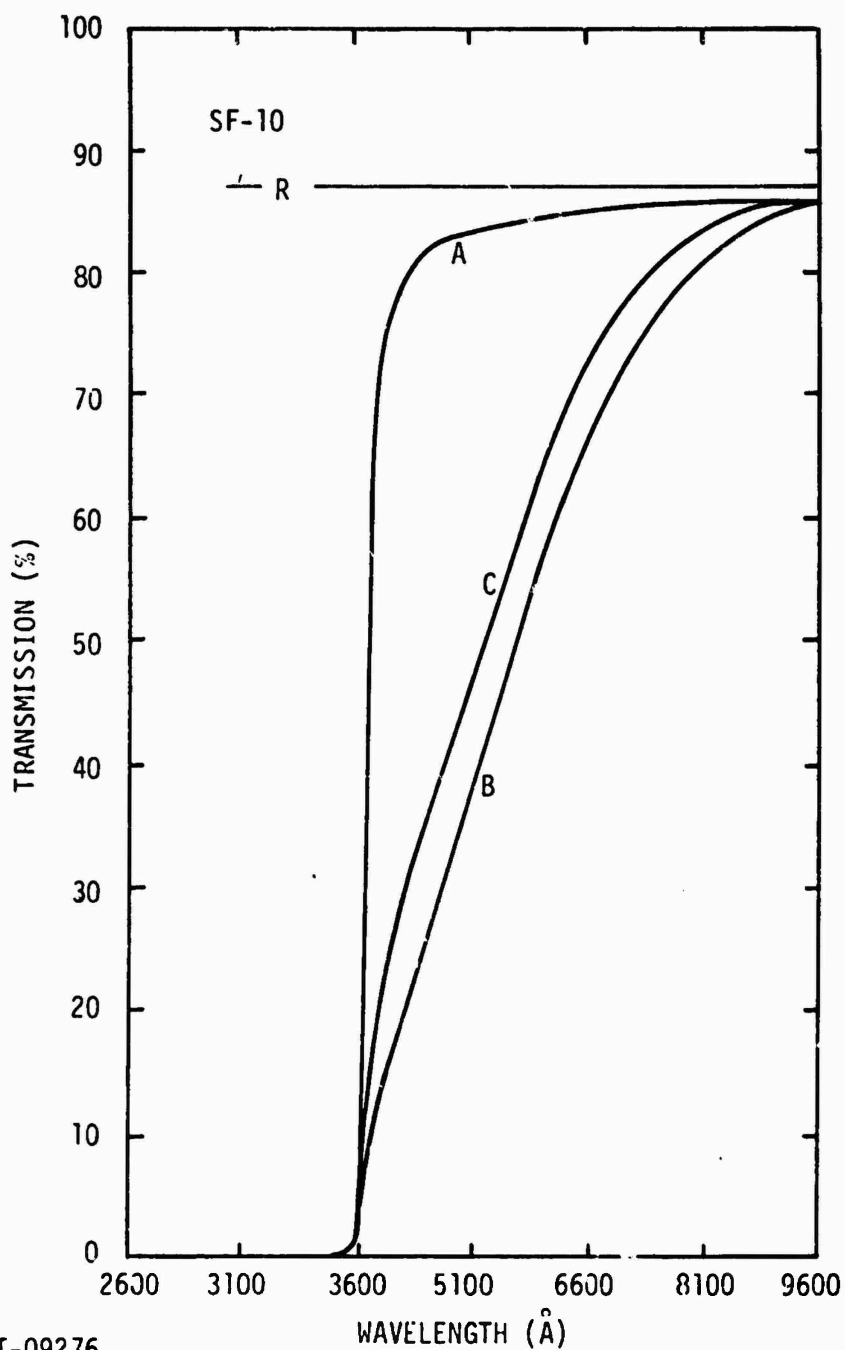
RT-09274

Figure A-3. Optical transmission of Schott glass BK-7 versus wavelength; A = preirradiation, B = 24 hours after irradiation to 0.5 Mrad (^{60}Co , room temperature, in dark), C = after 5 days at room temperature +5 hours room light, D = after 5 minutes of xenon light, 100 mW/cm², E = after 10 minutes of xenon light, F = after 20 minutes of xenon light, G = after 40 minutes of xenon light



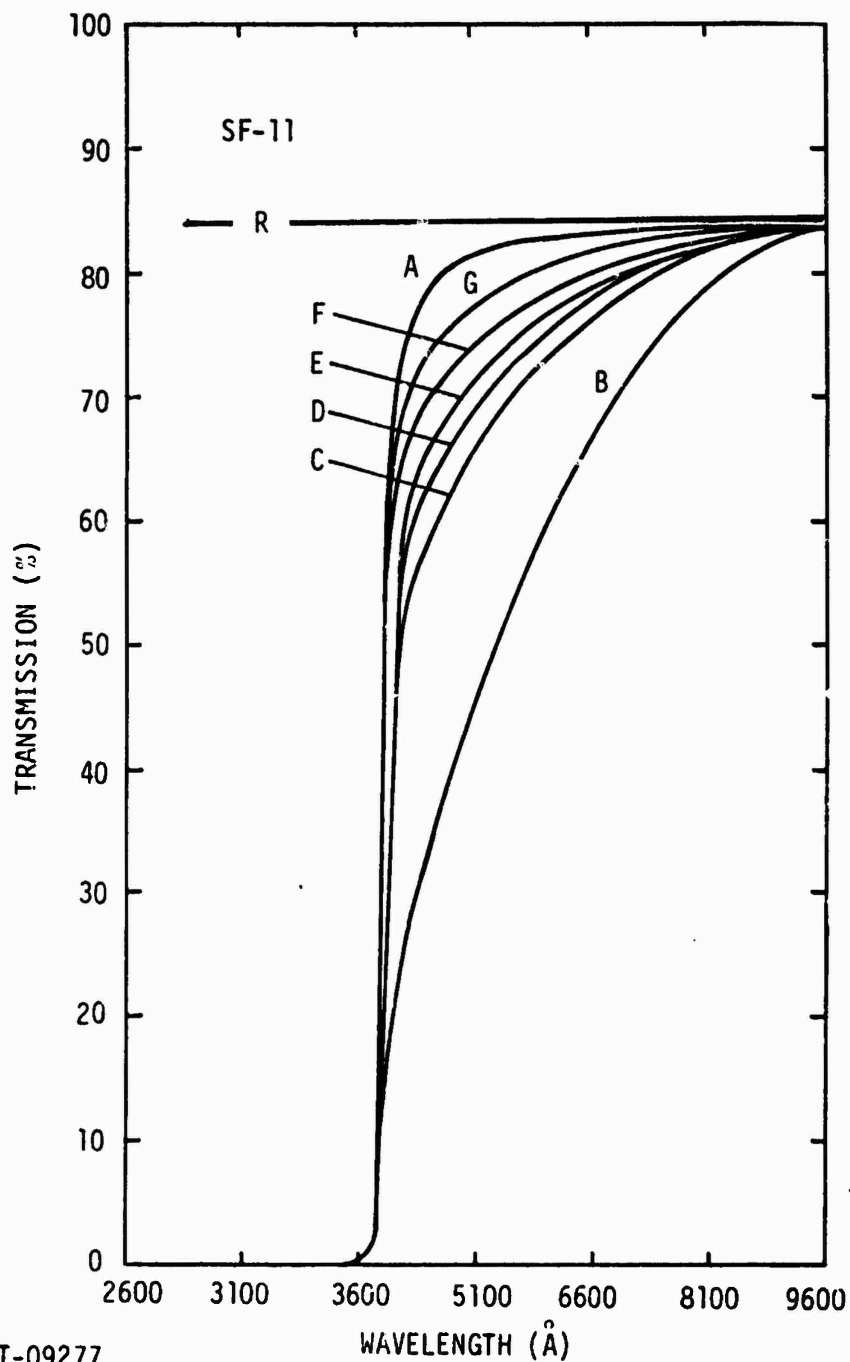
RT-09275

Figure A-4. Optical transmission of Schott glass BK7-14 versus wavelength; A = preirradiation, B = 24 hours after irradiation to 0.5 Mrad (^{60}Co , room temperature, in dark)



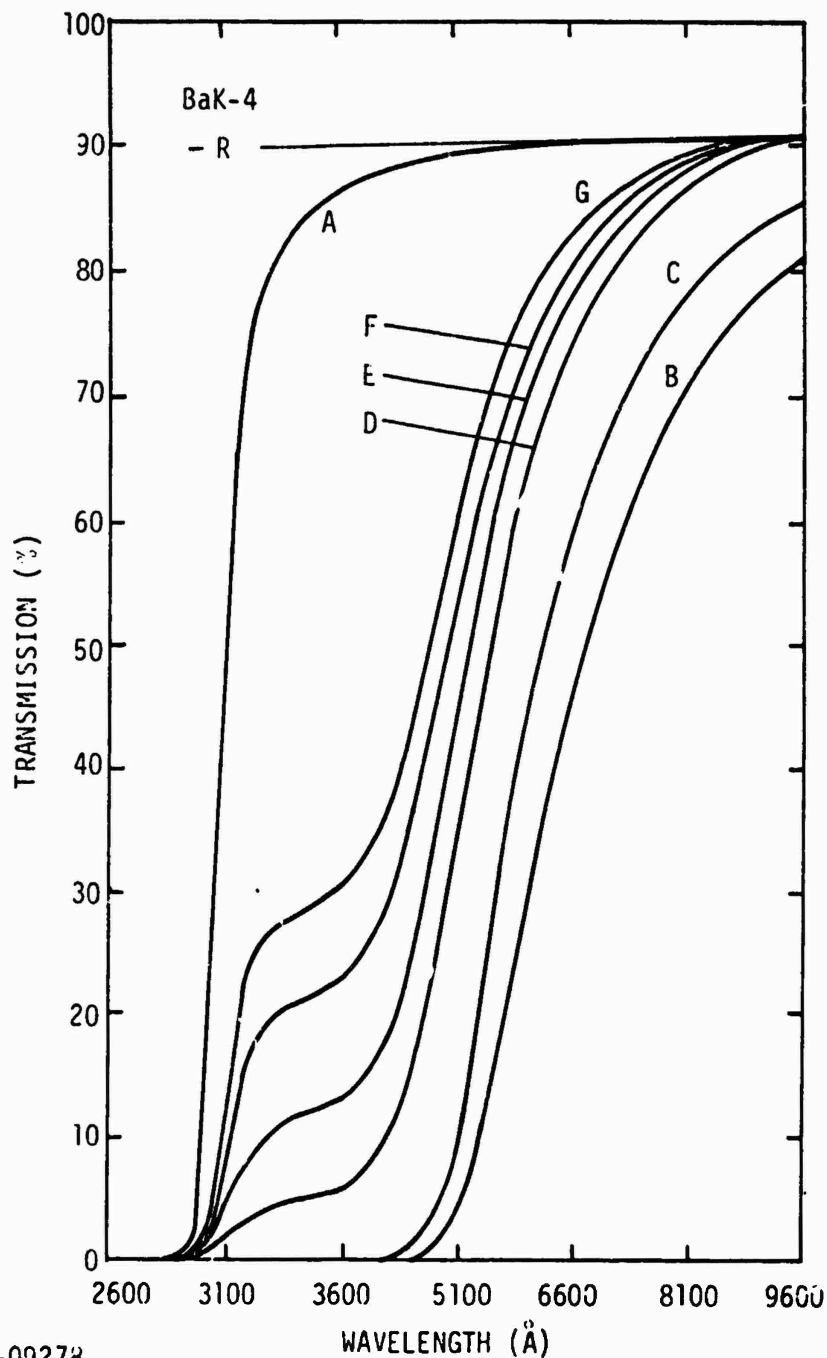
RT-09276

Figure A-5. Optical transmission of Schott glass SF-10 versus wavelength, A = preirradiation, B = 24 hours after irradiation to 0.5 Mrad (^{60}Co , room temperature, in dark), C = after 5 days at room temperature + 5 hours room light



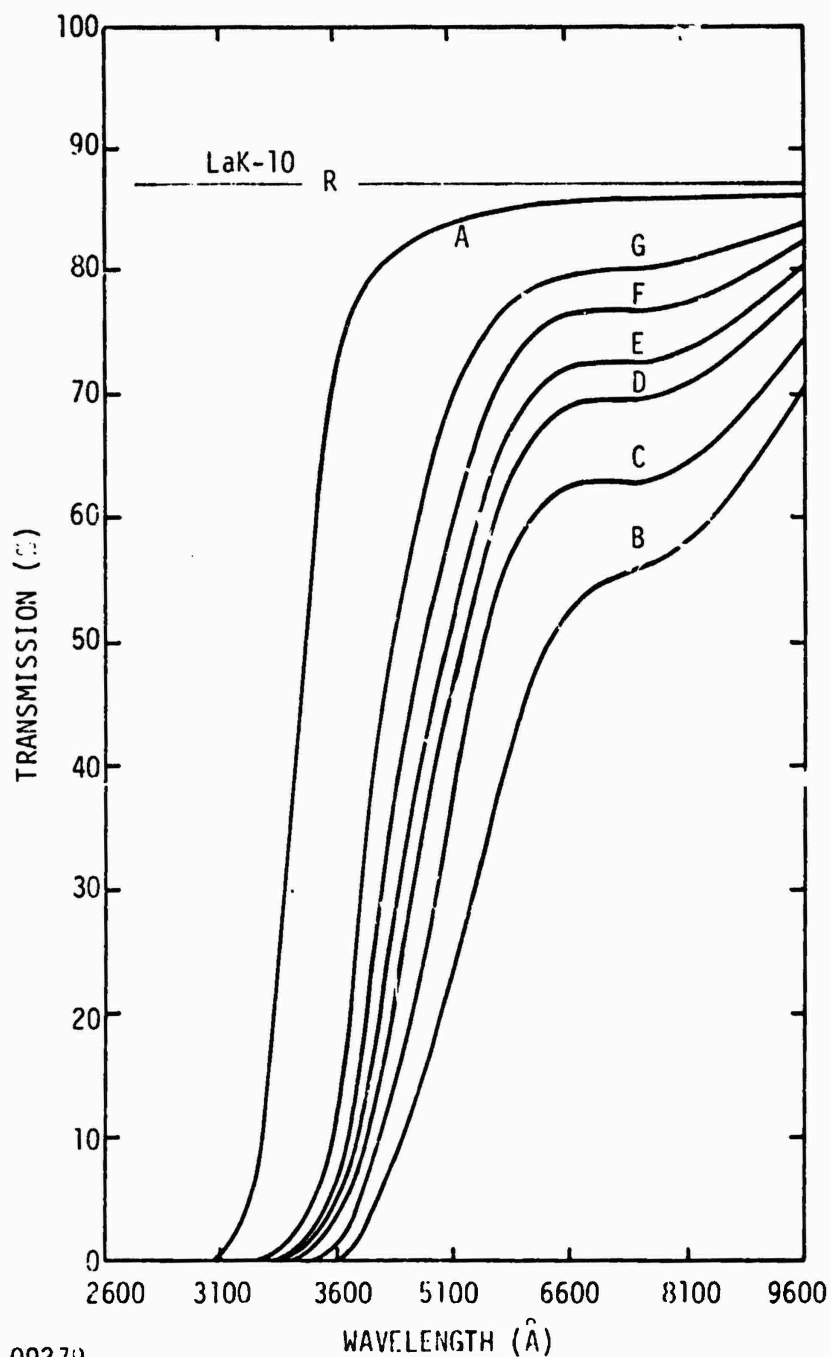
RT-09277

Figure A-6. Optical transmission of Schott glass SF-11 versus wavelength; A = preirradiation, B = 24 hours after irradiation to 0.5 Mrad (^{60}Co , room temperature, in dark), C = after 5 days at room temperature + 5 hours room light, D = after 5 minutes of xenon light, 100 mW/cm², E = after 10 minutes of xenon light, F = after 20 minutes of xenon light, G = after 40 minutes of xenon light



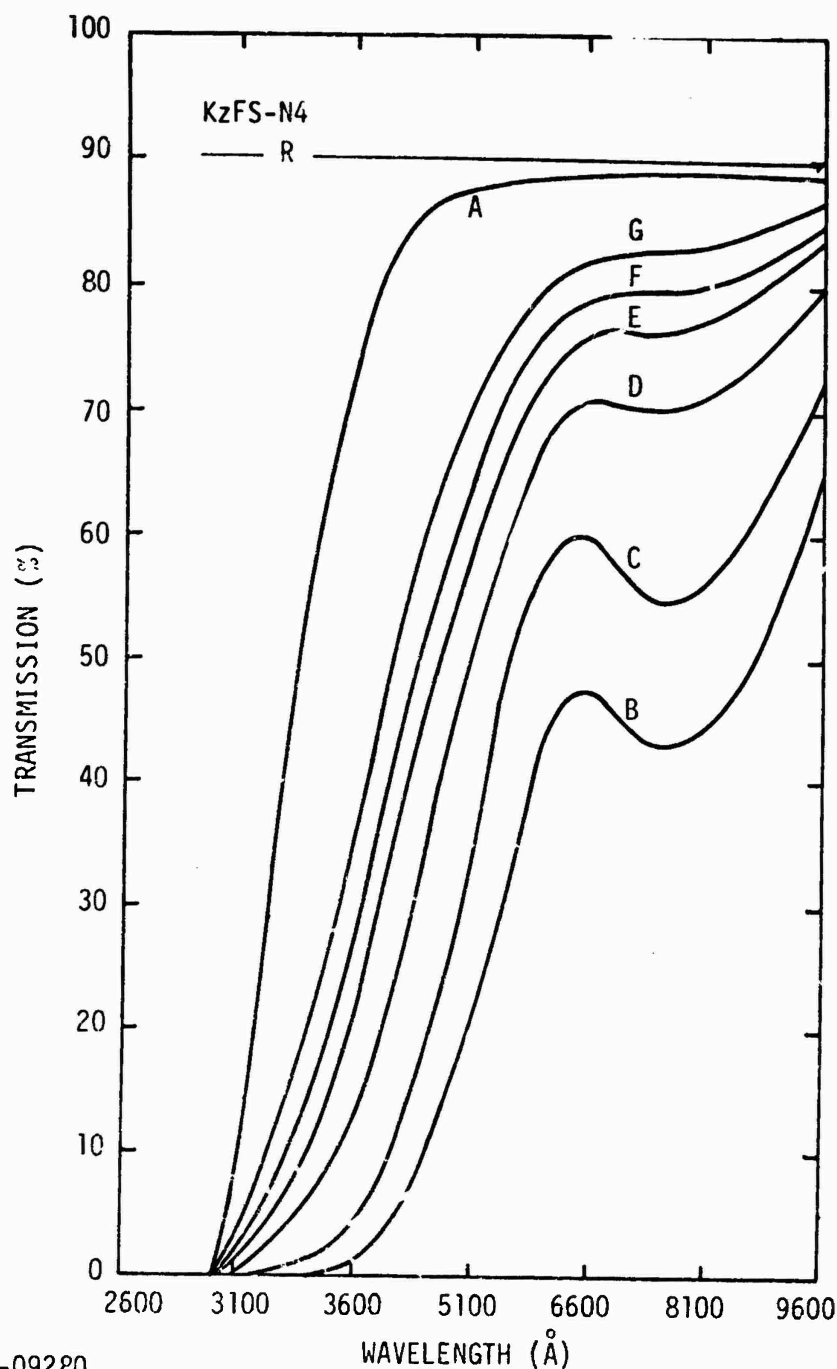
RT-09278

Figure A-7. Optical transmission of Schott glass BaK-4 versus wavelength; A = preirradiation, B = 24 hours after irradiation to 0.5 Mrad (^{60}Co , room temperature, in dark), C = after 5 days at room temperature + 5 hours room light, D = after 5 minutes of xenon light, 100 mW/cm², E = after 10 minutes of xenon light, F = after 20 minutes of xenon light, G = after 40 minutes of xenon light



RT-09279

Figure A-8. Optical transmission of Schott glass LaK-10 versus wavelength; A = preirradiation, B = 24 hours after irradiation to 0.5 Mrad (^{60}Co , room temperature, in dark), C = after 5 days at room temperature +5 hours room light, D = after 5 minutes of xenon light, 100 mW/cm², E = after 10 minutes of xenon light, F = after 20 minutes of xenon light, G = after 40 minutes of xenon light



RT-09280

Figure A-9. Optical transmission of Schott glass KZFS-N4 versus wavelength; A = preirradiation, B = 24 hours after irradiation to 0.5 Mrad (^{60}Co , room temperature, in dark), C = after 5 days at room temperature +5 hours of room light, D = after 5 minutes of xenon light, 100 mW/cm², E = after 10 minutes of xenon light, F = after 20 minutes of xenon light, G = after 40 minutes of xenon light

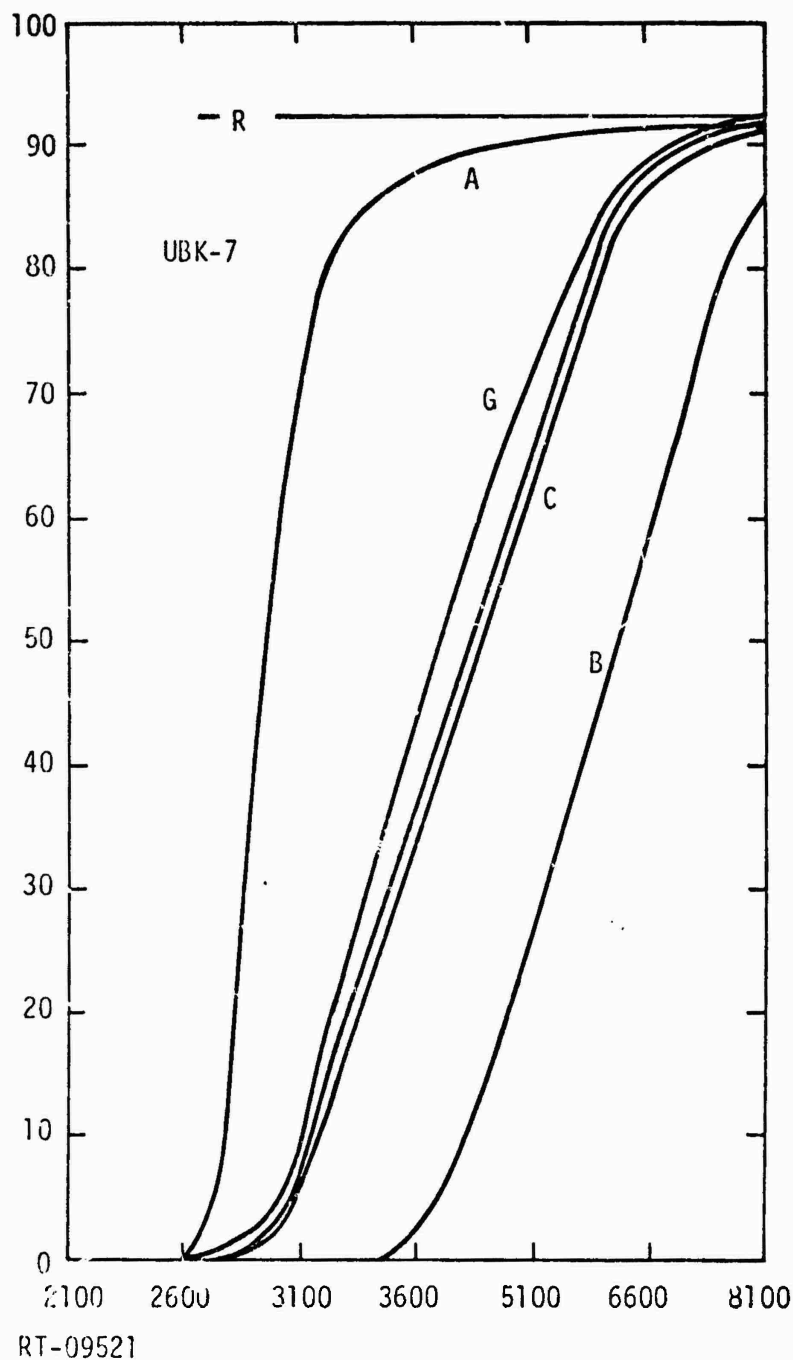


Figure A-10. Optical transmission of Schott glass UBK7 versus wavelength; A = preirradiation, B = 24 hours after irradiation to 0.5 Mrad (^{60}Co , room temperature, in dark), C = after 5 days at room temperature +5 hours room light, D = after 5 minutes of xenon light, 100 mW/cm², G = after 40 minutes of xenon light

The absorption, α_R , due to the radiation-induced defects is proportional to the number of defects present, n , by the equation

$$\alpha_R = \sigma_1 n_1 + \sigma_2 n_2 \quad (5)$$

If the samples are exposed to light of intensity I (W/cm^2) which bleaches the darkening, the bleaching can be characterized by a constant c ($\text{cm}^2\text{-W}^{-1}\text{-sec}^{-1}$).^{*} This constant contains the microscopic quantum mechanical statistical probabilities of absorption of a photon and the probability that this photon will bleach the absorbing center. The fact that c has been assumed to be a constant is an assumption of the kinetics involved in the bleaching. The time rate of change of the defect population can be written, then, as

$$\frac{dn}{dt} = -cIn = -vn \quad (6)$$

where $cI = v$ (sec^{-1}). Integrating Eq. 6 yields

$$n = n_0 \exp(-vt),$$

which, combined with Eq. 5, yields

$$\alpha_R = \sigma_1 n_1(0) \exp(-v_1 t) + \sigma_2 n_2(0) \exp(-v_2 t) \quad (7)$$

Attempts to fit our data to Eq. 7, assuming that only one type of defect was present (i.e., $n_2(0) = 0$), failed. The next attempt was to assume two types of defects were created, only one of which bleached (i.e., $v_2 = 0$), and this proved satisfactory. In this case, Eq. 7 becomes

$$\alpha_R = \sigma_1 n_1(0) \exp(-v_1 t) + \sigma_2 n_2(0) \quad (8)$$

The term $\sigma_2 n_2(0)$ can be determined from the spectra taken after bleaching for an infinite time by using Eq. 3:

$$\sigma_2 n_2(0) = \frac{1}{x} \ln \frac{T_P}{T_\infty} \quad (9)$$

^{*}Op. cit.

Combining Eqs. 3, 8, and 9 yields

$$\alpha_R = \frac{1}{x} \ln \frac{T_P}{T} = \sigma_1 n_1(0) \exp(-\nu_1 t) + \frac{1}{x} \ln \frac{T_P}{T_\infty} . \quad (10)$$

Rearranging, Eq. 10 becomes

$$\frac{1}{x} \ln \frac{T_\infty}{T} = \sigma_1 n_1(0) \exp(-\nu_1 t) .$$

Taking the natural log of both sides,

$$\ln \left(\frac{1}{x} \ln \frac{T_\infty}{T} \right) = \ln \sigma_1 n_1(0) - \nu_1 t . \quad (11)$$

The bleaching rate ν_1 can be determined by plotting the left-hand side of Eq. 11 versus bleaching time, and indeed, this fit the data well. The optical bleaching rates obtained in this manner are listed in Table A-1.

It is important to remember that the bleaching rates are dependent upon the light intensity and spectral distribution. The intensity of the

Table A-1
OPTICAL BLEACHING RATES, ν [(sec)⁻¹]

Sample	Wavelength			
	0.8 μm	0.66 μm	0.51 μm	0.36 μm
BaK-4		2.7×10^{-3}	3.1×10^{-3}	1.8×10^{-3}
UBK-7	Note 1			
BK-7		0.82×10^{-3}	0.59×10^{-3}	
SK-14				1.2×10^{-3}
SK-7			0.75×10^{-3}	0.89×10^{-3}
LaK-10	1.0×10^{-3}	1.0×10^{-3}	1.5×10^{-3}	1.6×10^{-3}
KZFSN-4	2.5×10^{-3}	2.5×10^{-3}	2.1×10^{-3}	2.1×10^{-3}
SF-10	Note 2			
SF-11		1.1×10^{-3}	1.2×10^{-3}	

1. This sample did not bleach significantly.
2. No bleaching measurements were made on this sample due to light source failure.

light falling on the sample was $\sim 0.1 \text{ W/cm}^2$, with a spectral distribution similar to the sun. If a source of a similar distribution, but with intensity I , were used to bleach the samples, the bleaching rate could be determined from the values listed in Table A-1 by

$$v_I = \frac{I}{0.1} v ,$$

where v_I is the bleaching rate at intensity $I \text{ (W/cm}^2\text{)}$.

APPENDIX B

TRANSMISSION LOSSES AND RECOVERY OF OTHER SCHOTT GLASSES EXPOSED TO 10-MeV ELECTRONS

Dr. Leonard Larks of Jet Propulsion Laboratory was able to obtain authority to release data and samples from NASA to IRT to be incorporated in this SAMSO project. On May 8-10, 1974, JPL irradiated five kinds of Schott glass at the IRT electron linear accelerator. Transmission spectra of these glass samples were measured with the Beckman DK-1A spectrometer prior to irradiation and after each stage of irradiation, after the last irradiation, after 10 hours of storage at room temperature in the dark, and again after 7 months of storage at room temperature in the dark. At least two samples of each glass type were investigated, and the results of this investigation are presented in Figures B-1 through B-10.

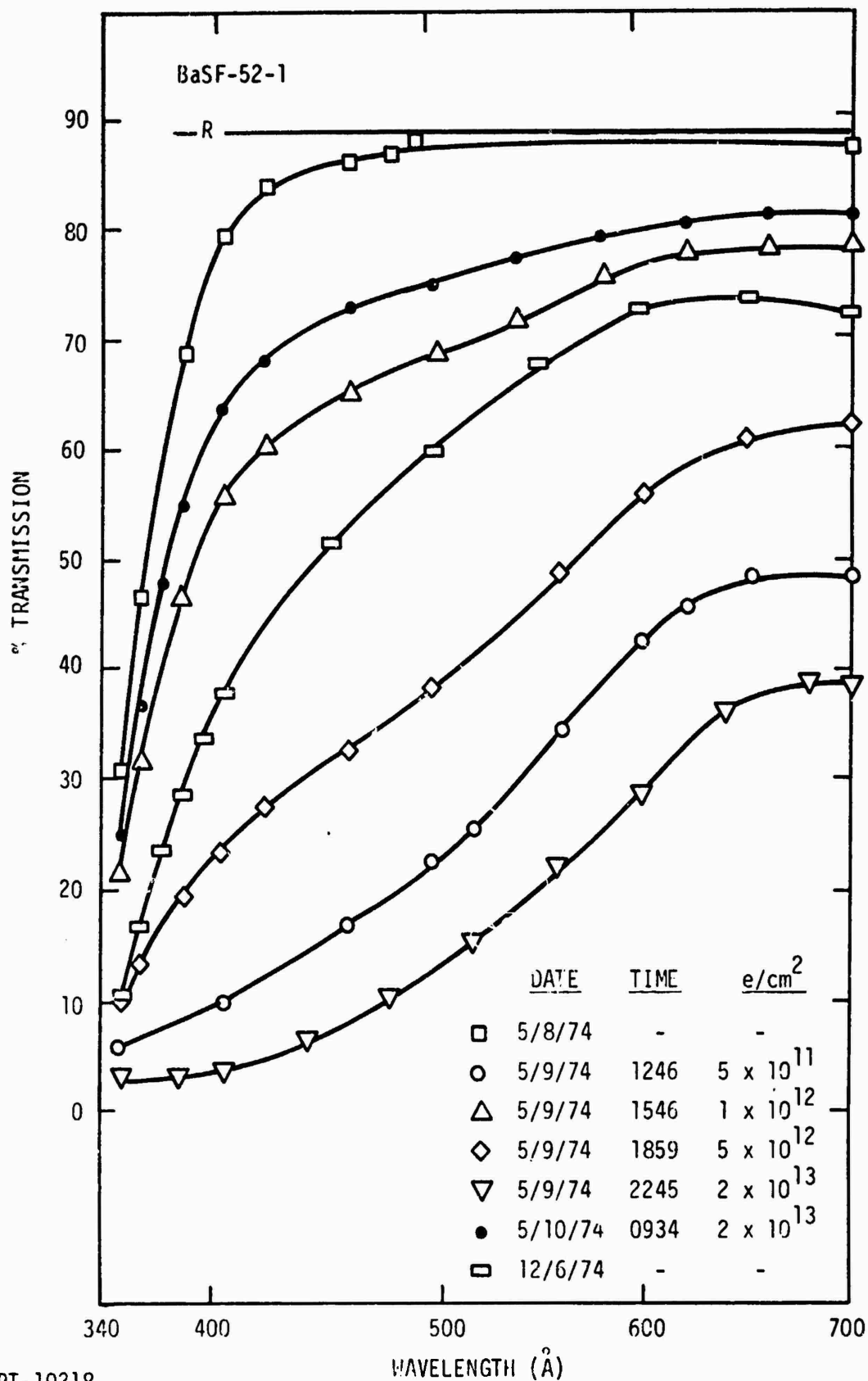
Each figure shows relative transmission of one particular glass sample before irradiation and after irradiation to cumulative fluences of 5×10^{11} , 1×10^{12} , 5×10^{12} , and 2×10^{13} e/cm² (E = 10 MeV). The irradiations were all at room temperature and the samples were kept in the dark during irradiation and during the 15 to 20 minutes needed to transport the samples from the Linac to the optics laboratory for measurement.

The five types of glass investigated were:

1. BaSF-52
2. FzG-20
3. SF1-G7
4. SF-8
5. SF-10

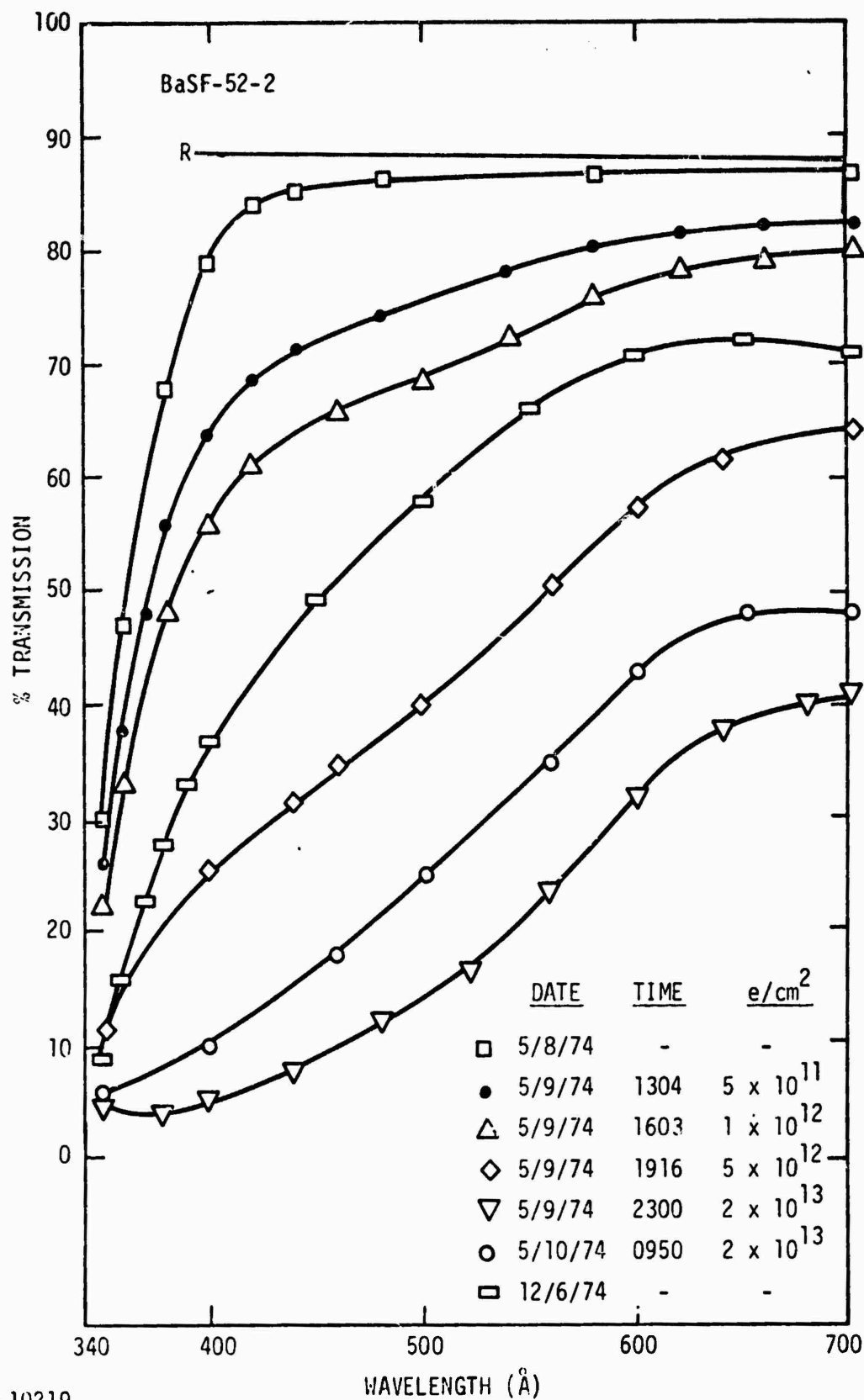
The results shown in the figures may be compared with results in other sections of this report by using the conversion factor $\sim 3 \times 10^7$ e/cm² (E = 10 MeV) = 1 rad(⁶⁰Co). The samples were all 1 cm thick.

Several observations may be made. One is that the cerium-doped glass, FzG-20 and SF1-G7, showed no change in transmission under this irradiation.



RT-10218

Figure B-1 Spectral transmission of BaSF-52-1 glass as a function of fluence and thermal bleach time (samples in the dark and at room temperature)



RT-10219

Figure B-2 Spectral transmission of BaSF-52-2 glass as a function of fluence and thermal bleach time (samples in the dark and at room temperature)

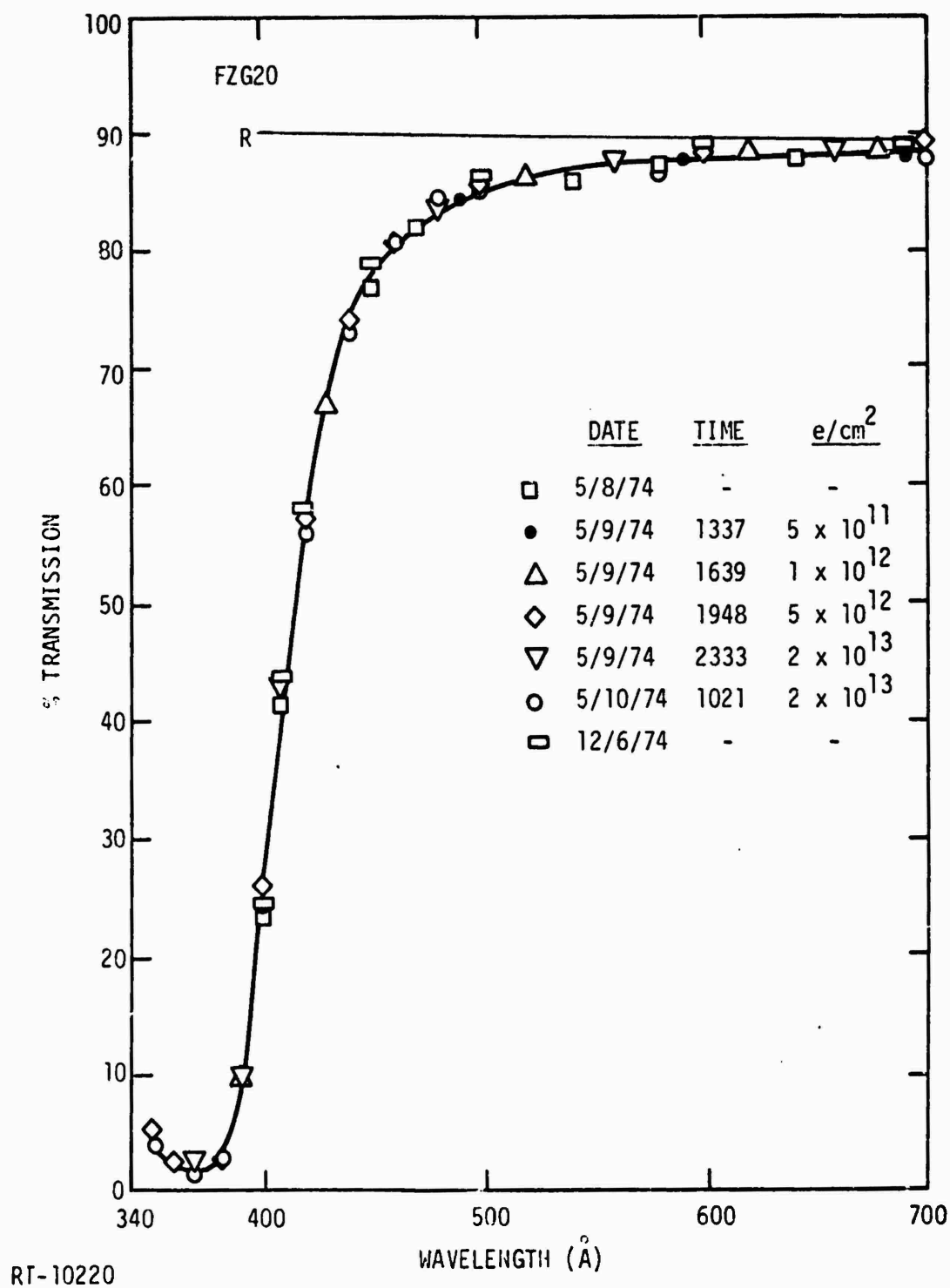


Figure B-3 Spectral transmission of FZG-20 glass as a function of fluence and thermal bleach time (samples in the dark and at room temperature)

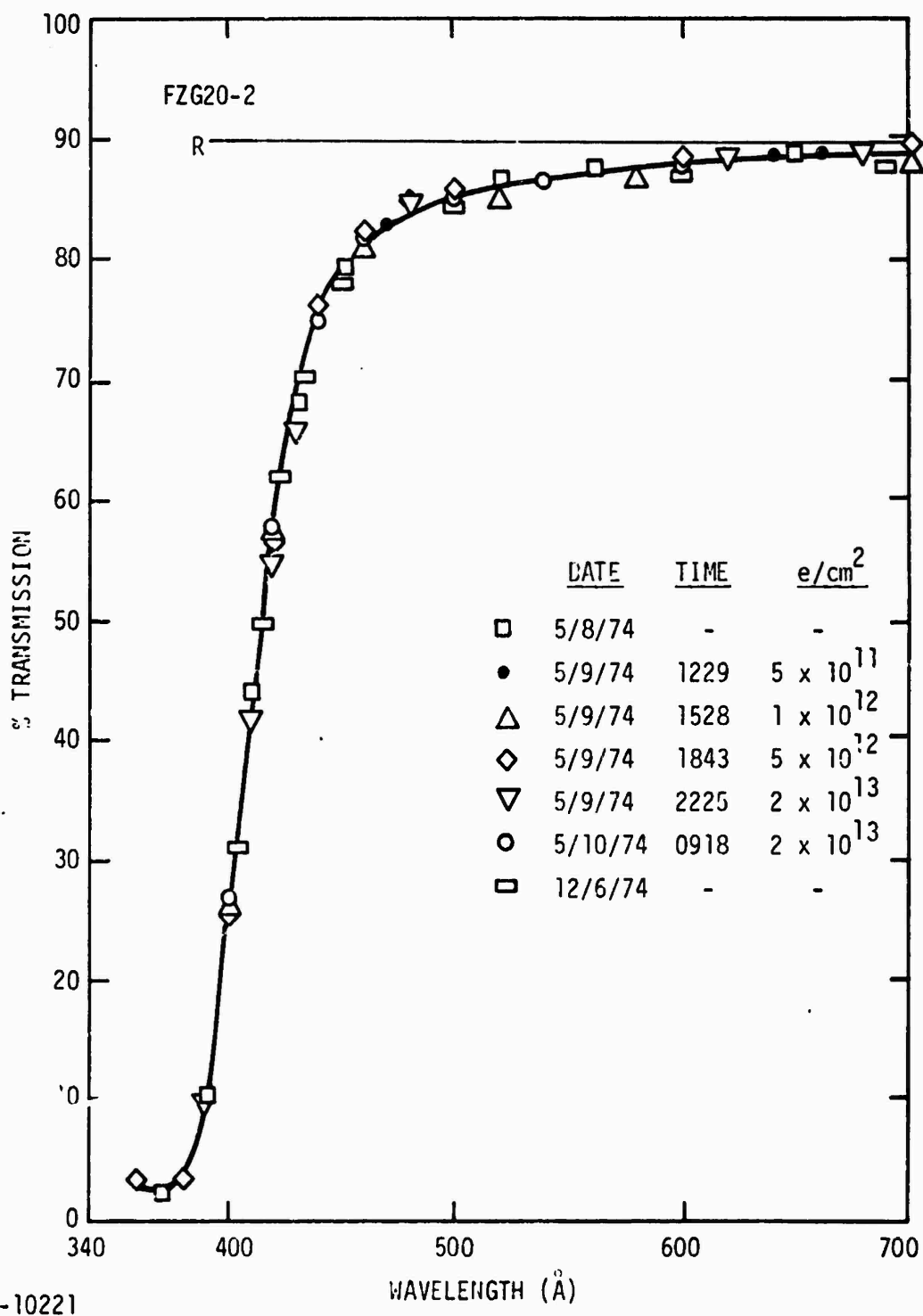
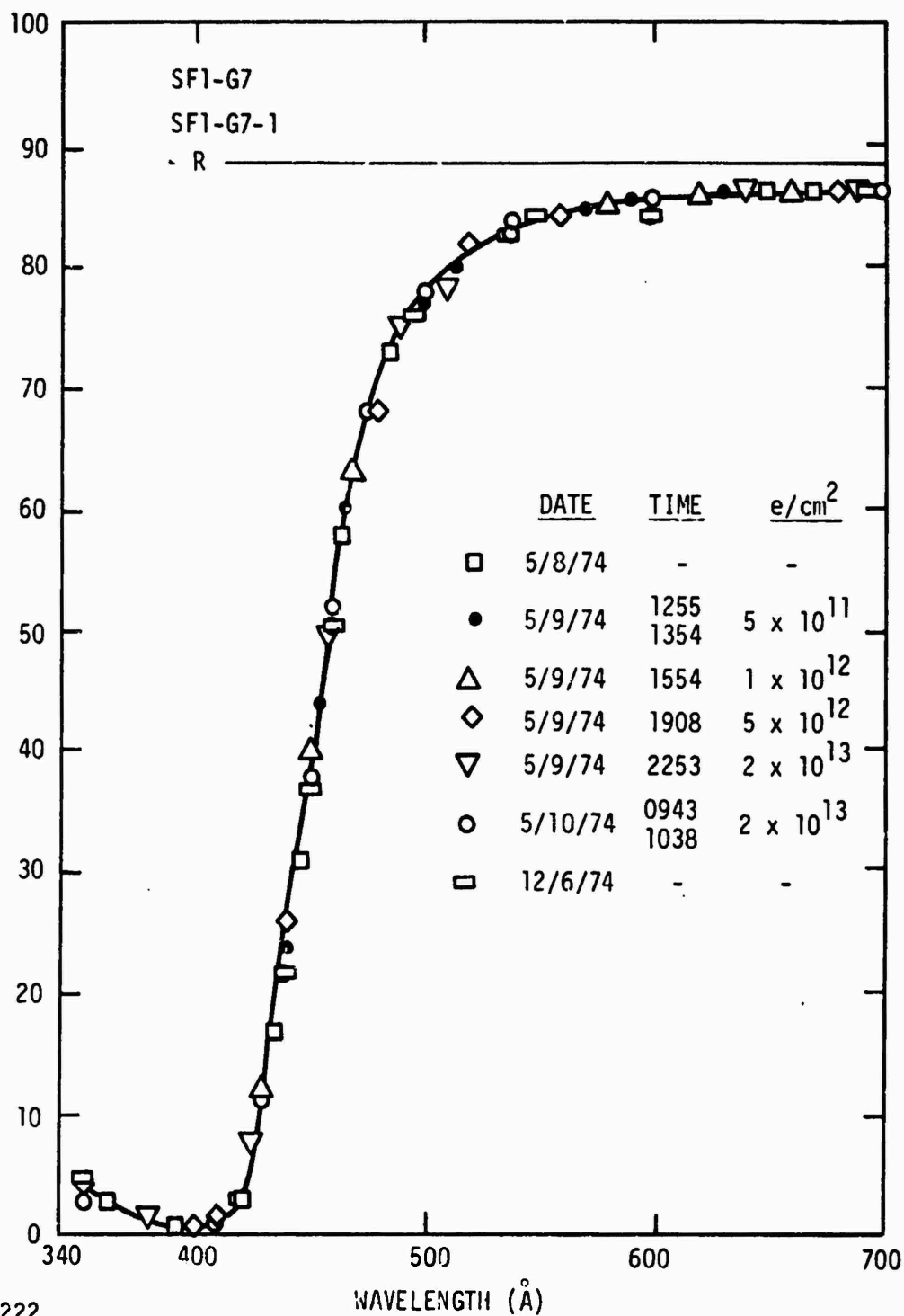


Figure B-4 Spectral transmission of FZG-20-2 glass as a function of fluence and thermal bleach time (samples in the dark and at room temperature)



RT-10222

Figure B-5 Spectral transmission of SF1-G7 and SF1-G7-1 glass as a function of fluence and thermal bleach time (samples in the dark and at room temperature)

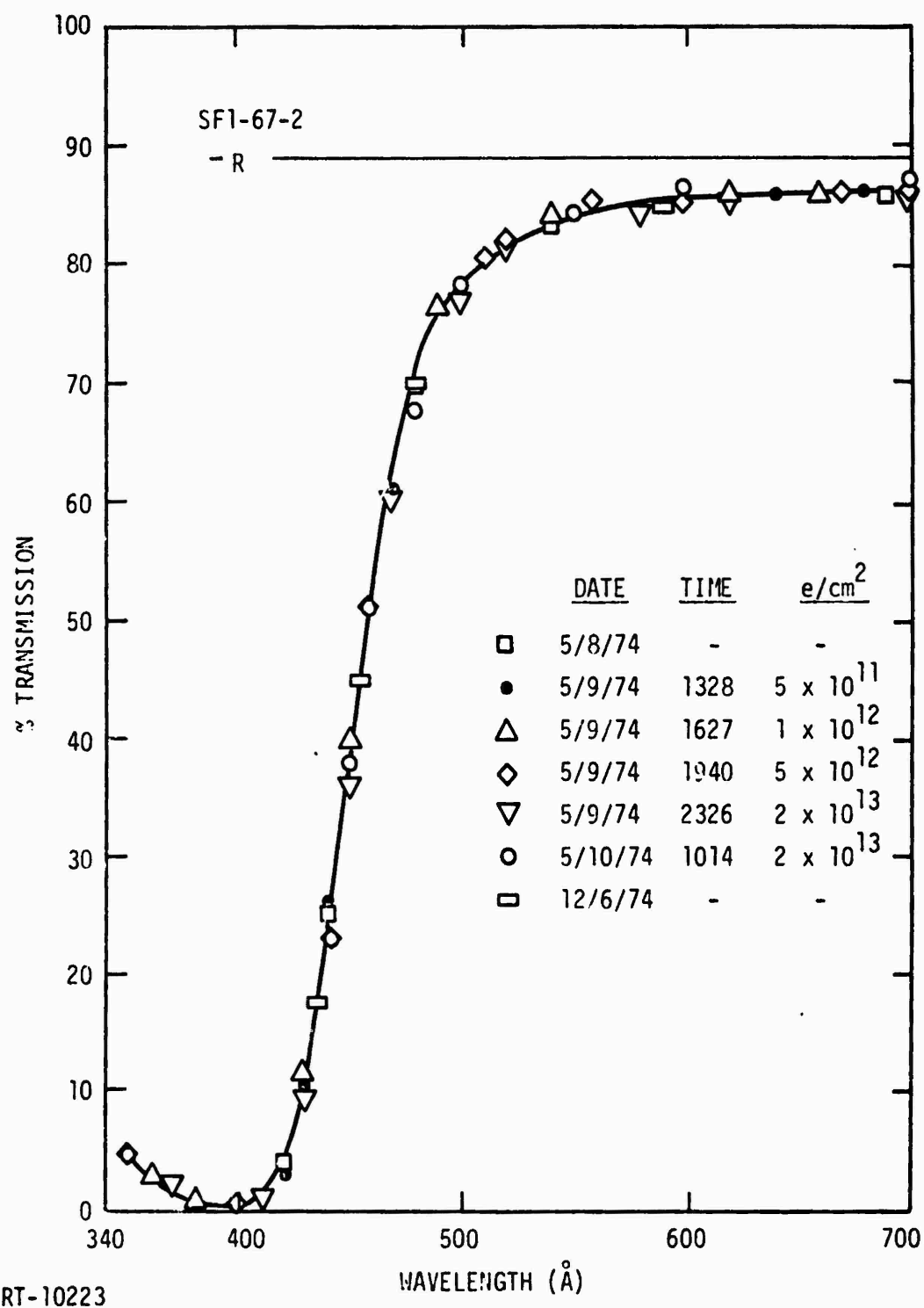
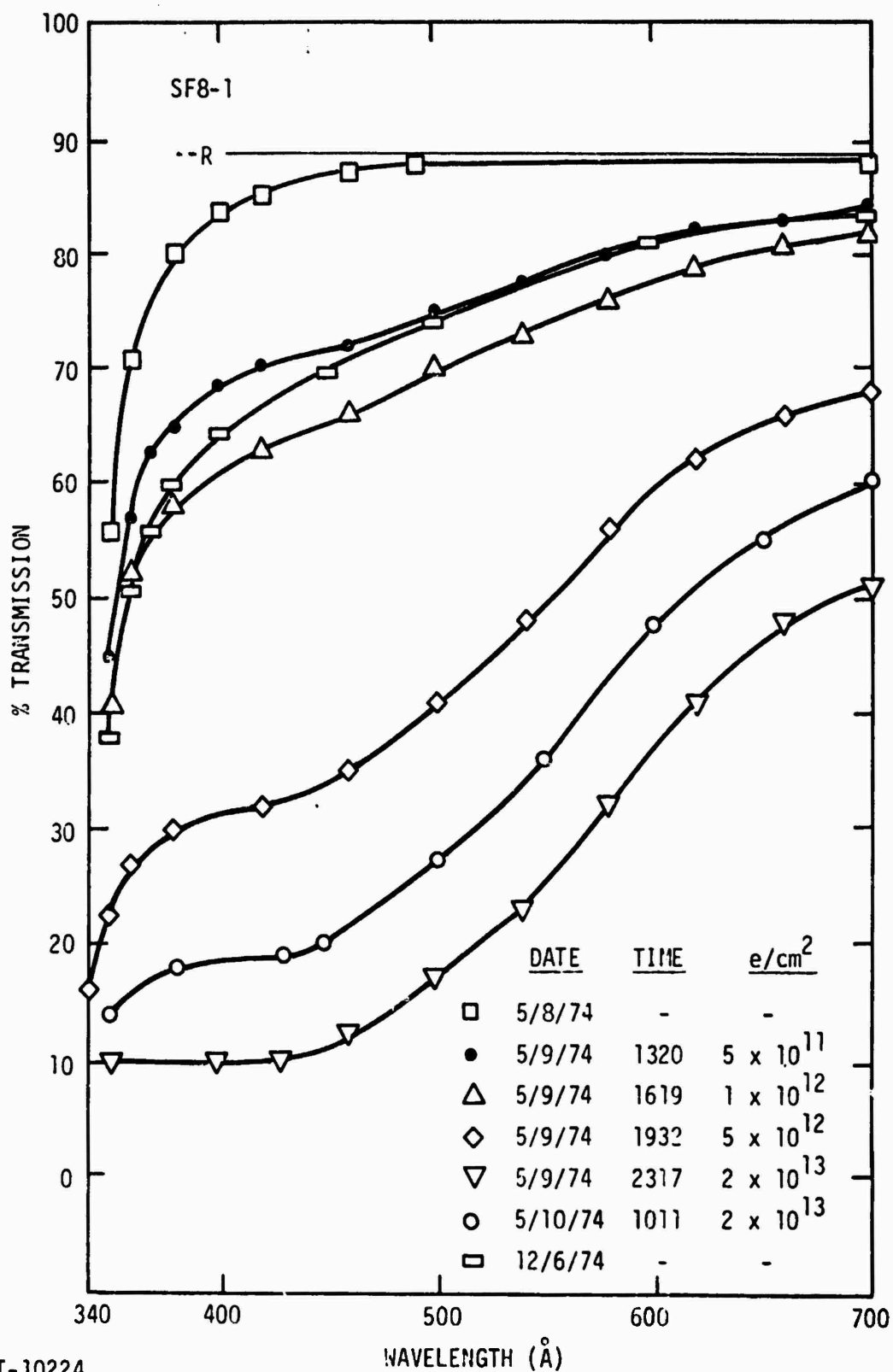
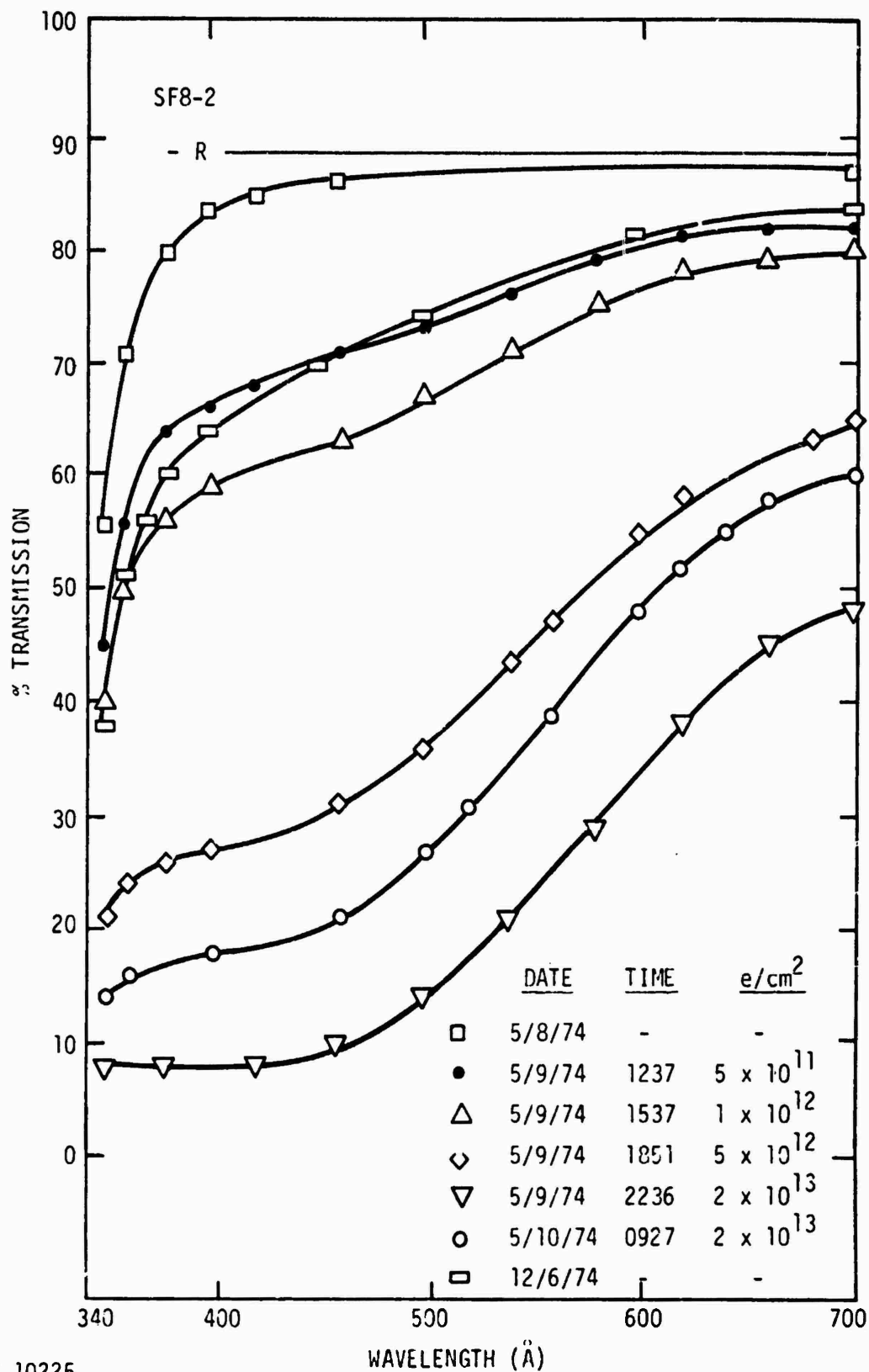


Figure B-6 Spectral transmission of SF1-G7-2 glass as a function of fluence and thermal bleach time (samples in the dark and at room temperature)



RT-10224

Figure B-7 Spectral transmission of SF8-1 glass as a function of fluence and thermal bleach time (samples in the dark and at room temperature)



RT-10225

Figure B-8 Spectral transmission of SF8-2 glass as a function of fluence and thermal bleach time (samples in the dark and at room temperature)

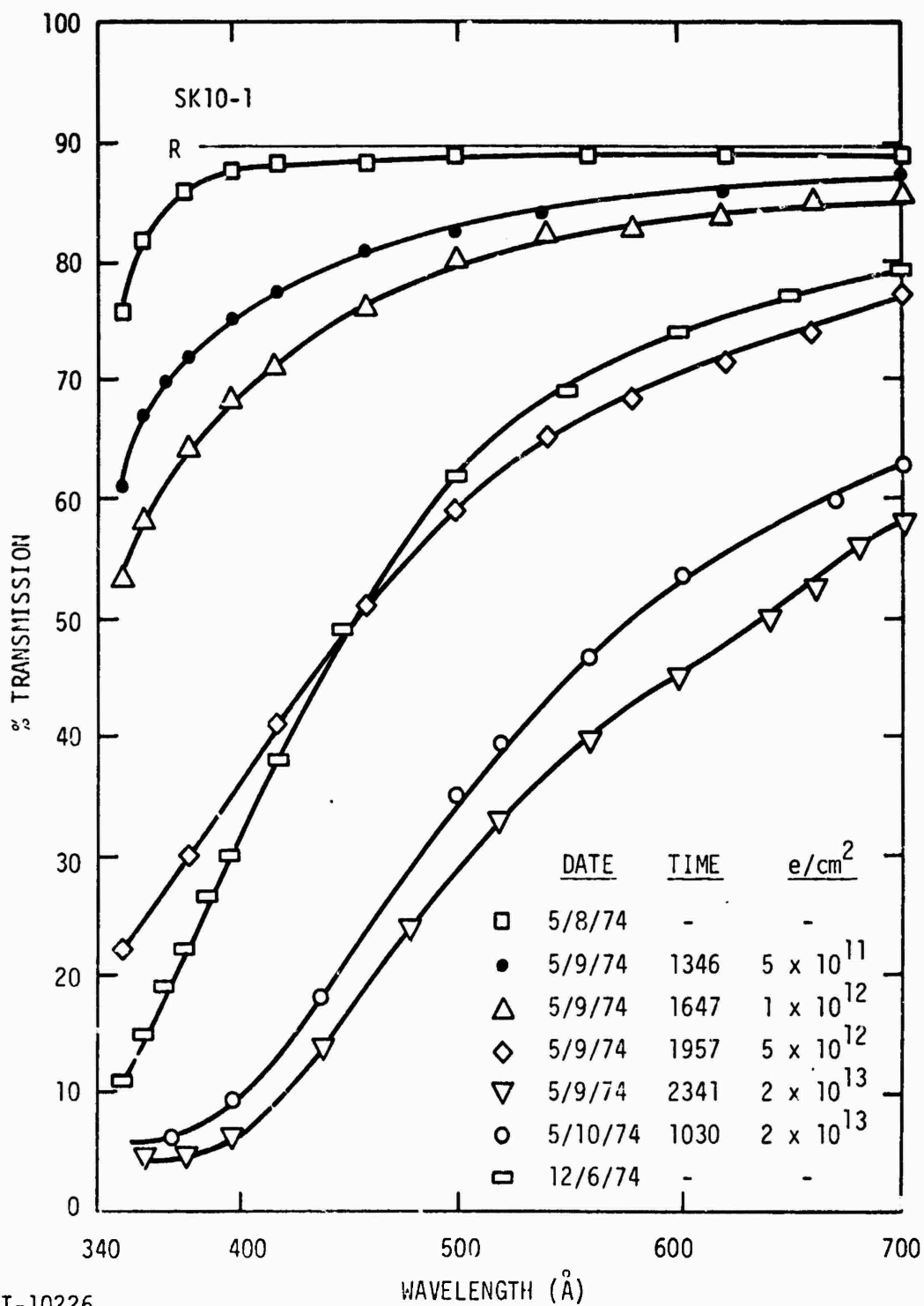
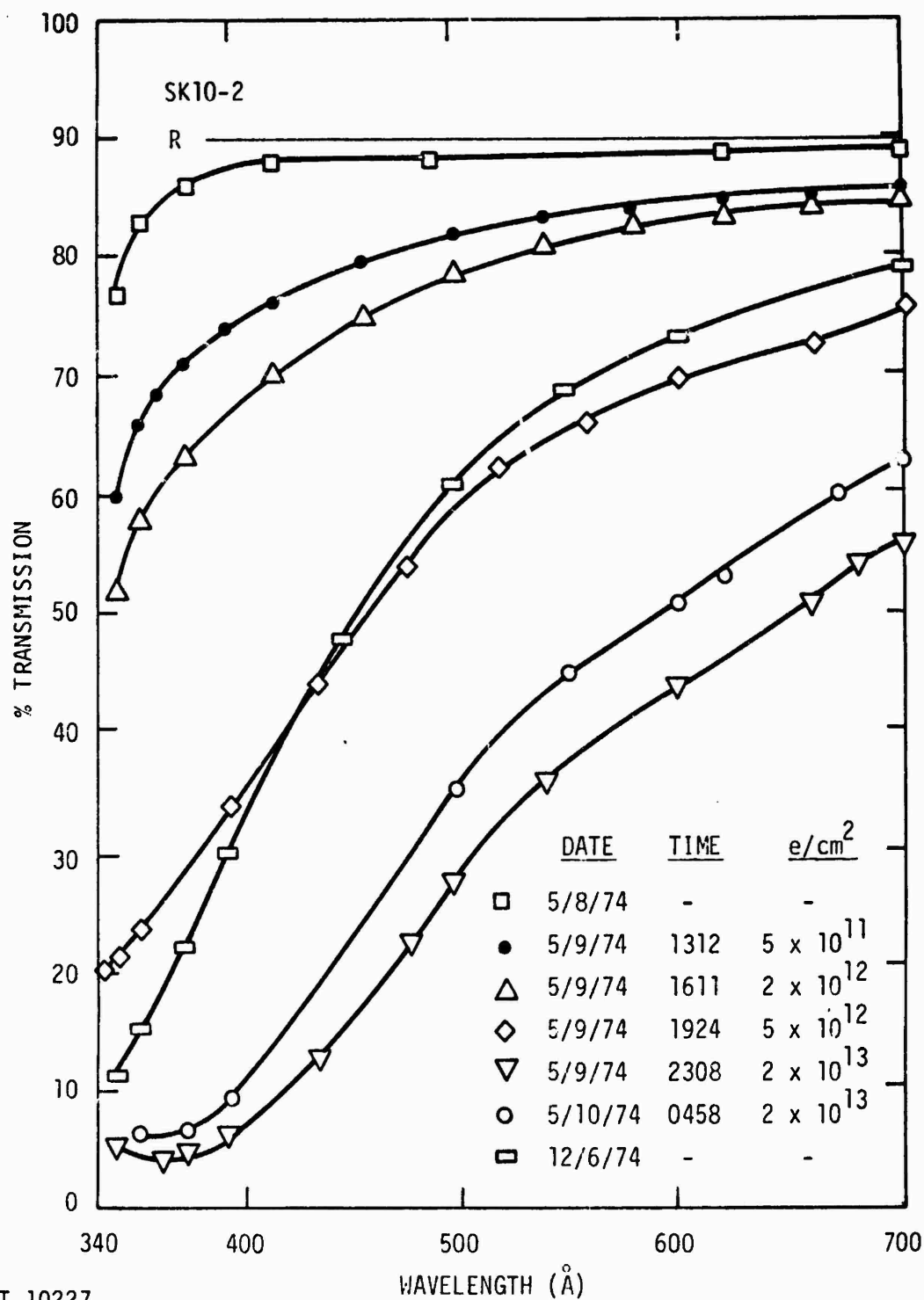


Figure B-9 Spectral transmission of SK10-1 glass as a function of fluence and thermal bleach time (samples in the dark and at room temperature)



RT-10227

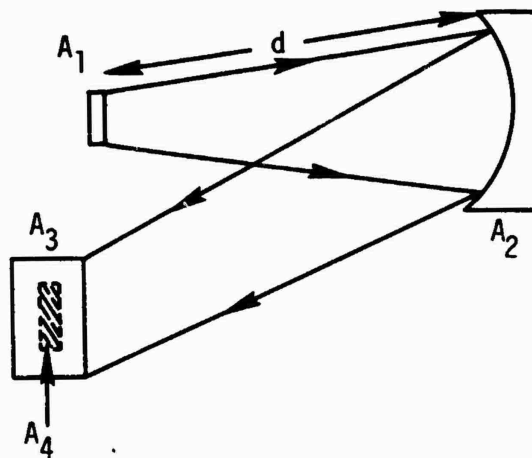
Figure B-10 Spectral transmission of SK10-2 glass as a function of fluence and thermal bleach time (samples in the dark and at room temperature)

The three other glass types — BaSF-52, SF-8, and SK-10 — showed appreciable loss in transmission at 5×10^{11} e/cm² and severe loss in transmission at 2×10^{13} e/cm². The darkened glass also showed significant recovery of transmission during the 10-hour storage at room temperature in the dark, and even greater recovery after extended storage. The horizontal line on each figure represents the calculated transmission loss due to surface reflection.

It is interesting to compare these glasses with those previously irradiated with ⁶⁰Co gammas (Appendix A) to look for similarities or differences within families of glasses. For example, Figure A-7 shows the relative transmission of BaK4 barium-doped crown glass, and there is strong evidence in that figure of an optical absorption band in the vicinity of 3600 Å. However, Figures B-1 and B-2 show no particular sign of the 3600 Å absorption band in BaSF-52, which is a barium-doped short flint glass. On the other hand, Figures A-5 and A-6, which show the change in transmission of two short flint glasses (SF-10 and SF-11), might be compared with Figures B-7 and B-8, which show the change in transmission of SF-8 glass. There seems to be some indication of an absorption band at about 4200 Å in SF-8, while no such band is readily observed in SF-10 or SF-11. Likewise, Figures A-1 and A-2 show some sign of absorption bands between 5000 and 6000 Å in SK-7 and SK-14 glass, whereas Figures B-9 and B-10 show little evidence of such a band in SK-10 glass, although the overall loss of transmission with fluence is relatively similar.

APPENDIX C ABSOLUTE INTENSITY CALIBRATION OF THE *IN-SITU* OPTICAL SYSTEM

The following model can be used to better understand the parameters contained in this calibration.



Consider a standard source* of spectral emittance[†] $M(\lambda)$ and area A_1 radiating into an optical system with entrance area A_2 at a distance d from A_1 to form an image of area A_3 . The power per unit wavelength at the image A_3 is, assuming the radiance $M(\lambda)/\pi$ is independent of angle (Lambertian) and $\cos \theta \approx 1$ (near normal viewing angle)

$$P_3(\lambda) = \frac{M(\lambda)}{\pi} \frac{A_1 A_2}{d^2} L(\lambda) ,$$

where $L(\lambda)$ is the optical loss factor for transmission from A_1 to A_3 . This would include atmospheric absorption and optical system losses. The factor $\frac{M(\lambda)}{\pi}$ is the spectral radiance (power emitted per unit source area per steradian per unit wavelength) into a small solid angle A_2/d^2 near the normal of a planar "Lambertran" source. This is a reasonable

*The spectral emittance₂ units here are power per unit source area per unit wavelength, or watts/cm²-μm.

†G. E. 30A/T24/3 tungsten lamp with a quartz window. These lamps have a large flat filament, which to our optical system looks like an infinite plane radiator.

approximation for the General Electric standard lamp and is thought to reasonably represent the irradiance from the emitting surface of a uniformly excited luminescence sample. If spherical luminescence samples had been employed, then a spherically emitting standard source would have been more appropriate in the calibration. In such a case the irradiance would have been $M(\lambda)/4$ but the calibration factor would be the same. The monochromator slit area, A_4 , selects a fraction A_4/A_3 of this power. The power is further reduced by the monochromator transmission function, $T(\lambda', \lambda)$, which allows a narrow band of wavelengths $\Delta\lambda$ through the monochromator when the dial is set for λ' , and then

$$dP(\lambda', \lambda) = P_3(\lambda) \frac{A_4}{A_3} T(\lambda', \lambda) d\lambda .$$

This produces a calibration current in the phototube,

$$dI_C(\lambda', \lambda) = P_3(\lambda) \frac{A_4}{A_3} T(\lambda', \lambda) S(\lambda) d\lambda ,$$

where $S(\lambda)$ is the photomultiplier response function. Thus, the total current for a monochromator setting of λ' is

$$I_C(\lambda') = \int_0^\infty \frac{M(\lambda)}{\pi} \frac{A_1 A_2}{d^2} \frac{A_4}{A_3} L(\lambda) T(\lambda', \lambda) S(\lambda) d\lambda .$$

The function $T(\lambda', \lambda)$ is also a function of A_4 . In our experiments, we held this constant for a given calibration. $T(\lambda', \lambda)$ is non-zero only for wavelengths near λ' , and if $M(\lambda)$ and $L(\lambda)$ are approximately constant over the $\Delta\lambda$ for which $T(\lambda', \lambda)$ is significantly different from zero, $I_C(\lambda')$ can be written as

$$I_C(\lambda') = \frac{M(\lambda)}{\pi} \frac{A_1 A_2}{d^2} \frac{A_4}{A_3} L(\lambda') \int_{\lambda' - \Delta\lambda/2}^{\lambda' + \Delta\lambda/2} T(\lambda', \lambda) S(\lambda) d\lambda .$$

As long as the optical system geometry, monochromator slit widths, photomultiplier voltage, and atmosphere do not change, one can lump the

above integral and certain constants in the single spectrally dependent calibration factor $\kappa(\lambda')$, so that

$$I_C(\lambda') = \kappa(\lambda') \frac{M(\lambda')}{\pi}.$$

Knowing $M(\lambda)$ and measuring $I_C(\lambda)$, $\kappa(\lambda')$ can be determined, and for a source of unknown spectral radiance $R(\lambda')$,

$$R(\lambda') = \frac{I(\lambda')}{\kappa(\lambda')}, \quad (1)$$

provided the geometrical factors are constant that the sample and calibration standard have the same radiation pattern and assuming that $R(\lambda')$ is approximately constant over the $\Delta\lambda$ bandpass around λ' .

It should be noted that while the luminescence sample dimensions were appreciably greater along the optic axis than the calibration sources, they were, nevertheless, small compared to the sample-collection mirror separation (d) so that no correction for sample size was considered necessary.

Spectrally integrated luminescence measurements were made by using the VUV monochromator zero order, where the grating acts much the same as a mirror. Absolute calibration of the optical system for making these measurements was performed in much the same as the calibration described above. The monochromator wavelength reading was set on zero, and a standard source was placed at the sample position. A narrow-band-pass filter with transmission centered at λ_1 was placed between the exit slit and the photomultiplier. The photomultiplier current was measured using a 1-M Ω resistor and a Texas Instruments strip chart recorder. The current was noted at the "zero order" $I(0)$ and then the monochromator was scanned through the region in which the band-pass filter transmitted while the "spectrum" was recorded on the strip chart recorder as a function of wavelength. This spectrum was corrected for the monochromator response by using the calibration curve shown in Figure 7 of the basic document. This corrected spectrum was plotted and the area under the curve was determined by mechanical integration to be some factor A (mW/cm²). The ratio of A to $I(0)$ yields the desired calibration factor (mW/cm²- μ A).

This procedure was carried out for three band-pass filters which peaked at 3670, 4910, and 6800 Å for which calibration factors of 0.086, 0.11, and 0.28 mW/cm²-μA, respectively, were calculated. Since the photomultiplier response is relatively wavelength-independent in this wavelength region, the factor of three variation in the calibration curve must be due to a spectral dependence of the reflectivity of the grating.

As shown in Figures 27-35 of the basic document, most of the glasses showed little transmission at wavelengths shorter than 3600 Å after exposure to low fluences. Consequently, the luminescence observed from these samples must be at wavelengths longer than 3600 Å. Since no information was available on the spectral nature of radioluminescence of the samples used in this investigation, and in view of the sample-darkening below 3600 Å, it was felt that an average of the 4910 and 6800 Å calibration factors would be a reasonably accurate value.

An estimate of the accuracy of the "zero-order" calibration was obtained by mechanically integrating the luminescent spectrum shown in Figure 54 and comparing this value to the spectrally integrated intensity obtained from Figure 48. (The latter was determined using the average zero-order calibration factor of 0.18 mW/cm²-μA.) The values obtained were 1.6×10^{-3} and 5.6×10^{-3} mW/cm², respectively. The agreement here is not as good as one would like, but it isn't bad when consideration is given to two facts: (1) As pointed out in Section 4.3, the BK7-G14 luminescence decreases with exposure time, and (2) luminescence signals which were too weak to be observed spectrally and which are very broad-band can greatly increase the spectrally integrated intensity. Both of these effects would result in the value obtained by the mechanical integration (1.6×10^{-3} mW/cm²) being smaller than its actual value.

APPENDIX D TEMPORAL BLEACHING CORRECTIONS TO DARKENING CURVES

This appendix describes the procedure used to obtain the corrected spectra shown in Figures 27 through 35 of the basic document. As described in Section 3.1.3, the Schott glass samples were irradiated to a fluence of $\sim 5.6 \times 10^{13} \text{ e/cm}^2$, and the induced absorption, $\alpha_1(\lambda)$, was measured within 2 to 3 min of the end of the irradiation. Approximately 1 hour later, the samples were exposed to $\sim 5.6 \times 10^{14} \text{ e/cm}^2$ (total), and the absorption $\alpha_2'(\lambda)$ was measured within 2 to 3 min of the irradiation. In some cases, $\alpha_1(\lambda) > \alpha_2'(\lambda)$. Why?

It is known that the Schott glasses exhibit temporal bleaching; spectra exist at various times after exposure to a fluence of $8 \times 10^{13} \text{ e/cm}^2$ (Figures 18-26). So the cause for $\alpha_1(\lambda) > \alpha_2'(\lambda)$ could be due mainly to bleaching which occurred between the irradiations, since the time between irradiations was much greater than the irradiation time. How, then, can the spectra be corrected for this bleaching?

Let

$\alpha_1(\lambda)$ = absorption at end of irradiation 1,

$\alpha_1'(\lambda)$ = absorption at beginning of irradiation 2,

$\Delta\alpha(\lambda)$ = absorption change due to irradiation 2,

$\alpha_2'(\lambda)$ = absorption observed at end of irradiation 2,

$\alpha_2(\lambda)$ = absorption that would have been observed at end of irradiation 2 if no bleaching occurred.

The desired quantity, $\alpha_2(\lambda)$, can be written as

$$\alpha_2(\lambda) = \alpha_1(\lambda) + \Delta\alpha(\lambda) \tag{1}$$

What we actually measured was $\alpha_1(\lambda)$ and

$$\alpha_2'(\lambda) = \Delta\alpha(\lambda) + \alpha_1'(\lambda) . \tag{2}$$

Combining Eqs. 1 and 2,

$$\begin{aligned}\alpha_2(\lambda) &= \alpha_1(\lambda) + \alpha_2'(\lambda) - \alpha_1'(\lambda) \\ &= \alpha_2'(\lambda) + [\alpha_1(\lambda) - \alpha_1'(\lambda)] ,\end{aligned}\tag{3}$$

which is simply the measured absorption at the end of the second irradiation plus the bleaching that occurred between the irradiations. The latter quantity is needed to obtain $\alpha_2(\lambda)$. This quantity can be determined if we assume that the bleaching can be described by

$$\frac{\alpha_1'(\lambda)}{\alpha_1(\lambda)} = A \ln t .$$

(This is a reasonable assumption in light of the results of Section 3.1.2.)

Knowing t , the time between irradiations, and $\alpha_1(\lambda)$, $\alpha_1'(\lambda)$ could be determined, and therefore, $\alpha_2(\lambda)$ could also be determined.

Despite the apparent simplicity of this procedure, it worked quite well (see Figures 27-35).

The uncorrected spectra are included here for completeness. Note that the SF-10 and SF-11 spectra (Figures 30 and 31) were not corrected due to the flux dependence of the bleaching rates for these samples, discussed in Section 3.1.4 of the basic document.

	SAMPLE NO.	FLUX (e/cm^2 -sec)	FLUENCE (e/cm^2)	TIME AFTER IRRAD (sec)	TIME BETWEEN DATA (min)
a	PREIRRAD	-	-	-	-
a	NV7	8.7×10^9	5.6×10^{10}	98	-
b	NV7	9.5×10^9	5.6×10^{11}	86	44.1
c	NV7	1.0×10^{10}	5.6×10^{12}	93	74.2
d	NV5	9.7×10^{11}	5.6×10^{12}	84	-
e	NV6	9.8×10^{11}	5.6×10^{13}	93	34.0
f	NV6	1.0×10^{12}	5.6×10^{14}	87	104.5
g	NV9	1.1×10^{11}	8.1×10^{13}	233	-
h	NV10	2.5×10^{11}	2.5×10^{13}	115	-

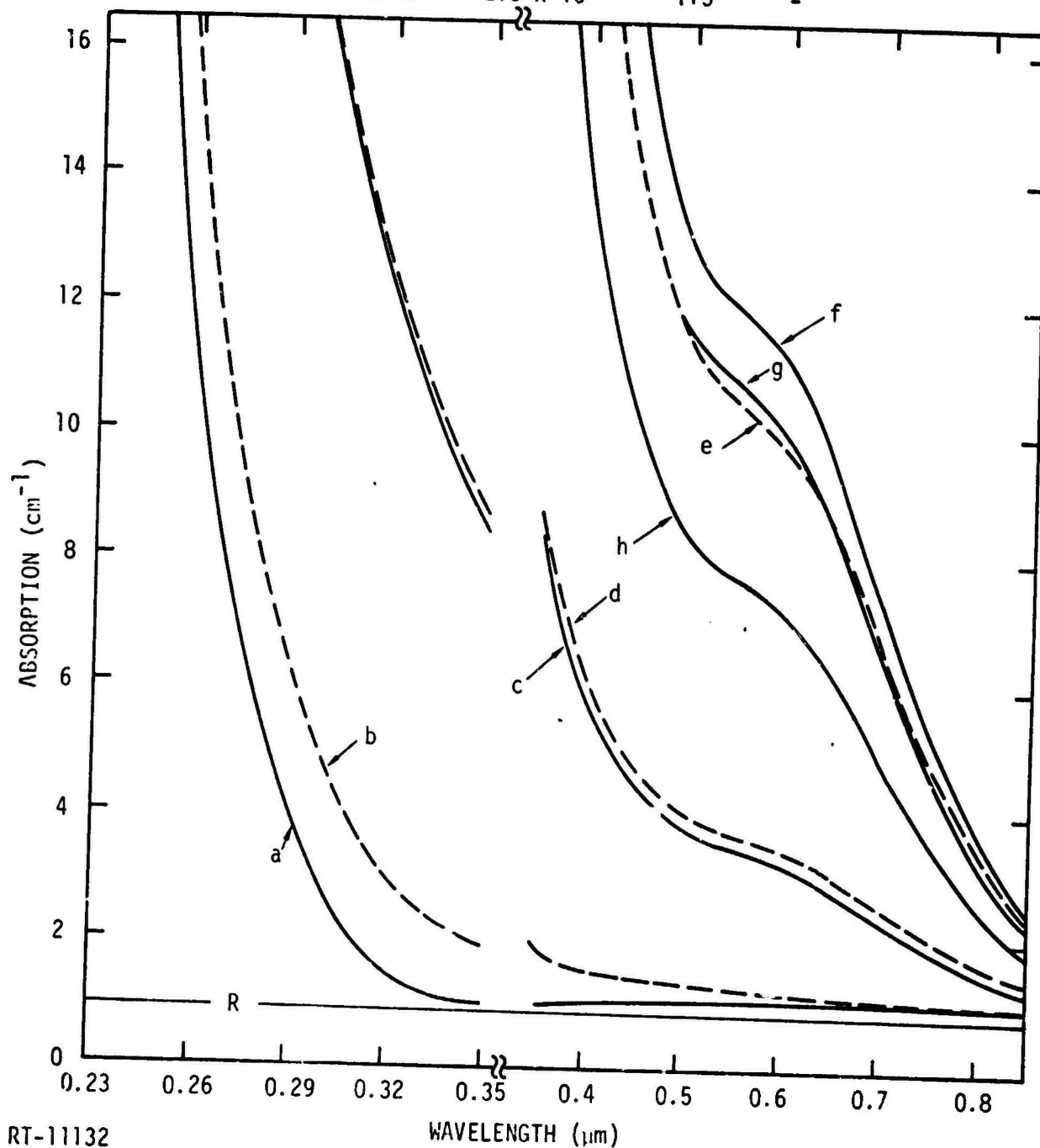


Figure D-1 SK-14 absorption spectra at several fluences; not corrected for bleaching

	SAMPLE NO.	FLUX (e/cm ² -sec)	FLUENCE (e/cm ²)	TIME AFTER IRRAD (sec)	TIME BETWEEN DATA (min)
a	PREIRRAD	-	-	-	-
a	XV7	8.7×10^9	5.6×10^{10}	423	-
b	XV7	9.5×10^9	5.6×10^{11}	476	45.2
c	XV7	1.0×10^{10}	5.6×10^{12}	423	73.2
d	XV6	9.8×10^{11}	5.6×10^{12}	414	-
e	XV6	9.8×10^{11}	5.6×10^{13}	348	33.6
e	XV6	1.0×10^{12}	5.6×10^{14}	201	102.1
f	XV9	1.1×10^{11}	8.1×10^{13}	222	-
g	XV5	2.5×10^{11}	2.5×10^{13}	460	-

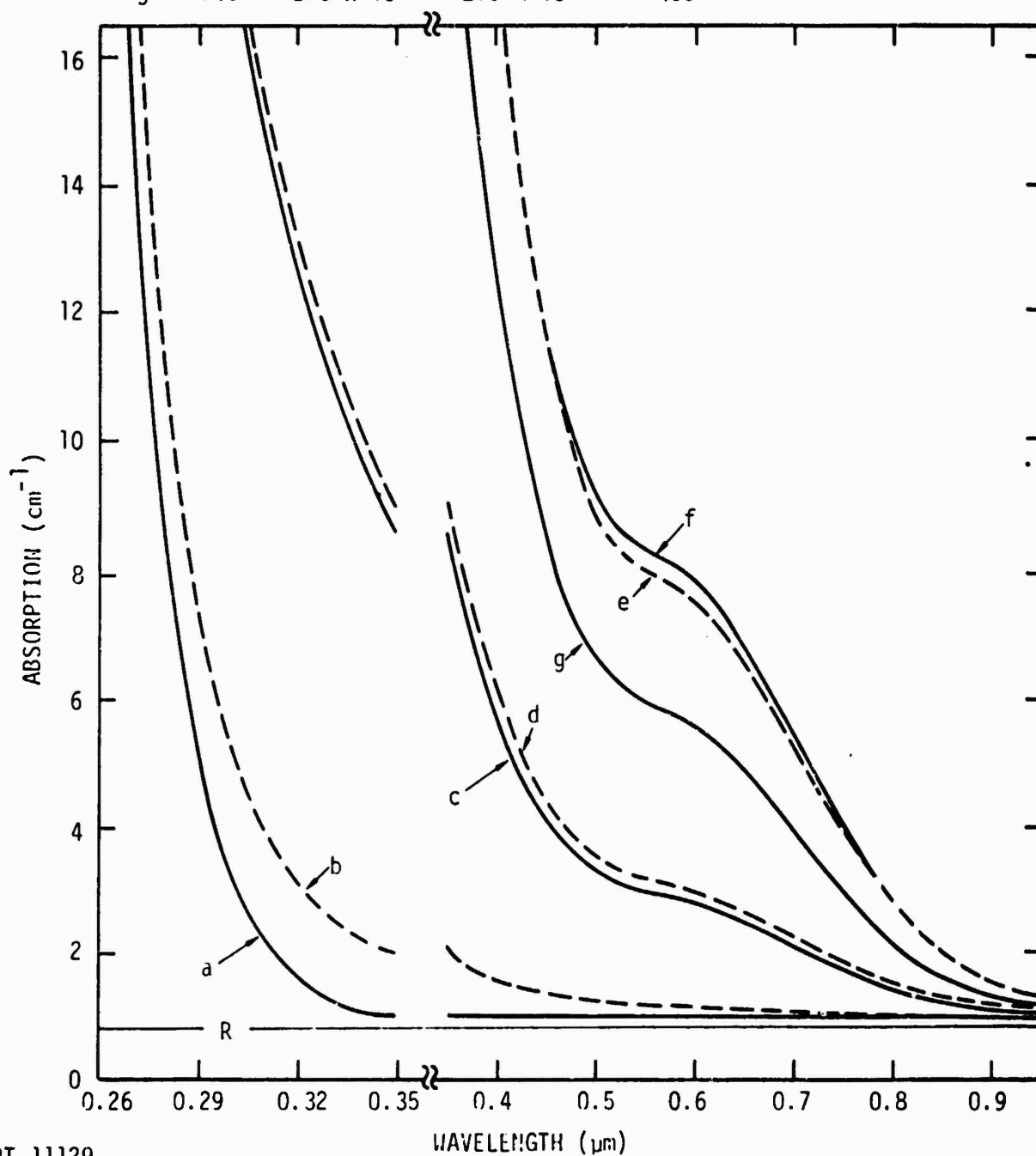
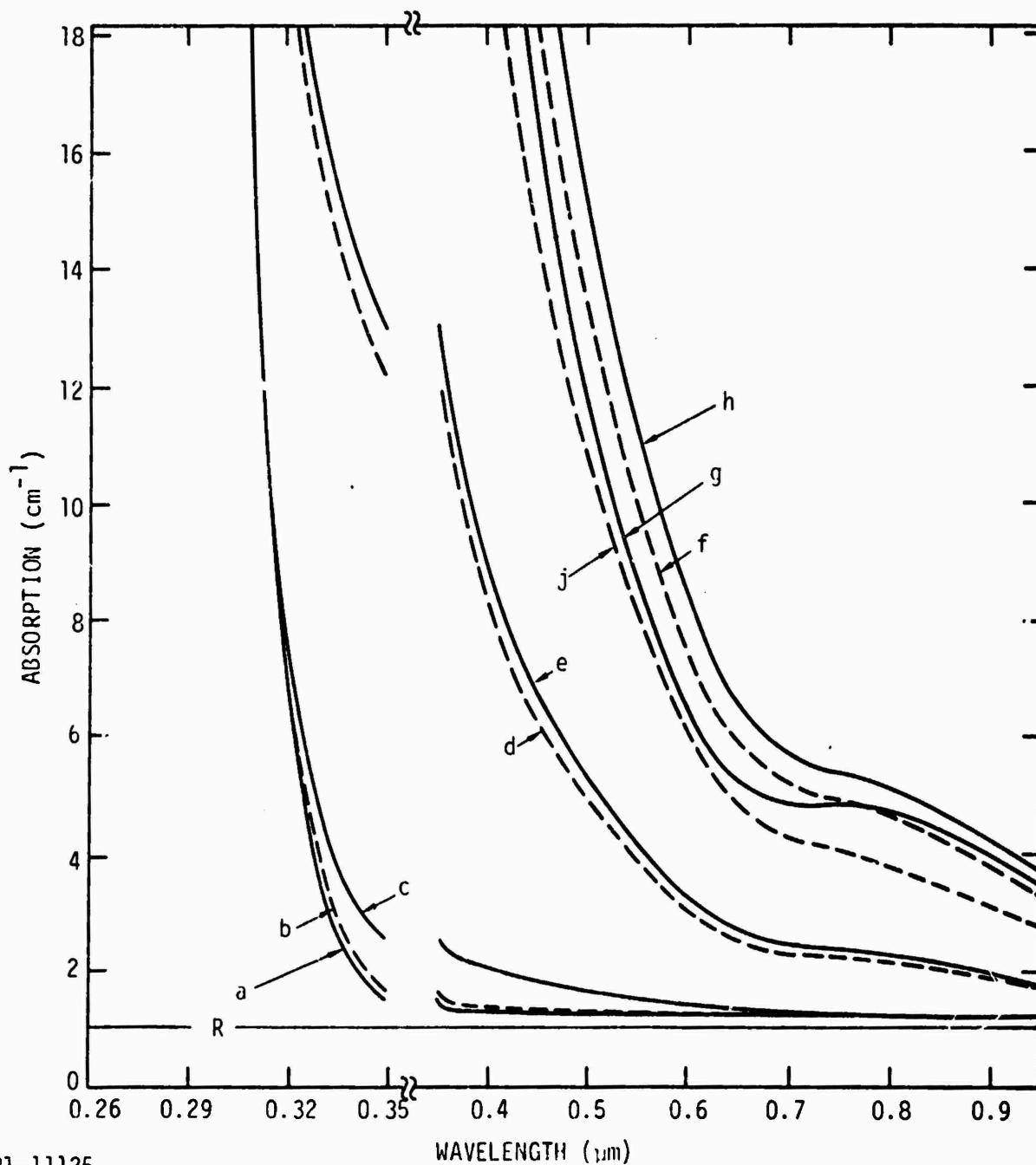


Figure D-2 SK-7 absorption spectra at several fluences; not corrected for bleaching

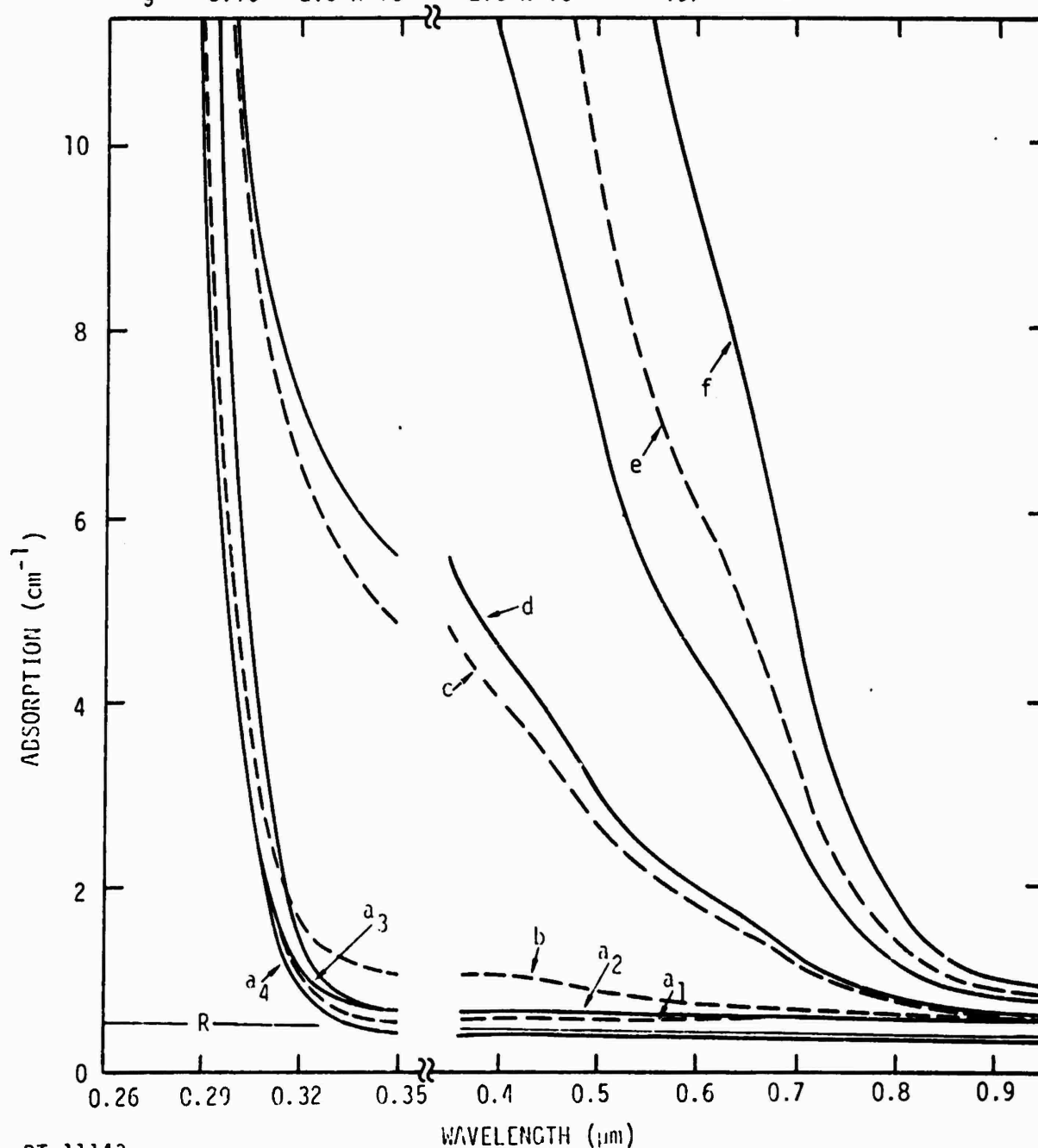
	SAMPLE NO.	FLUX (e/cm ² -sec)	FLUENCE (e/cm ²)	TIME AFTER IRRAD (sec)	TIME BETWEEN DATA (min)
a	PREIRRAD	-	-	-	-
b	LV7	7.5×10^9	5.6×10^{10}	514	-
c	LV7	8.7×10^9	5.6×10^{11}	482	39.6
d	LV7	1.0×10^{10}	5.6×10^{12}	554	71.2
e	LV6	9.2×10^{11}	5.6×10^{12}	423	-
f	LV6	1.0×10^{12}	5.6×10^{13}	569	40.2
g	LV6	1.0×10^{12}	5.6×10^{14}	269	70.8
h	LV9	1.1×10^{11}	8.1×10^{13}	102	-
j	LV10	2.5×10^{11}	2.5×10^{13}	620	-



R1-11125

Figure D-3 LaK-10 absorption spectra at several fluences; not corrected for bleaching

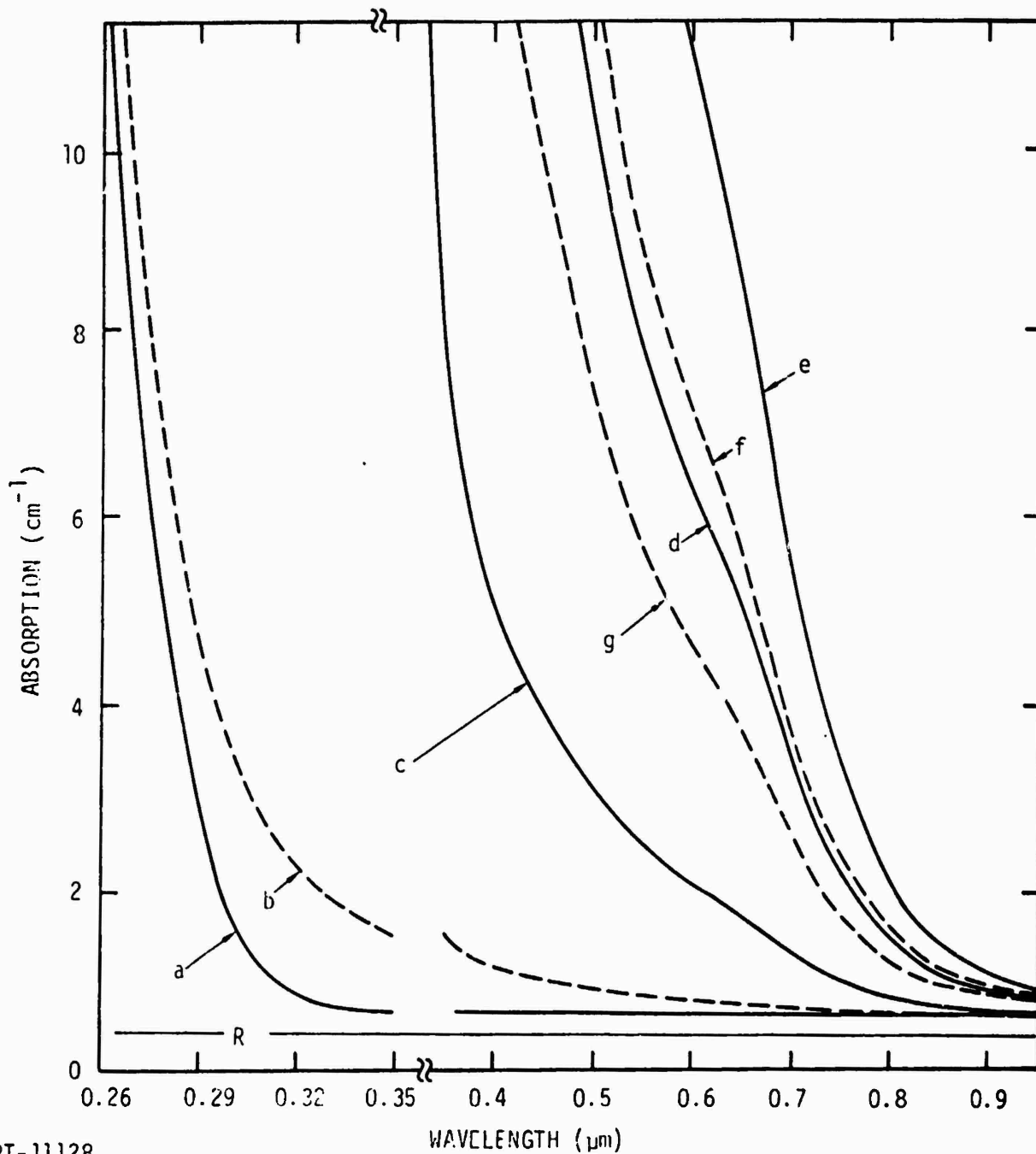
	SAMPLE NO.	FLUX ($\text{e}/\text{cm}^2\text{-sec}$)	FLUENCE (e/cm^2)	TIME AFTER IRRAD (sec)	TIME BETWEEN DATA (min)
a ₁	CV6	PREIRRAD		-	-
a ₂	CV7	PREIRRAD		-	-
a ₃	CV9	PREIRRAD		-	-
a ₄	CV10	PREIRRAD		-	-
a ₂	CV7	7.5×10^9	5.6×10^{10}	322	-
b	CV7	9.6×10^9	5.6×10^{11}	278	38
c	CV7	1.0×10^{10}	5.6×10^{12}	312	60.6
d	CV6	8.6×10^{11}	5.6×10^{12}	223	-
e	CV6	1.0×10^{12}	5.6×10^{13}	204	36.4
f	CV6	1.0×10^{12}	5.6×10^{14}	186	44.3
e	CV9	1.1×10^{11}	8.1×10^{13}	384	-
g	CV10	2.5×10^{11}	2.5×10^{13}	197	-



RT-11143

Figure D-4 BK-7 absorption spectra at several fluences; not corrected for bleaching

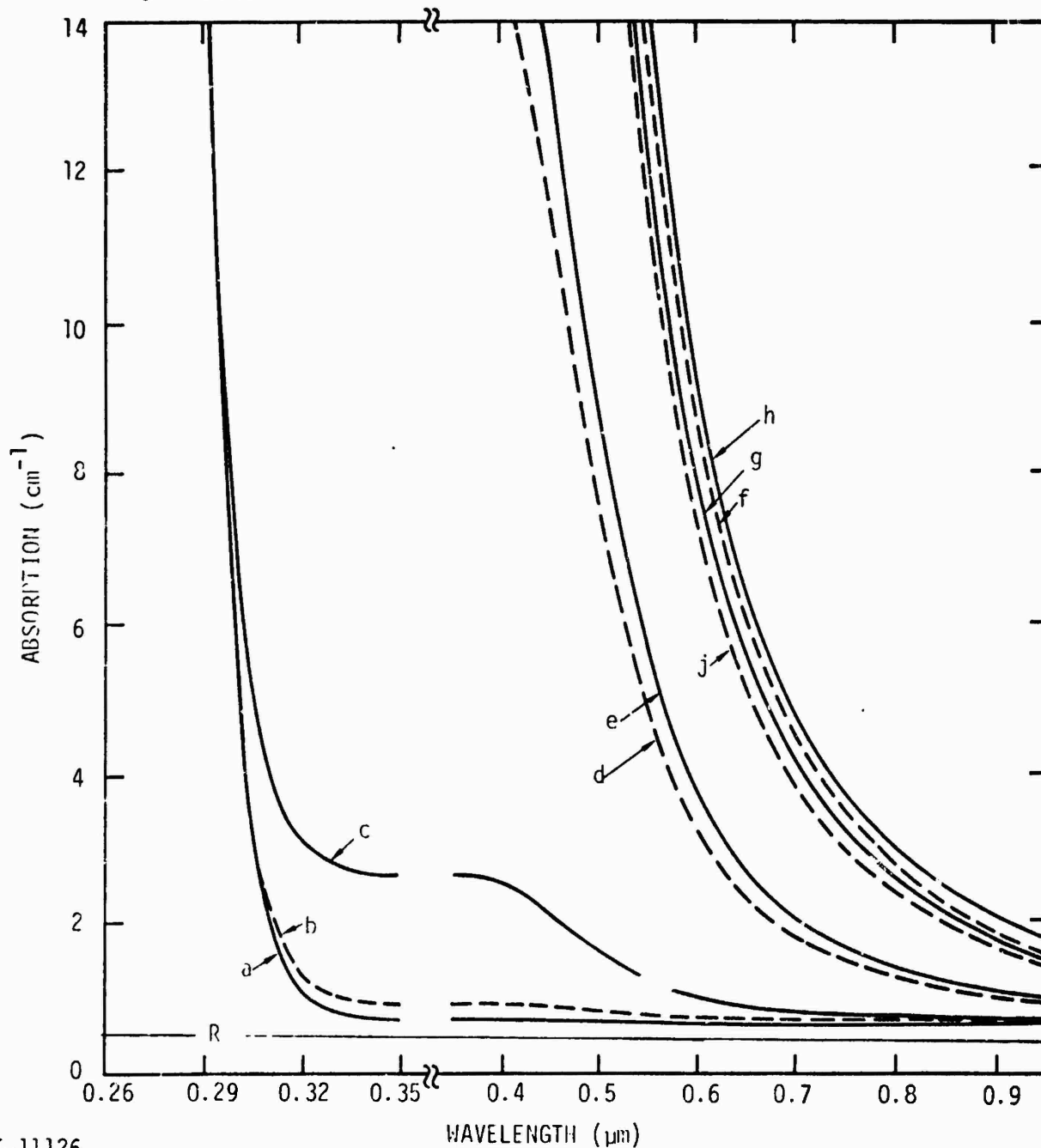
	SAMPLE NO.	FLUX ($\text{e}/\text{cm}^2\text{-sec}$)	FLUENCE (e/cm^2)	TIME AFTER IRRAD (sec)	TIME BETWEEN DATA (min)
a	PREIRRAD	-	-	-	-
a	HV7	7.5×10^9	5.6×10^{10}	86	-
b	HV7	8.7×10^9	5.6×10^{11}	86	40.3
c	HV7	1.0×10^{10}	5.6×10^{12}	100	70.2
c	HV6	9.2×10^{11}	5.6×10^{12}	97	-
d	HV6	1.0×10^{12}	5.6×10^{13}	79	37.4
e	HV6	1.0×10^{12}	5.6×10^{14}	77	95.5
f	HV9	1.1×10^{11}	8.1×10^{13}	98	-
g	HV10	2.5×10^{11}	2.5×10^{13}	110	-



RT-11128

Figure D-5 UBK-7 absorption spectra at several fluences; not corrected for bleaching

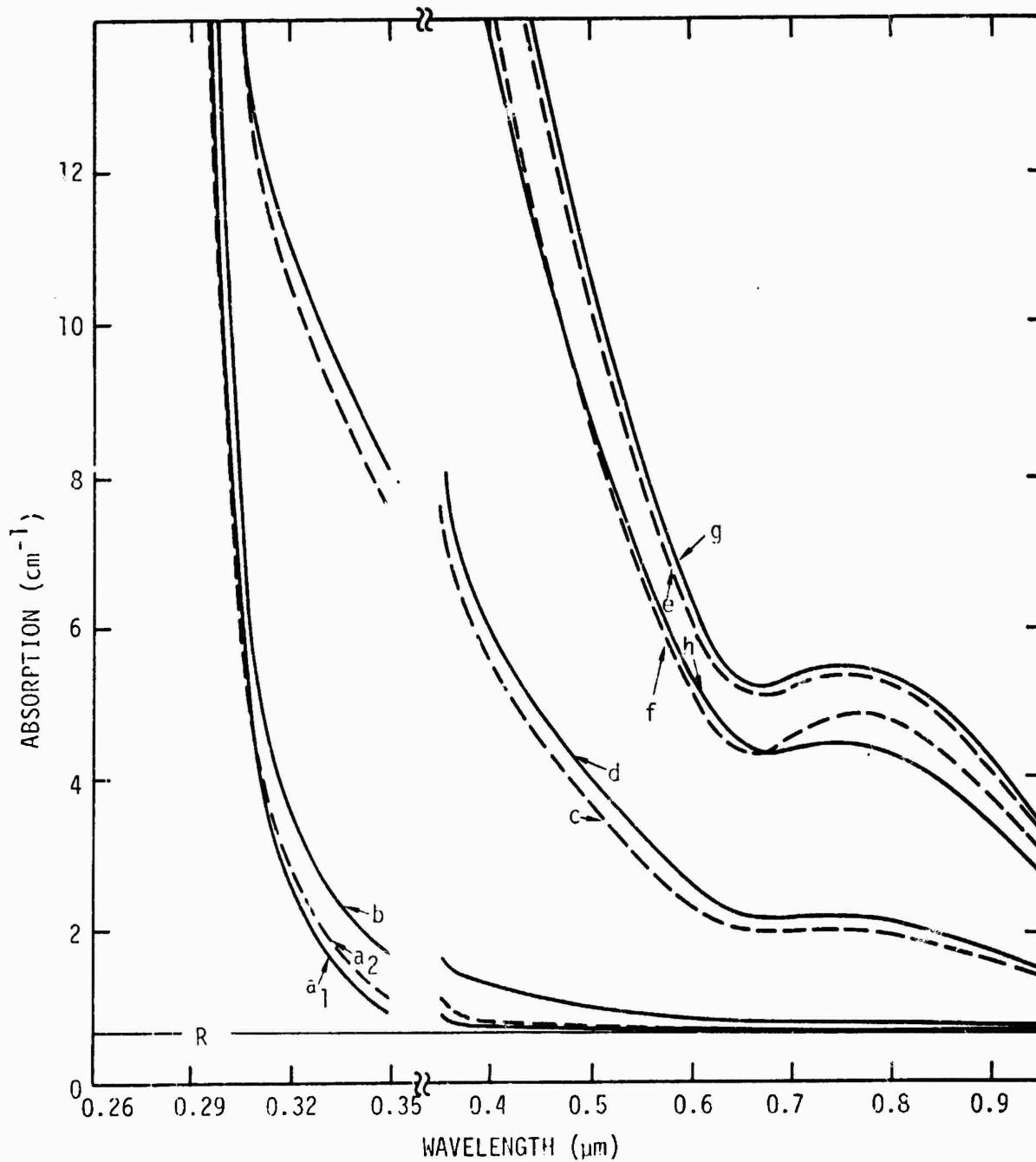
	SAMPLE NO.	FLUX ($\text{e}/\text{cm}^2\text{-sec}$)	FLUENCE (e/cm^2)	TIME AFTER IRRAD (sec)	TIME BETWEEN DATA (min)
a	PREIRRAD				
b	BA7	7.5×10^9	5.6×10^{10}	116	-
c	BA7	9.6×10^9	5.6×10^{11}	84	38.2
d	BA7	9.9×10^9	5.6×10^{12}	112	58.5
e	BA6	8.6×10^{11}	5.6×10^{12}	85	-
f	BA6	1.01×10^{12}	5.6×10^{13}	91	36.8
g	BA6	1.0×10^{12}	5.6×10^{14}	93	44.6
h	BA9	1.1×10^{11}	8.1×10^{13}	94	-
j	BA11	2.5×10^{11}	2.5×10^{13}	115	-



RT-11126

Figure D-6 BaK-4 absorption spectra at several fluences; not corrected for bleaching

	SAMPLE NO.	FLUX ($\text{e}/\text{cm}^2\text{-sec}$)	FLUENCE (e/cm^2)	TIME AFTER IRRAD (sec)	TIME BETWEEN DATA (min)
a ₁	KV6, KV7, KV9	PREIRRAD		-	-
a ₂	KV10	PREIRRAD		-	-
a ₁	KV7	7.5×10^9	5.6×10^{10}	308	-
b	KV7	8.7×10^9	5.6×10^{11}	282	39.9
c	KV7	1.0×10^{10}	5.6×10^{12}	259	69.6
d	KV6	9.2×10^{11}	5.6×10^{12}	248	-
e	KV6	1.0×10^{12}	5.6×10^{13}	179	36.5
f	KV6	1.0×10^{12}	5.6×10^{14}	164	95.2
g	KV9	1.1×10^{11}	8.1×10^{13}	203	-
h	KV10	2.5×10^{11}	2.5×10^{13}	207	-



RT-11142

Figure D-7 KzFSN-4 absorption spectra at several fluences; not corrected for bleaching

APPENDIX E
LITERATURE SURVEY

Considering the activity in radiation effects studies and optical investigations, and the ubiquitous nature of glass, there seems to be surprisingly little literature concerning radiation effects in glassy materials. Listed below, however, are twenty references which pertain to this subject. These could serve as a starting point for an investigator interested in this subject.

1. T. M. Flanagan and T. F. Wrobel, IEEE Trans. Nucl. Sci. **16**, 130 (1969).
2. E. J. Friebele, R. J. Ginther, and G. M. Sigel Jr., Appl. Phys. Lett. **24**, 412 (1974).
3. R. J. Ginther et al., "Physics and Chemistry of Glasses," NRL Memorandum Report 2590, May 1973.
4. M. Goldberg et al., Nucl. Instr. and Methods **108**, 119 (1973).
5. D. F. Heath and P. A. Sacher, Appl. Optics **5**, 937 (1966).
6. J. F. Holzrichter and J. L. Emmett, J. Appl. Phys. **40**, 159 (1969).
7. P. W. Levy, J. Am. Ceram. Soc. **43**, 389 (1960).
8. P. L. Mattern et al., "Radiation-Induced Absorption and Luminescence in Glass and Plastic Optical Waveguides," pres. at Integrated Optics and Fiber Optics Communication Conference, NELC, San Diego, May 15-17, 1974.
9. P. L. Mattern et al., "The Effects of Radiation on the Absorption and Luminescence of Fiber Optics Waveguides and Materials," pres. at 1974 IEEE Annual Conference on Nuclear and Space Radiation Effects, Fort Collins, Colorado, July 15-19, 1974.
10. C. A. Nicoletta and A. G. Eubanks, "Effects of Simulated Space Radiation on Selected Optical Materials," Appl. Optics **11**, 1365, June 1972.
11. N. F. Orlov and N. A. Leko, "Absorption Centers Forming at Low Temperatures in Certain Glasses of Simple Composition," Zh. Prikl. Spektrosk. **4**, 2, 23 (1966), translated for Battelle-Northwest.
12. G. E. Palma and R. M. Gagosz, "Optical Absorption in Transparent Materials During 1.5-MeV Electron Irradiation," United Aircraft Corporation, NASA-CR-110907, October 1970.
13. G. E. Palma and R. M. Gagosz, "Effect of 1.5-MeV Electron Irradiations on the Transmission of Optical Materials," United Aircraft Corp., NASA-CR-123187, September 1971.

14. G. E. Palma and R. M. Gagosz, "Optical Absorption in Fused Silica During Irradiation," J. Phys. Chem. Solids 33, 177 (1972).
15. K. Patek, Glass Lasers, CRC Press, Ohio, 79-81280 (1970).
16. J. Romanko et al., "Spectrographic Studies of Optical Materials," NASA-CR-66758, March 1969.
17. G. H. Sigel Jr., "Radiation Effects in Fiber Optic Waveguides," NRL Memorandum Report 2704, December 1973.
18. G. H. Sigel Jr. and B. D. Evans, Appl. Phys. Lett. 24, 410 (1974).
19. G. H. Sigel Jr., J. Phys. Chem. Solids 32, 2373 (1971).
20. J. A. Wall, "Transient Radiation Effects Tests on a Corning Radiation-Resistant Optical Fiber," AFCRL-TR-75-0012, January 6, 1975.